HZB Helmholtz Zentrum Berlin

Ultrafast Photodynamics in Catalytic Molecular Compounds Studied by Femtosecond Time-Resolved EUV Photoemission and UV-Vis Absorption Spectroscopy

Dissertation
zur Erlangung des Grades eines
Doktors der Naturwissenschaften (Dr. rer. nat)

am Fachbereich Physik
der Freien Universität Berlin

angefertigt am Helmholtz-Zentrum Berlin für Materialien und Energie
Institut für Elektronische Struktur Dynamik

vorgelegt von

Nataliia Kuzkova

Berlin, 2023

Erstgutachter: Dr. Iain Wilkinson
Institute of Electronic Structure Dynamics
Helmholtz-Zentrum Berlin für Materialien und Energie

Zweitgutachter: Prof. Dr. Martin Weinelt
Department of Physics
Freie Universität Berlin

Tag der Disputation: 14.07.2023

Abstract

These studies address the fundamentals of ultrafast photophysical processes, in particular, electronic dynamics in catalytic molecular systems, relevant to sustainable and environmentally benign light-harvesting and energy transfer applications. The revelation of mechanisms occurring on ultrashort time scales provides insight into the dynamic electronic and structural behaviours of molecular compounds, which determine the efficiency of catalysts and facilitate their further development. In this work, the ultrafast photodynamics of two catalytic molecular compounds were investigated: the ferricyanide, $[Fe(CN)_6]^{3-}$, transition metal complex dissolved in the ionic liquid [emim][DCA] and polymeric carbon nitride (PCN) thin films. The femtosecond time-resolved photoemission spectroscopy (TRPES) technique was used to interrogate both systems on their fundamental time scales, employing tunable, extreme-ultraviolet (EUV), ultrashort probe pulses, as generated through the laser-driven high-order harmonic generation (HHG) process. The coherent, ultrashort pulse, HHG-based, table-top EUV source, allowed the photodynamical processes in the liquid- and solid-phase systems to be monitored with a sub-100 fs time resolution.

In an initial study, the relaxation dynamics of the $[Fe(CN)_6]^{3-}$ complex was investigated in a novel, ionic liquid solvent, 1-Ethyl-3-methylimidazolium dicyanamid ([emim][DCA]), following 400 nm optical excitation of the lowest-energy doublet ligand-to-metal charge-transfer (^{2}LMCT) state. By measuring transient photoemission signals of the populated electronic states, changes in the electronic configuration and relaxation pathways were monitored on a vacuum-level-referenced electron binding energy scale. Although solvent-dependent studies of the relaxation dynamics in $[Fe(CN)_6]^{3-}$ were previously performed, the relaxation mechanism has received controversial interpretations. This work establishes an ultrafast biexponential decay behavior of the initially populated electronic states of $[Fe(CN)_6]^{3-}$ dissolved in [emim][DCA] solution, confirming the mechanism observed in aqueous solution, which is associated with a sequence of intersystem crossings in the molecular compound. Furthermore, the ionic liquid environment yields considerably faster biexponential transition rates compared to the more commonly studied aqueous solution. This behavior was qualitatively explained on the basis of time-dependent density functional theory (TDDFT) calculations.

To examine the photoinduced electron dynamics in different PCN thin films upon 400 nm excitation at the solid-vacuum interface, combined femtosecond TRPES and ultraviolet-visible (UV-Vis) transient absorption spectroscopy (TAS) studies were performed. The TRPES experiments allowed the early-time-dependent population of electronically excited states in the PCN thin films to be mapped on an absolute binding energy scale with respect to the Fermi level at the solid-vacuum interface. Based on the obtained kinetic and spectral information, the lifetimes of the initially populated excited states of less than 1 ps were determined. The UV-Vis TAS experiments revealed the long-lived photodynamics in the PCN thin films at the bulk-vacuum interface. From the TAS experiments, a parallel transfer of the early-time excited state population to charge-transfer and singlet exciton excited states was identified, followed by fluorescent relaxation processes occurring on ps–ns time scales. The joint TRPES and TAS studies enabled the development of a kinetic model, which was effectively implemented to describe the ultrafast photodynamics in the PCN thin films at the solid-vacuum interface. In addition, by means of steady-state solid and liquid jet PES experiments, the valence electronic structure of the PCN thin films and the aqueous triethanolamine solution ($TEOA_{(aq)}$), which is frequently used as a sacrificial agent in photocatalytic water splitting reactions, were determined on the Fermi-level-referenced energy scale. Overall, the methodology presented here can be extended to explore other photoactive molecular compounds and contribute to the development of efficient and selective functional materials.

Kurzzusammenfassung

Die vorliegende Studie befasst sich mit den Grundlagen ultraschneller photophysikalischer Prozesse, insbesondere mit der elektronischen Dynamik in katalytischen molekularen Systemen, die für nachhaltige und umweltfreundliche Lichtsammel- und Energieübertragungsanwendungen relevant sind. Die Aufdeckung von Mechanismen, die auf ultrakurzen Zeitskalen ablaufen, bietet Einblicke in das dynamische elektronische und strukturelle Verhalten molekularer Verbindungen, die die Effizienz von Katalysatoren bestimmen und deren Weiterentwicklung erleichtert. In dieser Arbeit wurde die ultraschnelle Photodynamik von zwei katalytischen molekularen Verbindungen untersucht: der Übergangsmetallkomplex Ferricyanid, $[Fe(CN)_6]^{3-}$, der in der ionischen Flüssigkeit [emim][DCA] gelöst ist, und polymere Kohlenstoffnitrid (PCN)-Dünnfilme. Die zeitaufgelöste Femtosekunden Photoemissionsspektroskopie (TRPES) wurde eingesetzt, um beide Systeme auf ihren grundlegenden Zeitskalen zu untersuchen, wobei abstimmbare ultrakurze EUV-Tastpulse verwendet wurden, die durch den Prozess der lasergetriebenen Erzeugung hoher Harmonischer (HHG) erzeugt wurden. Mit der kohärenten, ultrakurz gepulsten HHG-basierten EUV-Quelle konnten die photodynamischen Prozesse in den Flüssig- und Festphasensystemen mit einer Zeitauflösung von unter 100 fs verfolgt werden.
In einer ersten Studie wurde die Relaxationsdynamik des $[Fe(CN)_6]^{3-}$-Komplexes in einem neuartigen ionischen flüssigen Lösungsmittel, dem [emim][DCA], nach optischer Anregung des Ligand-Metall-Ladungstransfer-Doublettzustands (^{2}LMCT) bei 400 nm untersucht. Durch die Messung transienter Photoemissionssignale der besetzten elektronischen Zustände wurden Änderungen der elektronischen Konfiguration und der Relaxationspfade auf einer vakuumbezogenen Skala der Elektronenbindungsenergie überwacht. Obwohl lösungsmittelabhängige Untersuchungen der Relaxationsdynamik in $[Fe(CN)_6]^{3-}$ bereits durchgeführt wurden, wurde der Relaxationsmechanismus kontrovers interpretiert. In dieser Arbeit wird ein ultraschnelles biexponentielles Abklingverhalten der anfänglich besetzten elektronischen Zustände von $[Fe(CN)_6]^{3-}$ in [emim][DCA]-Lösung nachgewiesen, wodurch der in wässriger Lösung beobachtete Mechanismus bestätigt wird, der mit einer Abfolge von Intersystemübergängen in der Molekülverbindung verbunden ist. Darüber hinaus ergeben sich in der Umgebung der ionischen Flüssigkeit wesentlich schnellere biexponentielle Übergangsraten als in der häufiger untersuchten wässrigen Lösung. Dieses Verhalten wurde auf der Grundlage von Berechnungen der zeitabhängigen Dichtefunktionaltheorie (TDDFT) qualitativ erklärt.
Um die photoinduzierte Elektronendynamik in verschiedenen PCN-Dünnschichten bei 400 nm-Anregung an der Grenzfläche zwischen Volumen und Oberfläche bzw. Vakuum zu untersuchen, wurden kombinierte TRPES- und UV-Vis-Studien (Transiente Absorptionsspektroskopie, TAS) durchgeführt. Mit den TRPES-Experimenten konnte die frühzeitige, zeitabhängige Population elektronisch angeregter Zustände in den PCN-Dünnschichten auf einer absoluten Bindungsenergieskala in Bezug auf das Fermi-Niveau an der Oberflächen-Vakuum-Grenzfläche abgebildet werden. Auf der Grundlage der erhaltenen kinetischen und spektralen Informationen wurden die Lebensdauern der anfänglich besetzten angeregten Zustände von weniger als 1 ps bestimmt. Die UV-Vis-TAS-Experimente zeigten die langlebige Photodynamik in den PCN-Dünnschichten an der Grenzfläche zwischen Volumen und Oberfläche. Bei den TAS-Experimenten wurde eine parallele Relaxation der Population der früh angeregten Zustände auf Ladungstransfer- und Singulett-Exzitonenzustände festgestellt, gefolgt von Fluoreszenz-Relaxationsprozessen, die auf ps–ns-Zeitskalen stattfinden. Die gemeinsamen TRPES- und TAS-Studien ermöglichten die Entwicklung eines kinetischen Modells, das die ultraschnelle Photodynamik in den PCN-Dünnschichten an der Grenzfläche zwischen Volumen und Oberfläche bzw. Vakuum effektiv beschreiben kann. Darüber hinaus wurde mit Hilfe von stationären Festkörper- und Flüssigkeitsstrahl-PES-Experimenten die elektronische Valenzstruktur der PCN-Dünnschichten und der wässrigen Triethanolaminlösung ($TEOA_{(aq)}$), die häufig als Opferreagenz in photokatalytischen Wasserspaltungsreaktionen verwendet wird, auf der auf das Fermi-Niveau bezogenen Energieskala bestimmt. Insgesamt kann die hier vorgestellte Methodik auf die Erforschung anderer photoaktiver molekularer Verbindungen ausgeweitet werden und zur Entwicklung effizienter und selektiver Funktionsmaterialien beitragen.

Contents

List of Figures

List of Tables

List of Abbreviations

CB	**C**onduction **B**and
CC	**C**ross-**C**orrelation
CPA	**C**hirped-**P**ulse **A**mplification
CT	**C**harge-**T**ransfter
DCA	**D**i**C**yan**A**mide
DFT	**D**ensity-**F**unctional **T**heory
DM	**D**rift **M**ode
EMIM	**E**thyl**M**ethyl**I**midazoliu**M**
EUV	**E**xtreme-**U**ltra**V**iolet
FWHM	**F**ull-**W**idth at **H**alf-**M**aximum
HER	**H**ydrogen **E**volution **R**eaction
HHG	**H**igh **H**armonic **G**eneration
HOMO	**H**ighest **O**ccupied **M**olecular **O**rbital
IL	**I**onic **L**iquid
LADM	**L**ow-**A**ngular **D**ispersion **M**ode
LMCT	**L**igand-to-**M**etal **C**harge-**T**ransfer
LUMO	**L**owest **U**noccupied **M**olecular **O**rbital
MO	**M**olecular **O**rbital
NIR	**N**ear-**I**nfra**R**ed
OER	**O**xygen **E**volution **R**eaction
PCN	**P**olymeric **C**arbon **N**itride
PES	**P**hoto**E**mission **S**pectroscopy
SE	**S**inglet **E**xciton
SHG	**S**econd **H**armonic **G**eneration
TAS	**T**ransient **A**bsorption **S**pectroscopy
TEOA	**T**ri**E**than**O**l**A**mine
TM	**T**ransition **M**etal
TOF	**T**ime-**O**f-**F**light
TRPES	**T**ime-**R**esolved **P**hoto**E**mission **S**pectroscopy
UV	**U**ltra**V**iolet
VB	**V**alence **B**and
Vis	**V**isible
ZP	**Z**one **P**late
WAM	**W**ide-**A**ngle **M**ode
WLC	**W**hite-**L**ight **C**ontinuum

To my beloved parents
who instilled a love for physics in me

Chapter 1

Introduction

> "Every block of stone has a statue inside it and it is the task of the sculptor to discover it."
>
> — *Michelangelo Buonarroti*

With the rapidly growing environmental and economic challenges in the world over the past century, the development of efficient chemical processes based on catalysis provides sustainable alternatives to traditional non-renewable, wasteful, and outdated low-atom economy protocols. Catalysis complies with the twelve basic principles of "green chemistry" [1] and contributes to the expansion of a relatively new area of engineering of environmentally benign and sustainable chemical processes known as green engineering [2]. Catalysis occupies an important place in both applied research and industry, and is of fundamental importance in chemistry. To date, approximately 90% of all processes in the production of industrial chemicals are facilitated by catalysts [3]. Practical applications of catalysis are found in a wide variety of technologies and everyday life, including energy conversion and storage (petrochemicals, fuel cells, biofuel production, batteries, water splitting) [4, 5], healthcare (pharmaceuticals, biosensors) [6, 7], food processing (biocatalysis) [8], environmental remediation (air purification, CO_2 reduction, renewable materials) [9] and organic synthesis [10, 11].

Catalysis is a chemical phenomenon, in which the rate and/or outcome of a chemical reaction is enhanced by the presence of a natural or synthetic compound, the so-called *catalyst*, which does not undergo any net changes over the course of the complete chemical process. Nowadays, a broad range of catalysts are implemented in different forms and sizes, such as single atoms [12], small molecular compounds (acids or bases) [13], large molecular compounds (transition metal complexes) [10], supramolecular assemblies (metal-organic frameworks, 2D organic porous materials) [14], nanomaterials (particles, structures, colloids) [15] and many others. Catalysts are primarily classified into four main types: homogeneous catalysts (transition metal complexes, acid-base catalysis) in a single phase of matter [16], heterogeneous catalysts (metals, metal oxides, polymers, metal-free structures) in a multiple phases of matter [17–19], heterogenized homogeneous catalyst (immobilisation of homogeneous catalyst on solid support) [20] and biocatalysts (enzymes or nucleic acids) in soft-matter environments [21]. In general, they are categorised based on their ability to be soluble in the reaction medium: *homogeneous catalysts*, or not, *heterogeneous catalysts*. With such a variety of forms and possible applications, catalysts are of immense research interest across scientific communities, from manipulating single chemical bonds or molecular compounds to studying the mechanism and dynamics of catalytic reactions for the synthesis of new classes of catalytic materials. A deep understanding of the structure of a catalyst, which is composed of atoms and molecules, as well as knowledge of the physical, chemical and spectroscopic properties, is essential for the efficient development of catalysts and their practical application.

Since fundamental physical, chemical and biological phenomena - for example, photocatalysis, photochemical reactions and photosynthesis - are triggered by photoexcitation [22], exploring the electronic and structural dynamics of photocatalytic molecular and material systems in real-time is of particular interest. The study of light-matter interactions provides fundamental information about the

microscopic electronic structure and photoinduced dynamic processes occurring in and around catalysts, particularly, in light-harvesting and energy transfer applications [23]. Dynamic photophysical and photochemical processes, such as the formation or breaking of chemical bonds, motion of nuclei, nuclear geometry and associated electron configuration rearrangements naturally take place on a *femtosecond* timescale (1 fs = 10^{-15} s) and on picometer to nanometer (nm) length scale [24–27]. Therefore, the real-space, time-resolved observation of the electronic structure dynamics associated with such fast processes requires high-resolution spectroscopic techniques, with both fs time and at least nm spatial resolution. Various steady-state spectroscopic approaches with single electron, photon or neutron excitation sources (photoemission, X-ray absorption, diffraction and scattering, THz, optical absorption, fluorescence, and infrared absorption, Raman, and neutron scattering spectroscopies, etc.) have been employed to investigate static electronic and vibrational structure in physical, chemical or biological systems [28–30]. The advent of ultrashort (femtosecond to sub-picosecond) pulse lasers and related particle sources enabled studies of the dynamic processes that occur on very short timescales [31]. Thus, *ultrafast time-resolved spectroscopy* has emerged, incorporating a broad range of spectroscopic methods, which involve the measurement of time-dependent signals. The combination of optical spectroscopy with ultrashort, tunable pulsed lasers and high-efficiency detectors has made ultrafast spectroscopy the predominant tool for studying a large number of phenomena associated with electron and energy transfer as well as relaxation dynamics in molecular and material systems.

In an ultrafast spectroscopy experiment, a quantum system is excited at a well-defined time and subsequently interrogated at different, well-defined delay times. Therefore, the most widely used multi-pulse technique [32, 33], which allows the time-dependent (transient) changes of the photoexcited system to be tracked, is *pump-probe spectroscopy* [34]. A generic pump-probe approach is based on the use of two ultrashort laser pulses, a pump and a probe pulse, which interact sequentially with a sample. The pump pulse, applied with a desired photon energy at a specific time, initiates photophysical and/or photochemical processes in a sample and promotes the system, which was originally in equilibrium, to some excited, non-equilibrium state. Consequently, this nonstationary state will be perturbed from its equilibrium, resulting in the system evolving in time. The second, probe pulse, applied at a well-defined delay time, monitors the response of the system, which leads to the detection of any pump-induced changes in the system under investigation that may have occurred during a time interval after the initial photoexcitation process. Such changes are typically monitored by measuring outgoing charged particles or scattered photons. The optical intensity of the probe pulse is usually chosen to be lower than the pump pulse intensity, so as not to directly affect the sample.

Pump-probe spectroscopy methods can be implemented utilising pump and probe laser pulses in the visible (Vis), infrared (IR), ultraviolet (UV), extreme-ultraviolet (EUV), X-ray, radio, μ- or γ-wave. Accelerated particle pulses, such as electrons, protons, neutrons, can also be implemented. Furthermore, ultrafast pump-probe spectroscopy techniques can be classified into different groups according to the main spectroscopic processes involved, such as time-resolved infrared (TRIR) spectroscopy [35], time-resolved photoluminescence (TRPL) spectroscopy [36], time-resolved photoemission spectroscopy (TRPES) [37–39], transient absorption spectroscopy (TAS) [40, 41] and many others. These ultrafast spectroscopy methods can be implemented in a variety of optical configurations with appropriate temporal and spectral resolutions (from attoseconds to picoseconds, and tens of eV to few meV, respectively) and excitation spectral ranges that correspond to the photophysicochemical processes of interest. Furthermore, a combination of multiple ultrafast spectroscopy techniques may provide access to comprehensive photophysicochemical information on molecular and material systems and an understanding of their structural evolution and kinetics. In the present work, two pump-probe spectroscopic techniques have been used - femtosecond EUV TRPES and UV-Vis TAS - to investigate electronic dynamics in photocatalytic materials.

This thesis focuses on the study of ultrafast photodynamics in two different homogeneous and heterogeneous catalysts - the ferricyanide ($[Fe(CN)_6]^{3-}$) transition metal complex dissolved in the

ionic liquid [emim][DCA], and polymeric carbon nitride (PCN) thin films, respectively. Femtosecond EUV-based TRPES was employed as the main spectroscopic tool to investigate photoinduced dynamic processes in the two molecular and material systems. In TRPES, the kinetic energy of the electrons generated from either the liquid or solid sample was measured. In both TRPES studies, ultrashort laser pump pulses were applied with the desired photon energy to initiate electronic structure dynamics in the catalyst and promote the molecules to electronically excited states. The EUV probe pulses, with sufficiently high photon energy - generated via frequency up-conversion in the gas-phase high-order harmonic generation (HHG) process and delivered to the experiment by an ultrashort pulse monochromator - were applied after a precisely controlled time delay between the two pulses. This enabled direct photoionisation of the system, promoting the valence electrons above the vacuum level and generating photoelectrons with characteristic kinetic energies. The photoemission spectra were recorded as a function of pump-probe delay, reflecting the changes in the distribution of electron binding energies and showing the evolution of the sample electronic structure after photoexcitation. The time-delay-dependent binding energies of both the electronic ground and excited states of the investigated catalytic molecular compound were extracted due to the use of the EUV probe pulses. In addition, due to its inherently shallow probing depth of a few nanometres, TRPES provides a high surface-sensitivity [42]. This allowed the electronic structure and ultrafast dymanics following photoexcitation in a nm-thick layer of PCN solid samples to be probed at the solid-vacuum interface. This approach and depth sensitivity also mitigates pulse temporal broadening effects, e.g. as observed in TAS for scattering samples [40], thus facilitating time resolutions below 100 fs. Consequently, the time resolution in TRPES is limited by duration of the pump and probe pulses and mainly depends on the ultrafast laser system parameters and delivery of the produced pump-probe laser pulses to the interaction region of the setup.

Femtosecond UV-Vis TAS was used as an additional, well-proven, ultrafast spectroscopic technique to investigate photoinduced electronic dynamics in the PCN thin films at the bulk-vacuum interface with a-few-10-μm depth sensitivity. In TAS studies, the relative changes in the absorbance with respect to the pump-probe time delays were measured, indirectly probing the electronic transitions in the PCN samples that involve population and depopulation of the excited states. To monitor the ultrafast and long-lived photodynamics in the PCN thin films at the solid-vacuum interface, the TAS studies were performed in the diffuse reflectance geometry on time scales ranging from femtoseconds to nanoseconds. Analogous to TRPES experiments, relatively high-intensity ultrashort laser pump pulses were applied to promote a sub-ensemble of the PCN system from the electronic ground state to an excited state, generating a non-equilibrium state. White-light continuum probe pulses were used to map the pump-induced population dynamics of the excited states. The time-dependent spectral changes recorded in the transient diffuse reflectance spectra provided detailed information about the relaxation dynamics of the excited states at the bulk-vacuum interface in the PCN thin films.

The major objectives of this thesis are outlined in the following. For the $[Fe(CN)_6]^{3-}$ transition metal complex, first and foremost, to investigate the influence of different environmentally benign molecular solvent, the ionic liquid [emim][DCA], on the relaxation dynamics of electronically photoexcited lowest-lying doublet ligand-to-metal charge-transfer (^{2}LMCT) state of $[Fe(CN)_6]^{3-}$ ion following 400 nm optical excitation. Next, to reveal the previously disputed mechanism of photoinduced charge-transfer upon 400 nm excitation to the lowest-lying doublet ligand-to-metal charge-transfer (^{2}LMCT) states. Here the focus was on mapping the transient populations associated with the involved electronically excited states of the solvated $[Fe(CN)_6]^{3-}$ catalytic molecular compound in the [emim][DCA] solvent. This allowed the electron binding energies to be determined in the liquid-phase, using the TRPES technique. In the studies with the PCN thin films, to interrogate the ultrafast dynamics occurring upon 400 nm photoexcitation at the solid-vacuum interface on an electron binding energy scale with sub-100 fs time resolution using TRPES. An accurate determination of the valence band electron binding energies of the PCN thin films and the sacrificial agent triethanolamine (TEOA), obtained from steady-state PES studies, was also used to estimate the catalyst-sacrificial agent interfacial energetics for potential photocatalytic water splitting applications. Furthermore, the

photodynamics at the bulk-vacuum interface were studied on timescales spanning from femtoseconds to nanoseconds by applying UV-Vis TAS. The associated TRPES and TAS studies allowed the development of a kinetic model that describes the ultrafast photophysics of PCN thin films at the solid-vacuum interface and correlates the results with the current understanding of the nature of the photocatalytic activity of PCN materials.

This dissertation is structured in seven chapters. Chapter 2 introduces the investigated catalytic molecular systems, $[Fe(CN)_6]^{3-}$ transition metal complex dissolved in the [emim][DCA] ionic liquid, and polymeric carbon nitride samples. Chapter 3 describes the fundamental theoretical and methodological background underlying the results and discussions presented in this thesis. Chapter 4 is dedicated to the experimental setups, employed TRPES and TAS techniques and diagnostic methods, including the optimisation of the HHG setup applied in TRPES experiments. Chapter 5 presents the experimental data and the interpretation of the relaxation mechanisms in electronically photoexcited $[Fe(CN)_6]^{3-}$ ions dissolved in [emim][DCA], as assisted by quantum mechanical TDDFT calculations. Chapter 6 presents and discusses the experimental results for polymeric carbon nitride thin films, in which photoinduced electron dynamics were studied at the surface-vacuum interface and in the bulk of the material using two different spectroscopic ultrafast pump-probe techniques, TRPES and TAS, respectively. Finally, the main findings derived from this work are summarised in Chapter 7, and an outlook for further research activities is presented.

Chapter 2

Investigated Molecular Systems

> "In some cases we learn more by looking for the answer to a question and not finding it than we do from learning the answer itself."
>
> *— Lloyd Alexander, The Book of Three, 1964*

Chapter 2 presents the catalytic molecular systems investigated and discussed in this dissertation, including ferricyanide transition metal (TM) complex dissolved in the ionic liquid [emim][DCA], and bulk, mesoporous and ultrathin 2D nanosheets of polymeric carbon nitride (PCN) samples. Section 2.1 gives an overview on electronic configurations as well as charge-transfer processes and excited state dynamics in octahedral TM complexes. Firstly, the electronic structure and charge-transfer states of the ferricyanide TM complex are introduced, providing insights into the origin of the formation of molecular energy levels and photophysics of this compound. The main properties of the ionic liquid [emim][DCA], which was used as a solvent in the studies on the relaxation dynamics of electronically photoexcited ferricyanide ion, are discussed further. Lastly, different interpretations of the charge-transfer mechanism of the solvated ferricyanide complex following optically-induced excitation of the lowest-energy ligand-to-metal charge-transfer state, which represent one of the main scientific questions of the present research, are discussed. Section 2.2 introduces the PCN molecular system, including the main chemical, electronic, and optical properties, and possible ways to modify its structure for photocatalytic applications. In connection with the major application of PCN, the PCN-catalysed photocatalytic water splitting process is discussed further. The main thermodynamic and catalytic properties of the PCN material required for an efficient hydrogen and oxygen evolution reaction during water splitting are presented. The physical and chemical properties of the PCN samples, which were examined in the present studies are introduced further. Herein, the enhanced photocatalytic activity of mesoporous and ultrathin 2D nanosheets of PCNs in the water splitting reaction is elucidated.

2.1 Ferricyanide Transition Metal Complex

Transition metal (TM) complexes are molecules containing a central *d*-block metal atom or ion surrounded and bonded to a group of other ionic or molecular functional groups (ligands) that donate electrons to the central metal. The central metal ion forms coordinate covalent bonds with a number of ligands, sharing the donated valence electrons in a metal-ligand bond. The TM coordination compounds play an important role in biological, chemical, physical, material, and medical sciences. Due to their unique electronic configurations and transitions, TM complexes form colored compounds that, when exposed to UV-Vis radiation, can promote complex photophysical and photochemical processes. Therefore, TM complexes have received considerable attention for several decades and continue to be studied for catalytic [43–45], synthetic [46], photophysical [47, 48], biochemical [49–52], and photovoltaic [53, 54] applications. Of particular interest is understanding the nature of the intramolecular, and potentially intermolecular charge-transfer processes that occur when TM complexes are photoexcited and the optimisation of their function in catalytic and light-harvesting applications.

2.1.1 Electronic Configurations of Transition Metal Complexes

Transition metal complexes have (or readily form) partially filled *d* sub-shells in both ionic and neutral forms. In contrast to the alkali metals and alkaline earth metals, where one oxidation state is predominantly observed, the TMs have an open valence *d* sub-shell, which can be readily manipulated allowing them to occur in multiple stable oxidation states. The central *d*-block metal ion can form bonds with a number of ligands based on the coordination number, the so-called ligancy of the central metal atom, and the metal centre oxidation states. Coordination numbers of the TMs can range between 2 and 12 across the periodic table, while from 4 to 6 is fairly common in TM compounds. For 4-coordinate TM complexes, the molecular symmetry group can be described as square-planar (D_{4h}) or tetrahedral (T_d), for 5-coordinate square-pyramidal (C_{4v}) or trigonal-bipyramidal (D_{3h}) group symmetries occur. A large number of the TM compounds are hexacoordinated complexes that have octahedral (O_h) group symmetry [55]. In the present work, a TM complex with a coordination number of 6 and O_h symmetry was investigated.

The spectral properties of the TM complexes can be interpreted using ligand-field theory (LFT) [56, 57]. LFT can be considered as an extension of the crystal-field theory (CFT) [58], where metal-ligand interactions and possible interactions of molecular orbitals that have the same symmetry are taken into account, implying some degree of covalent metal-ligand bonding (metal electrons delocalised over the ligand and vice versa). This delocalisation leads to smaller energetic separations between the energy levels of the excited electronic states (e.g. Russell-Saunders thermal states [59]) in the TM complex than predicted for an ion using CFT. Moreover, LFT accounts for the expansion of the lobes of the *d* orbitals, that is, the expansion of *d* electron charge cloud during complexation by the transition metal ion, the so-called nephelauxetic effect, which depends upon both the central metal ion and the ligand [60]. The nephelauxetic series for common ligands (with increasing nephelauxetic effect) is $F^- < H_2O < NH_3 < en < SCN^- < Cl^- < CN^- < Br^- < I^-$, which reflects the capability of ligands to form stronger covalent bonds with metal ions. Here, *en* is an abbreviation for the ethylenediamine organic compound in a ligand form. The nephelauxetic series for central metal ions $Mn^{2+} < Ni^{2+} \approx Co^{2+} < Mo^{2+} < Re^{4+} < Fe^{3+} < Ir^{3+} < Co^{3+} < Mn^{4+}$ indicates that the nephelauxetic effect increases with an increase in the oxidation state of the metal ion. LFT specifically represents an application of molecular orbital (MO) theory [61] to TM complexes, which can be utilised to explain the covalent as well as ionic nature of the metal-ligand bond. Therefore, LFT incorporates an adequate description of the bonding between the metal core and the ligands, the molecular orbital arrangement, as well as the electronic and geometrical structures, stability, color, reactivity, magnetic and electronic properties of the TM elements and their compounds.

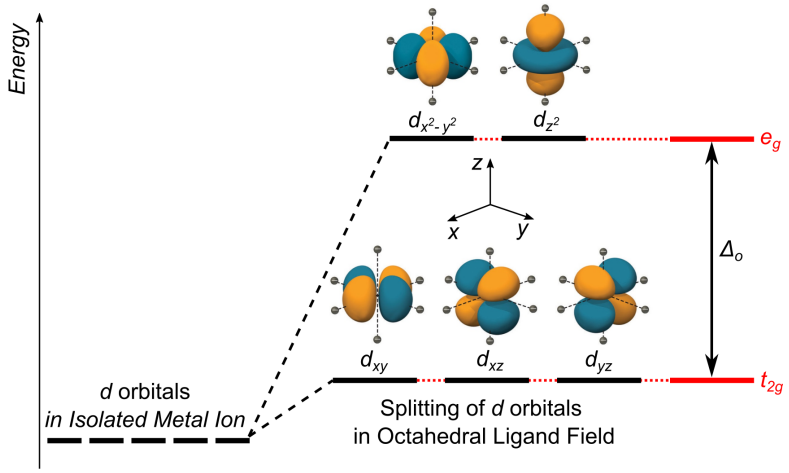

FIGURE 2.1: Ligand field splitting for an octahedral transition metal complex.

In octahedral TM complexes, six ligands are aligned relative to the x, y, and z molecular axes. In the absence of a ligand solvation, or crystal field, the five atomic d orbitals d_{xy}, d_{xz}, d_{yz}, $d_{x^2-y^2}$, and d_{z^2} of the TM are degenerate in energy. More generally, the energy levels of the molecular orbitals incorporating the d atomic orbitals depend on both the metal center, the ligand orbitals, and the local TM complex environment. Thus, to first order, the molecular orbitals are formed through a linear combination of atomic orbitals (LCAO) of the metal atomic orbitals (d, s and p) and the ligand molecular orbitals (σ and π) [62]. The electrons in two atomic d orbitals, $d_{x^2-y^2}$, which are aligned along the x and y axes, and d_{z^2}, which is aligned along the z axis in octahedral systems, will have higher energy relative to the electrons of the other three d orbitals, resulting in a strong interaction with the ligands. The interaction between the ligand orbitals and the orbitals of the metal center leads to stabilisation (destabilisation) of the bonding (antibounding σ^* and π^*) molecular orbitals. Consequently, in an octahedral ligand field, the five d orbitals of the central atom split into degenerate t_{2g} (d_{xy}, d_{xz}, d_{yz}) and e_g ($d_{x^2-y^2}$, d_{z^2}) sets of orbitals (Figure 2.1). The energy difference between the t_{2g} and e_g orbitals is called the ligand field splitting (Δ_o). The value of Δ_o depends on the number of electrons in the d sub-shell of the central metal ion, its oxidation state and the nature of ligands positioned around the central metal ion [63]. The energy difference between the split d orbitals give rise to absorption in the visible spectral region and is therefore responsible for the colour of TM complexes. The larger the d orbitals splitting, the shorter the wavelength required to promote an electron to the higher lying e_g orbitals. It is important to emphasise that the absorption of UV-Vis radiation by TM complexes will depend not only on the electronic properties of the solute/chromophore, but also on the characteristics of the local environment, e.g. surrounding solvent (with a specific concentration, pH, temperature, dielectric constant), or embedment in a crystal or amorphous solid (with a specific density, geometric structure, etc.).

2.1.2 Charge-Transfer and Excited State Dynamics in Transition Metal Complexes

TM complexes undergo electronic transitions by the absorption of light in the UV-Vis-NIR spectral regions. In general, the electronic spectra of TM complexes originate from three types of electronic transitions: transitions between MOs primarily localised on the central metal ion (d-d transitions between the t_{2g} and e_g orbitals), transitions in which there is a change in electronic distribution between MOs mainly localised on the central metal ion and MOs mainly localised around the ligand (charge-transfer, CT, transitions) or transitions between MOs primarily localised on the ligands (internal ligand or ligand field, LF, transitions) [63]. In quantum mechanics, allowed electronic transitions are governed by the spin selection rule (electronic transitions between the different states of spin multiplicity are forbidden) and Laporte's selection rule (electronic transitions within the same p or d sub-shell are forbidden, if the molecule has a centre of symmetry), imposing the conditions under which certain electronic transitions may occur [64]. The d-d transitions are Laporte-fobidden and potentially spin-allowed, resulting in weak absorption bands in the spectrum. The CT transitions are Laporte-allowed and can be spin-allowed, thus exhibiting intense absorption bands in the UV-Vis spectral region, due to the fact that there is a high probability of these transitions occurring.

The population of excited states via dipole-allowed electronic transitions, also requires consideration of the Franck-Condon principle [65, 66]. This principle states that when a molecule undergoes electronic transitions, the timescale of these transitions are very short compared to the nuclear motion of the molecule, so the transition probability can be calculated at a fixed nuclear position. The electronic transition is therefore considered to be a vertical transition, and the resulting state is called a Franck–Condon state. The nuclei generally the establishment of the new electronic configuration, with the gained electronic potential energy driving vibrations. Transitions that occur as a result of combined electronic-vibrational excitation of a molecule are termed vibronic transitions. Due to combined excitation of associated asymmetric oscillations, electronic transitions that would otherwise be forbidden, i.e. d-d transitions, become weakly allowed.

A wide range of electronic transitions are possible within TM complexes, which are typically named according to how the electronic density changes upon excitation [67, 68]. The CT transitions can occur between the metal-centered states (MC) or ligand field states (LF), ligand-centred states (LC), or involve both the central metal ion and the ligands. If electrons can be transferred from the full partially-occupied ligand MOs to the empty or partially filled central metal *d* orbitals, ligand-to-metal charge-transfer (LMCT) transitions can occur. If the transfer of electrons arise from the full or partially-occupied metal *d* orbitals to the unoccupied ligand MOs, metal-to-ligand charge transfer (MLCT) excitations can occur. Therefore, the MLCT or LMCT states lead to local oxidation or reduction of the central metal ion, respectively, although the oxidation state of the overall complex is initially, at least, unchanged. In addition to the formation of the aforementioned CT states (intermolecular), charge-transfer-to-solvent (CTTS) or ion-pair charge transfer (IPCT) states can be formed [69].

The photoinduced CT between the central metal ions and ligands is generally followed by molecular relaxation dynamics, involving ultrafast processes such as internal conversion, intersystem crossing, and intra- and intermolecular vibrational energy redistribution [70]. In the solution phase, such processes are also accompanied by solvent reorganisation. Furthermore, these non-radiative processes can be accompanied by radiative transitions such as fluorescence and phosphorescence [71]. Thus, the photoexcited state species form different electronic, as well as molecular structural, configurations of the TM molecular compound with respect to the initial electronic ground state. The molecular relaxation of the photoexcited species occurs on different timescales (ranging from femtoseconds to microseconds) and depends on the molecular configuration of the particular system, and the corresponding relaxation pathways. The revelation of relaxation pathways and corresponding lifetimes of the photoinduced electronic states is therefore essential for a correct description of the photochemical and photophysical processes in TM complexes embedded in their natural or applied environment. Such an understanding is also a key to the directed-design of more selective and/or efficient TM-complex-based functional materials.

2.1.3 Electronic Structure and Charge-Transfer States of the $[Fe(CN)_6]^{3-}$ Ion

Ferricyanide, $[Fe(CN)_6]^{3-}$, and ferrocyanide, $[Fe(CN)_6]^{4-}$, transition metal compounds are hexacoordinated complexes that can harvest light radiation in the UV-Vis spectral region and transfer it in the form of chemical energy to the reaction centers for the photoinduced redox processes. Due to the fact that iron is by far the most abundant and important transition metal used in living systems, these hexacyanoferrate TM complexes have found use in a large number of applications, such as sensors and indicators, blueprint drawing and photography, electroplating, as laboratory reagents, and as mild oxidising agents in organic chemistry [72–74]. In particular, potassium ferricyanide, $K_3Fe(CN)_6$, is broadly implemented in biochemistry and medical inorganic chemistry [75, 76]. For instance, it is used as a component of amperometric biosensors as an electron transfer agent in commercially available diabetes blood glucose meters [77]. Hexacyanoferrate TM complexes have been extensively studied to understand the electronic structure and CT mechanisms of TM complexes with O_h group symmetry [78–86]. Hexacyanoferrate compounds exhibit many interesting properties, such as low-lying unoccupied antibonding ligand-centered MOs of π symmetry, resulting in the stabilisation of low oxidation states of the central metal ion. The photophysics of these TM complexes is influenced by the properties of the molecule and the local environment, i.e. the surrounding solvent, which determines the course of CT processes and molecular dynamics, and hence, the light-harvesting efficiency of the compound.

The hexacyanoferrate ionic complexes, ferrocyanide and ferricyanide possesses very similar chemical structures, but different molecular and metal-atom oxidation states, Fe^{+2} and Fe^{+3}, respectively. The $[Fe(CN)_6]^{3-}$ anion consists of a low-spin iron metal center bound to six cyanide ligands, CN^- (Figure 2.3), which can be reduced to the $[Fe(CN)_6]^{4-}$ ion via a reversible redox couple that does

not involve the formation or breaking of Fe–C bonds. Despite the similarity of these two hexacyanoferrate complexes, their photophysics differ, which leads to various imprints on the CT dynamics. For instance, the appearance of the CTTS transition in the UV-Vis spectral region of the ferrous species [87, 88], is not observed in the ferric complex. The understanding of the electronic structure and CT dynamics of ferrous- and ferric hexacyanide complexes has generally been the subject of separate studies that can be examined using ultrafast spectroscopy experiments. In recent decades, a considerable emphasis has been placed on revealing the role of coupled electronic and vibrational dynamics [89, 90], non-equilibrium vibrational energy relaxation following CT excitation [91–94], photoaquation mechanisms [95, 96], and core and valence MOs changes following photooxidation in hexacyanoferrate complexes dissolved in various molecular solvents [86, 91, 93]. In particular, due to its strong photoabsorption in the visible spectral range, the $[Fe(CN)_6]^{3-}$ TM complex has received substantial interest as a paradigmatic system to investigate intramolecular CT processes in ligand coordination compounds.

UV-Vis absorption spectroscopy provides insight into the electronic transitions that can be photoinduced in the $[Fe(CN)_6]^{3-}$ molecular system. Figure 2.2 shows the room temperature UV-Vis absorption spectrum of potassium ferricyanide $K_3Fe(CN)_6$ (composed of K^+ cation and $[Fe(CN)_6]^{3-}$ ion) dissolved in the [emim][DCA] ionic liquid, which was investigated in the present work. The spectrum was measured with a potassium ferricyanide concentration of 400 mM in the [emim][DCA] solution, using a quartz cell with a liquid path length of 0.1 mm, and recorded using a Perkin Elmer - Lambda 950 UV/Vis/NIR spectrometer. The experimental spectrum was fitted to a superposition of Gaussian envelopes, described by the function $f(E)$, to roughly extract the energetic positions of the spectral bands corresponding to allowed electronic transitions in the $K_3Fe(CN)_6$ complex:

$$f(E) = \sum_i A_i e^{-\frac{4\ln(2)(E-E_i)^2}{\sigma_i^2}}, \tag{2.1}$$

where E is the photon energy, σ_i is the full-width at half-maximum (FWHM) of band i, E_i is the central peak position, and A_i is the peak amplitude.

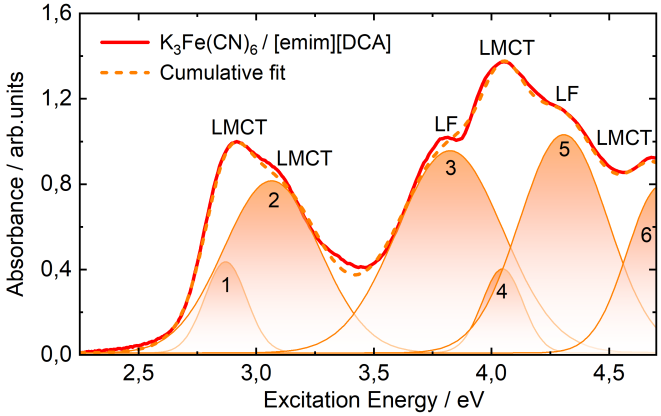

FIGURE 2.2: UV-Vis absorption spectrum of 400 mM $K_3Fe(CN)_6$ dissolved in [emim][DCA] ionic liquid. The measured spectrum was fitted to a superposition of Gaussian profiles using Equation 2.1. The numbers 1–6 are assigned to the decomposed absorption bands of $K_3Fe(CN)_6$ obtained from the fit (see Table 2.1).

The absorption spectrum of $K_3Fe(CN)_6$ highlights the presence of four absorption bands centred at 2.87 eV, 3.06 eV, 4.05 eV and 4.72 eV (see Table 2.1 for details) which can be attributed to intramolecular LMCT transitions in $[Fe(CN)_6]^{3-}$, as previously discussed in the literature [97–99]. Two other bands centred around 3.82 eV and 4.30 eV can be assigned to LF transitions [98, 99]. The absorption bands at higher photon energies, which are not displayed in the present spectrum, can be

TABLE 2.1: Fit parameters of the Gaussian envelopes used to describe the absorption bands of $K_3Fe(CN)_6$ in [emim][DCA] ionic liquid (Equation 2.1).

Assignment	Label	E / eV	FWHM / eV	A / cts
LMCT	1	2.87 ± 0.01	0.21 ± 0.01	0.09 ± 0.01
LMCT	2	3.06 ± 0.01	0.48 ± 0.02	0.41 ± 0.02
LF	3	3.82 ± 0.03	0.54 ± 0.02	0.53 ± 0.04
LMCT	4	4.05 ± 0.01	0.21 ± 0.01	0.09 ± 0.03
LF	5	4.31 ± 0.01	0.44 ± 0.01	0.48 ± 0.10
LMCT	6	4.72 ± 0.01	0.33 ± 0.04	0.28 ± 0.06

attributed to MLCT transitions of the $[Fe(CN)_6]^{3-}$ complex [96, 97, 99]. The absorption characteristics of the $[Fe(CN)_6]^{3-}$ ion in the [emim][DCA] ionic liquid are very similar to those of conventional molecular solvents consisting of neutral molecules in the liquid-phase, such as an aqueous solution. Nonetheless, the absorption bands are slightly broader and red wavelength shifted in the ionic liquid environment when compared to the aqueous solution [93]. Consequently, the molecular properties of the $[Fe(CN)_6]^{3-}$ ion may be affected by the ionic liquid environment, resulting in changes of the solvation dynamics and the electronic transition rates of the complex.

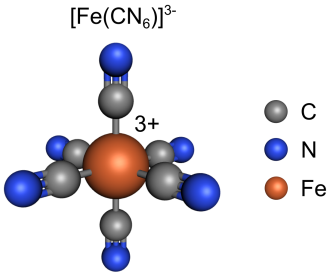

FIGURE 2.3: Molecular structure of the ferricyanide ion.

The assignment of the bands in the UV-Vis absorption spectrum of the $[Fe(CN)_6]^{3-}$ ion can be interpreted using MO theory, where, on the basis of the calculated electronic structure of the ferricyanide molecule, formation of the molecular orbitals and energy levels of the complex are given. Figure 2.4 shows the MO diagram of the $[Fe(CN)_6]^{3-}$ ion, comprising the principal orbitals of the TM complex, based on an extended Hückel molecular orbital calculation [99]. The $[Fe(CN)_6]^{3-}$ anion is a low-spin hexacyanide complex where the d^3 sub-shell of the central Fe^{3+} atom surrounded by a distorted octahedron of six CN^- ligands is energetically split into degenerate t_{2g} and e_g sets of orbitals by significant spin-orbit coupling [100]. The metal-ligand bonding between the Fe and the CN^- has prominent covalent character. This is a result of the transfer of electron density from the partially occupied iron *3d* (t_{2g}) orbitals to the unoccupied CN^- virtual valence orbitals and occupied CN^- valence orbitals, known as π-backbonding [101]. The CN^- ligands are thus acting as a σ-donor and a π-acceptor, which leads to a large ligand-field splitting and results in a low-spin iron complex (S = 1/2) with a $(t_{2g})^5(e_g)^0$ electron configuration. This configuration is orbitally degenerate with a single electron-hole in the *3d* (t_{2g}) orbitals, and hence the $[Fe(CN)_6]^{3-}$ complex experiences a weak Jahn-Teller distortion [102], resulting in the adoption of a D_{3d} point group symmetry.

The molecular orbitals of the $[Fe(CN)_6]^{3-}$ ion are formed by a LCAO of the iron atomic orbitals (*d*, *s* and *p*) and σ and π molecular orbitals of the CN^- ligands, as shown in Figure 2.4. The ground electronic state of the $[Fe(CN)_6]^{3-}$ ion has the predominant electronic configuration of $(a_{1g})^2(t_{1u})^6(e_g)^4(t_{2g})^5(e_g^*)^4(t_{2g}^*)^0$. The a_{1g} MO is formed by a combination of the *4s* atomic orbital of the Fe atom and the σ_{CN} MO of the CN^- ligands [84]. At the ground state equilibrium geometry, the highest occupied molecular orbital (HOMO), here referred to as the t_{2g} MO, is composed of 77% of Fe (d_{xy}, d_{xz}, d_{yz}) atomic orbitals and 11% of π_{CN}-donor and 12% of π_{CN}-acceptor MOs of the CN^- ligands. The associated lowest unoccupied molecular orbital (LUMO) is then assigned as e_g^* and is

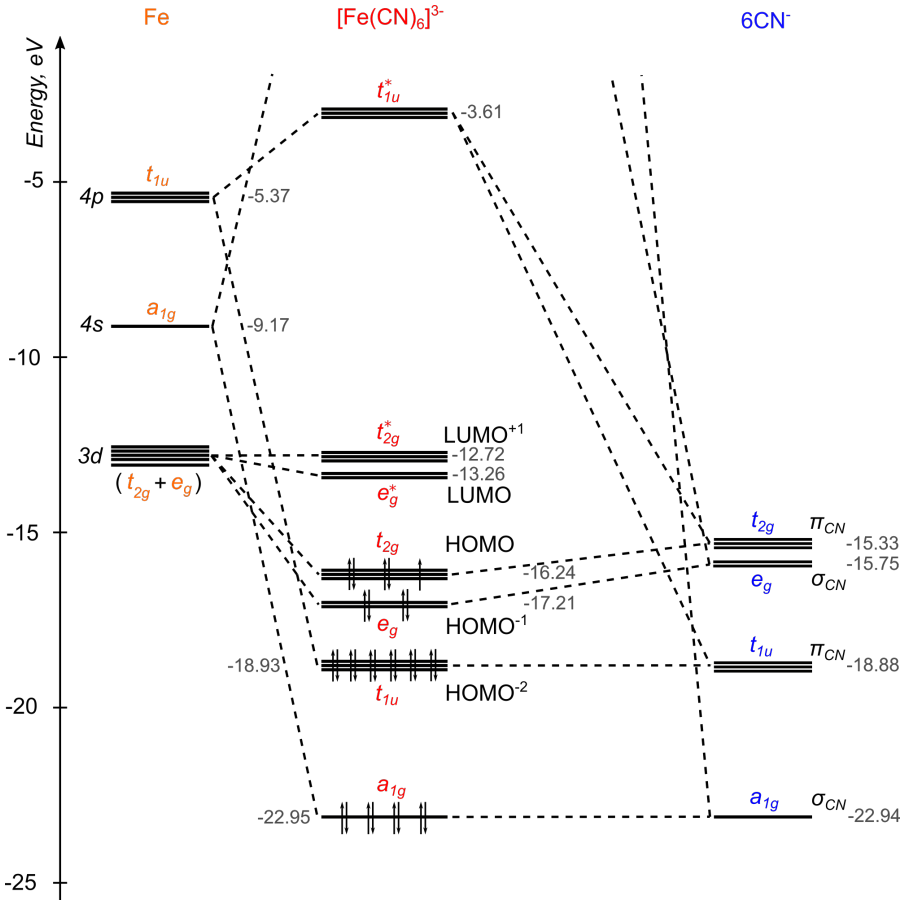

FIGURE 2.4: The molecular orbital diagram of the $[Fe(CN)_6]^{3-}$ complex. Adapted figure with permission from [103] © 2006 by the American Chemical Society.

formed by 54% of Fe ($d_{x^2-y^2}$, d_{z^2}) atomic orbitals and 42% of σ_{CN}-donor and 2% of σ_{CN}-acceptor MOs of the CN^- ligands. The HOMO-1 (e_g) is composed mostly of 78% of σ_{CN}-bonding MOs of the CN^- ligands contribution and 21% of Fe ($d_{x^2-y^2}$, d_{z^2}) atomic orbitals. Similar to the e_g, the HOMO-2 (t_{1u}) is composed by 86% of π_{CN}-donor MOs of the CN^- ligands and 10% of Fe (d_{xy}, d_{xz}, d_{yz}) atomic orbitals. The LUMO+1 is also formed by a major contribution of 86% of π_{CN}-acceptor MOs of the CN^- ligands and 14% of Fe (d_{xy}, d_{xz}, d_{yz}) atomic orbitals. The higher energy unoccupied MOs are primarily associated with the σ_{CN} and π_{CN} MOs of the CN^- ligands. The assignment presented above is based on experimental Fe L-Edge XAS studies and DFT calculations of $K_3Fe(CN)_6$ complex provided by Hocking *et al.* [103].

Since the structure of the $[Fe(CN)_6]^{3-}$ complex in the ground electronic state is weakly distorted from the O_h symmetry and has the D_{3d} point group symmetry, the dipole-allowed transitions from the gerade symmetry ground state should be to states with ungerade symmetry. Thus, the measured UV-Vis absorption spectrum of $K_3Fe(CN)_6$ (Figure 2.2) in the energy range below 5 eV, includes optically "bright" transitions which are associated with the LMCT states. In particular, the absorption bands centered around 2.87 eV and 3.06 eV are predominantly attributed to the $t_{1u} \rightarrow t_{2g}$ and $t_{1u} \rightarrow e_g$, i.e. LMCT transitions from CN^- ligand-centered MOs to iron-centered MOs [104]. Other CT transitions $t_{2g} \rightarrow t_{1u}$, $t_{2g} \rightarrow t_{eg}$, $t_{2g} \rightarrow t_{2u}$, and $t_{2g} \rightarrow t_{1g}$, which correspond to the absorption bands centered at 4.72 eV, 4.30 eV, 4.05 eV, and 3.82 eV, respectively, have been computed and reported [87, 88, 98]. In the present studies, intramolecular CT processes in the $[Fe(CN)_6]^{3-}$ TM complex were monitored following excitation by a pump pulse with a photon energy of 3.1 eV, as applied to excite the two associated lowest-excitation-energy LMCT bands, occurring at central energies of 2.86 and 3.06 eV in an [emim][DCA] ionic liquid solution.

2.1.4 The Ionic Liquid [emim][DCA]

An ionic liquid (IL) is a salt entirely composed of volumetric organic cations and inorganic or organic anions that have a bulky and asymmetrical structure, which dissociate to a major extent into ions. These liquids remain in the liquid-phase below 100°C, or even at room temperature. While conventional molecular solvents such as water are primary composed of neutral molecules in the liquid-phase, ionic liquids are mainly composed of ions, which possess negligible vapour pressures and are thermally stable, nonflammable, recyclable and able to dissolve organic, inorganic and polymeric materials [105, 106].

Since the initial discovery of the ILs in 1914 by P. Walden [107], there has been an ever growing research interest in their use as solvents for a wide range of applications. ILs are environmentally benign solvents and were named "solvents of the future" in 2003 [108], as a nonvolatile replacement for the volatile organic compounds (VOCs), that would prevent air and water pollution from VOCs emissions. Although ILs are not intrinsically environmentally benign, as some have been identified as extremely toxic [109, 110], their chemical structure (cation/anion, alkyl chain length, and functionalised alkyl groups) can be engineered to be environmentally friendly, with great potential benefits for sustainable chemistry. The possible number of different ILs that can be synthesised with desirable physical and chemical properties reaches a million for binary and 10^{18} for ternary ILs (compared with about 600 molecular solvents that are currently used) [111]. This diversity allows the use of ILs in many possible applications, such as synthesis, catalysis, electrochemistry, material science, cell biology, genetics heredity, nuclear physics, medicinal chemistry, engineering, and many others, both in industrial and academic settings [112].

By varying the cation/anion ratio, type and alkyl chain length properties, ILs can be divided into different classes. The most common ILs are based on organic cations such as imidazolium, pyridinium, pyrrolidinium, ammonium, and phosphonium associated with inorganic anions ($[Cl]^-$, $[AlCl_4]^-$, $[PF_6]^-$, $[BF_4]^-$, $[NTf_2]^-$, $[DCA]^-$, etc.) or organic anions ($[CH_3COO]^-$, $[CH_3SO_3]^-$, etc.) [106]. In this work, the 1-Ethyl-3-methylimidazolium dicyanamide [emim][DCA] ionic liquid ($C_8H_{11}N_5$) was chosen as a solvent to investigate the photoinduced dynamics in $[Fe(CN)_6]^{3-}$ compound. The molecular structure of the [emim][DCA] ionic liquid is shown in Figure 2.5.

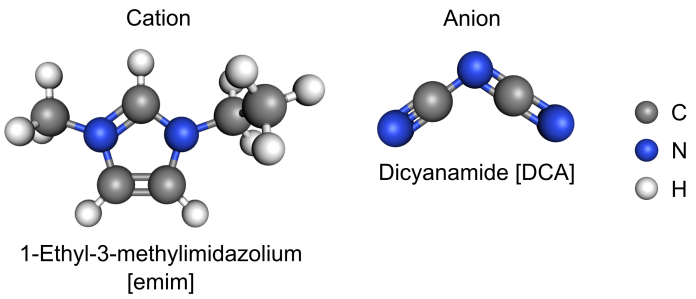

FIGURE 2.5: Molecular structure of the [emim][DCA] ionic liquid.

The physical and chemical properties of ILs are primarily determined by the Coulombic, van der Waals, and hydrogen bonding type forces. Unlike ordinary molecular liquids, where the van der Waals force makes the main contribution to intermolecular interactions, the Coulomb attractive force between two ions of opposite charge forms an ionic bond, which is considered the main interaction in ILs. This leads to the formation of stronger intermolecular forces and, hence, to a higher thermal stability of ILs as compared to non-ILs [113]. The strength of intermolecular interactions determine polarity, viscosity, density, surface tension, solubility, volatility and other macroscopic and microscopic properties of ILs [105, 106]. From the point of view of using IL as a molecular solvent for photophysical studies, polarity is one of the most important properties of a liquid, which on average determines how it will interact with a solute/chromophore. ILs are moderately polar, with a relatively

TABLE 2.2: Physicochemical properties of the [emim][DCA] ionic liquid at 298 K.

Molar mass	Surface tension	Density	Viscosity	ε	Melting point
177.23 g·mol^{-1}	66.07 cal·mol^{-1}Å^{-2}	1.1 g·cm^{-3}	39.8 cP	11	267.75 °C

low static dielectric constant, ε = 8–16 [114, 115], which is comparable to the dielectric constant of pyridine (ε = 12.4) and several times less than that of water (ε = 78.4 at 298 K). However, the viscosity of ILs is much higher than that of conventional molecular solvents such as alcohols and water (30 times more viscous) and ranges from 10 to 500 cP at room temperature [116]. Although the high viscosity of ILs is one of the main obstacles to their application, it was advantageous for the PES experiments reported in this dissertation. The surface tension of a viscous $[Fe(CN)_6]^{3-}$ dissolved in [emim][DCA] solution was used to hold a droplet of the sample within a thin loop of copper wire throughout the experiments. Moreover, [emim][DCA] is an ionic liquid with short alkyl chains and hydrophilic cyano groups that are highly soluble in water. Thus, due to the low solubility of $[Fe(CN)_6]^{3-}$ in imidazolium ILs, such as [emim][DCA], an aqueous ferricyanide solution was prepared first and mixed with the [emim][DCA] ionic liquid until it was homogeneously dissolved. The preparation process will be discussed in detail in Section 5.1. The main physicochemical properties of the [emim][DCA] ionic liquid are summarised in Table 2.2 [114, 117].

In recent decades, studies of various photophysical and photochemical processes in ILs have been performed using the X-ray photoemission spectroscopy [118, 119], soft X-ray emission and absorption spectroscopy [120, 121], transient absorption, and fluorescence spectroscopy methods [122–125]. However, the number of experiments aimed at the investigation of photoinduced processes on a dissolved solute/chromophore in IL, revealing the influence of the IL environment on the relaxation dynamics and the CT kinetics of the chromophore is still limited. Therefore, this work raises the question of whether and, if so, how the IL solvent affects the ultrafast deactivation processes of such systems, in this case of the $[Fe(CN)_6]^{3-}$ molecular compound.

2.1.5 Photoinduced Electron Dynamics of $[Fe(CN)_6]^{3-}$ upon 400 nm excitation

A fundamental objective in the study of pseudo-octahedral TM coordination complexes is the revelation of their ultrafast photodynamics. Recently, the relaxation dynamics of the $[Fe(CN)_6]^{3-}$ complex disolved in various molecular solvents following 400 nm optical excitation of the lowest-lying doublet ^{2}LMCT states has become a subject of discussion [91–93]. The first ultrafast time-resolution study of the early-time relaxation dynamics of the lowest-lying ^{2}LMCT state, at a wavelength of 400 nm, was performed by Zhang *et al.* [92] using UV pump – mid-IR probe transient absorption spectroscopy in acetonitrile (MeCN) and dimethyl sulfoxide (DMSO) solutions. Based on anisotropy measurements and the observed single band of the CN-stretch vibrational mode in the IR absorption spectrum, it was concluded that the fully octahedral point group symmetry of $[Fe(CN)_6]^{3-}$ is preserved during the LMCT excitation. Thus, the relaxation dynamics of photoexcited ferricyanide involves an intermediate, solvent-assisted molecular structural reorganisation linked to ligands hole delocalisation, which occurs on the picosecond timescale (1.9 ps in MeCN and 4.9 ps in DMSO). Subsequently, the excited system relaxes back to its ground electronic state with much longer transition rate, which depends significantly on the surrounding solvent (17.5 ps in MeCN and 28.1 ps in DMSO).

Further ultrafast photoemission spectroscopy and transient mid-IR absorption spectroscopy studies were reported by Ojeda *et al.* [91], providing a different interpretation of the deactivation pathways of $[Fe(CN)_6]^{3-}$. In this study, the relaxation dynamics of the 400-nm-excited LMCT state of $[Fe(CN)_6]^{3-}$ dissolved in H_2O, D_2O and ethylene glycol (ETG), were attributed to back electron transfer to the CN^- ligands, leading to population of vibrationally excited levels of the ground state. The prompt reduction of the Fe^{3+} metal center and the back electron transfer were reported to decay on the order of 500 fs, 600 fs and 1.2 ps in H_2O, D_2O and ETG solvents, respectively. This indicates that the characteristics of a particular molecular solvent can increase or decrease the deactivation

rate of $[Fe(CN)_6]^{3-}$. The complete decay of the vibrationally excited levels of the ground state was notably found to occur on a similar 10 ps time scale for the H_2O, D_2O and ETG solvents.

In parallel to the aforementioned studies, Engel *et al.* [93] performed ultrafast EUV photoemission spectroscopy experiments to investigate the relaxation dynamics of the 400-nm-photoexcited LMCT states of the $[Fe(CN)_6]^{3-}$ anion in aqueous solution with sub-100 fs time resolution. The authors proposed a different CT mechanism for the LMCT decay. From the experimental data analysis, assisted by time-dependent density functional theory (TDDFT) calculations, it was concluded that an intermediate LF state is involved in the LMCT relaxation. The transient population of this state was shown to be associated with geometrical distortions, due to vibronic interactions (Jahn-Teller effect), in the excited electronic state, instead of the transient electron hole localisation suggested by Zhang *et al.* The proposed mechanism also differs from the interpretation of Ojeda *et al.*, where a direct transition from the initially excited LMCT state to the vibrationally excited ground state was considered. Thus, Engel *et al.* suggested a sequential relaxation process with an ultrafast biexponential decay behaviour of the excited electronic state population in $[Fe(CN)_6]^{3-}$, taking place with 170 fs and 730 fs time constants, which are associated with a sequence of intersystem crossings in the molecular compound.

The present work aims at determining the relaxation dynamics of the lowest-lying electronically photoexcited ^{2}LMCT state of the $[Fe(CN)_6]^{3-}$ complex upon 400 nm excitation in a non-conventional molecular solvent, specifically the [emim][DCA] ionic liquid. Considering the previous solvent-dependent studies and controversial interpretations of the CT process induced by the LMCT excitation in ferricyanide, the study of the influence of the solvation environment on the $[Fe(CN)_6]^{3-}$ deactivation pathway, as well as an accurate description of the nature of the initially populated electronic states in $[Fe(CN)_6]^{3-}$, aims to address these points of contention. Thus, the transient populations associated with the involved electronically excited states of solvated ferricyanide have been monitored on a binding energy scale by employing the femtosecond TRPES technique.

2.2 Polymeric Carbon Nitrides

Polymeric carbon nitride (PCN) is a metal-free two-dimensional (2D) photocatalytic material, containing Earth-abundant elements of carbon (C) and nitrogen (N) atoms. As the most stable allotrope among the carbon nitride family with 2D-layered graphite-like structure [126], it has been proposed as a promising candidate for energy conversion and storage, as well as environmentally benign catalytic applications [127]. PCN has attracted much attention due to its wide-band-gap-semiconductor-like electronic structure, but with photocatalytic performance in the UV-Vis spectral range combined with modification flexibility, chemical robustness, abundant availability and low-cost [128]. Therefore, PCN has been extensively studied as an efficient photocatalyst for hydrogen and oxygen evolution in the water splitting reaction [129–132], CO_2 reduction to produce storable fuels [133, 134], and organic pollutant degradation [135–137], with prospects to expand its use in photovoltaic, electronic, bioimaging, and sensing applications [138–140].

2.2.1 Chemical and Electronic Structure of Polymeric Carbon Nitride

Depending on the synthetic conditions, the structure of PCN is based on two building blocks: the s-triazine (1,3,5-triazine, $C_3N_3H_3$) or the heptazine (tri-s-triazine, 1,3,4,6,7,9,9b-heptaazaphenalene, $C_6N_7H_3$) core of the heterocyclic aromatic units, composed of C and N atoms in ring structures [141]. PCN is usually prepared in the from of a powder, which is synthesised via high-temperature polymerisation of fine nitrogen-rich organic molecular precursors, such as urea, thiourea, cyanamide, dicyanamide, and melamine [142]. The synthetic pathways to C- and N-containing molecular compounds and the conversion process to the heptazine-based PCN (Figure 2.6) are described in the following. The precursor molecules go through step-wise conversion and polymerisation, such as that induced by heating and reaction of either cyanamide or ammonium dicyanamide to dicyandiamide, subsequent cyclisation of cyanamide or dicyandiamide (or urea) to yield melamine, formation

of melam from melamine dimers, and melam rearranging to melem. By heating further, melem oligomers are formed, which condense to melon. As a result, the polycondensation of precursors forms a melon polymer from melem units, which represents the structure of PCN [143]. Figure 2.7 shows the molecular structure of heptazine-based melon polymeric carbon nitride, which is most likely the closest representation of the real structure of PCN materials.

The electronic structure of PCN is most often described within an organic semiconductor band structure framework [144], in which the valence band maximum (VBM) and the conduction band minimum (CBM) are used to represent the HOMO and LUMO in the context of MO theory [61], respectively. The electronic band structure theory describes the quantum-mechanical behavior of electrons in solid-phase materials, postulating the existence of energy zones, which can also be considered as a large-scale limit of the MO theory. In other words, an energy band is formed by a large number of atomic orbitals (each of which has a discrete energy level) that are so closely spaced in energy that they can be considered as a continuous band. The minimum energy required to promote a valence electron bound to a molecule or unit cell in a solid from the highest occupied energy state of the VB to the lowest unoccupied state of the CB is known as the band gap energy, E_g, and is indicative of the electrical conductivity of a material.

Generally, solid materials are classified into three types in accordance with their E_g values: (1) conductors (metals), that have no band gap (E_g = 0 eV), because the VB overlaps the CB, which is partially occupied, (2) insulators, with fully occupied or empty energy bands, where the electrons in the VB are separated by a large gap from the CB ($E_g \geq 4$ eV), (3) semiconductors, that have a non-zero band gap between the VB and CB ($E_g \leq 4$ eV), allowing optical electronic transitions from the VB into the CB to occur, as long as the excitation energy is greater than or equal to the E_g. The

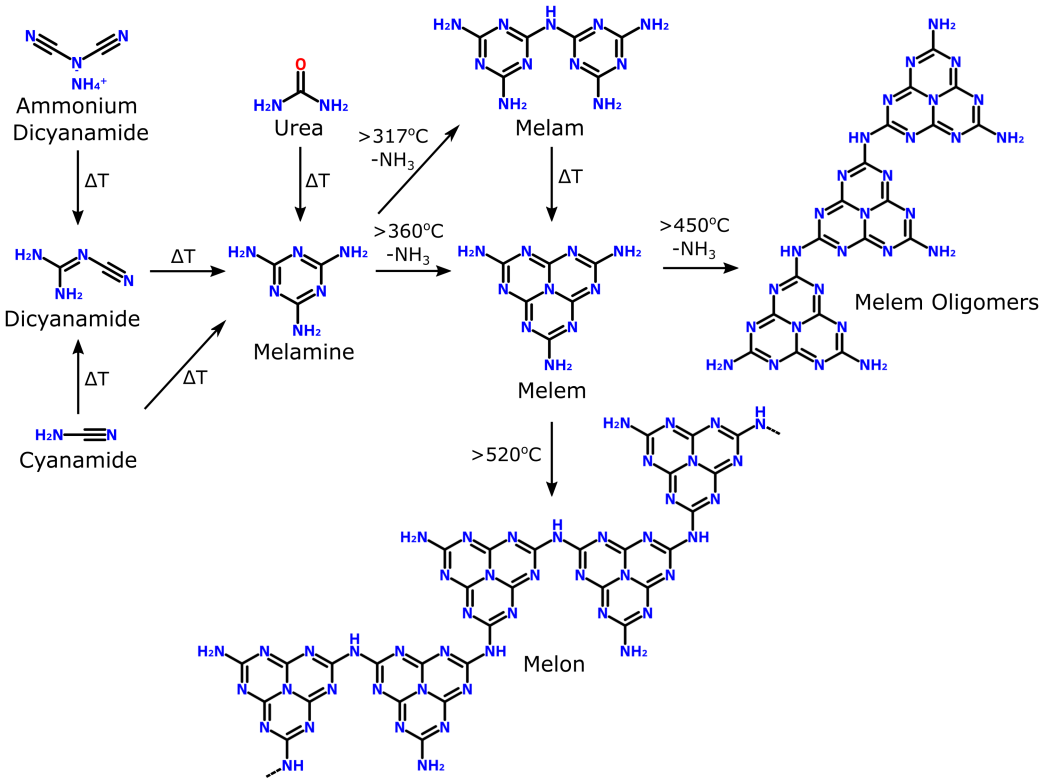

FIGURE 2.6: The synthetic pathways to C- and N-containing molecular compounds and the conversion process from the organic molecular precursors to the heptazine-based melon polymeric carbon nitride. A cascade of condensation reactions occur at elevated temperatures, which are accompanied by the evolution of ammonia, NH_3. Adapted figure with permission from [143] © 2017 by the Springer Nature.

theoretical, calculated energy band gap value of 2.6 eV between the CBM and VBM of polymeric melon was reported by Wang *et al.* [126]. The experimental optical band gap value, associated with the VBM and CBM of melon, as defined from a UV-Vis diffuse reflectance spectroscopy study, was found to be 2.85 eV [145]. This suggests that PCN has a wide-band-gap-semiconductor-like electronic structure. It is worth noting that PCN (heptazine-based melon) is often misleadingly named as a "graphitic carbon nitride" or "g-C_3N_4" in the scientific literature, due to appearance of a pseudo-graphitic peak in the measured X-ray diffraction patterns of melon powder. In contrast to the covalent bonded nature of graphite, in melon, all flat and aromatic molecules share the π–π layer of the heptazine units with a graphite-like arrangement. This is due to the oligomers of melem being linked to NH or NH_2 groups by hydrogen bonding in a zigzag manner between the different chains [146]. A PCN unit cell has the melon poly(aminoimino)heptazine $[C_6N_7(NH_2)(NH)]_n$ structure [143], as opposed to C_3N_4.

The chemical, electronic, and optical properties of PCN materials can be tuned by modification of its morphology, or by doping [143]. In addition, the precursors as well as the polymerisation temperature and heating rate in synthetic condensation of PCN play an important role in the photocatalytic performance of PCN-based materials [147]. To date, various nanostructured morphologies of PCN have been reported, such as nanosheets, nanotubes, hollow nanospheres, and quantum dots [148–151]. The implementation of nanostructured PCN has demonstrated superior photocatalytic performance in comparison to bulk PCN, with the capacity to enhance visible light absorption, enlarge the surface area, expose active sites, and facilitate the transport of photogenerated charge carriers in different morphologies. Alternatively, the incorporation of heteroatoms or functional groups into the framework of PCN, by interstitial or substitutional doping with either metal (Fe, Ag, Co, Zn, etc.) or non-metal (O, P, S, B, F, etc.) elements, has been found to be a suitable approach to tune the band structure of pristine PCN. Thus, the optical and electrochemical properties of the material can be tuned, leading to an improved photocatalytic ability of PCN, particularly, in promoting the H_2 evolution rate during the water splitting reaction [152].

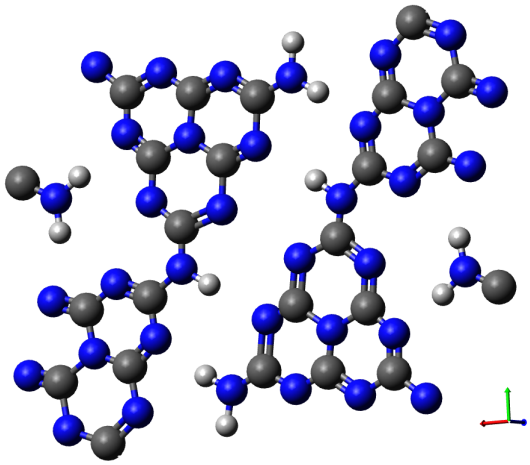

FIGURE 2.7: The molecular structure of heptazine-based melon polymeric carbon nitride, as formed from melem units. Atomic colour codes, carbon: dark gray, nitrogen: blue and hydrogen: light grey.

One of the key parameters, which determines the electronic structure and conductivity of a material is the Fermi level, E_F. The Fermi level is the electrochemical potential of electrons in a condensed-phase sample, which determines the probability of electron occupancy at different energy levels and is the energy at which the average number of particles per quantum state is equal to 1/2, that is, one half of the quantum states are occupied. At absolute zero (0 K), all electrons will occupy energy levels up to the Fermi level, and no higher energy levels will be occupied. In conductors E_F is positioned in the CB, while in insulators in the VB. For a sufficiently conductive condensed-phase samples,

i.e. a semiconductor, E_F is positioned between the VB and CB. The Fermi level is of considerable importance for interfacial electrochemistry when comparing the electrochemical potentials of solid-phase and liquid-phase materials and molecular systems on a common energy scale [153].

In the water splitting reaction, when a photocatalyst (e.g. PCN) is immersed in a liquid electrolyte solution (see Section 2.2.2 for a detailed description), the Fermi level (electrochemical potential) of electrons must be in equilibrium between the two phases to allow an electron transfer across the interface. The electrolyte solution consists of ionic species that can be reduced, *Red*, or oxidized, *Ox*, while exchanging a certain number of electrons, n, with the photocatalysts, in the oxidation-reduction (redox) reaction. The redox half electrochemical reaction occurring at a photocatalyst-electrolyte interface can be expressed as:

$$Ox + ne^- \rightleftharpoons Red, \tag{2.2}$$

While for solid-phase systems E_F is determined relative to the local vacuum level, E_{vac}^{loc}, energy scale, the electrochemical potential of the electrons in the redox species, $E_{F,redox}$, are equivalent to the Fermi level in the liquid-phase. From Equation 2.2, it follows that the electrochemical potential of the electrons in the photocatalyst (E_F) is equal to the electrochemical potential difference between the *Red* and *Ox* ($E_{F,redox}$) couple. $E_{F,redox}$ depends on the standard redox potential of the *Ox*/*Red* couple, ΔE^0, as well as the reduced and oxidized species concentrations. The redox couple energetics are measured relative to a reference electrode, typically the standard hydrogen electrode (SHE). The SHE is defined as an electrode in which H_2 gas at a pressure of 1 bar and a standard temperature of 298 K is bubbled over a platinum electrode coated with platinum black in an electrolyte containing H^+ ions at unit cavity [154]. SHE is assigned a reduction potential equal to zero volts at 0 pH and at any temperature. The relationship between the $E_{F,redox}$ and its reduced and oxidized species in an electrolyte solution and at thermodynamic equilibrium on a standard hydrogen electrode scale is given by the Nernst equation [153]:

$$E_{F,redox} = \Delta E^0 + \frac{RT}{nF} lnQ, \tag{2.3}$$

where ΔE^0 is the standard redox potential of the *Ox*/*Red* couple, R is the universal gas constant, T is the temperature in K, n is the number of electrons transferred in the redox reaction, F is the Faraday constant (F = 96485 C/mol), and Q is the reaction quotient.

When E_F and $E_{F,redox}$ are in equilibrium, the difference between the two energy scales for the solid-phase material and liquid-phase molecular system, is the E_0^{SHE} of the hydrated proton at unit activity, relative to the electron in vacuum close to the solution surface, i.e. E_{vac}^{loc}, which is equal to - 4.44 $\pm$ 0.02 eV (or V) at 298 K [155]. In a real system, that involves equilibria with hydrogen and protons, the pH of the solution must also be taken into account at the liquid-solid interface, as it can modify the redox potentials of the electrolyte as well as the photocatalyst and shift the energy levels. Therefore, in such systems the redox potentials are referenced against the reversible hydrogen electrode (RHE). The potential of the reference, RHE, changes with pH with respect to the SHE as follows [154]:

$$E_0^{RHE} = E_0^{SHE} - 0.05916\ eV \times pH, \tag{2.4}$$

2.2.2 Photocatalytic Water Splitting

The global downward trend in fossil fuel-based energy resources (coal, oil, and gas) availability determines the need for alternative and renewable energy sources. The use of sunlight as an environmentally benign, sustainable and inexhaustible source of energy has attracted great attention worldwide as the most likely replacement for traditional energy sources in the past few decades. At present, two principal directions for solar energy conversion have been established: the creation of solar elements that allow conversion of solar energy directly into electricity (solar concentrators, photovoltaic and

dye-sensitized solar cells) [156, 157], and the development of photocatalytic materials for direct storage of solar energy in chemical bonds [158, 159]. The latter has received considerable interest, due to the potential for low-cost and pollution-free applications, such as the reduction of CO_2 to produce formic acid or methanol (solar fuels production) [9], and splitting of water to H_2 and O_2 [5]. In particular, water splitting has become a promising method to store solar energy in chemical bonds.

Photocatalytic water splitting is a process that involves the dissociation of liquid water, H_2O_{liq}, into gaseous molecules of hydrogen H_{2_g} and oxygen O_{2_g}, based on the activation of a catalyst by irradiation with a light source. In general, water splitting involves several principal steps: (1) absorption of light by the photocatalyst and generation of excited electron-hole pairs, (2) internal charge carrier separation and intermolecular charge transfer to initiate a chemical reaction, and (3) catalytic formation of H_2 and O_2 by the reduced and oxidised photocatalyst, respectively. The photocatalyst can be provided either in the form of a powder or an immersed electrode/thin-film, which are implemented in photocatalytic or photoelectro-catalytic water splitting devices, respectively.

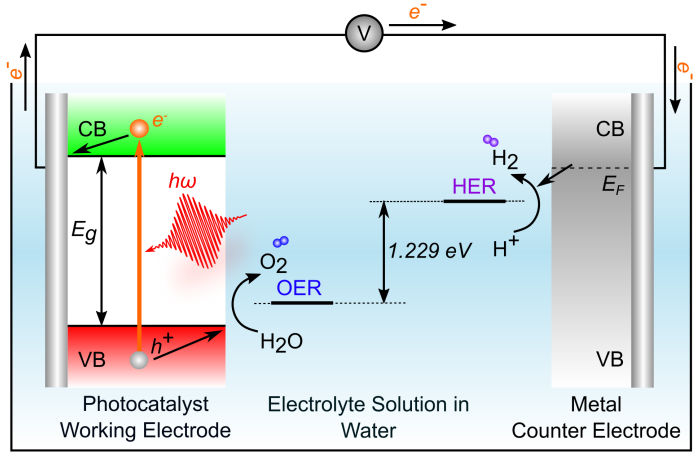

FIGURE 2.8: Schematic view of the overall water splitting reaction and energetic diagram of a photoanode-based photoelectrochemical cell under light irradiation. The scheme shown here is based on a photocatalyst working electrode and a metal counter electrode immersed in an electrolyte solution.

The phenomenon of H_2 production from photocatalytic water splitting was first demonstrated by Fujishima and Honda in 1972, using single-crystal titanium dioxide (TiO_2) as the photocatalyst in a photoelectrochemical (PEC) cell [160]. Typically, a PEC water splitting experimental setup consists of either two or three electrodes with an anode, a cathode and potentially a reference electrode immersed in an electrolyte (specifically water and a sacrificial agent), anode and cathode connected and externally biased (Figure 2.8). Depending on the configuration of the PEC cell, it can be photoanode-based, with a light-harvesting photocatalyst being supported at the anode (working electrode) and a metal (e.g. platinum, Pt) cathode (counter electrode). Alternatively, the PEC cell can be photocathode-based, where the photocatalyst and the metal are oppositely applied in the electrical circuit. Under irradiation, a photocatalyst absorbs photons with a photon energy, $\hbar\omega$, exceeding its optical band gap, E_g, promoting electrons from the VB to the CB and, consequently, generating photoexcited electron-hole pairs (see Equation 2.6). The photogenerated electron-hole pairs can either recombine or be separated under external bias to the anode, leading to interfacial electron transfer processes between the photocatalyst and the electrolyte. As a result, photogenerated holes on the photoanode surface split water molecules, producing O_2 and protons, which is called the oxygen evolution reaction (OER). Subsequently, hydronium ions migrate through the electrolyte to reach the counter electrode, thereby reducing protons at the cathode's surface and generating gaseous H_2 in a process known as the hydrogen evolution reaction (HER).

From a thermodynamic perspective, the overall water splitting into H_2 and O_2 is an energetically uphill and endothermic reaction, accompanied by a large positive change in the Gibbs free energy [161]:

$$\Delta G^0 = -nF\Delta E^0 = +\,237.2\ kJ\ mol^{-1}, \tag{2.5}$$

where n is the number of transferred electrons (n = 2), F is the Faraday constant, and ΔE^0 is the standard redox potential of the O_2/H_2O couple (ΔE^0 = 1.229 V) at standard temperature (298 K) and concentrations (1 mol L^{-1}, 1 bar).

The HER and OER of PEC water splitting - for an acidic electrolyte referenced to the SHE at 0 pH - can be expressed for the reduction, E^0_{red}, and oxidation, E^0_{ox}, half-reactions as [162]:

$$4h\nu \rightarrow 4e^- + 4h^+, \tag{2.6}$$

$$4H^+ + 4e^- \rightarrow 2H_{2_g} \qquad E^0_{red} = +\,0.000\,V, \tag{2.7}$$

$$2H_2O + 4h^+ \rightarrow 4H^+ + O_{2_g} \qquad E^0_{ox} = -\,1.229\,V, \tag{2.8}$$

In the case of an alkaline environment, hydroxyl anions are formed from the dissociation reaction of water; the two reduction and oxidation half-reactions can be written as:

$$4H_2O + 4e^- \rightarrow 2H_{2_g} + 4OH^- \qquad E^0_{red} = -\,0.828\,V, \tag{2.9}$$

$$4OH^- + 4h^+ \rightarrow 2H_2O + O_{2_g} \qquad E^0_{ox} = +\,0.401\,V, \tag{2.10}$$

Thus, the overall water splitting reaction can be defined as:

$$2H_2O \xrightarrow{4h\nu} O_{2_g} + 2H_{2_g}, \tag{2.11}$$

Photocatalytic water splitting is typically performed in a quartz reactor, where a photocatalyst is dispersed in an aqueous solution [163, 164]. Similar to PEC water splitting, when the photocatalyst is irradiated by light, the photocatalyst absorbs photons and promotes electrons from the VB to CB, generating electron-hole pairs. The electron-hole pairs that remain separated diffuse from the bulk to the surface reactive sites, reacting with adsorbed species on the surface leading to the HER and OER. Thus, the photocatalytic suspension reacts over a solid, three-phase (solid-liquid-gas) interface. Since the water splitting reaction is a four-electron process, with the simultaneous generation and back-reaction of H_2 and O_2 gases, there is a probability for a backward reaction to occur. This imposes one of the main limitations on effective photocatalytic water splitting when using aqueous solution.

To facilitate the oxidation or reduction of water and to increase the overall efficiency of photocatalytic water splitting, sacrificial agents (electrons donors or acceptors) are often mixed with water, which can scavenge electrons or holes and suppress recombination of the excited charge carriers, therefore accelerating the rate of photocatalytic H_2 production. In the presence of a sacrificial agent, the positive holes irreversibly oxidise the sacrificial reagent instead of water. The most commonly used sacrificial agents for polymeric carbon nitride photocatalysts are Na_2S, Na_2SO_3, lactic acid, methanol, and triethanolamine (TEOA) [165]. In addition to the use of sacrificial agents, noble metal co-catalysts (Pt, Au, Pd) and recently implemented, non-metal (carbon dots) and transition metal oxides (NiO, MnO_2, CoO) are also utilised in photocatalytic water splitting, with the main purpose of reduction of charge carrier recombination and to spatially separate HER and OER sites [166].

The thermodynamic condition for driving a single-step, overall water splitting reaction implies several requirements on the electronic band structure of a photocatalyst. In particular, to initiate photocatalytic reactions, the energy band gap of a photocatalyst immersed in an acidic electrolyte solution must be greater than 1.229 eV, and the top of the VB should be more positive than 1.229 V *versus* SHE, while at 0 pH the bottom of its CB should be more negative than 0 V *versus* SHE. In addition, the effectiveness of a photocatalyst will depend on its physical, chemical, and opto-electronic properties, including good thermal and chemical stability, inertness in aqueous solution,

alcohol and different pH environments, high visible light-harvesting capacity, and long lifetime of the photogenerated electron-hole pairs. Since the discovery of the water splitting using TiO_2 as a photocatalyst [160], a large number of metal-based semiconductor catalysts have been investigated to efficiently split water into H_2 and O_2 under UV-Vis light irradiation. The most employed semiconductor photocatalysts are oxides and chalcogenides such as TiO_2, ZnO, WO_3, Nb_2O_5, $BiVO_4$ Ta_2O_5, CdS, and Cu_2S [167–169]. Figure 2.9 shows the energy band gaps and the electronic VBM and CBM positions of the commonly used photocatalysts or co-catalysts in water splitting, including oxides, nitrides, and chalcogenides. Despite the large variety of semiconductor photocatalysts, most of them have a number of significant disadvantages. Many metal-based semiconductor photocatalysts have a wide energy band gap (TiO_2, ZnO, ZrO_2), which leads to their inefficiency when exposed to visible light and limits their use to the UV spectral region (≈ 4 % of solar energy). In certain cases the VBM and CBM positions of photocatalysts are not favorable for the production of either O_2 or H_2 with respect to the water redox reaction potentials, for example, Ta_2O_5 and WO_3, respectively. Moreover, some efficient narrow band gap photocatalysts (CdS, CdSe) suffer from severe photocorrosion under light irradiation [170], which greatly complicates their long-term photocatalytic application.

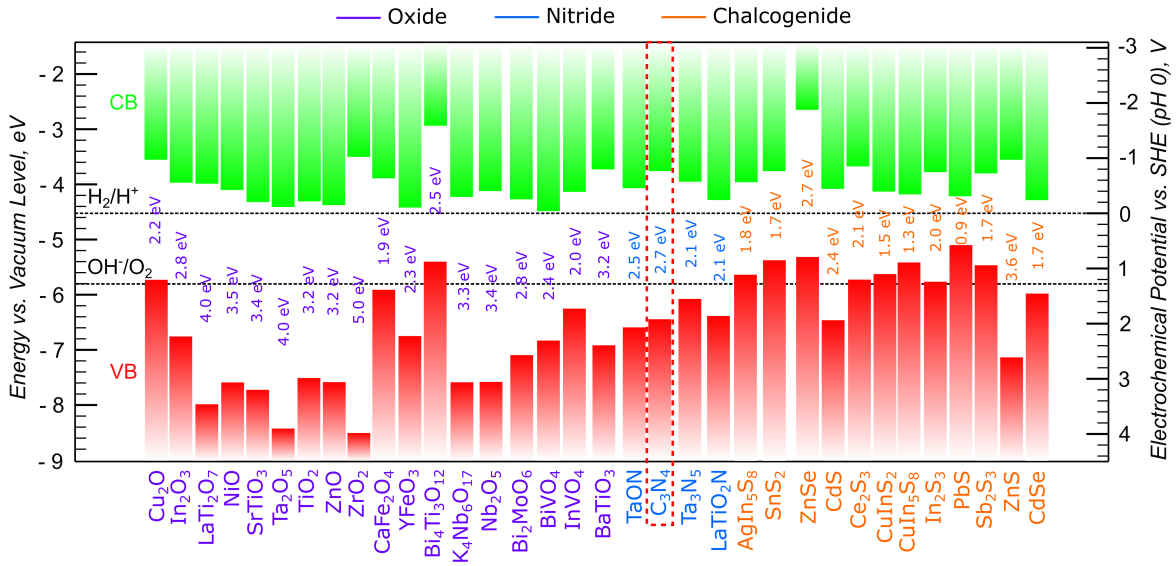

FIGURE 2.9: Energy band gaps and VBM (red) and CBM (green) positions of the selected oxides, nitrides and chalcogenides with respect to the vacuum level and standard hydrogen electrode (SHE). The two black dashed lines indicate the water redox reaction potentials. The PCN sample (C_3N_4) is highlighted by the red dashed line. Adapted figure with permission from [171] © 2016 by the Wiley-VCH.

While much of the research in the past decades has focused on metal-based semiconductor photocatalysts, the development of efficient metal-free polymer carbon nitride photocatalysts is currently an active area of research for water splitting applications [172]. This is primarily due to the fact that PCN is one of the few visible-light-harvesting photocatalysts with an energy band gap of approximately 2.7 eV. That possesses a sufficiently large thermodynamic driving force for H_2 and O_2 production in the water splitting reaction, as highlighted by the red dashed line in Figure 2.9. Beyond the ability to easily modify the electronic and chemical structure of this material, as described in detail in Section 2.2.1, PCN has excellent chemical and thermal stability, minimising photocorrosion in the water splitting reaction compared to metal-based semiconductor catalysts.

2.2.3 Bulk, Mesoporous and Porous Ultrathin Nanosheets of Polymeric Carbon Nitrides as Efficient Photocatalysts for Hydrogen Production

In view of numerous effectively developed PCNs with different morphologies, porosities, surface functional groups and electronic band structures, it was noticed that two-dimensional (2D) atomically-thin nanosheets of PCN exhibit enhanced photocatalytic activity [173, 174]. In particular, recently engineered atomically-thin porous sheets of oxygen-containing and amino co-functional group PCN are found to be relatively efficient photocatalysts for H_2 production in the water splitting reaction [175]. These 2D porous ultrathin nanosheets, as well as pristine bulk PCNs, were investigated in this work.

Figure 2.10 shows the hypothetical chemical structure and the sequence of preparation of three PCN photocatalysts, which were synthesised and provided by the group of Prof. Bin Zhang from Tianjin University [175]. The polymeric bulk carbon nitride (CNB) was synthesised by the thermal polymerisation of melamine at 520 °C. The obtained CNB powder of nanosheets product had a bulk density of 544 mg cm^{-3}, sheet thickness of 16 nm, and a Brunauer-Emmett-Teller (BET) surface area of 8 m^2 g^{-1}. The porous oxygen-rich carbon nitride nanosheets (CNPS-O) were synthesised by the oxidation and etching of the initially produced CNB. The amino functional group, atomically-thin porous carbon nitride sheets (CNPS-NH_2) were synthesised using the same procedure as CNPS-O, with ammonia (NH_3) treatment subsequently implemented to exfoliate and form -NH_2 groups on the resulting 2D porous nanosheets.

The bulk densities of CNPS-O and CNPS-NH_2 were calculated to be 134 mg cm^{-3} and 12 mg cm^{-3}, respectively, which are considerably lower than that of CNB. The produced macroscopic, ultralight structures result in abundant active sites and a highly solvent accessible surface area at the micrometer level. Atomic force microscopy images and associated height profiles demonstrated that the thickness of CNPS-O was about 10 nm, and after a further thermal treatment of CNPS-O in a NH_3 atmosphere, the thickness of CNPS-NH_2 was substantially reduced, forming atomically-thin 2D porous sheets of 0.4 nm. The CNPS-NH_2 surface area was determined to be 195 m^2 g^{-1}, compared to the CNPS-O of 48 m^2 g^{-1}, which can be affected by the ultrathin morphology and enhanced pore density. A more detailed description of the preparation and characterisation of the CNB, CNPS-O and CNPS-NH_2 powder photocatalysts can be found in [175].

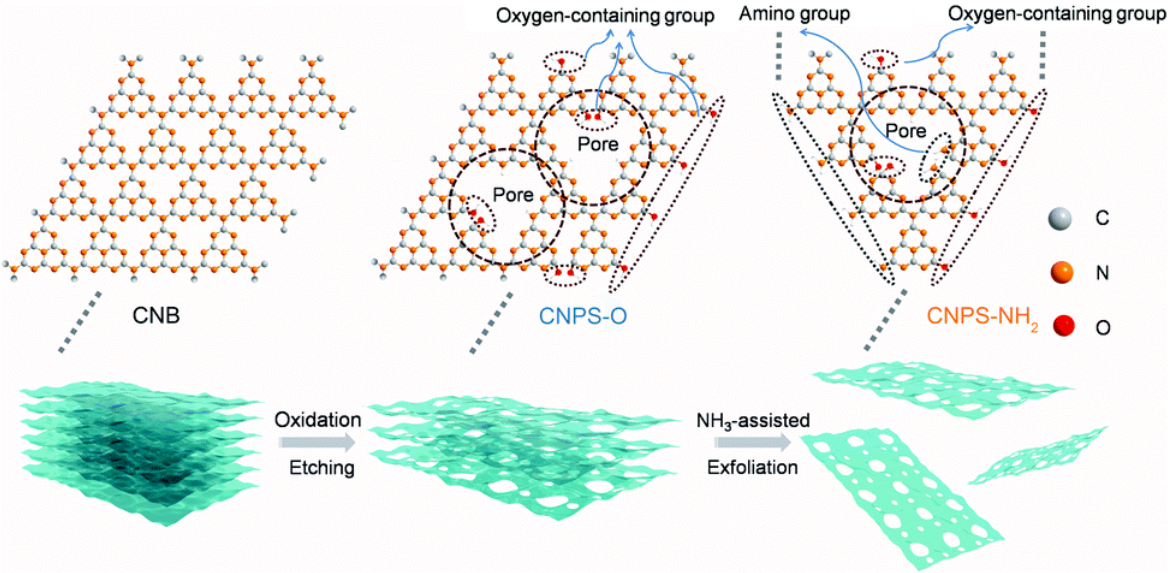

FIGURE 2.10: The hypothetical structure and the preparation process of the bulk (CNB), 2D porous nanosheets of oxygen-containing (CNPS-O) and amino co-functional groups (CNPS-NH_2) polymeric carbon nitrides. Reprinted figure with permission from [175] © 2018 by the Royal Society of Chemistry Publishing.

The photocatalytic H_2 evolution reaction performance of the CNB, CNPS-O and CNPS-NH_2 powders, with the presence of Ni co-catalyst contents up to 5 wt% and a TEOA sacrificial electron donor, was investigated under visible light irradiation by Meng *et al.* [175]. The H_2 production rates of CNB, CNPS-O and CNPS-NH_2 were reported to be 110.1, 471.1 and 1233.5 μmol h^{-1} g^{-1}, respectively. The visible-light activity of the CNPS-NH_2 was 11 times higher than that of CNB, which indicates that changing the structure and surface area of PCN can enhance its photocatalytic activity. Further, the HER was performed under simulated sunlight irradiation (AM 1.5 G), where CNPS-NH_2 exhibited the highest H_2 evolution rate of 8134.1 μmol h^{-1} g^{-1} compared to 4375.8 μmol h^{-1} g^{-1} of CNPS-O and 1403.5 μmol h^{-1} g^{-1} of CNB. In addition, the H_2 evolution activity of the PCN powders with a Pt co-catalyst was investigated under visible light as well as with simulated AM 1.5 G sunlight irradiation. A H_2 evolution rate of 20948.6 μmol h^{-1} g^{-1} for CNPS-NH_2 was achieved under AM 1.5 G solar irradiation, yielding one of the highest photocatalytic performances among the self-modified PCN/Pt systems reported so far [176–178]. However, the reason for the significant increase in the photocatalytic H_2 production rate of CNPS-NH_2 and the corresponding improvement in the charge carrier kinetics upon light excitation of the 2D porous ultrathin PCN nanosheets, as compared to bulk PCN, remains an open question.

Since it has been shown that PCNs with increased surface area and porosity can enhance their photocatalytic water splitting performance, various approaches have been used to synthesise porous PCN structures. One of the well-established techniques for producing nanoporous structures of PCNs is the sol-gel method [179, 180]. The advantage of this method compared to the thermal polymerisation method is that the growth and individual design of the pore structure of the PCN material can be controlled. In the present work, mesoporous PCN prepared by a combined sol–gel and thermal condensation method was also investigated. This preparation approach involves simultaneous mixing and condensation of the PCN (cyanamide) precursor with the silica (tetraethylorthosilicate) precursor [180]. The mesoporous PCN is obtained after condensation and heat treatment, which includes sol mixing, gel formation, calcination of the gel, and silica removal. PCN retains its structure even in the spatial constraint created by the surrounding silica phase. Since both precursors are liquids, this approach allows one to conveniently form thin and thick films or blocks of mesoporous PCNs.

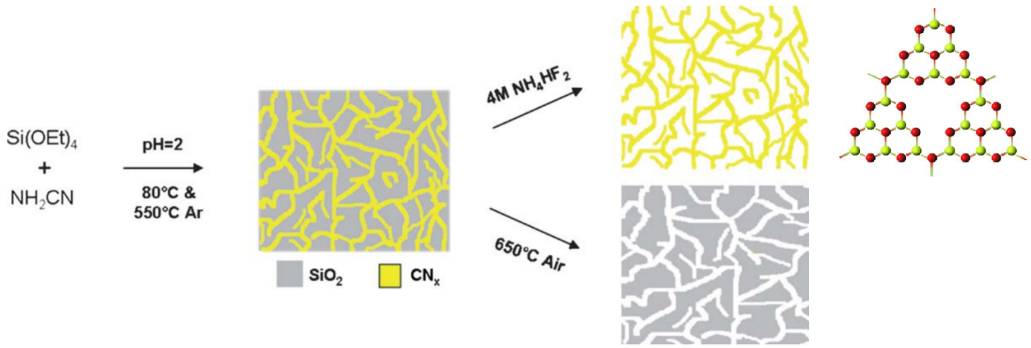

FIGURE 2.11: The sol–gel/thermal condensation preparation process of the mesoporous polymeric carbon nitride (sg-CN) (left panel) and the hypothetical structure of a tri-s-triazine sheet of sg-CN (right panel). Atomic colour codes, carbon: yellow and nitrogen: red. Reprinted figure with permission from [180] © 2011 by the Royal Society of Chemistry Publishing.

Figure 2.11 shows the hypothetical chemical structure and the combined sol–gel/thermal condensation preparation process of the mesoporous PCN (sg-CN) used in this work, which was synthesised by the group of Prof. Arne Thomas from Technische Universität Berlin. The sg-CN powder was synthesised at 550 °C according to the procedure previously reported in literature [180]. The BET surface area of the obtained sg-CN powder was determined to be 140 m^2 g^{-1} [181], comparable to that of the aforementioned CNPS-NH_2 [175]. Further, the mesoporous sg-CN was found to be highly

photocatalytically active under visible light irradiation in the presence of Ni or Ni_2P co-catalyst, and the TEOA sacrificial electron donor in the H_2 evolution reaction [181, 182]. An enhanced H_2 evolution rate of 8400 μmol h^{-1} g^{-1} was reported by Indra *et al.* [181], when a Ni_2P nanoparticle co-catalyst was loaded on the surface of sg-CN. This is comparable to the H_2 evolution rate of the highly efficient PCN photocatalysts [183]. The authors performed time-resolved photoluminescence (TRPL) spectroscopic studies to reveal the photophysics of the enhanced charge transfer upon optical excitation of the Ni_2P/sg-CN system. However, TRPL only detects the radiative decay of the photogenerated electron-hole pairs, by collecting photons spontaneously emitted by the PCN powder. In addition, TRPL is based on a time-correlated single photon counting technique [184], which allows the kinetics of the photoexcited species to be monitored out to ms timescales, but has a limited time resolution of the order of few ten ps. Therefore, the early-time dynamics of photogenerated charges in mesoporous sg-CN remains poorly understood. Table 2.3 summarises the main structural properties, as well as highest H_2 evolution rates obtained, for the PCN samples used in the present studies. A bulk density of the sg-CN powder was not determined in the aforementioned studies and is therefore not presented in the table.

TABLE 2.3: Comparison of the structural properties and photocatalytic activity of the as-prepared PCN powders implemented in this work.

Sample	CNB	CNPS-O	CNPS-NH_2	sg-CN
Bulk density / mg·cm^{-3}	544	134	12	-
Sheet thickness / nm	16	10	0.4	5
BET surface area / $m^2 \cdot g^{-1}$	8	48	195	140
H_2 evolution rate / $\mu mol \cdot h^{-1} \cdot g^{-1}$	110.1	471.1	1233.5	8400
(under $\lambda > 420$ nm)	TEOA + Ni	TEOA + Ni	TEOA + Ni	TEOA + Ni_2P

This work explores uncharted areas of the photophysical processes occurring in PCNs on femtosecond to nanosecond timescales, following their initial photoinduced charge carrier dynamics using high-time-resolution ultrafast spectroscopy studies. By employing the femtosecond time-resolved EUV photoemission spectroscopy and UV-visible transient absorption spectroscopy techniques, the photoinduced early-time charge separation dynamics in sg-CN, CNB, CNPS-O and CNPS-NH_2 photocatalysts can be monitored with sub-100 fs time resolution. The former technique specifically addresses the dynamics occurring in the top few-nm of the solid powder, in vacuum. Whereas the latter allows the material bulk to be predominantly probed. Understanding the kinetics of photogenerated carrier lifetimes in the bulk, mesoporous and 2D porous ultrathin nanosheets of PCNs can reveal the nature of their ultrafast photophysical processes and is expected to complement the previous research of Meng *et al.* [175] and Indra *et al.* [181]. The ultrafast studies of the surface-bulk photoinduced charge separation dynamics of the PCNs may also provide an avenue to develop highly-efficient photocatalysts for water splitting, and potentially for a broad range of other applications.

Chapter 3

Experimental Procedures and Methods

> "Energy rightly applied and directed will accomplish anything."
>
> — *Nellie Bly*

Chapter 3 provides an overview of the experimental procedures and methods, encompassing the fundamental theoretical concepts and physical principles implemented in this dissertation work. Section 3.1 introduces the generation of the ultrashort laser pulses employed in time-resolved spectroscopy experiments. Section 3.2 describes the main non-linear processes that occur during the light-matter interactions induced by intense laser fields. This includes (Section 3.2.3) the coherent generation of ultrashort EUV pulses through the laser-driven high-order harmonic generation (HHG) process. Therein, the theoretical aspects as well as the optimal phase matching conditions for efficient HHG in gaseous media are explained. Section 3.3 presents the principles of the photoemission spectroscopy technique, based on the three-step model of photoemission from condensed-phase targets. Further, the concept of the femtosecond time-resolved extreme-ultraviolet (EUV) photoemission spectroscopy (TRPES) technique is presented, and its main advantages and limitations are clarified. Section 3.4 introduces the fundamentals of the complementary femtosecond time-resolved ultraviolet-visible absorption spectroscopy (TAS) technique. Finally, the global fitting data analysis procedure is described in Section 3.5.

3.1 Ultrashort Laser Pulse Generation

The time-domain study of dynamic processes in matter requires research methods with time-resolutions that exceed the rate of change of the process of interest. In molecular systems, the natural photochemical and photophysical processes occur on the femtosecond time scale, which is the unit of time equal to 10^{-15} seconds. Ultrashort laser pulse generation with a duration of several femtoseconds has proven to be a versatile tool for ultrafast spectroscopic investigations of the electronic and structural dynamics of atoms and molecules in matter, which has found applications in natural and medical sciences, as well as engineering and manufacturing technologies [34, 185, 186]. In this dissertation, femtosecond laser pulses were employed to study the electronic dynamics of liquid-phase molecular and solid-phase material catalysts following photoexcitation and interrogation of chromophores on their fundamental time scales. Correspondingly, a basic description of the fundamental physical processes for the generation of femtosecond laser pulses is provided in the following.

3.1.1 Mathematical Description of Ultrashort Laser Pulses

Ultrashort laser pulses are bursts of electromagnetic radiation, namely optical wave packets that are described as temporally and spatially dependent electric fields. The propagation of the electric field and its interaction with matter is governed by Maxwell's electromagnetic wave equations in the framework of a semi-classical interpretation [187]. The electric field of an ultrashort laser pulse can be described through a complex representation of the oscillating electric field in the temporal domain

(see Figure 3.1). Neglecting the spatial and polarisation dependence of the field, $E(x, y, z, t) = E(t)$, the field can be described as follows [31]:

$$E(t) = A(t)\, e^{-i\omega_0 t}, \tag{3.1}$$

where $A(t)$ is the complex amplitude envelope, and ω_0 is the carrier frequency.

The complex representation of the electric field of the laser pulse in the time domain can be further decomposed into a rapidly oscillating part of the electric field and a slowly varying envelope $A(t)$ as:

$$E(t) = |E(t)|\, e^{-i\phi_0}\, e^{-i(\phi(t)+\omega_0 t)}, \tag{3.2}$$

Here, $|E(t)|$ is called the electric field envelope, $\phi(t)$ is the time-dependence of the temporal phase, and ϕ_0 is the phase between the carrier wave and the peak of the temporal pulse envelope, which is often referred to as the carrier-envelope phase (CEP) (see Figure 3.1). The CEP becomes a very important feature of few-cycle ultrashort laser pulses, where the instantaneous strength of the field has bearing on its application.

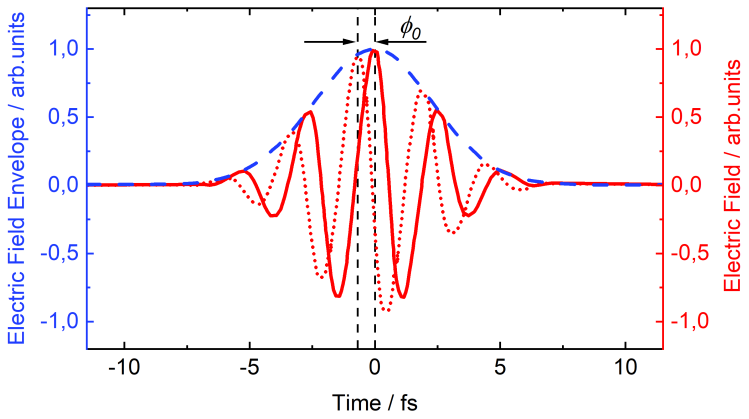

FIGURE 3.1: The electric field and envelope of a Gaussian pulse. The red solid and dotted lines represent the electric field for different values of the CEP. The blue dashed curve is the electric field envelope.

In Equation 3.2, the time-dependent phase $\phi(t)$ determines the variation of the carrier frequency in time. Thus, a pulse which has its (instantaneous) carrier frequency varying in time, a so-called chirped pulse, is described by the instantaneous frequency given by:

$$\omega(t) = \omega_0 + \frac{d\phi(t)}{dt}, \tag{3.3}$$

If $d^2\phi(t)/dt^2 > 0$, the carrier frequency increases along the time scale of the laser pulse, which can be described as a positively or up-chirped pulse. For the case $d^2\phi(t)/dt^2 < 0$, the instantaneous frequency decreases, producing a negatively or down-chirped pulse (see Section 3.1.2 for more details).

The electric field of an ultrashort laser pulse can be described in the frequency domain as:

$$E(\omega) = |E(\omega)|\, e^{i\phi(\omega)}, \tag{3.4}$$

where $\phi(\omega)$ is the spectral phase. In the frequency domain, in addition to the measurement of an intensity spectrum, the spectral phase contributes to the pulse characterisation. For instance, $\phi(\omega)$ can be measured using the spectral phase interferometry for direct electric field reconstruction (SPIDER) [188] and frequency-resolved optical gating (FROG) [189] diagnostic techniques for ultrashort pulse characterisation in time and frequency space.

The Equations 3.2 and 3.4 are related to each other through the time and frequency Fourier transforms of a laser pulse that can be expressed in terms of the electric field as:

$$E(t) = \frac{1}{2\pi}\int_{-\infty}^{+\infty} E(\omega)\, e^{-i\omega t} d\omega,$$
$$E(\omega) = \int_{-\infty}^{+\infty} E(t)\, e^{i\omega t} dt, \tag{3.5}$$

Subsequently, the pulse duration Δt and spectral bandwidth $\Delta\omega$ can be determined as follows:

$$\langle \Delta\omega^2 \rangle = \frac{\int_{-\infty}^{+\infty} \omega^2 |E(\omega)|^2 d\omega}{\int_{-\infty}^{+\infty} |E(\omega)|^2 d\omega},$$
$$\langle \Delta t \rangle = \frac{\int_{-\infty}^{+\infty} t|E(t)|^2 dt}{\int_{-\infty}^{+\infty} |E(t)|^2 dt}, \tag{3.6}$$

Considering that the relationship between the temporal and spectral characteristics of the electric field are interrelated through Fourier transforms, the spectral bandwidth and pulse duration are related to each other by the following uncertainty principle inequality [31]:

$$\langle \Delta\omega \rangle \langle \Delta t \rangle \geq \frac{1}{2}, \tag{3.7}$$

where $\langle \Delta\omega \rangle \langle \Delta t \rangle$ is known as the time-bandwidth product. This indicates that for generating femtosecond laser pulses, it is necessary to implement a sufficiently broad spectral bandwidth. If the equality in Equation 3.7 is reached, the generated laser pulse has a frequency-independent spectral and temporal phase and is called a bandwidth-limited or a Fourier-transform-limited pulse. In this case, the pulse is unchirped (see Figure 3.2 (a)).

Experimentally, the temporal and spectral intensity profiles are readily measured and associated full-width at half-maximum (FWHM) values are established. Correspondingly, the Δt is defined as the FWHM of the intensity profile, and the $\Delta\omega$ is given in terms of the optical frequency bandwidth $\Delta\nu$ (in Hz) measured at the FWHM of the spectral intensity, where $\Delta\omega = 2\pi\Delta\nu$. Thus, the Fourier inequality can be written as:

$$\Delta\nu\Delta t \geq K, \tag{3.8}$$

where K is a numerical constant on the order of 1, which depends on the temporal pulse envelope shape. Values of K for the most commonly used pulse shapes and their time-bandwidth product can be found in Ref. [31]. Using Equation 3.8, the minimum pulse duration can be determined as:

$$\Delta t \geq K \frac{{\lambda_0}^2}{\Delta\lambda \cdot c}, \tag{3.9}$$

Here, λ_0 and $\Delta\lambda$ are the central wavelength and the FWHM of the spectrum of the laser pulse (in nm), c is the speed of light. Ultrashort pulse temporal profiles can often be described by a Gaussian envelope:

$$|E(t)| = A(t) = A_0\, e^{-\frac{(t-t_0)^2}{2\sigma^2}}, \tag{3.10}$$

where A_0 is the peak amplitude, t_0 is the central peak position, and σ is the width (standard deviation) of the Gaussian envelope.
The parameter σ is related to the FWHM of the Gaussian peak, represented by τ:

$$\tau = 2\sqrt{2\ln 2}\sigma, \tag{3.11}$$

For a Fourier-transform-limited Gaussian pulse, the time–bandwidth product, i.e. K value is 0.441 for a Gaussian function [31]. Hence, the spectral bandwidth is $\Delta\nu \approx \frac{0.441}{\Delta t}$.

3.1.2 Effect of Material Dispersion on Propagation of Ultrashort Pulses

Dispersion of optical materials is one of the main obstacles to maintaining a short pulse duration during the propagation of ultrashort pulses through air and optical components (e.g. lenses, polarisers, non-linear crystals, etc.). In bulk dispersive media, the refractive index of the medium is frequency-dependent; therefore, it changes the temporal and spectral phase of the propagating pulse. Thus, short optical pulses experience a linear-optical distortion known as the optical dispersion. The dispersion induces the broadening of a pulse duration.

When a laser pulse propagates through a transparent medium with refractive index $n(\omega)$ and length L, the spectral phase change is given as follows:

$$\phi(\omega) = n(\omega)\, L\, \frac{\omega}{c}, \tag{3.12}$$

In order to calculate the effect of dispersion, the spectral phase can be expressed using a Taylor series expansion around the carrier frequency, ω_0, of the pulse:

$$\phi(\omega) = \phi_0 + \phi^{'}(\omega-\omega_0) + \frac{1}{2!}\phi^{''}(\omega-\omega_0)^2 + \frac{1}{3!}\phi^{'''}(\omega-\omega_0)^3 + ..., \tag{3.13}$$

The derivatives of the spectral phase in Equation 3.13 are most often expressed in terms of $n(\omega)$ and commonly termed the group delay (GD), the group delay dispersion (GDD), and the third order dispersion (TOD) [31]:

$$\begin{aligned} GD \equiv \phi^{'} &= \frac{d\phi(\omega)}{d\omega}\Big|_{\omega=\omega_0} = \frac{1}{c}\left(n - \lambda\frac{dn}{d\lambda}\right), \\ GDD \equiv \phi^{''} &= \frac{d^2\phi(\omega)}{d\omega^2}\Big|_{\omega=\omega_0} = \left(\frac{\lambda}{2\pi c}\right)\frac{1}{c}\left(\lambda^2\frac{d^2n}{d\lambda^2}\right), \\ TOD \equiv \phi^{'''} &= \frac{d^3\phi(\omega)}{d\omega^3}\Big|_{\omega=\omega_0} = \left(\frac{\lambda}{2\pi c}\right)^2\frac{1}{c}\left(3\lambda^2\frac{d^2n}{d\lambda^2} + \lambda^3\frac{d^3n}{d\lambda^3}\right), \end{aligned} \tag{3.14}$$

The first derivative term defines the propagation time of the pulse envelope. The second derivative term leads to the temporal broadening of a pulse due to a linear chirp. This means that the GDD results in a linear variation of the propagation time with frequency. Depending on the sign of $\phi^{''}$, two types of temporal broadening can be defined. When GDD > 0, the longer wavelengths propagates faster than the shorter wavelengths in the pulse, producing a linear positive or up-chirp (see Figure 3.2 (b)). On the contrary, when the shorter wavelengths propagate faster than the longer ones with GDD < 0, a linear negative or down-chirp occurs (see Figure 3.2 (c)). The third derivative term in Equation 3.14 causes a quadratic variation in delay with frequency and can lead to an asymmetric pulse distortion and lower the quality of a laser pulse. The higher-order derivatives in the Taylor expansion induce additional phase shifts contributing to further, more complicated pulse chirping and distortion.

In an ultrafast time-resolved spectroscopy experiment, the time resolution is determined by the durations of the implemented laser pulses, which are typically < 100 fs. Thus, the temporal broadening of an ultrashort pulse derived from the linear dispersion of the optical materials is one of the limiting factors for conducting experiments with high temporal resolution. For this reason, the optical components in the beam path of the femtosecond pulse are usually constructed as thin as possible (taking into account the laser-induced damage threshold (LIDT) of an optical element [190] and induced stresses and distortions). Moreover, a dispersion of the opposite sign can be introduced to recompress the pulse by employing bulk materials with dispersions of opposite sign, e.g. by implementing angular dispersing pairs of prisms [191], diffraction gratings [192], chirped mirrors [193] or optical fibers [194] as chromatic dispersion elements. Such approaches are typically applied in mode-locked-based chirped-pulse amplified laser systems, where a seed pulse is stretched with one of these methods to lower the peak intensity of the amplified pulse, the seed pulse is amplified, and a dual grating compressor compensates the linear dispersion of the stretcher and bulk material of the amplifier in the time-domain. A more detailed description of the latter is presented in the following section.

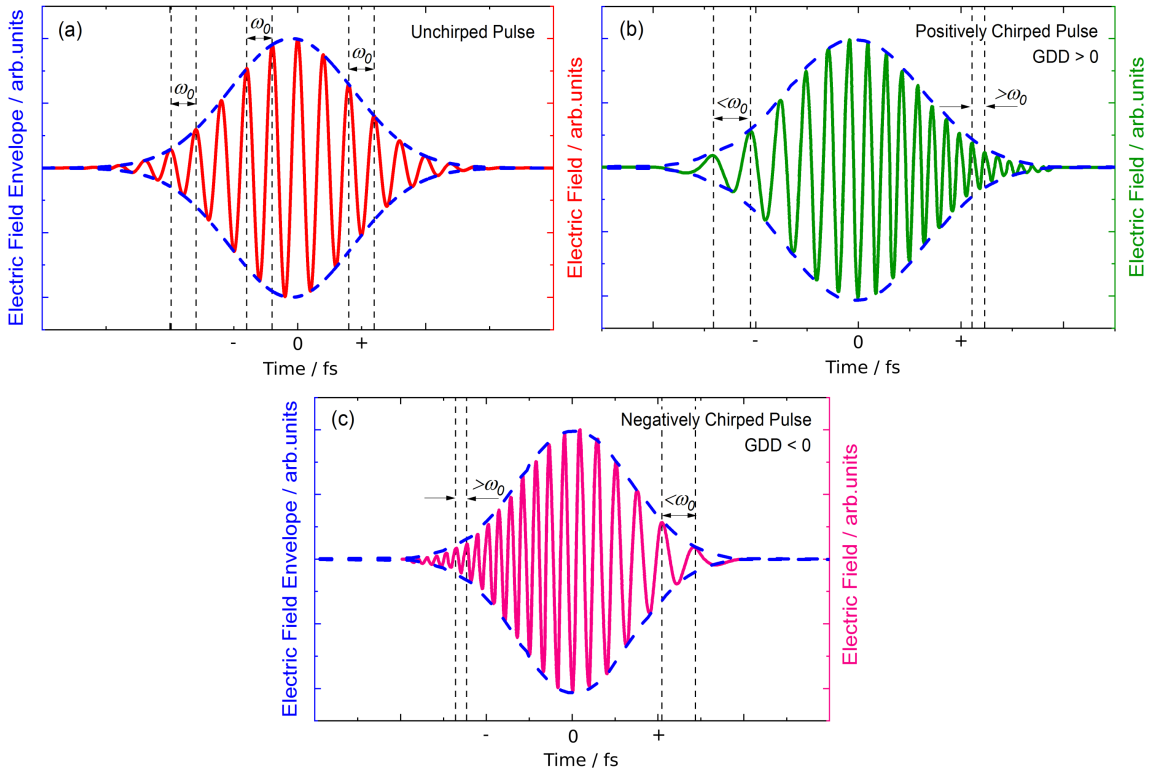

FIGURE 3.2: Exemplary linear frequency chirps, $\omega(t)$, of ultrashort laser pulses before (a) and after (b) – (c) propagation in a dispersive medium. In media with increasing n with frequency over the pulse bandwidth and corresponding positive GDD, the unchirped laser pulse (a) experiences a positive linear chirping (b). In media with decreasing n with frequency and corresponding negative GDD, negative linear chirping of the unchirped pulse occurs (c).

3.1.3 Ultrashort Pulse Laser Systems

In this dissertation, ultrashort laser pulses were generated by a tabletop femtosecond laser system which consists of two main components: a mode-locked oscillator and a chirped-pulse amplifier (CPA). The discovery of the broad gain bandwidth medium titanium-doped sapphire [195] and the expansion of the Kerr-lens mode-locking technique [196] in conjunction with the CPA technique [197] have facilitated the generation of ultrafast laser pulses with ultrashort pulse durations and ultra-high peak power levels up to petawatts and beyond [198]. Such laser systems have become the standard in ultrashort laser laboratories around the world. The fundamental properties of such standard femtosecond oscillator-amplifier laser systems are presented in the following.

To generate femtosecond pulses, passive mode-locking of visible and near-infrared (NIR) solid-state lasers is generally used [199]. A typical femtosecond-pulse-duration mode-locked laser oscillator consists of several principal functional elements: an optical resonator, a broadband gain medium, an output coupler, a dispersive element, and a gain-loss element. The optical resonator contains the gain medium, several dielectric mirrors, including highly reflective and a semi-transparent output coupler mirror, and additional dispersive elements (a pair of prisms or chirped mirrors) to compensate for the positive chirp accumulated in the resonator. Since 1982 [200], titanium-doped sapphire (Ti: Sapphire) has been widely used as an efficient, broadly tunable (in the spectral range of 650 – 1100 nm) gain medium for solid-state femtosecond laser oscillator sources [201–203], which can deliver ultrashort laser pulses with durations down to sub-5 fs [203, 204]. Central to the ultrashort pulse generation is the optical resonator, where the pulses are formed by constructive interference of many longitudinal modes of the resonator which oscillate in phase at different frequencies within

the amplification range attributable to the gain medium. The longitudinal modes satisfy the standing wave condition $m\lambda_m = 2L$, where m is a number of the mode, which is equal to the number of half wavelengths inside the optical resonator, λ_m is the wavelength of mode m inside the optical resonator, and L is the length of the optical resonator. The frequency separation between any two longitudinal modes, m and $m+1$, is determined as $\Delta\nu = c/2L$, where c is the speed of light.

The train of potentially short pulses results from the leakage of a pulse (from a partly transmitting output coupler mirror) travelling back and forth in a resonator of constant length. The separation between the pulses in the train is equal to the round-trip time of the resonator [31]:

$$T = \frac{2L}{c}, \tag{3.15}$$

Consequently, an ideal comb of laser pulses is generated in both the time and frequency domains under the proviso the pulses in the resonator remain compressed in successive round trips.

A passive mode-locking mechanism is most often used to generate pulses of femtosecond pulse duration. For ultrashort Ti: Sapphire laser oscillators, the Kerr lens mode-locking (KLM) method has become the leading passive mode-locking technique. It relies on the optical Kerr effect [205] in the gain medium, in which the index of refraction is altered by the applied high-intensity laser beam, in accord with the following equation:

$$n(I) = n_0 + n_2 I, \tag{3.16}$$

where n_0 is the linear and n_2 is the non-linear refractive index, and I is the intensity of the applied electromagnetic field.

When a high-intensity pulse with a Gaussian spatial envelope propagates through the Kerr non-linear medium, a change of the medium's refractive index occurs. Specifically, the high intensities occurring in the center of the beam profile cause a larger change in refractive index than at the edges, resulting in a transient lensing and beam focusing. In such a case, a Ti: Sapphire crystal is engineered, generally in combination with other focusing elements in the cavity, to act as a lens for the high-intensity pulse, known as a Kerr lens, which results in a self-focusing effect [206] in the gain medium. Often, the gain medium of the femtosecond laser oscillator is continuously pumped and an aperture (hard-aperture KLM) is inserted into the optical resonator in order to enable only the self-focused, high-intensity pulses to pass through. As an alternative to using the hard aperture in the resonator, most modern femtosecond oscillators utilise a soft-aperture KLM, in which a gain medium (e.g. Ti: Sapphire crystal) can be used for gain, (partial-)focusing, and as a soft aperture for the intraresonator beam. If such a mechanism is implemented into the optical resonator, eventually the phase-locked modes will travel in the resonator and be selectively amplified. As a result, a train of pulses will be produced after passing through the output coupler mirror of the resonator.

For the self-focusing to be useful, it is essential to balance the so-called critical power, determined by the peak power carried by laser pulses and the non-linear refractive index of the self-focusing [207]:

$$P_{cr} = \alpha \frac{\lambda^2}{4\pi n_0 n_2}, \tag{3.17}$$

where α is a constant which depends on the initial spatial distribution of the beam (for a Gaussian beam $\alpha \approx 1.8962$). For powers $P \gg P_{cr}$, the beam will undergo collapse until further non-linear effects, i.e. multiphoton absorption or photoionisation, terminates the collapse; for powers $P \ll P_{cr}$, the beam will diverge because of diffraction effects; for the powers $P = P_{cr}$ the beam will (ideally) propagate with a constant diameter resulting in an invariable intensity distribution, known as the self-trapping effect [208]. Furthermore, an enhancement of the Kerr-lens effect by focusing the beam more tightly into the non-linear medium can lead to sufficiently high peak intensities that can damage the material. Prior to the development of the optical CPA technique, such problems were the major impediment to the development of higher power oscillator and amplifier sources.

Since the maximum peak power of ultrashort laser pulses is constrained by self-focusing effects, resulting in laser beam distortions and damage or even complete destruction of an amplifying material, one of the methods to overcome these effects is to stretch the laser pulses in time, limiting their peak power. If then the pulse is amplified and consequently compressed in time, the peak pulse power increases dramatically. This technique known as a chirped-pulse amplification was applied to optical pulses by D. Strickland and G. Mourou in 1985 [197], which has permitted the generation of optical pulses with ultrashort pulse durations and ultra-high peak pulse powers. In CPA, a low-energy ultrashort seed pulse generated from an oscillator (Ti: Sapphire mode-locked laser) is temporally dispersed (stretched) to a long pulse using a pair of diffraction gratings [192] or prisms [209]. The resulting pulse has a duration of up to hundreds of picoseconds or few nanoseconds with the peak intensity decreased by several orders of magnitude after stretching. Then, the stretched pulse is amplified by many orders of magnitude in a laser amplifier without damaging the gain medium. After amplification of the stretched pulse, which now carries a sufficiently high energy, it is temporally recompressed to an ultrashort pulse duration by a second pair of gratings or chirped mirrors, introducing a GDD of oposite sign, which removes the pulse chirp.

The development of non-linear optical techniques along with CPA-based laser systems over the past decades has made it possible to generate tunable ultrashort pulses across the entire electromagnetic spectrum. Access to ultrashort pulses with high peak powers allowed shorter wavelength pulses to be generated through non-linear optical processes, for example, they can be used for generation of coherent high harmonic light pulses in the extreme ultraviolet and soft X-ray domain. This can be achieved by focusing the ultrashort optical pulses in a gas-filled cell [210–212]. The generated pulses are an important tool for ultrafast time-resolved spectroscopy, specifically for studying the electronic, chemical and structural dynamics of atoms and molecules.

3.2 Non-linear Optical Processes

At high intensities, optical media exhibit non-linear properties such as the refractive index dependency on the intensity of light that occurs when intense light beams interact with each other via non-linearly polarisable media, and the corresponding frequency conversion of light when propagating through such media. The discovery and development of non-linear optical processes has significantly expanded the capabilities of laser technology, enabling conversion of optical frequencies (generation of harmonics, sum and difference frequencies and supercontinua) and amplification of the resulting fields to produce intense, frequency-tunable radiation (parametric amplification).

When an intense laser pulse interacts with matter, the response of the material is defined by the polarisation, *P(E)*, as a function of the electric field [205]:

$$\begin{aligned} P(E) = \varepsilon_0 \chi(E) E &= \varepsilon_0 \chi^{(1)} E + \varepsilon_0 \chi^{(2)} E^2 + \varepsilon_0 \chi^{(3)} E^3 + ... + \varepsilon_0 \chi^{(n)} E^n + ... \\ &= P^{(1)} + P^{(2)} + P^{(3)} + ... + P^{(n)} + ... = P^{(1)} + P^{(NL)}, \end{aligned} \tag{3.18}$$

where ε_0 is the permittivity of vacuum, $\chi^{(n)}$ are the non-linear optical susceptibilities of the material of nth order, and $P^{(1)}$ and $P^{(NL)}$ represent the linear and non-linear contributions to the polarisation, respectively.

The wave equation for the electric field in the presence of an induced non-linear polarisation can be expressed in the form:

$$\nabla^2 \vec{E} - \frac{n^2}{c^2} \frac{d^2 \vec{E}}{dt^2} = \frac{1}{\varepsilon_0 c^2} \frac{d^2 \vec{P}^{(NL)}}{dt^2}, \tag{3.19}$$

where n is the linear refractive index and c is the speed of light in vacuum. This equation can be interpreted as an inhomogeneous wave equation, where a wave of electric field intensity drives a wave of non-linear polarisation in the medium, which, in turn, becomes a source of new electromagnetic waves, i.e. waves at other frequencies.

In the present work, second-, third- and higher-order susceptibilities were employed. Second harmonic generation ($\chi^{(2)}$) of the fundamental laser pulses with 800 nm central wavelength, was used to produce a 400 nm wavelength pump pulse for both time-resolved EUV photoemission and UV-visible absorption spectroscopy experiments. An 800-nm-driven $\chi^{(3)}$ white-light generation process and a pair of difference frequency generation ($\chi^{(2)}$) optical parametric amplification processes were also used to produce a 1300 nm wavelength probe pulses for the TAS experiments, using an optical parametric amplifier (OPA). These 1300-nm pulses were used to generate another white-light continuum ($\chi^{(3)}$), which were finally applied as a probe for the TAS experiments. Higher-order ($\chi^{(n)}$) processes were used to generate higher-order harmonics [213] that were used as ultrashort probes in the TRPES experiments, following monochromatisation. In the next sections, these non-linear processes are described in more detail. The fundamental processes occurring during the propagation or/and focusing of intense laser pulses in a non-linear medium are correspondingly detailed in the following.

3.2.1 $\chi^{(2)}$ Processes: Second Harmonic, Sum- and Difference Frequency Generation

When a laser field, $E(t) = A\,cos(\omega t)$, with frequency ω propagates in a non-linear medium with a $\chi^{(2)}$ susceptibility, the $\chi^{(2)}$ response of the medium (second-order non-linear polarisation) will be time-dependent and proportional to the electric field in accordance with the following:

$$P^{(2)}(t) = \chi^{(2)}E(t)^2 = \frac{1}{2}\chi^{(2)}A^2 + \frac{1}{2}\chi^{(2)}A^2 cos(2\omega t), \tag{3.20}$$

This means that the polarisation will have a constant component $\frac{1}{2}\chi^{(2)}A^2$, and an oscillating component $\frac{1}{2}\chi^{(2)}A^2\cos(2\omega t)$, at twice the frequency of the input light, 2ω. The first term in Equation 3.20 corresponds to a frequency independent non-linear process named optical rectification, and the second term relates to second harmonic generation (SHG).

For two waves of frequencies ω_1 and ω_2, and the incident laser field, $E(t) = \frac{1}{2}\,(A_1 cos(\omega_1 t) + A_2 cos(\omega_2 t))$, the second-order non-linear polarisation can be expressed as:

$$P^{(2)}(t) = \chi^{(2)}E^2 = \frac{1}{4}\chi^{(2)}(A_1^2 cos(2\omega_1 t) + A_2^2 cos(2\omega_2 t) + \\ +2A_1A_2 cos((\omega_1+\omega_2)t) + 2A_1A_2^* cos((\omega_1-\omega_2)t) + 2(\left|A_1\right|^2 + \left|A_2\right|^2)), \tag{3.21}$$

where A_1 and A_2 are the amplitudes of incident fields 1 and 2, respectively.

In Equation 3.21, the first two terms correspond to oscillation at twice the input frequencies of the incident light, $2\omega_1$ and $2\omega_2$ (SHG). The second term refers to the sum of the input frequencies, ω_1 + ω_2, resulting in a generation of a new higher frequency, called sum frequency generation (SFG). The third term represents the difference-frequency generation (DFG). The last two terms correspond to the time-independent optical rectification of the two input fields. The $\chi^{(2)}$ non-linear optical processes as well as the corresponding energy level diagrams are shown in Figure 3.3. In a quantum-mechanical picture, for example, when generating the second harmonic, we can assume that two photons of the input frequency ω are simultaneously absorbed in the non-linear medium, promoting the system to a virtual level with an energy $2\hbar\omega$, after which the system relaxes from this level to the ground state with the emission of a photon with a frequency 2ω.

As can be seen from Equation 3.21, the non-linear polarisation consists of four non-zero frequency components. Usually, only a specific frequency component is generated efficiently due to the engineering of specific phase-matching conditions. In other words, when the spatial dependence of the non-linear polarisation and the harmonic field are taken into account, the correct phase relationship between the interacting waves will lead to a flow of energy along the direction of propagation. Such phase-matching for $\chi^{(2)}$ processes is typically achieved using an anisotropic non-linear medium, a non-linear crystal, due to the dependence of its refractive index and polarisability on the polarisation introduced by the applied field. This technique is often referred to as birefringent phase-matching,

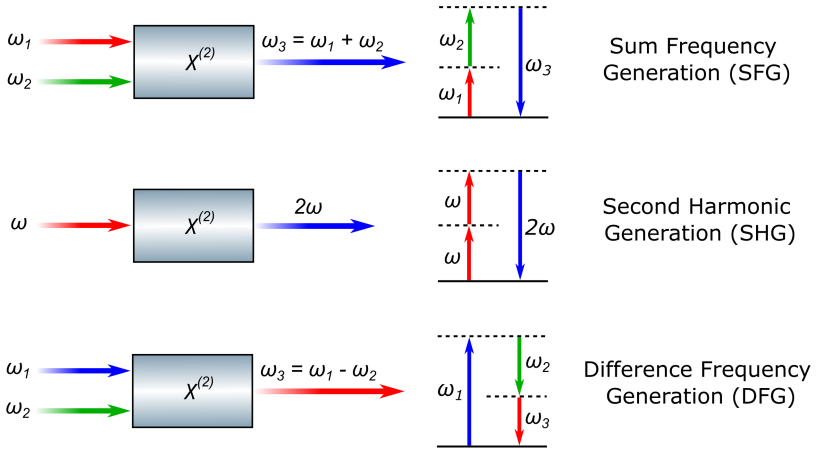

FIGURE 3.3: Schematic view of $\chi^{(2)}$ non-linear optical processes (left panels) with corresponding energy level diagrams (right panels).

which exploits the natural birefringence or double refraction of non-linear crystals [214]. In a birefringent crystal, the polarisibility of the electron clouds varies in the different directions along the principal axes of the crystal structure, which experience varying degrees of linear and non-linear electron oscillation, with the vector of polarisation not necessarily being parallel to the electric field.

Depending on the symmetry of the crystal structure, a birefringent optical material can be categorised in four types, positive and negative uniaxial or positive and negative biaxial. The simplest type of birefringence is that of uniaxial crystals (i.e. calcite, quartz, sapphire, barium borate). Such crystals have a special direction governing the optical anisotropy, the so-called optical axis, with the effective refractive index being dependent on frequency of the incident fields and the mutual orientation of the electric field direction and the optical axis. When the incident wave propagates in the direction z through uniaxial crystal at an angle θ with respect to the crystallographic axis, it is governed by the linear and non-linear polarisations associated with different refractive indices. In the linear case, these are the so-called ordinary, n_o, and extraordinary, n_e, indices. The ordinary index of refraction ($n_o = n_x = n_y$) is isotropic (angle-independent) and perpendicular to the optical axis, whereas the extraordinary index of refraction ($n_e = n_z$) is dependent on the angle θ and perpendicular to n_o. The refractive index at the propagation angle, θ, can be determined as $1/(\mathrm{n}(\theta)^2) = \cos^2\theta/n_o^2 + \sin^2\theta/n_e^2$. The refractive indices of uniaxial birefringent crystals can be described by the surface of a sphere and a spheroid, with n_o and n_e being equivalent along the optical axis. When $n_e > n_o$, the uniaxial crystal is classified as positive (n_e ellipsoid encompasses the n_o spheres), whereas in negative crystals $n_e < n_o$ (the n_o sphere encompasses the n_e ellipsoids). Thus, for example, in a negative uniaxial crystal, it is possible to achieve a birefringent phase-matching for a SHG (SFG or DFG) process by matching the angle θ between the propagating optical beam and the optical axis of the crystal for which, in the SHG case, $n_o(\omega) = n_e(2\omega)$.

Two types of phase-matching are possible in birefringent crystals. Type I refers to the case for which both lower-frequency generated waves have the same polarisation, and in type II - they have orthogonal polarisations. A detailed description of phase-matching in birefringent crystals can be found in Ref. [215]. Generally, birefringent phase-matching is performed either by tuning the angle (critical phase-matching, $\theta \neq 90°$) or temperature (non-critical phase-matching, $\theta = 90°$) of a non-linear crystal. In the first technique, the crystal orientation is adjusted precisely with respect to the propagation direction of the fundamental beam and the interacting n_e beam (considering that n_o is angle-independent) in such a way that optimum phase-matching is achieved. Critical phase-matching is only useful for a specific range of beam angles, known as the acceptance angle or angular phase-matching bandwidth. Consequently, the fundamental beam divergence must be minimised.

3.2.2 $\chi^{(3)}$ Processes: White-Light Continuum Generation and Self-Phase Modulation

With the discovery of white-light continuum (WLC) generation by R. R. Alfano and S. L. Shapiro in 1970 [216–218], novel methods of generating intense ultrashort laser pulses became available [219, 220]. Since then, white-light continuum generation has been developed into an effective method of converting laser pulses with relatively narrow spectral bandwidth to pulses with extremely broad spectral bandwidth (e.g., 300 – 2400 nm wavelength range for an 800-nm or 1300-nm driver), which found applications in a diverse range of fields, including non-linear frequency conversion [221], optical communications [222], biomedical optics [223], optical metrology [224] and many others. Following the advent of the CPA technique, WLC generation has been widely applied in ultrafast time-resolved spectroscopy experiments as a seed for OPA systems [225] and as a supercontinuum and potentially ultrashort pulse probe source [226].

Essentially, supercontinuum generation is the result of various non-linear processes such as self-phase and cross-phase modulations, stimulated Raman scattering and non-resonant four-wave mixing. Predominantly, WLC generation originates from the self-phase modulation (SFM) effect, which can occur in gaseous, liquid, and solid media. When an intense ultrashort laser pulse interacts with a non-linear medium, the pulse changes the medium's refractive index. Consequently, the spectral phase, amplitude, and frequency of the incident pulse are modified. SFM refers to the phenomenon of changing the time-dependent phase of a Fourier-transform-limited pulse, resulting in a broadening of the pulse spectrum.

The $\chi^{(3)}$ susceptibility contribution to the non-linear polarisation in an isotropic medium can be described similarly to the second-order susceptibilities presented in Equation 3.18, neglecting all terms except the linear $\chi^{(1)}$ and $\chi^{(3)}$ terms, the following expression emerges:

$$P = \varepsilon_0 \left[\chi^{(1)} cos(\omega t) + \chi^{(3)} A^2(t) cos^3(\omega t)\right] A(t) =$$

$$= \varepsilon_0 (\chi^{(1)} cos(\omega t) + \frac{\chi^{(3)}}{4} A^2(t)[3cos(\omega t) + cos(3\omega t)]) A(t), \tag{3.22}$$

Here, the $3\omega t$ term is responsible for third harmonic generation, which may be disregarded for the case where this process is sufficiently weak and has no effect on the propagation of the driving laser beam. Accordingly, Equation 3.22 simplifies to:

$$P = \varepsilon_0 ((\chi^{(1)} + \frac{3\chi^{(3)}}{4} A^2(t)) A(t) cos(\omega t), \tag{3.23}$$

Taking into account the linear and non-linear contributions to the optical susceptibility $\chi^{(L)}$, $\chi^{(NL)}$ and the dielectric permittivity $\varepsilon^{(L)}$, $\varepsilon^{(NL)}$, the non-linear polarisation results in the following intensity-dependent index of refraction, varying in time as:

$$n(t) = n_0 + \frac{3\chi^{(3)}}{8n_0} \left|A(t)\right|^2 = n_0 + n_2 I(t), \tag{3.24}$$

The temporal phase of the laser field propagating in a medium of length L is given by:

$$\phi(t) = \omega_0 t - \frac{n(t)\omega_0}{c} L, \tag{3.25}$$

Substituting for *n(t)* into Equation 3.24 yields:

$$\phi(t) = \omega_0 t - \frac{\omega_0}{c}[n_0 + n_2 I(t)]L = \omega_0 t - k_0 L - \frac{n_2 \omega_0}{c} I(t) L, \tag{3.26}$$

where k_0 is the wave number at frequency ω_0.
Here, the non-linear portion of the temporal phase is:

$$\phi^{(NL)} = -\frac{n_2 \omega_0}{c} I(t) L, \tag{3.27}$$

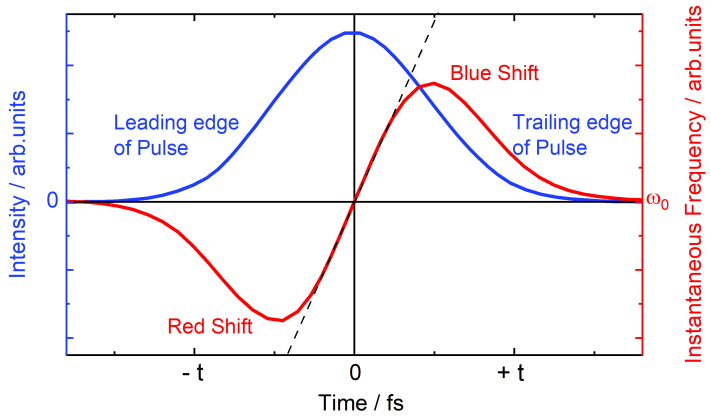

FIGURE 3.4: Intensity, *I(t)*, and instantaneous frequency, ω_0, of an initially unchirped Gaussian pulse that propagated through a non-linear medium with $n_2 > 0$ and experienced SFM. The leading edge of the pulse is red shifted to lower frequencies, the trailing edge is blue shifted to higher frequencies, causing the broadening of the pulse spectrum and its temporal profile.

The non-linear temporal phase shift results in a frequency change of the pulse. The instantaneous frequency variation in time is then given by:

$$\omega(t) = \frac{d\phi}{dt} = \omega_0 - \frac{n_2\omega_0}{c} L \frac{dI(t)}{dt}, \tag{3.28}$$

where the second term is the frequency shift induced from the non-linear refractive index (SPM). Figure 3.4 shows the intensity envelope and the instantaneous frequency in the time domain for a Fourier-transform-limited Gaussian pulse that has experienced SPM.

3.2.3 $\chi^{(n)}$ Processes: High-Order Harmonic Generation

Higher-order $\chi^{(n)}$ non-linear processes can also be driven adopting similar principles as those described in the context of $\chi^{(2)}$ and $\chi^{(3)}$ processes. An extreme example is the non-perturbative $\chi^{(n)}$ processes associated with high-order harmonic generation (HHG). In a laser-driven HHG process, a very intense, short laser pulse is focused into a gas, liquid, solid or plasma target and interacts non-perturbatively with the medium, leading to the generation of very-high, odd harmonics of the optical frequency of the laser pulse, in a high-order non-linear frequency up-conversion process [227–233]. This phenomenon occurs at high optical intensities of the order of 10^{14} W cm^{-2} when the electric field of the laser becomes comparable to the atomic Coulomb field strength experienced by electrons bound to or in the vicinity of ionic nuclei [210, 234].

The advances in laser-based HHG probe sources have opened up many new scientific possibilities. Laboratory-based EUV/soft X-ray ultrashort pulse sources, with femtosecond-to-attosecond pulse durations [235, 236], have allowed the coupled motions of electrons, atoms, and molecules to be monitored in real time. Moreover, a number of unique characteristics of the generated HHG light - such as high temporal and spatial coherence with a photon energy range spanning the EUV to soft X-ray range, high temporal resolution, low divergence and high photon flux - have enabled static and ultrafast atomic-timescale dynamic studies to be performed. Thus, HHG-based, pulsed EUV sources have been practically implemented in studies of surface dynamics [237], dynamic diffraction and high-resolution imaging [238, 239], molecular dynamics [240, 241] together with static molecular structure [242], and attosecond dynamics [232] studies. The combination of an ultrafast femtosecond laser source based on Ti: Sapphire CPA system, as employed here, and the ability to select specific photon energies from a wide range of generated harmonics, while preserving an ultrashort pulse duration, allows time-resolved photoemission studies to be performed on a variety of condensed-phase materials.

3.2.3.1 Semi-Classical Three-Step Model of High Harmonic Generation

Laser-driven HHG can be achieved by several different methods: through the interaction of ultrashort laser pulses with noble-gas jets, filled cells or pressurised waveguides [210–212, 227], solids [229, 232, 243], liquids [244, 245], and laser-produced plasma media [246–248]. High-order harmonics generated in gases have proven the most robust method for applications, while the development of HHG in other media remains an open research activity and offers the potential for much higher single pulse conversion efficiencies. In the past few years, there have also been reports of increasingly successful attempts to improve the performance of such HHG sources, setting new records for the generation of EUV and soft X-ray pulses using gas-phase HHG [249, 250]. In this dissertation, HHG from gaseous media is specifically considered, and all subsequent descriptions will relate to this.

The spectrum of phased-matched harmonic photon emission peaks, as generated in a gas, has the following prominent features (Figure 3.5): (1) The HHG spectrum consists of high harmonics of the driving frequency $N\omega_0$ of the fundamental laser pulse, where N is an odd number. The peak width of the individual harmonics depends on the pump pulse length as $\Delta\omega \approx 2\pi/T$. (2) A plateau region is observed, where the generated harmonics have approximately equal intensities. The plateau appears after a rapid decrease in intensity - with an increase in harmonic order. (3) A cut-off frequency is observed, where the harmonic intensity drops rapidly at the end of the plateau. The single-atom cut-off can be estimated from the maximum energy that an electron accelerated by the laser field can have while still recombining with an atom (see Equation 3.32). The presence of the plateau and the sharp cut-off is the key distinguishing feature between perturbative harmonic generation and non-perturbative HHG [213].

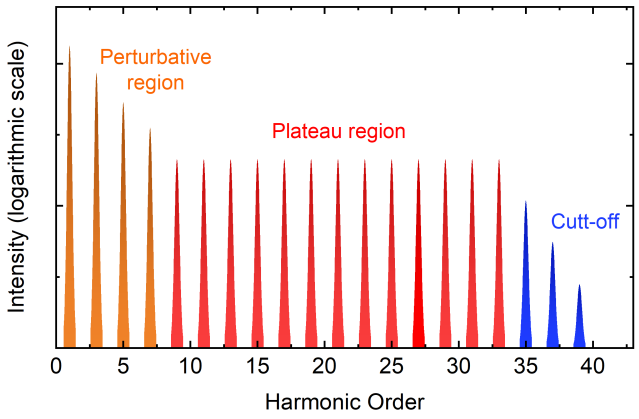

FIGURE 3.5: A schematic illustration of the comb-like HHG spectrum. The efficiency of the harmonics decreases rapidly for the low-order harmonics in the perturbative region, then flattens over the broad plateau region of intermediate orders, and diminishes at the cut-off photon energy, which is dependent on the atom ionisation potential and on the intensity and wavelength of the driving laser pulse.

Since the HHG spectrum contains a broad plateau region, with harmonics of comparable efficiency, in contrast to the power law dependence predicted by a perturbative model of harmonic generation [213], an alternative mechanism was required to describe the HHG process. In 1993, K. Kulander [251] and P. Corkum [213] first proposed a semi-classical "three-step model" of the gas-phase high harmonic generation process, as shown in the Figure 3.6. The semi-classical theory effectively reproduces the plateau and cut-off behaviour observed in the experimental HHG spectra. This theory, derived from the "re-collision picture" [252], involves three steps in the single-atom response:

(1) *Tunnel ionisation*: bound electrons are ionised from a parent atom via the periodic distortion of the Coulomb potential barrier that occurs in the presence of a sufficiently strong laser field. The electron escape into the continuum is most probable when the laser electric field is close to the peak of its optical cycle, and when the highest field strength cycles of the pulse.

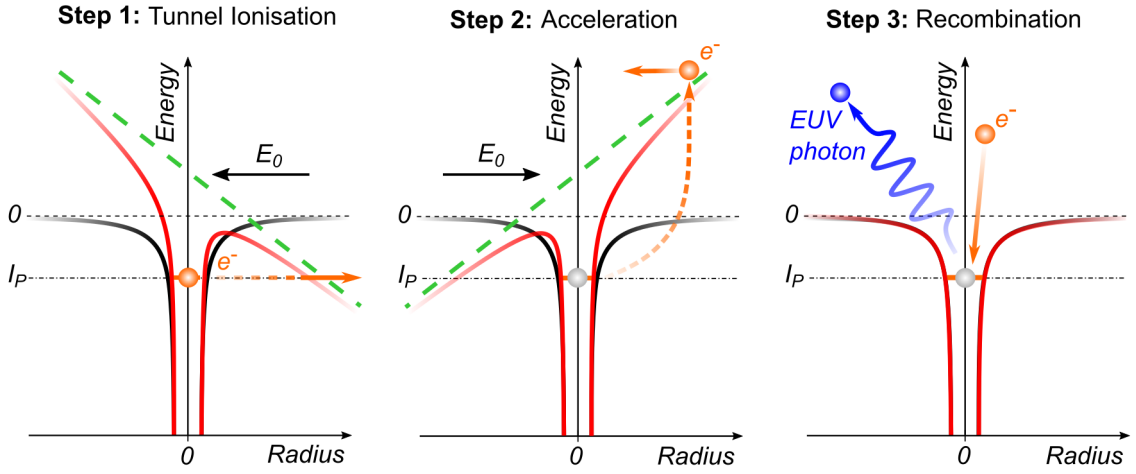

FIGURE 3.6: Schematic view of the three-step model of HHG.

(2) *Acceleration*: The generated free electrons are accelerated in the combined oscillating laser (and, in reality, Coulomb) field, with a portion of the ionised electrons that were produced at the right phase of the laser cycle being returned to the parent ion after the laser field switches sign.

(3) *Recombination*: The returning electrons re-collide with its parent ion, with the excess energy of the electron being emitted as a single photon. The photon energy is equal to the kinetic energy of the electron upon recombination plus the ionisation potential of the atomic species.

Each step of the three-step model, which is invoked to describe HHG at a single-atom level, is discussed in more detail below. The validity of the semi-classical theory was proven by M. Lewenstein *et al.* [253] and P. Antoine *et al.* [254], who introduced a quantum-mechanical analytical theory of HHG that considers, in particular, the depletion of the ground state and the wave packet propagation based on a strong-field approximation (SFA). Here, the Coulombic field of the parent ion, that is experienced by the electron during its excursion in the continuum, is treated as negligible in comparison to its reaction to the strong laser field. Besides the response from a single atom, the emission of high-order harmonics is also influenced by macroscopic phase-matching effects associated with the ensemble of atoms, molecules or their ions, i.e. the response of the whole irradiated medium. In order to achieve a high HHG flux, the emission of the individual emitters must sum up constructively. A detailed description of such macroscopic effects will be discussed in the Section 3.2.3.2.

- **Step 1: Tunnel Ionisation**

When a strong external laser field is applied to a parent-atom-bound electron, the Coulomb potential of the atom is severely distorted, resulting in the release of the electron with near zero kinetic energy via the tunneling process. Depending upon the external electric field strength of the laser pulse, three non-resonant ionisation mechanisms can be defined [255]. The ionisation process is defined to occur via the tunneling mechanism when the adiabaticity parameter $\gamma = \sqrt{I_p/2U_p}$, introduced by L. Keldysh [256], is less than 1, $\gamma < 1$. Here, I_p is the ionisation potential of the atom, and U_p is the ponderomotive energy. In the limit $\gamma \gg 1$, the ionisation process is defined to occur via a multiphoton mechanism and can be described using time-dependent perturbation theory.

The ponderomotive energy is the cycle-averaged kinetic energy of a free electron oscillating in the laser electric field, defined as follows::

$$U_p = \frac{e^2E^2}{4m_e\omega_0^2} = \frac{e^2I}{2m_e\varepsilon_0^2c\omega_0^2} \propto 9.33\times10^{-14}I\lambda^2, \tag{3.29}$$

where e is the electron charge, m_e its mass, E_0 is the laser electric field, ω_0 is the angular frequency of the laser field, ε_0 is the permittivity of free space, and c is the speed of light.

In terms of the intensity and driving wavelength of the incident laser radiation, the ponderomotive energy is proportional to the laser intensity, I_0, and the square of the ionising wavelength, λ. The ionisation rates in the tunneling regime can be calculated using the Ammosov-Delone-Krainov (ADK) theory [257]. Utilising an ultrashort laser pulse at the fundamental wavelength of 800 nm, which interacts with a gaseous medium, for instance an argon-gas-filled cell, with a single atom ionisation potential energy of 15.76 eV [258], the tunneling regime can be reached at laser intensities higher than 10^{14} W cm^{-2}, as typically applied for high harmonic generation.

- **Step 2: Acceleration**

After the ionised electron is released into the continuum with zero velocity at time $t = t_i$ and has been driven away from the atomic core by a laser field, $E(t) = E_0 cos(\omega_0 t)$, the laser electric field vector changes its direction and the electron can be accelerated back towards the atomic core. The motion of the ionised free electron in the oscillating laser field can be described classically by applying Newton's laws of motion [259], while neglecting the influence of the atomic potential (SFA approximation). The force experienced by the electron is $F(t) = - eE(t)$. Its velocity, v, and displacement from the atomic core, x, as a function of time $t \geq t_i$ have the form:

$$v(t) = -\frac{eE_0}{m\omega_0}[cos(\omega_0 t) - cos(\omega_0 t_i)],$$
$$x(t) = \frac{eE_0}{m\omega_0}[sin(\omega_0 t) - sin(\omega_0 t_i) - \omega_0(t - t_i)cos(\omega_0 t_i)], \tag{3.30}$$

where the initial conditions for the electron motion are $x_i = 0$ and $v_i = 0$ at t_i.

According to Equation 3.30 it is possible to define the tunneling times, t_i, with respect to the electric field cycle for which the free electron may or not may return to the ion core. The trajectory of the electron in the continuum depends on the phase $\phi_0 = \omega_0 t_0$ of the driving laser at the time of tunnel ionisation.

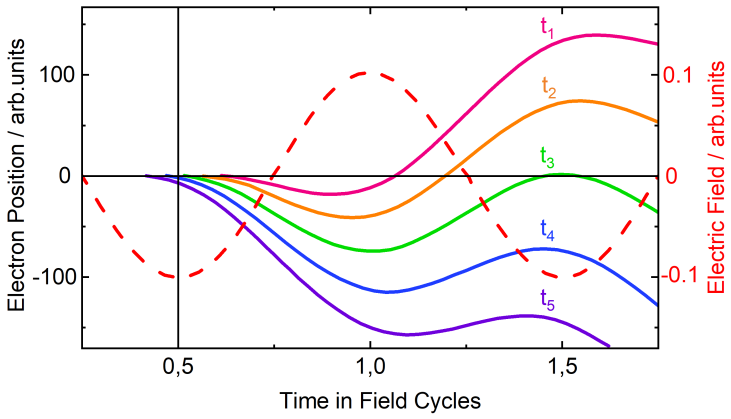

FIGURE 3.7: Time-dependent electron trajectories in a laser field (dashed red line) calculated for different ionisation times: $t_{1,2} > 0.5$ field cycles (pink and orange lines), $t_3 = 0.5$ field cycles (green line), and $t_{4,5} < 0.5$ field cycles (blue and violet lines); the origin electron position is depicted by the horizontal line.

Figure 3.7 shows the electron trajectories for a few chosen values of ϕ_0 at the time of tunneling. Only some of the electrons that were ionised by the laser field after a given extremum of the field will revisit the parent ion (pink, orange, and green lines in the Figure 3.7 represent trajectories for such electrons). Electrons that return to the ion at tunneling times $t_i > t_0$ can contribute to the HHG process through recombination.

- **Step 3: Recombination**

After gaining kinetic energy upon acceleration in the laser field, the electron loses that energy when it recombines with the parent ion and the gained energy is released as a HHG photon. The HHG photon energy is determined by the sum of ionisation potential, I_p, of the atom and momentary kinetic energy of the electron, E_{kin}, upon recombination, which depends on the birth phase, ϕ_0, at the moment of ionisation:

$$\hbar\omega = I_p + E_{kin}, \tag{3.31}$$

The maximum emitted photon energy can be derived from the analysis of the electron trajectories, which determines the "cut-off" photon energy for the generated high harmonics [213] as:

$$\hbar\omega_{max} = I_p + 3.17U_p, \tag{3.32}$$

where ω_{max} is the maximum angular frequency of the generated high harmonics.

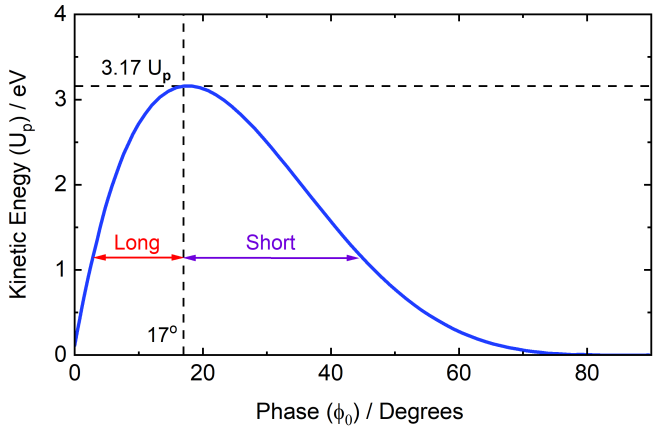

FIGURE 3.8: Kinetic energy of the returning electron to the parent ion as a function of the birth-phase with respect to the laser field. The most energetic trajectory is associated with a birth-phase of $\phi_0 \approx 17^\circ$, resulting in a $3.17U_p$ re-collision energy and a $(3.17U_p + I_p)$ cut-off photon energy.

The cut-off trajectory corresponds to the case when the tunneling event (step 1) takes place at a phase of $\phi \approx 17^\circ$. Further details of the trajectory contributions to the HHG spectrum can be seen in Figure 3.8. In particular, it is shown that the electron ionised at the peak of the laser field ($\phi_0 = 0^\circ$), gains zero kinetic energy upon its return to the parent ion. In every half-cycle of the laser pulse, at any other HHG energy than the cut-off energy, there are two possible electron trajectories leading to the same return kinetic energy, for example, trajectories at a phase of $\phi = 45^\circ$ and $\phi = 3^\circ$.

The two energetically-degenerate pathways are named the short and long trajectories, according to the excursion length they experience in the continuum. Contributions to the short and long trajectories also arise in the quantum-mechanical HHG model, within the SFA [253]. The phase of the generated harmonic not only depends on the phase of the laser field, but also on the specific trajectory followed by the electron. This additional non-perturbative term, named the intrinsic phase, is proportional to the ponderomotive potential times the excursion time of the quantum path [253]. Accordingly, the structure of the HHG spectrum can be complex, since it arises due to the interference of the emissions from different quantum paths [260].

3.2.3.2 Phase Matching of High Harmonic Generation in Gaseous Media

High conversion efficiency HHG requires optimisation of both the microscopic and macroscopic properties of the process. The microscopic response is well described by the semi-classical three-step model of HHG for the specific case of rare gas atoms, as described in the previous section. The properties of the macroscopic harmonic emission - such as the ultrashort pulse duration, high temporal and spatial coherence, relatively high photon flux - result from HHG being a coherent process, so that the phase of the harmonic emission at a given time and position is determined by both the driving laser and existing harmonic fields. In order to obtain the highest possible harmonic emission, the phase-mismatch between the generated high harmonic field and the driving laser field in the non-linear medium needs to be examined and optimised. This includes reabsorption [261], differential linear refractive indices [262], and plasma defocusing [263] effects on the HHG light.

Similar to low-order harmonic generation processes, the maximum efficiency of frequency up-conversion can be achieved when the fields emitted by various atoms in the generating medium volume are coherently superimposed using phase-matching techniques. Explicitly, the phase difference between the fundamental wave and the wave of harmonic order, q, has to be minimised. This phase-mismatch can be defined along the propagation direction as a difference between the wave-vector of the fundamental field, k_0, multiplied by the harmonic order and the harmonic field wave-vector, k_q:

$$\Delta k = qk_0 - k_q, \tag{3.33}$$

The characteristic length in which the phase of the harmonically generated light interferes constructively, the so-called coherence length, is inversely proportional to the phase-mismatch Δk as:

$$L_{coh} = \frac{\pi}{\Delta k}, \tag{3.34}$$

The resulting intensity, I_q, of the generated harmonic light at the end of nonlinear medium of the length L without considering absorption nor driving laser depletion, is dependent on the phase-mismatch as [205]:

$$I_q \propto L^2 sinc^2 \frac{\Delta kL}{2}, \tag{3.35}$$

The phase-mismatch in an ideal phase-matched HHG process is equal to zero, Δk = 0, and the harmonic intensity increases as L^2 with the propagation distance [264]. In practice, $\Delta k \neq 0$, and Δk = 0 is unachievable, even over a single harmonic bandwidth. Typically, L is compared to L_{coh} under the imposed phase-matching conditions, which are generally engineered for just one driving laser frequency and just one generated frequency. All other frequencies accumulate an ideally tolerable phase-mismatch. Where this is not tolerable, the output spectrum is diminished.

For gas-phase HHG, the wave-vector mismatch between the laser-induced polarisation and the generated high-order harmonics can be expressed as a sum of four terms [265, 266]:

$$\Delta k = \Delta k_{\varphi,G} + \Delta k_{\varphi,D} + \Delta k_{n,NG} + \Delta k_{n,P}, \tag{3.36}$$

Here, $\Delta k_{\varphi,G}$ denotes the geometrical wave-vector mismatch from the Gouy phase shift caused by focusing, $\Delta k_{\varphi,D}$ is the wave-vector mismatch caused by the atomic dipole phase, resulting from the frequency- and intensity-dependent electron trajectory in the continuum, $\Delta k_{n,NG}$ is due to dispersion in the neutral gas medium, and $\Delta k_{n,P}$ accounts for free-electron dispersion in the generated plasma. In the following, each of these contributions will be discussed in more detail.

- **Geometric Phase Matching**

Considering a HHG driving laser system that provides a Gaussian beam with a TEM_{00} transverse mode, focusing the Gaussian beam can result in a phase shift that is different from that for a plane wave with the same optical frequency. This difference is called the Gouy phase shift [267]. Its value as a function of longitudinal propagation length is:

$$\varphi_G(z) = -arctan\frac{z}{z_R}, \tag{3.37}$$

where z is the distance from the beam focus along the axis of propagation, and $z_R = \pi w_0^2/\lambda$ is the Rayleigh range for the driving laser and for the q^{th} generated harmonic with a similar confocal parameter. The geometric contribution to the phase mismatch from the Gouy phase is:

$$\Delta k_{\varphi,G} = \frac{q-1}{z_R}, \tag{3.38}$$

Figure 3.9 depicts the Gouy phase of a focused Gaussian TEM_{00} laser beam. From Equation 3.37, it becomes apparent that the laser phase is shifted by π with respect to the phase of the incident beam before focusing. This phase evolves from z = - ∞ to + ∞, resulting in an increase of the phase velocity of the focused laser field on the z axis in contrast to a plane wave. On this basis, within the depth of focus ($2z_R$ around the beam waist), the phase change exhibits its largest rate of change. It is possible to estimate the coherence length based on Equation 3.37 by taking the derivative of the Gouy phase and setting it equal to π, so that Equation 3.37 can be rewritten for the generated q^{th} harmonic as:

$$L_{coh,G}(z) = \frac{\pi(z_R + (z^2/z_R))}{q}, \tag{3.39}$$

Hence, through changing the focus position of the laser beam with respect to the generating medium, the phase mismatch induced by the Gouy phase shift can be controlled [268]. Thus, determined by the focus position, different phase matching regimes can be realised, optimising macroscopic emission from short [268] as well as long [269, 270] electron trajectories and efficient generation of high-order harmonics. Detailed analysis of the HHG conversion efficiency, as influenced by the focusing geometry, is described in the studies of Heyl and co-workers [271, 272].

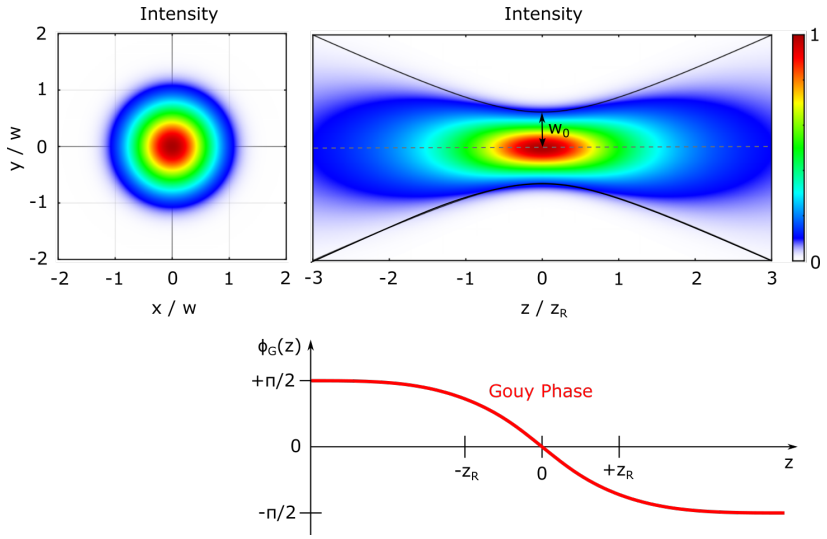

FIGURE 3.9: Illustration of the Gouy phase shift encompassing a focused Gaussian driving laser pulse that propagates through the non-linear gas medium.

- **Atomic Dipole**

The phase of the high-order harmonics has a strong dependence on the fundamental laser intensity. This is due to the linear variation of the atomic dipole phase with the applied laser field, so the term of the atomic dipole phase mismatch is proportional to the laser intensity gradient. The intensity of a Gaussian beam along the direction of propagation z is given by

$$I(z) = \frac{I_0}{1 + (2z/z_R)^2}, \tag{3.40}$$

where I_0 is the peak intensity of the beam in the focus.

Accordingly, the dipole phase contribution to the phase mismatch of the on-axis q^{th} harmonic can be written as [273]:

$$\Delta k_{\varphi,D} = \frac{8z}{{z_R}^2 \left(1 + (2z/z_R)^2\right)^2} \alpha_q I_0, \tag{3.41}$$

where α_q denotes a coefficient associated with the electron trajectories.

The change of the driver intensity changes the atomic dipole phase, which results in a contribution that depends not only on the focusing geometry, but also on the peak intensity of the laser beam, as well as on the length of the electron trajectory. For the short electron trajectories $\alpha_q \approx 1 - 5 \times 10^{-14}$ W^{-1} cm^2, and for the long electron trajectories $\alpha_q \approx 20 - 25 \times 10^{-14}$ W^{-1} cm^2. The dipole phase has a further impact on the spectral broadening of the generated harmonics because the change of the high driving laser intensity over time causes a frequency chirp, due to SPM effects, as described in Section 3.2.2. To enhance the HHG efficiency, in a simple case, it is possible to find a condition under which the eigenphases of the geometric and atomic dipole phase mismatch and compensate each other [268, 274].

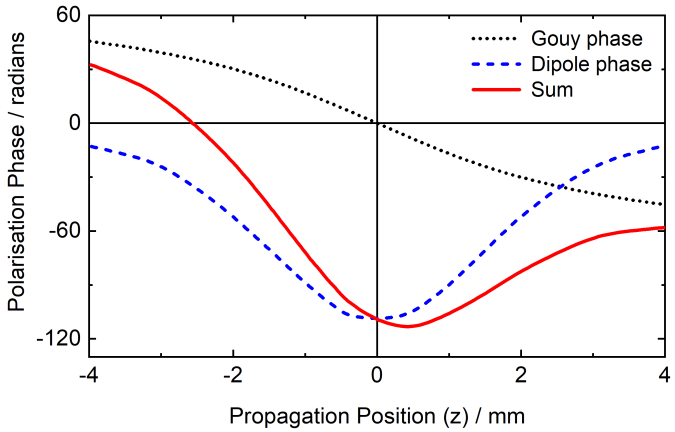

FIGURE 3.10: Harmonic polarisation phase as a function of the propagation distance relative to the focus. The Gouy phase shift, dipole phase and the sum of two contributions are indicated by the black dotted, blue dashed and red solid line, respectively. Adapted figure with permission from [268] © 1995 by the American Physical Society.

Figure 3.10 illustrates the generated harmonic phase as a function of propagation distance relative to the focus at the maximum of the pulses temporal envelope. As can be seen in the figure, the phase matching is highly dependent on the position of the medium relative to the focus. For the range $z > 0$, the Gouy and dipole phase add, resulting in a prompt decrease of the total phase. For the range $z < 0$, the phases have opposite signs and can be nearly compensated. Thus, for the given case, when the laser is focused ≈ 3 mm before the generating medium, the total harmonic phase variation is minimal, i.e., the phase mismatch is minimised.

- **Neutral Gas Dispersion**

Due to the difference between the refractive indices of the gas per unit atmosphere at the fundamental laser and harmonic wavelengths, a neutral-gas-dispersion-related phase mismatch occurs. This phase mismatch contribution associated with the material dispersion, can be expressed as [264]:

$$\Delta k_{n,NG} = \frac{2\pi q}{\lambda}(n_\omega - n_{q\omega}), \tag{3.42}$$

where q is the generated harmonic order, (n_ω - $n_{q\omega}$) denotes the difference of the refractive indices of the gas per unit atmosphere at the fundamental and harmonic wavelengths.

The refractive index of the noble gases, being very close to unity under non-resonant conditions, is often reported in the form $\delta(\lambda) = n(\lambda)$ - 1, at STP (1 atm and 298 K) [275, 276], utilising the Sellmeier equation to represent the incident frequency dependence. The refractive index is also proportional to the gas pressure, and due to ionisation of the gas medium, the density of neutral atoms is scaled by a factor for the free electron density associated with ionisation, $\eta = N_e/N_a$, where N_e and N_a are the electron and neutral atomic number density, accordingly. Thus, the atomic neutral gas dispersion can be obtained as:

$$\Delta k_{n,NG} = \frac{2\pi q}{\lambda} p\ \delta n(1-\eta), \tag{3.43}$$

Here, p is the HHG gas pressure, and δn is the difference of the refractive index between the driving laser and the q^{th} harmonic, δn = (n_ω - $n_{q\omega}$).

- **Plasma Dispersion**

The last term of Equation 3.36 is due to ionic and electronic plasma dispersion phase mismatch, which is introduced by free electrons generated in the ionisation processes. This term has the form [277]:

$$\Delta k_{n,P} = -N_e r_e \lambda = p N_{atm} \eta r_e \lambda \left(\frac{q^2 \text{ - } 1}{q}\right), \tag{3.44}$$

where p is the gas pressure, N_{atm} is the atomic number density at 1 atm, η is the ionisation fraction, and r_e is the classical electron radius. In both equations 3.43 and 3.44, the dependence of the dispersion on the wavelength is specified for the q^{th} harmonic. The contribution of plasma dispersion to the wave-vector mismatch is always negative, whereas the contribution of neutral gas dispersion is positive. This permits the overall phase mismatch to be reduced by varying the laser intensity to adjust the ionisation fraction. Since the atomic and electronic dispersions depend on the density of the non-linear medium, their contribution to the overall phase mismatch can be controlled by changing the target geometry and gas pressure in addition.

Furthermore, it is necessary to consider the critical value of the ionisation fraction, η_c, at which the dispersion of the remaining neutral atoms as well as the dipole and geometric phases are insufficient to balance the dispersion of free electrons. Thus, to fulfill the condition of phase matching in the HHG process, the ionisation fraction should not exceed a critical ionisation fraction. Based on the Equations 3.43 and 3.44, the critical value can be expressed as [234]:

$$\eta_c = \left(1 + \frac{N_{atm} r_e \lambda^2}{2\pi\delta n}(1 - \frac{1}{q^2})\right)^{-1}, \tag{3.45}$$

Given that both phase mismatch terms are proportional to pressure, the critical ionisation is independent of the pressure. Specifically, Equation 3.45 applies to the weak focusing limit, where the contribution of the Gouy phase to the dispersion is insignificant. Beyond this limit, Equation 3.45 represents an upper limit on the η_c and is usually a good approximation of the critical ionisation fraction for all geometries, except for the tight focus.

- **Reabsorption of High-Order Harmonic Emission**

When the conditions for macroscopic wave-vector phase matching are met (or closely met), it is also necessary to take into account the limiting effects, such as reabsorption, dephasing, and defocusing of the driving laser and harmonic emission in the generating gas medium. These effects decrease the HHG efficiency in a gas-filled cell or in a hollow-core fiber, as well as in the short-pulse, loose-focusing regime [265, 278]. Importantly, the generated high-order harmonic photons can be reabsorbed by the same medium that generates them. Constant *et al.* [278] conducted an analysis of the time-dependent factors that govern HHG efficiency, comprising the atomic response, phase matching conditions and absorption of the atomic medium. They obtained conditions for the optimal conversion efficiency, modeling the generated harmonic photon flux as a function of longitudinal position. The transmission of a gaseous medium with length L_{med} at a given pressure p and at a particular photon energy E, can be defined as:

$$T(E,p,L_{med}) = exp\left(-\frac{L_{med}}{L_{abs}(E,p)}\right), \tag{3.46}$$

Here, $L_{abs}(E,p)$ denotes the absorption length for the medium, which limits the useful medium lengths, and can be expressed as:

$$L_{abs}(E,p) = \frac{1}{\sigma p}, \tag{3.47}$$

where σ is the absorption cross-section, which is frequency and, hence, harmonic-order-q-dependent.

Thus, the number of photons emitted on axis per unit time and area for a medium with constant density is given by [278]:

$$N_{out} \propto p^2 A_q^2 \frac{4L_{abs}^2}{1+4\pi^2(L_{abs}/L_{coh})^2}\left[1+exp(-\frac{L_{med}}{L_{abs}})-2cos(\frac{\pi L_{med}}{L_{coh}})exp(-\frac{L_{med}}{2L_{abs}})\right], \tag{3.48}$$

where A_q is the amplitude of the atomic response at the harmonic frequency ω_q.

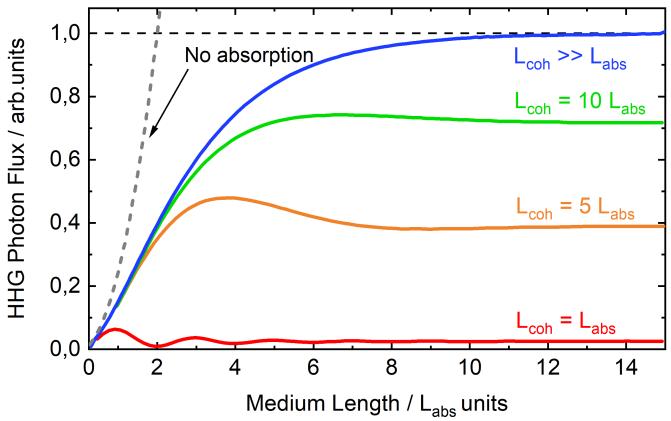

FIGURE 3.11: HHG photon flux as a function of the medium length, L_{abs}, for different coherence lengths, L_{coh}. The grey dashed line indicates absorption-free HHG. Adapted figure with permission from [278] © 1999 by the American Physical Society.

Equation 3.48 can be used to determine the overall harmonic build-up behavior in terms of L_{abs}, L_{coh}, and L_{med}. Figure 3.11 shows the evolution of the HHG photon flux as a function of the medium length for several coherence lengths. Although L_{coh} can be large, the high-order harmonic emission saturates once L_{coh} exceeds a few L_{abs}, due to the fact that the harmonics emitted and propagated over lengths beyond that are efficiently reabsorbed. As L_{coh} decreases, the efficiency reaches saturation at lower L_{abs} values. Where there is no absorption, the HHG photon flux grows quadratically with the

medium length, as is the case for any phase-matched, two-wave process. (see Figure 3.11). Optimisation of the conditions under which the macroscopic response will be more than half of the maximum response were correspondingly defined to be the following [278]:

$$\begin{aligned} L_{med} &> 3L_{abs}, \\ L_{coh} &> 5L_{med}, \end{aligned} \tag{3.49}$$

The EUV-absorption lengths as function of photon energy for various noble gases were previously estimated by Heyl *et al.* [272]. Assuming a non-guiding geometry for HHG, i.e., a non-hollow-core-fibre gas cell, they approximated the maximum coherence length as $L_{coh} \approx z_r$, and calculated the corresponding absorption length $L_{abs}(q)$ for a defined Rayleigh range z_r and a given harmonic order q. Supposing that there are no constraints on L_{med}, Equation 3.48 can be simplified to [272]:

$$N_{out}/N_{out,max} \propto \frac{1}{1+4\pi^2(L_{abs}{}^2/L_{coh}{}^2)}, \tag{3.50}$$

where $N_{out,max}$ is the normalised, maximum, absorption-limited harmonic signal.

Figure 3.12 illustrates the $L_{abs}(q)$ dependence on photon energy for argon (Ar), helium (He), and neon (Ne) gases at a fundamental laser wavelength of 800 nm on a double logarithmic scale. For gas-phase HHG, depending on the magnitude of L_{coh}, N_{out} approaches different limits for increasing medium length. Thus, at least half of the maximum conversion efficiency achieved for absorption-limited generation is obtained when the requirements from Equation 3.49 are fulfilled, as depicted by the grey area in Figure 3.12. This implies upper limiting photon energies of 40 eV for Ar, whereas for He and Ne, the limiting photon energies are 75 eV and 180 eV, respectively.

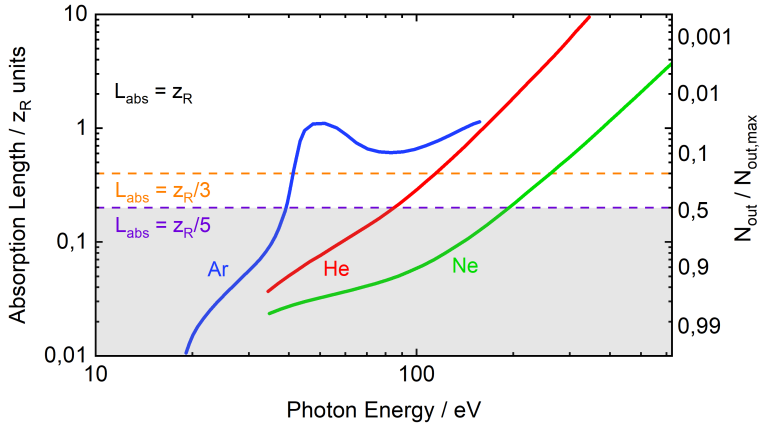

FIGURE 3.12: EUV-absorption length as a function of photon energy for argon (Ar), helium (He), and neon (Ne) gases at a driving laser wavelength of 800 nm. For each photon energy, the gas pressure was selected to maximise L_{coh}. The right vertical axis corresponds to the ratio of the maximum harmonic signal to the normalised maximum absorption-limited signal, with $L_{coh} >> L_{abs}$. The parameter range for which $N_{out}/N_{out,max} \geq 0.5$ is depicted by the gray shading. Adapted figure with permission from [272], licensed under a Creative Commons Attribution 3.0 Unported License.

3.3 Photoemission Spectroscopy

Photoemission spectroscopy (PES) has proven to be an outstanding technique to examine the electronic structure of matter in the gas-, liquid- or solid-phases. In general, electron spectroscopy methods are based on exciting an electronic sub-system of a substance to liberate electrons with light (photoelectrons) or an incident electron beam (electron-impact ionisation electrons) [279]. In the case of liberation of electrons by light, the release of electrons from matter is described by the photoelectric effect, which was first discovered by Becquerel in an electrolyte (in 1839) [280], Smith - in selenium (in 1873) [281], and was examined by Hertz and Stoletov in 1887-1889 [282, 283]. The photoelectric effect was explained in 1905 by Einstein, based on the Planck hypothesis of the quantum nature of light [284], for which he received the Nobel Prize in 1921. In 1907, Innes conducted experiments with an X-ray tube, Helmholtz coils, a hemispherical magnetic field, and photographic plates, recording the velocities of emitted photoelectrons. Intrinsically, this was the first experiment to record a kinetic-energy-resolved photoemission spectrum.

In the fifties, Siegbahn and his research group at Uppsala University in Sweden developed equipment that significantly improved the quality of the spectra, and in 1954 the first high-resolution photoemision spectrum of sodium chloride was obtained [285]. Several years later in 1967, Siegbahn published a paper describing the possibilities of using electron spectroscopy for chemical analysis (ESCA). In 1981, Siegbahn received the Nobel Prize in Physics for his discoveries and contributions in developing the photoemission technique [286]. Over a similar period, Turner published his first paper on "Determination of ionization potentials by photoelectron energy measurement" [287], and developed a method of ultraviolet photoemission spectroscopy using a gas-discharge lamp.

Initially, PES covered two relatively narrow energy ranges that were realised under laboratory conditions: the first region is provided by gas-discharge sources, typically, He discharge lamps emitting discrete lines at 21.22 eV (He I radiation) or 40.81 eV (He II radiation) photon energy at low gas pressures [288]. The second region is associated with a broadband source of photons - X-ray tubes that emit X-rays in the 20 – 150 keV range [289]. The non-monochromatic Mg and Al anode K_α radiation, in particular the emission lines at photon energies of 1486.6 eV and 1253.6 eV, respectively, are most commonly used in laboratory X-ray sources. The large energy gap between the two aforementioned sources and energy ranges leads to a natural separation into ultraviolet photoemission spectroscopy (UPS), utilising vacuum ultraviolet (VUV) (10 – 45 eV photon energies) radiation, which is used to study valence electronic structure, and X-ray photoemission spectroscopy (XPS), employing soft X-ray (200 – 2000 eV photon energies) radiation to primarily examine core-level.

Laser-based HHG light sources were successfully implemented in time- and angle-resolved photoemission spectroscopy (TRPES and ARPES) experiments to investigate electronic structure and ultrafast dynamic processes in solids at the surfaces and interfaces. HHG-based PES allowed to study shallow core levels at high binding energies in semiconductors [290, 291] and to probe electronic states in the full Brillouin zone of two-dimentional and layered materials [292, 293], which was not accessible by conventional laser-based PES. The use of coherent high-photon-energy EUV radiation in ARPES and TRPES provided insights into attosecond time delays between photoemission processes from core and valence electrons in various metals [294–296] as well as band structure dynamics in rare-earth metals employing time-, energy- and spin-resolved studies [297, 298]. Over the last years, HHG-based time- and angle-resolved PES experiments have been also realised on strongly correlated materials [299, 300].

3.3.1 Fundamentals of Photoemission Spectroscopy

The principle of PES is based on the photoelectric effect [301], which occurs when electromagnetic radiation of sufficiently high photon energy is incident on a sample and photons are absorbed, resulting in photoexcitation of electrons from a bound electronic state to a state above the vacuum ionisation threshold. PES is a surface-sensitive technique, which requires an ultra-high vacuum conditions to

prevent a collision of the ejected photoelectrons from the surface of a sample with the gas molecules in the chamber, and ensure that the photoelectrons can reach the electron detector without losing their energy. The spectrum of the emitted photoelectrons from solids, gases or liquids is detected with respect to their kinetic energy E_{kin} in an electron analyser. In the condensed-phase, the measured quantities can also carry information about the angular distribution of the ejected photoelectron from the surface (ϑ_e, ϕ_e), momentum distribution for the parallel, $k_{\parallel}$, and perpendicular, $k_{\perp}$, to the sample surface and the incident light (ϑ_p, ϕ_p), and the electron spin polarisation, $\vec{\sigma}$. A schematic view of the photoemission process is presented in Figure 3.13.

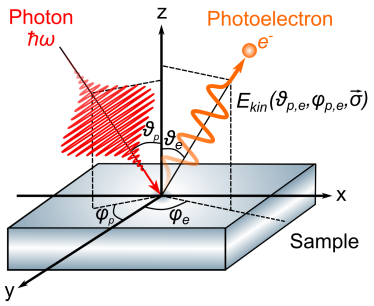

FIGURE 3.13: Schematic view of the photoemission process. A solid surface is irradiated with a laser pulse of a photon energy $\hbar\omega$, and after absorption of the photon, one or more photoelectrons are emitted from the surface in a given direction (θ_e, ϕ_e) with respect to the incident photon beam direction (θ_p, ϕ_p).

Knowledge about the energy of the absorbed incident photons, $\hbar\omega$, and the measured E_{kin} of the emitted photoelectrons, in principle, allows the determination of the population density of the electronic states in a sample, assuming they have different electron binding energies, E_B. Following the energy conservation rule [288], the photoelectrons are ejected into the vacuum with kinetic energy:

$$E_{kin} = \frac{\vec{p}^2}{2m} = \hbar\omega - E_B, \tag{3.51}$$

where $\vec{p}$ is the momentum of the outgoing photoelectron.

For condensed-phase samples, the kinetic energy of the photoelectrons emitted into vacuum are measured with respect to the local vacuum level, E_{vac}^{loc}, which is both sample- and detection geometry-dependent [302]. It is important to emphasize that E_{vac}^{loc} and the vacuum level at infinity, E_{vac}^{inf}, which is the common energetic reference in the gas-phase PES experiments [303] are different. In addition, the measured E_{kin} of the photoelectrons for solid samples is often presented with respect to the so-called Fermi level, E_F, alternatively with respect to the local vacuum level E_{vac}^{loc}. Taking into account the sample's work function, $e\phi$, the kinetic energy of the photoelectrons emitted into vacuum measured with respect to the E_F can be defined as:

$$E_{kin} = \hbar\omega - E_B - e\phi, \tag{3.52}$$

$e\phi$ represents the sum of the electrochemical potential, $\vec{\mu}$, and outer potential, and is defined as the minimum energy required to remove an electron from E_F and place it at the closest point outside the surface, so that its image potential is zero but close enough so that its distance from the surface is much smaller than the dimensions of the surface [304, 305].

Accordingly, $e\phi$ is defined as:

$$e\phi = E_{vac}^{loc} - E_F, \tag{3.53}$$

Figure 3.14 shows a schematic energy-level diagram illustrating the energetics of a photoemission process in PES, when a sufficiently conductive condensed-phase sample and the spectrometer are in electrical contact. The electrons excited from a valence electronic state into a state above the local

vacuum level E_{vac}^{loc}, leave the sample surface with a kinetic energy E_{kin}. The resulting spectrum of the electronic states is measured by an electron spectrometer. The sample is held in electrical equilibrium with the spectrometer, typically both grounded to the Earth. This can lead to electrostatic potential difference between the surfaces of the sample and the spectrometer, specifically due to the contact potential, $e\phi_{cpd}$, or, equivalently, work function differences [305, 306]:

$$e\phi_{cpd} = e\phi - e\phi_s, \tag{3.54}$$

where $e\phi_s$ is the work function of the spectrometer. As a result, the experimental photoemission spectra, with measured kinetic energies, E_{kin}^{meas}, with respect to E_{vac}^{loc} of the spectrometer can be related to the spectra measured with respect to the Fermi level by the work function of the spectrometer as:

$$E_{kin}^{meas} = \hbar\omega - E_F - e\phi_s, \tag{3.55}$$

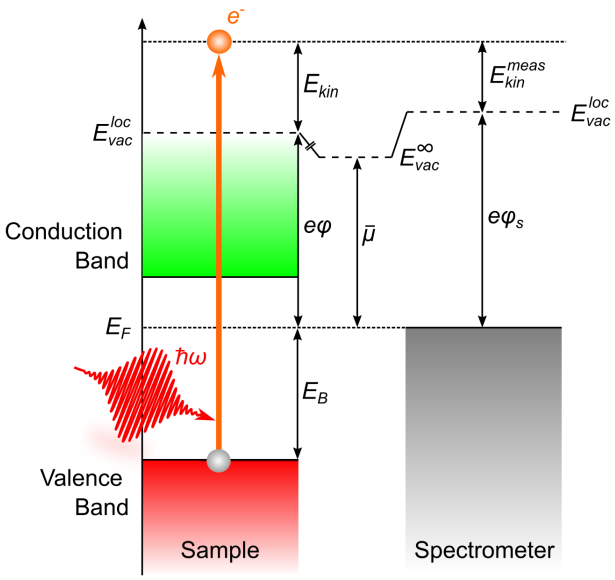

FIGURE 3.14: Schematic energy-level diagram illustrating the energetics of a photoemission process and PES. When a sufficiently conductive condensed-phase sample and the spectrometer are in electrical contact, the Fermi levels can be assumed to be equilibrated and vacuum-level offsets will generally occur between the sample and spectrometer, potentially affecting the measured electron kinetic energies.

3.3.2 Photoemission in the Condensed-Phase

In general, the photoemission process, including the photoexcitation of the electronic sub-system of a sample, is a much more complex process than introduced in the macroscopic representation above. The photoemission process is a many-body problem, in which the photon, photoelectron, and other particles in the system (i.e. nuclei and electrons) are correlated and interact with each other during the light-matter interaction and the release of the electrons.

Considering the condensed-phase photoemission process within a single-particle framework [288], the absorption of an incident photon with energy $\hbar\omega$ initiates the excitation of the N-particle system ground state with energy E_i^N, characterised by wave function ψ_i^N, to an excited state of the (N – 1)-particle system described by ψ_f^{N-1} with energy E_f^{N-1}, and an emitted photoelectron with the kinetic energy E_{kin}, which can be defined as:

$$E_i^N + \hbar\omega = E_f^{N-1} + E_{kin}, \tag{3.56}$$

Accordingly, the binding energy is determined as the difference of the total energies of the excited final state and the ground state, $E_B = E_f^{N-1} - E_i^N$.

This assumption is called the sudden approximation, and is applicable where the time scale of the photoexcitation is much shorter compared to the electron-electron interactions, so the emitted photoelectron is assumed to be instantaneously created by the photon-electron interaction. Based on this assumption, that the remaining (N – 1) particles have the same energies in the initial electronic state E_i^N and in the final electronic state E_f^{N-1} upon emission of the photoelectron, i.e. (N – 1) electrons are "frozen" in their original single-particle states (frozen-orbital approximation), it follows that the ionisation potential I_p required to remove an electron from the orbital E_i^N is equal to the negative value of the orbital energy of the emitted photoelectron ε_k, where k denotes the initial level from which the electron was removed:

$$I_p = -\varepsilon_k, \tag{3.57}$$

This approximation referred to as Koopmans' theorem [307]. Koopmans' theorem can only be applied to treat the vertical ionisation of the system. This approximation neglects electron-electron correlation effects, relaxation of the remaining electrons, relativistic effects, and is limited to closed-shell N-particle systems [308]. In the case of photoemission at low photon energies just above the vacuum level, these effects have to be considered.

Even though the concept of the photoemission process is based on a simple idea, the analysis of the electronic structure from photoemission spectra in the condensed- or gas-phase is highly complex. A variety of models have been introduced to explain and treat photoemission processes [309, 310]. The most established models are the so-called "three-step model" and "one-step model" of photoemission, mainly used to describe the photoemission process in solid materials and at solid-vacuum interfaces. The "three-step model" of photoemission reflects the basic physics of the photoemission process, and is commonly used to (qualitatively) explain condensed-phase photoemission. A description of the "three-step model" of photoemission will be discussed in the next paragraphs.

In a widely adopted theory of condensed-phase photoemission developed by W. Spicer [311], which became known as a "three-step model", the photoemission was considered as a bulk process. Here the process was viewed from the standpoint of bulk optical constants and electron scattering lengths along with surface properties, such as the position of the vacuum level at the solid-vacuum interface. In 1964, C. Berglund and W. Spicer [309], presented a more complex formalisation of the "three-step model", which aimed to model the overall photoemission processes in terms of the probabilities associated with three independent, subsequent steps:

(1) *Photoexcitation* of an electron in the bulk of a solid (generation of a photoelectron).

(2) *Transport* of the photoelectron toward the sample surface, with associated scattering processes.

(3) *Penetration* of sufficiently energetic electrons through the surface and escape of the photoelectron from the condensed material into vacuum.

The corresponding contributions to the measured photoemission intensity I_{PE} as a function of the photoelectron kinetic energy and the excitation photon energy is given by probabilities of each individual step, which can be modelled as follows [42]:

$$I_{PE}(E_{kin}, h\nu) = P_P(E_{kin}, h\nu)P_T(E_{kin}, h\nu)P_E(E_{kin}), \tag{3.58}$$

where $P_P(E_{kin}, \mathrm{h}\nu)$ is the probability of photoexciting electrons in the bulk above the vacuum level, i.e. from the E_i^N to the E_f^{N-1} state. $P_T(E_{kin}, \mathrm{h}\nu)$ is the probability of the photoelectron transport to the surface without significant inelastic scattering. $P_E(E_{kin})$ is the probability of an electron reaching the surface with sufficient energy to escape and being emitted into the vacuum. In the following, these processes are described in more detail.

- **Step 1: Photoexcitation of the Electron**

The quantum mechanical description of the photoexcitation process is given by the Fermi's Golden rule [312] (otherwise known as, the Golden Rule of time-dependent perturbation theory), which describes the transition-probability per unit time between a pair of electronic states $|i\rangle$ and $|f\rangle$ with binding energies E_i^N and E_f^{N-1}, respectively, with E_f^{N-1} corresponding to the energy of the (N - 1) + 1 system:

$$\Gamma_{i\to f}(t) = \frac{2\pi}{\hbar}|T_{i\to f}|^2\delta(E_f^{N-1} - E_i^N - h\nu), \tag{3.59}$$

where $T_{i\to f}$ is the transition matrix element of the perturbation Hamiltonian ($\hat{\mathrm{H}}$) between the final and initial states, while the δ-function provides energy conservation in the photoexcitation process.

In the dipole approximation, the transition matrix element has the form $T_{i\to f} = \langle \mathrm{f}|\vec{e}\cdot\vec{r}|\mathrm{i}\rangle$, where $\vec{e}$ is the polarisation vector. Thus, $T_{i\to f}$ can be estimated for selected wave function symmetries and yields dipole selection rules [313]. Therefore, the function $P_P(E_{kin},\, h\nu)$ can be represented as:

$$P_P(E_{kin},\, h\nu) \propto \sum_{f,i} |\langle f|\hat{H}|i\rangle|^2 \;\delta(E_B + e\phi + E_{kin} - h\nu), \tag{3.60}$$

- **Step 2: Transport Toward the Surface**

The transport of the photoexcited electron toward the surface of the solid is explained in the second step of the "three-step model". Throughout this process, the photoelectrons can experience highly elastic and inelastic scattering processes. The main energy loss mechanisms are caused by electron-electron, electron-phonon or electron-impurity interactions. These scattering processes have impact on the energy (inelastic collisions) and angular distribution (elastic and inelastic collisions) of the photoelectrons and lead to the loss of information about the initial state. The primary, non-scattered photoelectrons, i.e. those directly photon-generated and not affected by such collisions, offer direct insights into the electronic structure of the system before ionisation, although additional electrons can also be generated as products of photoelectron collisions, with a loss of primary electron kinetic energy, producing so-called "secondary" electrons.

The effect of the inelastic scattering (collisions) is usually described by the inelastic mean free path (IMFP) λ_{IMFP} of the photoelectrons, which represents the average distance between two subsequent inelastic scattering events of a photoelectron in gaseous or condensed-phase media. If the elastic scattering effects are neglected, experimentally, the IMFP value can be obtained by detecting the photoemission intensity signal I_{PE} from a marker layer buried at a specific depth, d, and another marker layer deposited at the specimen surface, which is associated with maximally intense photoemission with intensity, I_0, and is related to as [314]:

$$I_{PE} = I_0 exp\left(-\frac{d}{L\, cos\theta}\right), \tag{3.61}$$

where L is the effective attenuation length, which roughly corresponds to the λ_{IMFP} and θ is the emission angle of the photoelectron signal measured with respect to the surface normal.

The probability $P_T(E_{kin},\, h\nu)$ of the photoelectron transport from the bulk of the sample to the surface as a function of energy, E_{kin}, from a depth d without inelastic scattering is described by:

$$P_T(E_{kin},\, h\nu) = \alpha(h\nu)\; \lambda_{IMFP}(E_{kin}), \tag{3.62}$$

where $\alpha(h\nu)$ denotes the absorption coefficient for the incident photon, which reflects the absorption cross-sections per unit volume of a material for an optical process.

The IMFP depends on the kinetic energy of the electrons, which is represented by the so-called "universal" curve of the energy dependence of λ_{IMFP} [315] (Figure 3.15). The curve is universal in the sense that it exhibits a common shape, with the details depending on the electronic and geometric

structure of a particular material, especially at low kinetic energies [316, 317]. The IMFP curves exhibit a minimum of 0.3 – 2 nm (3 – 20 A°) for photoelectron kinetic energies in the 5 – 200 eV range, and an increase at both the lower and higher energies, in the various cases. For the low kinetic energy electrons (10 – 124 eV), that is the common energy range for the EUV PES, the λ_{IMFP} is rather small, and about 95% of the photoemission signal (according to the Equation 3.61) derive from $3 \cdot \lambda_{IMFP}$, which is often perceived as the probing depth of PES. Therefore, the PES spectra predominantly reflect the surface electronic states, which makes PES a technique with extremely high surface sensitivity, allowing the study of surface related phenomena. Another outcome of the very short escape depths is related to the cleanliness of the surface region in PES experiments. The contaminants at the surface of the sample can result in electron binding energy shifts and peak broadening of the detected photoemission spectra upon irradiation, changing the spectroscopic signatures of the system under investigation. In order to maximise the penetration of electrons through the surface, the solid-state PES experiments, in particular, have to be carried out under ultra-high vacuum conditions, maintained at a base pressures $\geq 10^{-10}$ mbar.

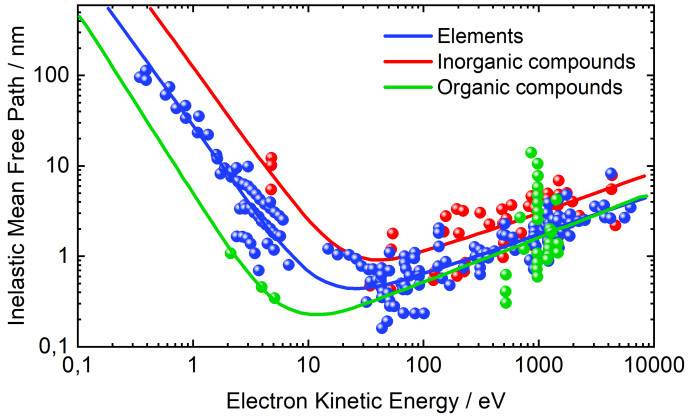

FIGURE 3.15: Compilation of the IMFP measurements for elements, organic and inorganic compounds as a function of electron kinetic energy above the Fermi level, revealing the "universal" curve behaviour. Adapted figure with permission from [315] © 1979 by the John Wiley & Sons Ltd.

- **Step 3: Escape from the Surface into Vacuum**

The third and final step of the "three-step model" concerns photoelectron penetration through the surface potential barrier and escape into vacuum. Only the photoelectrons, for which the perpendicular wave-vector component $k_\perp$ is sufficient to overcome the surface potential barrier, V_0, can escape from the surface. The in-plane momentum wave-vector component, $k_\parallel$, remains undisturbed because the transverse symmetry parallel to the surface is held in planar samples. Therefore, the condition for escape into vacuum is determined by [318]:

$$\left(\frac{\hbar^2}{2m}\right) {k_\perp}^2 \geq E_v^{loc} - E_0 \equiv V_0, \tag{3.63}$$

where E_0 denotes the energy of the bottom of the conduction band relative to the Fermi level, and V_0 is called the inner potential at the surface.

The term $P_E(E_{kin})$, which describes the probability of the emission of the photoelectron from the surface into vacuum and is calculated as:

$$P_E(E_{kin}) = \frac{1}{2}\left(1 - \sqrt{V_0/(E_{kin}+V_0)}\right), \tag{3.64}$$

3.3.3 Femtosecond Time-Resolved EUV Photoemission Spectroscopy

Femtosecond time-resolved photoemission spectroscopy (TRPES) has become a powerful technique for studies of surface, bulk and interfacial electronic dynamics of condensed-phase samples on the femtosecond time scale, specifically utilising the pump-probe principle [31]. TRPES is based on static PES with the additional possibility to directly observe transient changes of the electronic structure after the system is driven out of equilibrium by a short optical pump pulse. TRPES has a major advantage over conventional time-resolved photoluminescence and UV-visible absorption spectroscopies in that ionisation is always an allowed process, regardless of the nature of the excited state. The technique enables direct measurement of the electronic population transfers that occur in photoexcited electronic systems as they evolve over time. By measuring the energy of the photoelectrons as a function of the pump-probe delay, information on the energy distribution within the substance can be obtained as a function of time.

Over the last decades, TRPES experiments have been implemented using nanosecond, picosecond, and femtosecond laser pulses, especially in the gas-phase [37, 319, 320]. Depending on the temporal resolution of the used laser system, different types of photodynamical processes can be followed. Through the utility of femtosecond pump and probe pulses, TRPES allows relaxations of the electronic and vibrational structure to be tracked on ultrashort time scales in molecules [38, 321], clusters [322], metals, semiconductors, organic thin-films and at their surfaces [323–326], as well as charge transfer processes at molecular interfaces [327], localisation and solvation of electrons at surfaces [328] and phase transitions [240]. To be able to ionise system in a single-photon process the photon energy of the probe pulse has to be greater than the ionisation potential of the system. Recently developed coherent light sources of ultrashort pulse duration in the EUV and soft X-ray domain, such as laser-based HHG sources [329, 330], synchrotron light sources [331] and accelerator-based FELs [332] have opened up new perspectives in this field. All of the TRPES experiments presented in this thesis were enabled by femtosecond EUV pulses generated from femtosecond NIR pulses from a Ti: Sapphire CPA system and HHG.

In a femtosecond TRPES experiment, an ultrashort pump laser pulse with photon energy $\hbar\omega_{pump}$ initiates changes in the atomic, molecular, or material structure of the sample, promoting the system to an excited non-equilibrium state within a few femtosecond. After a well-defined time delay, the second ultrashort probe laser pulse with photon energy $\hbar\omega_{probe}$ is used to generate photoelectrons above the vacuum level through ionisation. The kinetic energy of the emitted photoelectrons is measured as a function of pump-probe time delay by an electron analyser with a sufficiently high energy and potentially angular resolution. The recorded photoemission spectra reflects the changes in the distribution of electron kinetic energies and generally shows the evolution of the sample electronic structure after the photoexcitation. From the kinetic energy spectrum and the used photon energy, conclusions about the binding energy of the electronic state from which the electron was removed can be drawn (see Equation 3.52). Further insights about the electronic structure dynamics can be gained by additionally measuring the electron ejection angle and spin distributions. A schematic representation of the TRPES principle for a condensed-phase sample within a molecular orbital framework is illustrated in the Figure 3.16.

In the following, the electronic photoexcitation and EUV ionisation case of TRPES experiments are specifically considered. In the most commonly used two-photon photoemission spectroscopy (2PPE) [39] variant of this technique, the applied pump and probe pulses have NIR to UV central wavelengths. This results in sequential excitation and ionisation of the sample and generation of low-kinetic-energy electrons from the highest-energy, transiently-populated states. In contrast, the EUV probe pulses, in principle, enable ionisation of the entire valence electron manifold and the population of both the ground and excited electronic states of the sample to be followed in time. Furthermore, EUV ionisation generates photoelectrons with sufficiently high kinetic energies to minimise electron-phonon scattering processes, resulting in photoelectron spectra that can be more readily linked to the sample electronic structure prior to ionisation. The electronic-excitation-pump and EUV-probe

TRPES process is discussed in more detail below.

Ultrashort pump pulses in the UV-Vis-NIR wavelength range, as generated by an intense femtosecond pulse laser source, is used to excite electrons from one of the highest occupied molecular orbitals (HOMO, HOMO-1, etc.) into one of the lowest unoccupied molecular orbitals (LUMO, LUMO+1, etc.) in a molecular system and, for example, from the top of the valence band (VBM) into the bottom of the conduction band (CBM) in a solid-state quantum system. After the pump pulse has induced dynamics in the sample, the ultrashort EUV probe pulse, which exploits EUV photons of high photon energy, is applied at a time delay, Δt, to photoionise the system. Hence, the initially occupied and partially depleted ground state along with the populated excited states are promoted simultaneously above the local vacuum level, E_{vac}^{loc}, producing photoelectrons with characteristic kinetic energies. In a condensed-phase system, the probed excited states have an energy lying between the Fermi level, E_F, and below the E_{vac}^{loc}, thus the photon energy of the probe pulse should exceed the work function $e\phi$ of the measured sample ($\hbar\omega_{probe} > e\phi$) to generate photoelectrons through a one-photon process. Thus, the excited state lifetimes and the electronic relaxation pathways to the initially-excited ground state, or the ground states of any generated photoproducts, can be interrogated using the TRPES technique.

When the system in the equilibrium is promoted to one or more initially unoccupied excited states with pump pulses that spatially and temporally overlap with the EUV probe pulse at the sample position, the zero time delay, t_0, of the TRPES experiment can be determined. The convolution of the pump and probe pulses, called a cross-correlation, allows t_0 and the time resolution of the TRPES experiments to be accurately determined using different targets and the sample under study (see Section 4.4.4 for more details).

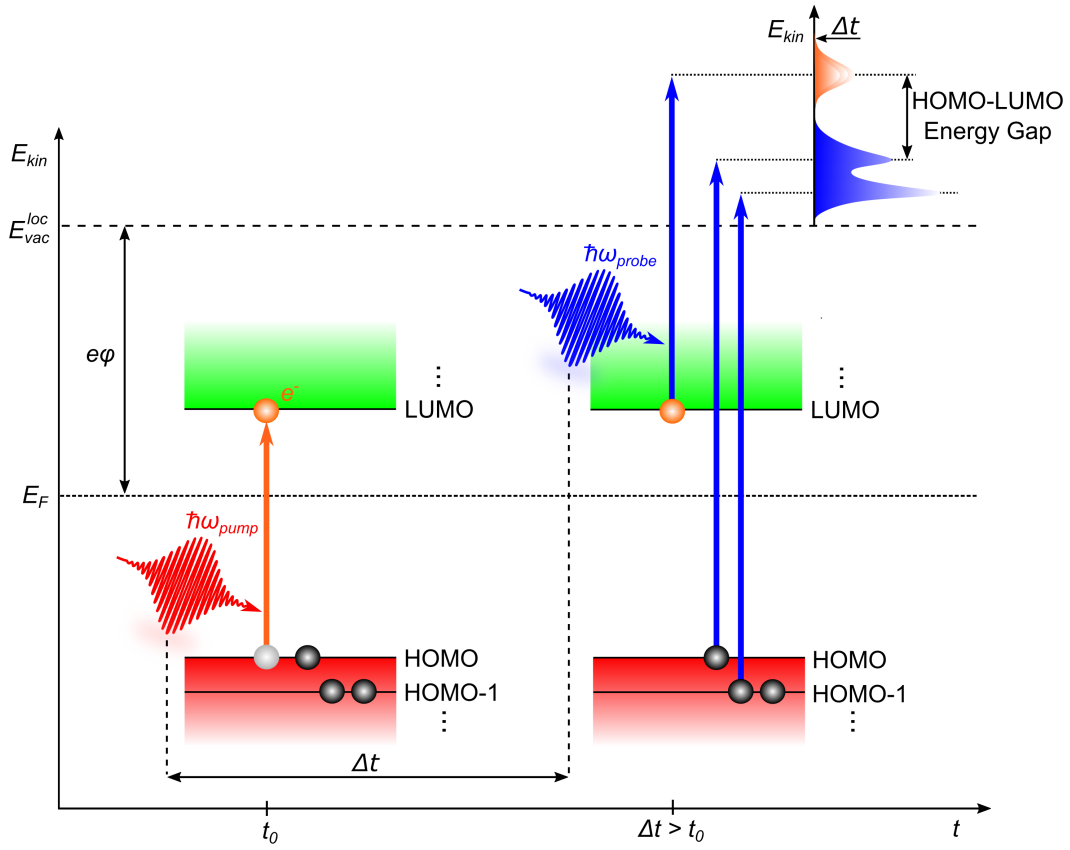

FIGURE 3.16: Schematic view of the TRPES principle for a condensed-phase sample within a molecular framework. The measured kinetic energies of the electronic ground and excited states of the sample, depicted in the figure, are presented on an energy scale with respect to the local vacuum, E_{vac}^{loc}, and Fermi, E_F, levels.

The EUV probe pulse is used to monitor the changes in the relaxing system at various Δt values of the pump with respect to the probe pulse. The corresponding ultrafast decay of the excited state signals can often be defined by exponential decay behavior, $e^{-\Delta t/\tau}$, where τ represents the lifetime of an excited state. By recording the photoemission spectrum over a broad range of pump-probe time delays, the relaxation dynamics of the system can readily be characterised with sub-100 fs time resolution and out to ns pump-probe time delays.

3.3.4 The Space-Charge Effect

The application of high peak intensity must be limited in condensed-phase PES and TRPES experiments, due to the so-called space-charge (SC) effect [333, 334]. In general, the SC effect can occur from both pump and probe laser pulses. When an intense laser pulse is applied to a sample, the emitted photoelectrons form an electron cloud, which may have a high charge density. This results in a Coulomb interaction involving the photoelectrons emitted from the sample, and the remaining electrons and positive ions, with an associated charge imbalance at the sample surface. Due to redistribution of the photoelectrons kinetic energies and spectral perturbations, the kinetic energy of the charged particles, which is affected by the forces of attraction or repulsion, can be increased or decreased. This results in a broadening and a shift of the electron velocity distribution and can lead to a misinterpretations of the obtained energy spectra. Such effects can be particularly dramatic in TRPES experiments, particularly, as the effect is generally time- and space-dependent [333–341].

In the TRPES technique, the primary Coulomb interaction manifests itself in two separate electron clouds ejected by the intense pump and EUV probe pulses, which strongly depend on the pump-probe time delay [340, 342]. This can cause positive or negative time-dependent electron kinetic energy shifts or broadening of the spectral components, and often represents a limiting factor in experiments. Thus, the pump and probe pulse peak intensities have to be reduced to minimise this effect. Nevertheless, it is important to recall that to achieve reasonable integration times in TRPES experiments, high pulse fluences are required. Hence, high repetition rate laser sources would be of assistance to resolve this problem [343], especially in cases where transient relaxation dynamics and heat dissipation processes are complete in the time interval separating two successive pump pulses. Studies of the SC effect have been performed [333, 334, 336, 344, 345] over a wide kinetic energy range of 5–100 eV, applying various sub-picosecond pulse durations. These studies demonstrated that the broadening and spectral shifts of photoemission peak kinetic energies scales with the charge density, ρ, as [346]:

$$\rho \approx \frac{N}{d}, \tag{3.65}$$

where N is the total number of electrons emitted from the sample per pulse and d is the diameter of the laser spot size on the sample.

Thus, the shift or broadening of kinetic energy peak can be described with the relation:

$$\Delta E_{kin} = m \frac{I}{f_{rep}\, de}, \tag{3.66}$$

where I is the average sample current, f_{rep} is the laser repetition rate, e is the elementary charge, and m is the empirical scaling factor. According to the Equation 3.66, the ΔE_{kin} is directly proportional to the current of the sample under investigation and inversely proportional to the laser repetition rate and the beam spot size on the sample surface. Two important parameters, f_{rep} and d impose conditions on the charge cloud volume in front the sample surface right after escaping from the sample.

A schematic illustration of the SC effect is presented in the Figure 3.17. In the TRPES experiment, two possible cases must be considered: (1) *when the pump pulse arrives at the sample first* (panel (a) in Figure 3.17) at so-called positive pump-probe time delays ($\Delta t \geq 0$) and (2) *when the probe pulse arrives prior to the pump pulse at the sample* (panel (b) in Figure 3.17), corresponding to negative pump-probe time delays ($\Delta t < 0$). The resulting SC cases are described as follows:

(1) An intense pump laser pulse can release the photoelectrons through the (potentially above-threshold) multiphoton photoemission (MPPE) process [347], in which the intensity of the emitted electrons increases non-linearly with the peak power of the pump fluence until significant saturation effects are initiated. Consequently, the density of a charge cloud - produced by the photoemitted electrons and generally decreasing in time - depends on the intensity of the pump pulse. After a certain time delay, Δt, the EUV probe pulse interacts with the sample, resulting in a second cloud of photoemitted electrons. The mutual Coulomb interaction between the two charge clouds is determined by the Δt between the pump and probe pulses. Thus, at short pump-probe delays, when the two charge clouds are close to each other, the strongest mutual Coulomb interaction can be observed. An intense low photon energy pump pulse brings the photoelectrons above the vacuum level to produce a charge cloud of slow electrons. Whereas, a high photon energy EUV probe pulse ionises the sample to produce a charge cloud of fast electrons. As a result, the probe pulse photoelectrons will pierce through the charge cloud of the slow pump-induced photoelectrons at some point in time on the way to the detector. In this manner, the pump pulse that arrives first at the sample generates a high-density charge cloud at $\Delta t \geq 0$. The interaction between the pump and probe electron clouds and the SC effect will correspondingly cause the photoelectrons produced by the EUV pulse to first slow down and then accelerate as a function of time delay, respectively, inducing positive and negative energy shifts in the photoemission spectrum on the kinetic energy scale as a function of pump-probe delay.

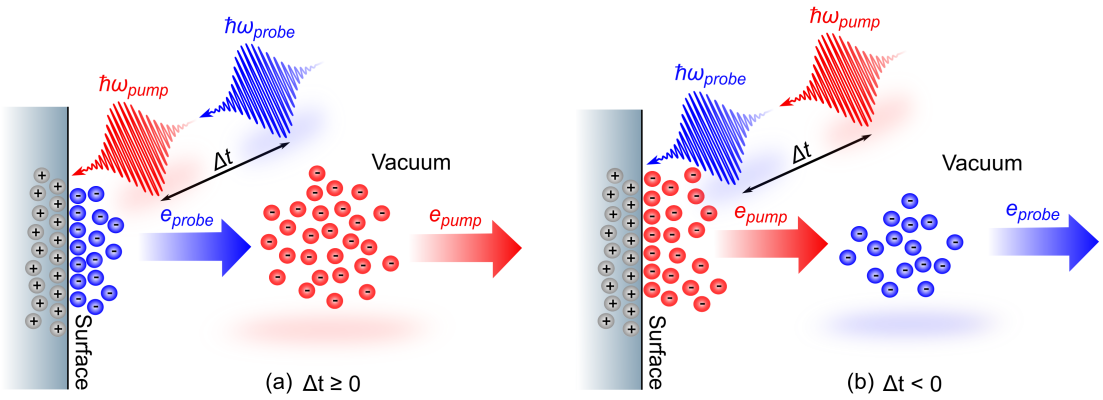

FIGURE 3.17: Schematic illustration of the space-charge effect induced via the interaction of the pump and probe pulses with a condensed-phase sample at different pump-probe time delays, Δt. Panel (a): the pump pulse arrives first at the sample at $\Delta t \geq 0$ pump-probe time delays; Panel (b): the probe pulse arrives prior to the pump pulse at the sample at $\Delta t < 0$ time delays.

(2) At the negative time delays ($\Delta t < 0$), the EUV probe pulse arrives prior to the pump pulse at the sample and the opposite case to the previous scenario happens. The high photon energy EUV probe pulse produces a charge cloud of photoelectrons before the pump pulse-induced photoelectrons. Due to the attraction between the probe pulse-generated ions and the pump pulse-induced photoelectrons, a positive SC effect occurs. At the same time, as a result of the repulsion between the photoemitted pump and probe pulses charge clouds, a negative SC effect arises. In the probe-pump configuration, i.e. at negative time delays, the energy shift caused by the SC effect will always be positive, since the slow pump pulse-induced electrons follow the fast probe pulse-generated photoelectrons, but can never catch up to them. Thus, the probe pulse-generated photoelectrons contribute to the photoemission spectrum with a positive kinetic energy shift, at least within the vicinity of tempero-spatial overlap of the pump and probe laser pulses.

3.4 UV-Vis Transient Absorption Spectroscopy

Some of the experiments discussed in this work were carried out using the femtosecond ultraviolet-visible (UV-Vis) time-resolved absorption spectroscopy technique. UV-Vis time-resolved absorption spectroscopy or so-called UV-Vis transient absorption spectroscopy (TAS) has become a powerful and well-established pump-probe technique for studying liquid- or solid-phase electronic dynamics in physical, chemical, and biological systems [24, 40, 41, 348, 349] that measure the photogenerated excited state absorption energies and associated lifetimes of the transient species as a function of time.

Due to the rapid development of ultrafast laser sources over the last decades, the improved time resolution in TAS experiments, utilising sub-100 fs pulse durations, has facilitated the study of radical ions, excited singlet and triplet states [350], to isomerization transitions [351], photo-product reactions [352] as well as internal conversion, intersystem crossing, relaxation, charge and energy transfer mechanisms [353]. Although the TAS technique in some way complements time-resolved fluorescence techniques [354, 355], it is readily applicable to any sample where a transition from an excited state to higher excited states is an allowed process and has a dipole moment strong enough to make it observable. Therefore, the TAS technique has been widely used to understand light-harvesting mechanisms in photophysical and photochemical systems [356, 357], the optimisation of solar cells [358, 359] and light-driven photocatalysis [360], as well as the development of novel materials for various optoelectronic and material science applications [361, 362].

3.4.1 Fundamentals of Femtosecond UV-Vis Transient Absorption Spectroscopy

Femtosecond UV-Vis transient absorption spectroscopy utilises ultrashort laser pulses to monitor ultrafast electronic dynamics of atoms and molecules in liquid- or solid-phase molecular systems as a function of time delay between the pulses [40]. In TAS, the laser pulse is split into two parts. A relatively high-intensity excitation (pump) pulse (tunable to resonantly excited a chromophore) is used to promote a sub-ensemble of a molecular system under investigation from the ground state, e.g., S_0 to an electronically excited state, e.g., S_1, generating a non-equilibrium state. A second low-intensity probe pulse (preventing multiphoton processes during probing) is used to monitor the pump-induced changes in the optical properties of the sample. Measurement of the difference in the transmittance or reflectance as a function of the probe wavelength, λ, and time delay, Δt, between the pump and probe pulses provides information about the relaxation of excited states in the sample. The pump pulse central wavelength is selected taking into account the linear absorption properties of the investigated sample. The spectrum of the probe pulse can be generated in the UV-Vis, NIR or MIR spectral regions using a white-light continuum built upon $\chi^{(3)}$ non-linear optical interactions (and cascaded Raman scattering in such a solid) (see Section 3.2.2).

In a typical TAS experiment, firstly, the pump and probe beams are spatially overlapped on the sample, and the pump beam is blocked following the interaction with the sample. Depending on the configuration of the TA optical scheme, the probe beam either passes through the sample, i.e. is transmitted, or is reflected from the surface of the sample to a detector (spectrograph combined with a charge-coupled device, CCD, camera). The arrival time between the pump and probe pulses at the sample can be controlled by using a variable linear translation delay stage, usually positioned in the optical path of the pump beam, spanning delay times from fs to ns. Thus, the probe spectrum is recorded as a function of the delay time, Δt, between the pump and probe pulses. By placing a mechanical chopper wheel in the optical path of the pump beam, the measurement of the (transmitted) intensity of the probe beam in the excited (pump-probe) or unexcited (probe-only) system is allowed. Consequently, the obtained transient absorption signal can be determined as a function of λ and Δt. A schematic view of the TAS principle is depicted in Figure 3.18.

The obtained transient absorption signal is usually defined as follows. Based on the Beer–Lambert law [363], the absorbance or optical density $OD(\lambda)$ of the sample is determined by the intensity of the incident $I_0(\lambda)$ and transmitted light $I(\lambda)$ as:

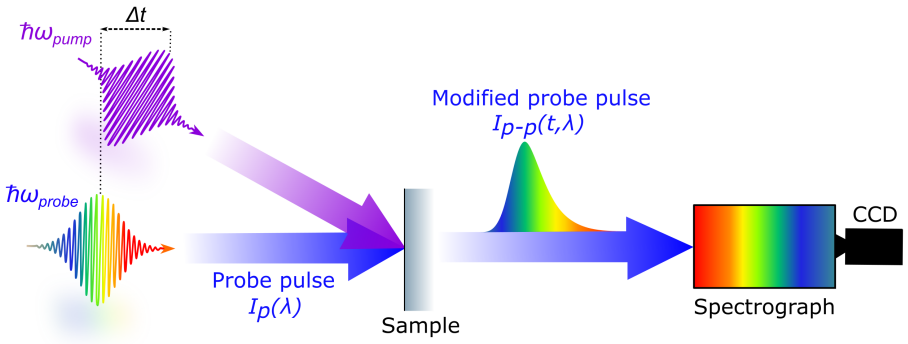

FIGURE 3.18: Schematic view of the principle of TAS technique.

$$OD(\lambda) = lg\left(\frac{I_0(\lambda)}{I(\lambda)}\right), \tag{3.67}$$

Equation 3.67 is also valid for diffuse reflected light, if the measured transient absorption signals are small enough and therefore are proportional to the $OD(\lambda)$ quantities in the Beer-Lambert law.

The change in optical density $\Delta OD(t, \lambda)$ induced by the pump pulse is determined as the difference between the optical densities in the pump-probe, $OD_{p-p}(t, \lambda)$, and probe-only, $OD_p(\lambda)$, cases. The sample absorption is correspondingly modeled as follows:

$$\Delta OD(t,\lambda) = OD_{p-p}(t,\lambda) - OD_p(\lambda) = lg\left(\frac{I_0(\lambda)}{I_{p-p}(t,\lambda)}\right) - lg\left(\frac{I_0'(\lambda)}{I_p(\lambda)}\right), \tag{3.68}$$

Experimentally, the incident probe intensities $I_0(\lambda)$ and $I_0'(\lambda)$ are not measured, instead the change in the optical density is calculated in a simplified form assuming that $I_0(\lambda) = I_0'(\lambda)$:

$$\Delta OD(t,\lambda) = lg\left(\frac{I_p(\lambda)}{I_{p-p}(t,\lambda)}\right), \tag{3.69}$$

Thus, $\Delta OD(t, \lambda)$ provides information about the electronic dynamic processes (in the UV-Vis range) and the vibrational or vibronic dynamic processes (in the NIR or MIR range) occurring in the molecular system under investigation. For this reason, a global fitting analysis procedure can be used to state-associated temporal and spectral [364]. From Equations 3.68 and 3.69 it follows that if the incident probe pulse intensities are consistent between successive measurements, the change in optical density is the same. This means that Equation 3.69 is applied as long as the pulse intensities between consecutive measurement events are commensurate. At present, for femtosecond laser systems with a kHz repetition rate, this condition is met on a shot-by-shot basis, using shot-to-shot detection in TAS experiments, by means of blocking every successive pump pulse with a mechanical chopper [365].

The transient absorption spectrum, i.e. $\Delta OD(t,\lambda)$, comprises four signal contributions from various photophysical and photochemical processes, as shown in Figure 3.19. Ideally, each of these components occurs in the spectrum at a distinct spectral position with the corresponding sign of the $\Delta OD(t,\lambda)$. The four contributions to the transient signal are the following:

(1) *Ground state bleach* (GSB) or depopulation signal, which occurs instantaneously when the pump pulse promotes a certain fraction of the molecules from the ground state, S_0, to their excited state, e.g. S_1, leading to a decrease in the fraction of the molecules in the ground state. As a result, the probe pulse will be absorbed to a lesser degree at the spectral positions associated with the steady-state absorption bands, thus contributing to a negative change of absorbance, $\Delta OD < 0$ (blue colour in the Figure 3.19).

(2) *Stimulated emission* (SE) processes induced by the probe pulse, occurring from the pump-pulse-excited state of the molecule, which can be projected onto a lower-lying state, i.e. the ground state, S_0, via the emission of light. Since the emitted photons propagate in the same direction as the probe pulse, an apparent additional bleaching will be detected, resulting in a negative signal in the SE region of the $\Delta OD\,(t,\lambda)$ spectrum. (Figure 3.19 orange colour). The SE spectrum is usually observed in the same spectral region as the spontaneous emission spectrum with a characteristic red-shift, and is Stokes-shifted relative to the GSB spectrum. Depending on the molecular system, the SE and GSB signals can overlap, emerging as one signal with $\Delta OD < 0$.

(3) *Excited state absorption* (ESA) processes, which take place when the pump pulse populates the excited state and optically allowed transitions to higher-lying excited states (S_n, T_n, D_n, etc.) may exist in certain spectral regions, so absorption of the probe pulse will occur. As a consequence, a positive signal is observed in the spectral region of the ESA (Figure 3.19 violet colour). Although the ESA process is a result of photoabsorption from the probe pulse, the population of the excited state is assumed to be unaffected by this probe pulse due to its low intensity [40].

(4) *Photoproduct absorption* (PA) processes may occur after excitation and photodissociation or chemical reaction of molecules in photobiological or photochemical systems. Following excitation, a photo-reaction in the system may result in a transient state, such as charge-separated states, metastable states, isomerised states or radical formation. The PA process contributes to the TA spectrum as a positive signal $\Delta OD > 0$ (Figure 3.19 red colour).

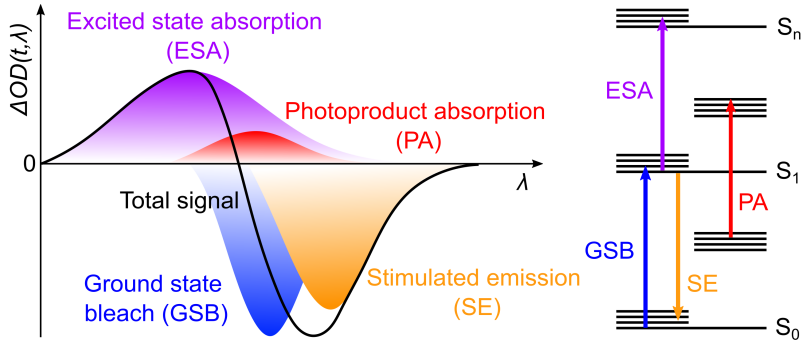

FIGURE 3.19: Schematic view of the various signal contributions to the absorbance, $\Delta OD\,(t,\lambda)$ spectrum in TAS, represented as the energy levels of a molecule (right panel) and the measured probe beam spectrum (left panel).

3.5 Global Analysis Procedure

Model-based analysis of time-resolved data is a key tool for characterising the experimentally observed spectral features encompassing the electronic dynamical processes in a molecular complex or material upon photoexcitation. In this dissertation, a global analysis procedure [364, 366, 367] was used as the mathematical tool to describe the measured time-resolved (kinetic) data. One of the advantages of the global fitting is that the behaviour of a real photophysical/photochemical system can be mathematically described and fitted directly to the data, extracting the physical parameters of interest, e.g. state-associated or species-associated spectra and kinetic rate parameters (lifetimes). The procedure based on a fitting of a real physical model to the data is called kinetic modelling [368]. Modeling the kinetics and associated energetically-dispersed spectra of evolving electronic states in photoexcited molecular systems generally leads to more accurate spectral-temporal modelling.

In the present work, global fitting was used to numerically solve the system of differential kinetic equations, associated with a proposed kinetic model to represent the population dynamics of electronically excited states in the studied condensed-phase samples. The results obtained provide spectral

and kinetic information on time-dependent changes in the electronic structure, as well as on individual contributions from the involved excited states of the photoexcited molecular system. The spectral information associated with excited state signals was modeled and extracted using the global fitting procedure by employing two different methods. In the first method, the spectral distribution of the transient signals from the involved electronics states was introduced explicitly and decomposed into a sum of Gaussian envelopes (explicit global fitting). Alternatively, a least-squares algorithm [369] was used in the global analysis to represent the transient spectra implicitly. The explicit global analysis of TRPES data for $[Fe(CN)_6]^{3-}$ dissolved in [emim][DCA] solution sample was performed using a Wolfram Mathematica script, written in-house. All global analysis scripts applied to the TRPES and TAS data for the PCN samples were written in MATLAB by Dr. Christoph Merschjann (Helmholtz-Zentrum Berlin) and used to implicitly fit the data.

Typically, the measured transient spectrum represents a three-dimensional (3D) data set that corresponds to different (distinct) delay times, electron kinetic energies or probe pulse wavelengths, as well as the magnitude of the photoemission or relative changes in the absorbance signals, which can be obtained from the TRPES or TAS experiments, respectively. Global analysis allows simultaneous fitting of the measured multidimensional data sets with the same fit function. Therefore, the analysis of the 3D time-resolved data using the global fitting procedure overcomes the main limitation of conventional two-dimensional (2D) fitting, which is often subjective when one data set or spectral region is selected over another for analysis. The global analysis procedure, which was used to describe the temporal and spectral spectroscopic changes in the photoexcited condensed-phase samples studied in this thesis, is presented in detail below.

3.5.1 TRPES and TAS Data Analysis

The fit function applied in the TRPES experiments, which describes the dependence of the measured transient photoemission signal on the time delay, t, and photoelectron kinetic energy, E, is given by:

$$TS(E,t) = \sum_{Q} \mathrm{S}_Q(E) \cdot [Q]^*(t) \ , \tag{3.70}$$

where $\mathrm{S}_Q(E)$ represents the photoemission spectrum from the transient state Q, $[Q]^*(t)$ is the transient population of state Q convolved with the Gaussian temporal envelope of the EUV probe pulse with a width of σ_{probe} (FWHM):

$$[Q]^*(t) = \frac{1}{\sqrt{\pi}\sigma_{probe}} \int_{-\infty}^{\infty} [Q](t) \cdot \exp(-t^2/\sigma_{probe}^2) dt \ , \tag{3.71}$$

In addition, the cross-correlation signal denoted by $CC(E,t)$ was taken into account in the numerical procedure, where the convolution of the Gaussian temporal envelopes of the pump and probe pulses gives the measured CC width:

$$CC(E,t) = CC(E) \cdot \exp(-t^2/(\sigma_{pump}^2 + \sigma_{probe}^2)) \ , \tag{3.72}$$

where σ_{pump} is the width (FWHM) of pump pulse.

For a photophysical system under investigation, a system of differential kinetic equations can be introduced, for a pre-proposed kinetic model to represent the transient population of the electronic states with corresponding kinetic parameters, such as rate constants (k_i), as well as spectra associated with the involved states. The system of differential equations is solved numerically for a given set of rate constants, k_i, which are treated as fit parameters, with the initial condition that all involved excited states were unpopulated at $t \rightarrow -\infty$ and only the electronic ground state (GS) is initially occupied ([GS]=1). As a result, a population density matrix, $[Q]^*(t)$, is defined by the numerical solution of the differential equations describing the population dynamics of the involved states for a particular kinetic model.

The Chi-square, χ^2, goodness of fit test was used to evaluate the quality of the global analysis by minimising the χ^2 value when comparing the modeled signal, *TS(E,t)*, with the experimental transient signal, $TS_{exp}(E,t)$, which can be described as follows [367]:

$$\chi^2 = \left\| \frac{TS_{exp}(E,t) - TS(E,t)}{s(E,t)} \right\|^2 , \tag{3.73}$$

Here, *s(E,t)* is the standard deviation of the corresponding data points in the experimental data and the model. In case of TRPES experiments, the statistics follow a Poissonian distribution and the standard deviation is expected to be equal to $s(E,t) = (TS_{exp}(E,t))^{1/2}$.

In the explicit global analysis of the TRPES data for the $[Fe(CN)_6]^{3-}$ dissolved in [emim][DCA] solution sample, the photoemission spectrum, $S_Q(E)$, of each transient state Q and $CC(E)$ was represented by a superposition of Gaussian envelopes with amplitudes, positions, and widths treated as fit parameters. The fit parameters extracted from the explicit global analysis results to the photoemission spectra were obtained using the following expression:

$$\mathrm{S}_Q(E) = \sum_i \mathrm{A}_i^Q e^{-\frac{(E-E_i^Q)^2}{(\sigma_i^Q)^2}} , \tag{3.74}$$

where A_i^Q is the amplitude, E_i^Q is the central binding energy position, and σ_i^Q is the width (FWHM) of the corresponding Gaussian peak associated with the electronic state Q.

For the PCN thin film samples, the photoemission spectra were implicitly derived from the least-squares method, which was used in the global analysis to represent the spectra obtained from the experiment. The implicit global analysis based on the least-squares method employs the matrix formalism [370]. Thus, the experimental transient signal, TS_{exp}, can be represented by the number of $N \times M$ data points on the energy and time scale, which form the transient signal matrix product:

$$TS_{exp} = S_Q \times ([Q]^*)^T , \tag{3.75}$$

where the matrix $S_Q(N,Q)$ describes the photoemission spectra of Q transient states at the set of N data points on the energy scale and the matrix $[Q]^*(M,Q)$ describes the population of these states at the set of M data points on the time scale. The CC signal is treated as a transient state as well. The photoemission spectra, S_Q, can be obtained using matrix operations, supposing that the kinetic rate parameters are known or presumed, while computing the matrix $[Q]^*$ for each time delay and rate parameter as:

$$S_Q = TS_{exp} \times [Q]^* \left(([Q]^*)^T \times [Q]^* \right)^{-1} , \tag{3.76}$$

Analogous to the TRPES data analysis procedure, the fit function in the TAS experiments, $TS(\lambda,t)$, which describes the dependence of the relative changes in the absorbance signal, ΔOD, on the pump-probe time delay (t) and wavelength (λ) can be expressed as:

$$TS(\lambda,t) = \sum_Q \mathrm{S}_Q(\lambda) \cdot [Q]^*(t) , \tag{3.77}$$

where, in this case, $\mathrm{S}_Q(\lambda)$ represents the diffuse reflectance spectrum from the transient state Q, and $[Q]^*(t)$ is the transient population of state Q, convoluted with the Gaussian temporal envelope of the WLC probe pulse, σ_{probe}, as described by Equation 3.71. The CC signal between the pump and probe pulses in the TAS experiments appears as a cross-phase modulation (XPM) signal [371], and is equivalent to the CC signal in TRPES, where the latter is caused by the multiphoton or laser-assisted photoelectric effect (see Section 4.4.4). In the diffuse reflectance spectra, the XPM signal emerges with a temporal chirp, which is taken into account in the numerical correction of the time zero position in the time-dependent matrix. Similar to TRPES, the modeling of the time-dependent spectral changes in the TAS results involves solving the system of kinetic rate equations numerically. The species-associated, diffuse reflectance spectra, were obtained employing the implicit global analysis, which is based on the matrix formalism described by Equation 3.76.

Chapter 4

Experimental Setups

> "I am among those who think that science has great beauty. A scientist in his laboratory is not only a technician: he is also a child placed before natural phenomena which impress him like a fairy tale."
>
> *— Marie Skłodowska-Curie, During a debate in Madrid, 1933*

Femtosecond time-resolved extreme-ultraviolet (EUV) photoemission spectroscopy (TRPES) and ultraviolet-visible (UV-Vis) transient absorption spectroscopy (TAS) have been applied throughout the investigations presented in this dissertation. Chapter 4 describes the experimental setups and procedures used for the data acquisition. Section 4.1 gives a detailed description of the femtosecond Ti: Sapphire CPA laser system applied in the TRPES and TAS experiments. Section 4.2 provides an overview of the TRPES experimental setup. In Section 4.3, generation of the second harmonic of the laser fundamental and the ultrashort UV pump pulses is presented. Section 4.4 describes generation of the ultrashort pulses in the EUV spectral region for the TRPES experiments via frequency up-conversion in the gas-phase high-order harmonic generation (HHG) process. In addition, the reflective zone plane monochromator and optimisation of the HHG beamline efficiency are described in Sections 4.4.1 and 4.4.2, respectively. Sections 4.4.3 and 4.4.4 provide details on the characterisation of pump and probe pulses in the spectral, spatial and temporal domains in associated TRPES experiments. In Section 4.5, the detection of photoemitted electrons using a time-of-flight (TOF) electron spectrometer is explained. In Section 4.6 an overview of the TAS experimental setup and associated beam characterisation techniques is presented.

4.1 Femtosecond Ti: Sapphire CPA Laser System

For the experiments discussed in this dissertation, a commercial femtosecond Ti: Sapphire laser amplifier system (Coherent Inc., Legend Elite Duo) was used (Figure 4.1). The laser system consists of two main components: a mode-locked oscillator and a chirped-pulse amplifier, as well as an intermediate pulse shaper. The Ti: Sapphire, Kerr-lens mode-locked seed laser oscillator (Coherent Vitara) generates approximately 6 nJ pulse^{-1} energies at a central wavelength of 800 nm with sub-10 fs (FWHM) pulse durations at a repetition rate of 80 MHz. The oscillator is pumped by a continuous wave (CW) optically-pumped semiconductor laser (Coherent Verdi G5) at 532 nm wavelength with an average output power of 5 W. In the oscillator, the Ti:Sapphire crystal acts as the Kerr medium, with a passive self mode-locking scheme.

The ultrashort laser pulses produced in the Ti:Sapphire oscillator must be amplified in order to generate high peak pulse intensities. Thus, the pulses are amplified using the chirped-pulse amplification (CPA) technique (see Section 3.1.3) in a Ti: Sapphire gain medium, pumped by an external pump laser. The CPA can be divided into three steps: stretching, amplification and compression of the pulses. Firstly, the duration of the incoming seed pulse is stretched using an angularly dispersive grating in order to avoid damage of the amplifier by the high pulse peak intensity. The pulse is initially stretched (chirped) up to a 100 ps pulse duration. Then, the lower-intensity chirped pulse passes

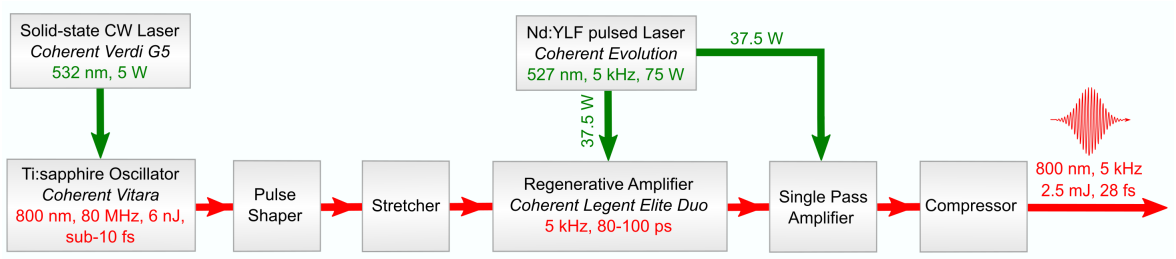

FIGURE 4.1: Schematic view of the components in the femtosecond Ti:Sapphire CPA system in the configuration used in the experiments.

through the regenerative amplifier (Coherent Legent Elite Duo), where the instantaneous intensity is below the self-focusing and damage threshold of the amplifier optics. The regenerative amplifier is an optical resonator which contains a Ti: Sapphire crystal placed inside the resonator and pumped by a pulsed Nd:YLF solid-state laser (Coherent Evolution) at 527 nm wavelength with a pump power of 75 W. The chirped seed pulse is injected into the regenerative amplifier using an electro-optical switch (a Pockels cell combined with a polariser) which is open for a time shorter than the round-trip time. After that, the pulse can undergo many resonator round trips through the Ti: Sapphire crystal, being amplified to a high energy level. In the end, the pulse is released from the resonator using a second electro-optical switch after the amplifier gain has started to saturate. The injection of the seed pulse and the release of the amplified pulse takes place at 5 kHz repetition rate. The regenerative amplifier is followed by a single pass amplifier, which allows the pulse energy to be further amplified. The amplified pulses pass through a set of gratings in the compressor, which removes the frequency chirp in the amplified pulse. After the compression, the Ti: Sapphire CPA laser system provides an output energy of 2.5 mJ pulse^{-1}, 28 fs (FWHM) pulse durations with a 800 nm central wavelength pulses at a 5 kHz repetition rate.

Figure 4.2 shows pulse duration characterisation SPIDER measurements of the compressed output, with 800 nm central wavelength, from the Ti: Sapphire CPA laser system. The left panel displays the measured spectral intensity (white) and reconstructed spectral phase (cyan). The corresponding inverse Fourier transformed temporal reconstructions of the pulse are shown in the right panel. Therein, the Fourier-transform-limited intensity (green), recovered temporal intensity (white) and recovered temporal phase (cyan) of the output pulse envelope is presented. The FWHM pulse duration was determined to be 27.6 $\pm$ 0.5 fs.

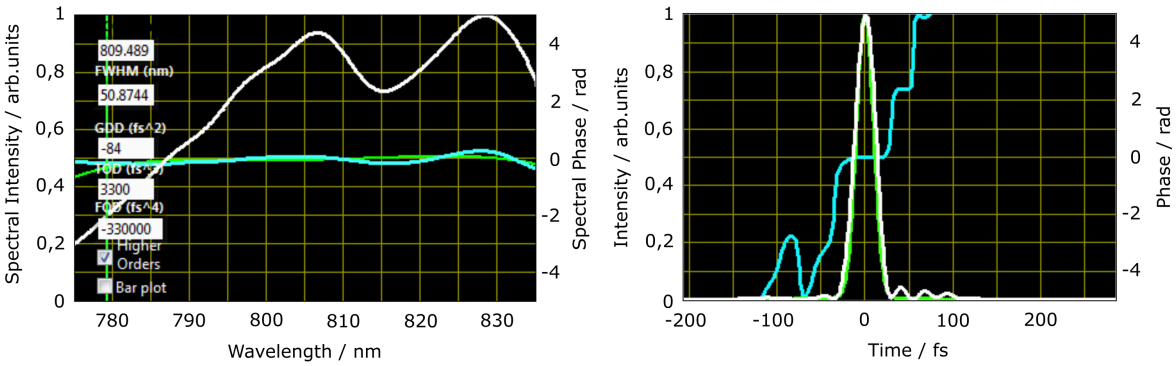

FIGURE 4.2: SPIDER measurements of the output pulses from the Ti: Sapphire CPA laser system. The measured spectral intensity (white) and reconstructed spectral phase (cyan) is shown in the left panel. The temporal reconstruction, including the Fourier-transform-limited temporal intensity (green), intensity (white) and temporal phase (cyan) of the pulse is presented in the right panel.

4.2 Overview of the Time-Resolved Photoemission Spectroscopy Setup

The Ti: Sapphire CPA laser system, delivering 2.5 mJ pulse^{-1} energies, 28 fs (FWHM) pulse durations with a central fundamental wavelength of 800 nm (1.55 eV photon energy) at a 5 kHz repetition rate was used to generate both the pump and probe pulses for the TRPES experiments. A schematic overview of the main components of the TRPES setup is illustrated in the Figure 4.3. The laser output was split by a beam splitter (BS1) into two parts, where 1 mJ pulse^{-1} energies were directed to an optical parametric amplifier (OPA), which was available for tuning the fundamental wavelength of the laser system output in a wide range of wavelengths (240 – 2600 nm), but was not used in the TRPES experiments. Another part, 1.5 mJ pulse^{-1} energies, was split by a second beam splitter (BS2) resulting in 0.3 mJ pulse^{-1} energies used to pump a second harmonic generation (SHG, for the TRPES pump beam) setup, which produces ultrashort laser pulses in the ultraviolet (UV) spectral region (see Section 4.3 for the detailed description).

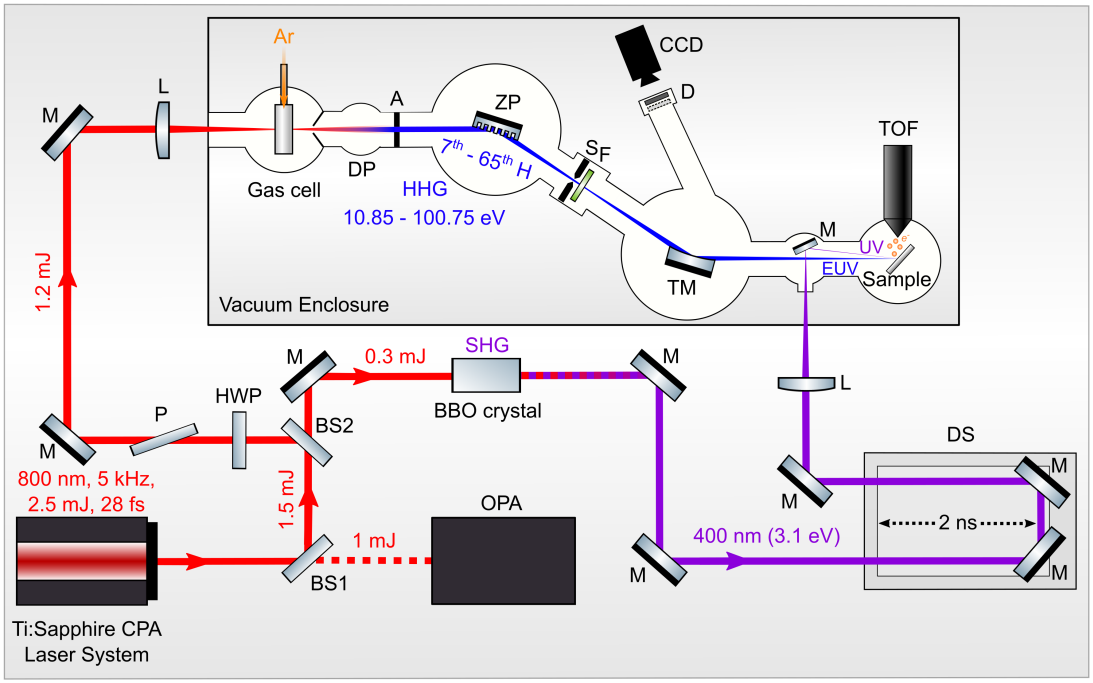

FIGURE 4.3: Schematic view of the time-resolved photoemission spectroscopy setup.

The remaining, fully-reflected, 1.2 mJ beam component was used to generate EUV TRPES probe pulses via the HHG beamline (described in Section 4.4). After the generation of the pump and probe pulses, they were spatially overlapped at the sample in the interaction region at a mutual angle of 1° between the beams. The pump beam was focused by a lens (L) and reflected into the interaction region by a mirror placed slightly aside the EUV beam path before the sample chamber. The time delay between the pump and probe pulses in the interaction region was scanned by tuning the optical delay stage (DS) (FMS300PP, Newport Corp.) in the pump beam path. This allowed the delay range to be swept over an up to 2 ns temporal range. The photoemission kinetic energy spectra were recorded using a time-of-flight (TOF) electron spectrometer, which is described in Section 4.5.

4.3 Second Harmonic Generation Pump Beam Setup

In both the TRPES and TAS experiments, a component of the femtosecond NIR pulse generated by the Ti: Sapphire CPA system (0.3 mJ pulse^{-1} energies) was used to produce 400 nm wavelength pump pulses via second harmonic generation (SHG) in a beta-barium borate (BBO) non-linear crystal. In

order to minimise the accumulated temporal mismatch between the input pulse and the frequency-converted generated pulse, group velocity mismatch, and the frequency chirp in a non-linear crystal, GDD (see Section 3.1.2), a 150-μm-thin BBO crystal (Newlight Photonics Inc.) was chosen for the frequency conversion process for the TRPES and TAS experiments.

BBO is a negative uniaxial crystal and can be phase-matched for Type 1 SHG with fundamental wavelengths from 410 to 3300 nm. It has a high optical homogeneity and a high NIR damage threshold, which is, in particular, needed for efficient generation of ultrashort sub-50 fs pulses. Considering that BBO crystals are birefringent, their refractive index and therefore their phase-matching depends not only on wavelength, but also on the polarisation direction of incoming light relative to the crystal axes. Practically, aligning the input beam polarisation to the slow axis of the crystal, it is possible to compensate for the natural index dispersion and accomplish efficient phase-matching with the second harmonic propagating along the fast axis.

The orientation of the polarisation of the incident Ti: Sapphire laser system pulse was parallel (p-polarised light) relative to the crystal axis. Thus, by rotating the polarisation axes of the fundamental laser pulse using an 800 nm half-wave plate (HWP) placed in front of the BBO crystal, the conversion efficiency of SHG process was controllable. The crystal axis was set vertically, therefore the generated 400 nm light had a vertical polarisation axis (s-polarised light) with respect to the laser table. The alignment of the polarisation axis of the generated second harmonic plays an important role in the time-resolved experiments. By rotating the polarisation of the SH pump, it is possible to carry out polarisation-state-resolved experiments. The remaining 800 nm fundamental light was filtered out using the transmission of highly-reflective second harmonic (>99.9 %, HR 365–545 nm) dichroic mirrors (DM) and dumping the residual 800 nm beam (BD). A schematic layout of the SHG setup, as well as the propagation of pump pulses in the configuration used in the TRPES experiments (see Section 4.2), is shown in Figure 4.4. The pump beam propagation scheme employed in the TAS experiments will be presented in Section 4.6.

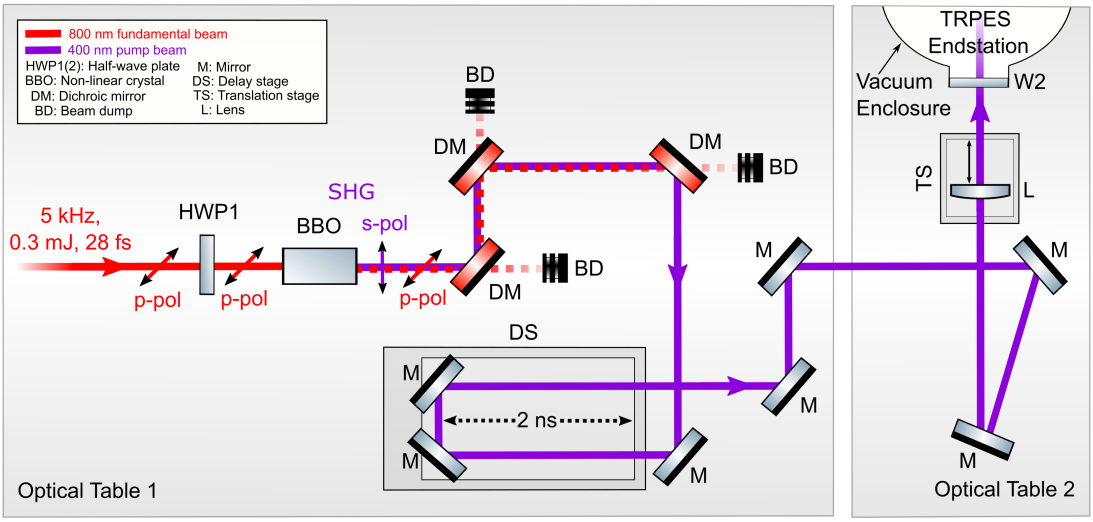

FIGURE 4.4: Schematic layout of the SHG setup and propagation of pump pulses in the configuration used in the TRPES experiments.

In the TRPES experiments, the pump beam was directed by mirrors (M) and sent through a variable optical delay linear translation stage (DS) (Newport Corp.). It was subsequently focused with a 384 mm focal length CaF_2 lens (L) into the interaction region, resulting in a typical focal spot size of 100 – 300 μm (FWHM). The lens was mounted on a three-dimensional mechanical translation stage (TS) outside the vacuum chamber to control the position and size of the pump beam with respect to the probe beam in the interaction region. The focused pump beam was sent towards the TRPES endstation through a 0.5 mm thick CaF_2 glass window (W2) that was installed at the entry point to

the vacuum chamber. The pump and probe beams were spatially overlapped on the sample in front of the entrance aperture of the electron spectrometer with a mutual angle of 1° between the beams. The pump beam intensity was attenuated by the fundamental HWP before the SHG crystal in order to prevent significant multi-photon ionisation of the sample and, thus, to reduce the vacuum space-charge effect (see Section 3.3.4) that perturbs the photoemission spectra. The pump pulse durations were broadened to sub-40 fs (FWHM) in the optical path, based on the cross-correlation measurements of the generated pump and probe pulses in the electron spectrometer (see Section 4.4.4).

4.4 High Harmonic Generation Setup

The time-delay-preserved, ultrashort, monochromatised EUV probe pulses obtained via the femtosecond laser-driven HHG process, allow ultrafast electronic dynamics to be probed using TRPES studies, as reported here. The gas-phase, non-perturbative HHG phenomenon can be robustly driven using three approaches when a strong laser field is either focused into a noble gas-filled cell, free gas jet expansion, or hollow-core fiber [271, 372, 373]. In the configuration utilised for the work reported here, the EUV generation occurs through the HHG process and the focusing of intense, 800-nm-wavelength ultrashort laser pulses (28 fs duration at FWHM) into a short cell (4 or 8 mm length) filled with argon gas. A schematic layout of the HHG setup, encompassing propagation of the generated EUV probe pulses in the TRPES experiments, is shown in Figure 4.5.

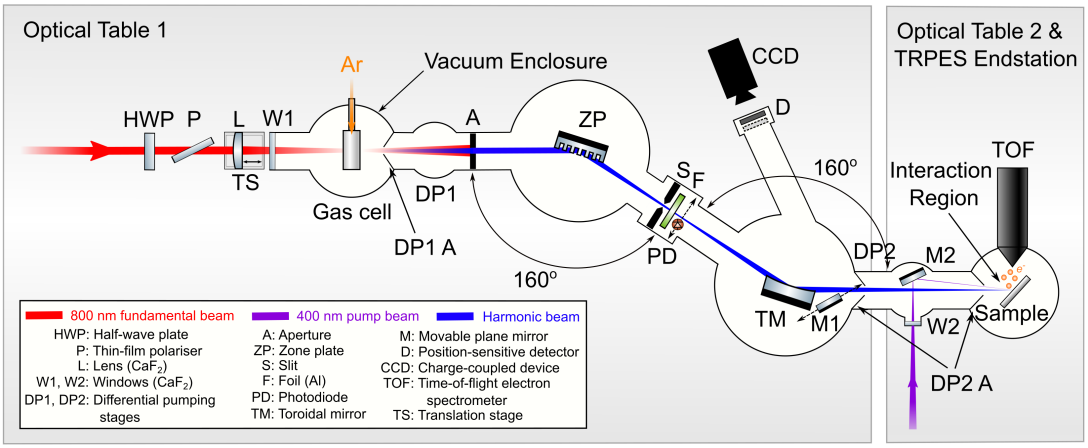

FIGURE 4.5: Schematic layout of the HHG setup and propagation of EUV probe pulses including the interaction region for TRPES experiments.

To generate the ultrashort EUV pulses, the 1.2-mJ HHG driving laser beam was directed to a in-vacuum HHG cell and vacuum monochromator system. The discussions in Section 3.2.3.2, highlight the importance of controlling the intensity, focus position, and gas pressure of the fundamental laser beam to achieve efficient HHG through phase matching. Thus, the input laser intensity was regulated using a combination of a half-wave plate (HWP) and a thin-film polariser (P) (FemtoLasers Inc.) placed before the lens (L) used to focus the laser beam into a gas-filled cell. The HWP rotation governs the ratio of the s- to p-polarised light, and thereby the portion of the transmitted laser intensity through the polariser. As a result, the spatial profile and the focal spot size of the beam essentially remain unchanged when the HHG driving laser intensity is adjusted. The linearly polarised laser pulses were focused directly after the argon-filled cell with an achromatic 600 mm CaF_2 lens. The lens was mounted on a mechanical translation stage (TS) outside the vacuum chamber in order to adjust the position of the pump beam laser focus. A 1.5 mm thick CaF_2 glass window (W1) was installed at the entry point to the vacuum chamber containing the gas cell.

The gas cell was a 4 mm long stainless steel tube with two drilled 3 mm holes, through which the laser beam was propagating. The cell holes were sealed with an aluminum foil that was pasted

around it. The cell was filled with Ar gas utilising a gas feed-through to the vacuum chamber. While the focused laser beam propagated through the cell, the inlet and outlet holes were laser-drilled into the foil to prevent gas leakage. The HHG light emerged at the exit of the cell when the laser pulse interacted with the Ar gas. During the TRPES experiments, the pressure in the Ar cell was varied between 15 to 50 mbar, depending on the desired photon flux of a specific harmonic. During such operation, the generation chamber was maintained at a residual pressure of 10^{-3} to 10^{-4} mbar. As mentioned in Section 3.2.3.2, the efficiency of the HHG output is strongly influenced by the laser input pulse energy and duration, the focusing geometry, the gas cell length and gas pressure. Optimisation of the specific harmonic yields in three critical and related dimensions, such as the laser intensity, gas pressure, and focus position for the gas cells of different length, will be discussed in Section 4.4.2.

To maintain low pressures in the subsequent vacuum chambers - with a reflective zone plate (ZP) monochromator assembly (developed and fabricated at the Helmholtz-Zentrum Berlin) and a refocusing toroidal mirror (TM) embedded inside - a differential pumping stage chamber (DP1) was employed between the HHG and next optic chambers. The DP1 chamber was separated from the HHG chamber by an aperture, allowing low pressures of the order 10^{-8} mbar to be maintained in the monochromator and TM chambers throughout the TRPES experiments. A 2 mm diameter aperture (A) was installed in front of the following reflective ZP chamber to obstruct a significant part of the divergent HHG driving laser beam, which considerably reduces potential heating and melting of subsequent 200 nm thick meshless aluminum (Al), indium (In) or zirconium (Zr) foil spectral filters (F) (Luxel Corp.). In addition, the aperture potentially minimises the number of illuminated reflective ZP grooves and the associated HHG pulse elongation.

The reflective ZP [374], housed in the third vacuum chamber, is a 7-element, $+1^{st}$-order 2D diffractive optic (laminar grating), which consists of gold-coated zone structures fabricated on a single silicon substrate of 50.8 mm diameter by e-beam lithography and reactive ion etching. In the current setup, the 7^{th} (10.85 eV), 9^{th} (13.95 eV), 17^{th} (26.35 eV), 21^{st} (32.55 eV), 25^{th} (38.75 eV), 51^{st} (79.05 eV), and 65^{th} (100.75 eV) harmonic of the fundamental frequency can be spectrally selected with the use of the reflective ZP monochromator. Specifically, by translating the reflective ZP up/down into the HHG beam and rotating the optic to reach the design input angle of the specific reflective ZP element. The reflective ZP substrate was installed on a set of motorized stages equipped with piezo-driven motors (Nanomotion Ltd. and Nanon GmbH) in order to adjust the position and reflection angles of the zone plate. The motors for the translational directions provided a positioning precision of 0.1 µm and the rotational direction had a precision of 1 µrad with a step size of 30 nm. The working principle of the ZP will be described in detail in Section 4.4.1. The majority of the fundamental beam was specularly reflected or diffracted by the reflective ZP and dumped in an aperture before the slit plane or at the slit (S), depending on which ZP element was implemented. The ultra-thin foils installed behind the exit slit of the monochromator were exchangeable depending on the selected harmonic, thus for the spectral selection of the 17^{th}, 21^{st}, and 25^{th} harmonic of the fundamental wavelength, the Al filter was used. In such a manner, the remaining part of any scattered 800 nm light that propagated along the path of the harmonic beam was filtered out. Thereafter, the HHG photon flux was detected by a removable photodiode (PD) (Hamamatsu Photonics, model G1127-04) inserted into the beam path after one of the metal foils.

The reflective ZP angularly dispersed the harmonics and the adjustable slit (S) was placed perpendicular to the plane of dispersion and along the EUV beam path in the focal plane and design photon energies of the monochromator, selecting the desired harmonic. Thereupon, the selected harmonic was redirected and refocused by a grazing-incidence gold-coated toroidal mirror (TM) into the interaction chamber, resulting in a typical focal spot size of 40 – 60 µm (depending on the slit width). The TM was mounted on a movable stage, which had three translational and three rotational dimensions of freedom inside a vacuum chamber, similar to that of the chamber housing the monochromator. Consequently, the TM position control facilitated setting the EUV beam on the sample in front of the electron spectrometer entrance aperture. The EUV beam was refocused without magnification

at 1173 mm^2 by the TM, which is equivalent to the distance between the mirror and the slit, minimising the imaging aberrations. The TM chamber includes an additional Al-coated flat mirror (M1) that was inserted into the beam path after the TM to monitor the intensity distribution in the EUV beam focus spot using a home-built position sensitive imaging detector (D). The detector was composed of a translatable double-stack multi-channel plate (MCP) and a phosphor screen, and an optical CCD camera enabling the imaging of the refocused harmonic at an equivalent propagation distance to that of the electron spectrometer. Following the passage through a second differential pumping stage (DP2) towards the PES endstation, the selected harmonic beam was sent into an interaction chamber, passing horizontally in front of the time-of-flight (TOF) electron spectrometer entrance aperture. The detailed description of the TOF spectrometer will be described in Section 4.5. The pump beam was introduced through a 0.5 mm thick CaF_2 glass window (W2) prior to the PES endstation and redirected into the interaction region by an in-vacuum Al mirror (M2) positioned aside the EUV beam before the sample chamber. Thus, the pump and probe pulses were spatially overlapped at the sample in the interaction region at a mutual angle of 1° in front of the electron spectrometer.

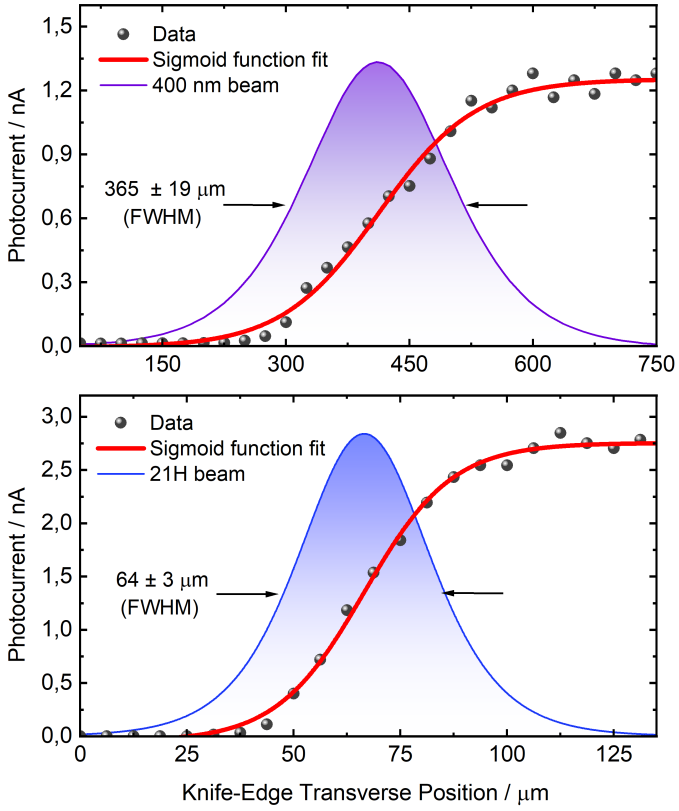

FIGURE 4.6: Transmitted power profile (grey dots) of the 400 nm pump (upper panel) and the 21st harmonic probe (bottom panel) beams fitted by the sigmoid function and encompassing the focal spot sizes to reveal the waist diameters.

The size of the focal spots of the pump and probe beams in the TRPES experiments were measured by the scanning knife-edge method, where a sharp-edged razor blade was moved across the Gaussian laser beam perpendicular to the beam using a high-precision 3D translation stage and the integral transmitted light was measured with a photodiode (Hamamatsu Photonics, model G1127-04) and ammeter (Keithley picoammeter, Series 6400). The razor blade was placed in the interaction region in front of the skimmer of the electron spectrometer instead of the sample. Assuming that the beam propagates in a direction parallel to the axis z, its waist is located at the initial coordinates (x_0, y_0, z_0), and the edge of the blade is parallel to the y-axis so that the x-axis is the "cut" direction, the transmitted

power, $P(x,z)$, detected by the photodiode as a function of the blade-edge's transverse position, x, and axial position, z, is determined by integrating the Gaussian beam profile over the entire y and x ranges.

The collected transmitted light intensity data was fitted to the complementary error function, $erfc(x)$, as described in the following:

$$P(x,z) = \frac{P_0}{2} erfc\left[\frac{\sqrt{2}(x-x_0)}{w(z)}\right],$$
$$w(z) = w_0\sqrt{1+\left(\theta\frac{(z-z_0)}{w_0}\right)^2}, \tag{4.1}$$

Here, $P(x,z)$ is a sigmoid function, where $P_0 = (\pi/2)I_0{w_0}^2$, $w(z)$ describes the z dependence of the beam radius, w_0 is a beam waist radius, θ is a beam divergence angle, and I_0 is a maximum irradiance. Figure 4.6 shows a representative signal of the transmitted power measured by the photodiode as a function of the knife-edge transverse position, resulting in a focal spot size beam diameter of 365 ± 19 µm (FWHM) for the pump and 64 ± 3 µm (FWHM) for the probe beam, respectively. The pump beam spot size must be at least twice (preferably 3 – 5 times larger) than that of the probe beam in order to ensure a one-photon excitation process in TRPES experiments and maintain the spatial and temporal overlap of the pump and probe beams on the sample.

4.4.1 Reflective Zone Plate Monochromator

In order to perform the EUV-probe TRPES experiments, a single high-order harmonic of the fundamental frequency has to be spectrally selected and refocused into the interaction region. The spectral selection is usually implemented using a monochromator. Monochromatisation and focusing of HHG light in the EUV spectral region has a number of specific requirements that must be addressed to conduct an ultrafast time-resolution spectroscopic experiment. Firstly, the monochromator should offer a sufficient energetic dispersion to isolate a spectral region of interest, in this case a single harmonic, with a strong suppression of the neighboring harmonics. Secondly, the generated divergent EUV radiation should be refocused into the interaction region with a good pointing stability. And lastly, but equally importantly, the monochromator has to ideally keep the time duration of pulses as short as during the generation process. In the present setup, the EUV light monochromatisation setup meets all of the above requirements using a single optical element: an off-axis reflective ZP.

The off-axis reflective ZP adopts a similar approach to a conventional Fresnel zone plate [376], where in the former instead of a full elliptical structure, only a peripheral fraction of the angle-of-incidence projected structure is used. The off-axis reflective ZP incorporates a focusing ability with the ability of diffraction grating to separate wavelengths depending on the incoming wavelength. A schematic view of an off-axis reflective ZP, imprinted as a projection onto a fully reflective mirror surface, is shown in Figure 4.7. Upon irradiation by the HHG source, the off-axis peripheral fraction of the ZP deflects harmonics in the $+1^{st}$ diffraction order with respect to the incidence direction and refocus as them along the optical axis due to the high off-center mean line density, thereby providing the desired angular dispersion. The specular reflection (zero-order reflection) can be separated from the energy-dispersed fraction and can be directed outside the optical axis, allowing the use of a slit in the plane perpendicular to the optical axis for energy selection.

When a HHG source with a focal spot size of ΔS hits the reflective ZP surface at a grazing angle of incidence, α, and at a distance $R_1^{'}$ from the HHG source to the center of the off-axis reflective ZP fraction, a focal spot with a size $\Delta x^{'}$ is produced at a distance $R_2^{'}$ following diffraction at grazing angle β. $\Delta x^{'}$ is correspondingly defined as:

$$\Delta x^{'} \geq \frac{\Delta S}{M}, \tag{4.2}$$

where M is the geometrical demagnification factor of the ZP, $M = R_2^{'} / R_1^{'}$. $\Delta x^{'}$ corresponds to the minimum size of the slit width of the ZP monochromator that results in an improvement of the system's resolving power, $E / \Delta E$, while M is associated with the adjustment of the beam spot size of the spectrally selected harmonic from the (real or virtual) source to the ZP image point and imposes a limitation on $\Delta x^{'}$.

The energy dispersion at the slit plane of the ZP monochromator is given by [377]:

$$\frac{\Delta E}{\Delta x^{'}} = \frac{E^2 d sin\beta}{R_2^{'} hc}, \tag{4.3}$$

where d is the grating period in the middle of the irradiated fraction of the ZP, h is the Planck constant, and c is the speed of light.

Based on the Equation 4.3 and the general grating equation, $m\lambda = d(cos\alpha - cos\beta)$, where m is the diffraction order ($m = 0, \pm1, \pm2, ...$) and λ is the radiation wavelength, the local grating period of the off-axis reflection ZP for $m = +1$ order can be defined as [377]:

$$d = \frac{\lambda}{sin\alpha}\left[\sqrt{1 + cot^2\alpha + \left(\frac{R_2^{'}}{\Delta x^{'}}\frac{\Delta E}{E}\right)^2} - cot\alpha\right], \tag{4.4}$$

In the present setup, seven reflective ZP elements are patterned as an array on a single 50.8 mm diameter substrate, designed for the spectral selection of the 7^{th}, 9^{th} harmonic (VUV region), 17^{th}, 21^{st}, 25^{th} harmonic (EUV-A region), and 51^{st}, 65^{th} harmonic (EUV-B region) of the fundamental wavelength. The arrays have a width of 4 mm and a length of 25 mm for the VUV and EUV-B regions, and 40 mm for the EUV-A region, respectively. A schematic and image of the 7-element ZP array optic, fabricated as laminar grating structures, on a crystalline silicon mirror surface are shown in Figure 4.8. The patterned silicon optic was gold-coated to improve grazing incidence reflectivity between 10.85 – 100.75 eV.

For the geometry adopted for TRPES, taking into account an estimated focal spot size of the HHG source of 100 μm (FWHM) and the distances $R_1^{'}$ and $R_2^{'}$ of 1000 mm and 350 mm, respectively, the resulting minimum useful slit width size in the focal plane of the reflective ZP monochromator, $\Delta x^{'}$, should be greater than 35 μm (FWHM). Table 4.1 summarises the geometrical (α, β) and energy

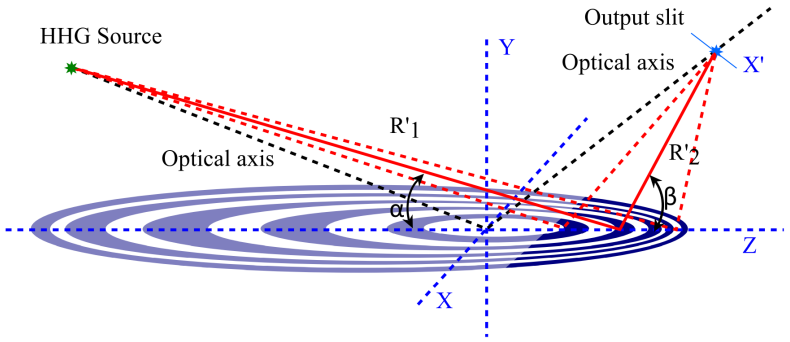

FIGURE 4.7: Schematic view of an off-axis reflection zone plate. The illuminated off-axis peripheral fraction (dark blue shading) of the full elliptical structure (light blue shading) of a typical Fresnel zone plate is used for monochromatisation of the EUV light. The odd harmonics generated by the HHG source are diffracted and then refocused by the ZP structure to different focal spot positions on the optical axis. $R_1^{'}$ represents the distance from the HHG source to the center of the off-axis fraction, where $R_2^{'}$ is the distance to the focal spot position. Reproduced figure with permission from [375] © 2014 Optical Society of America.

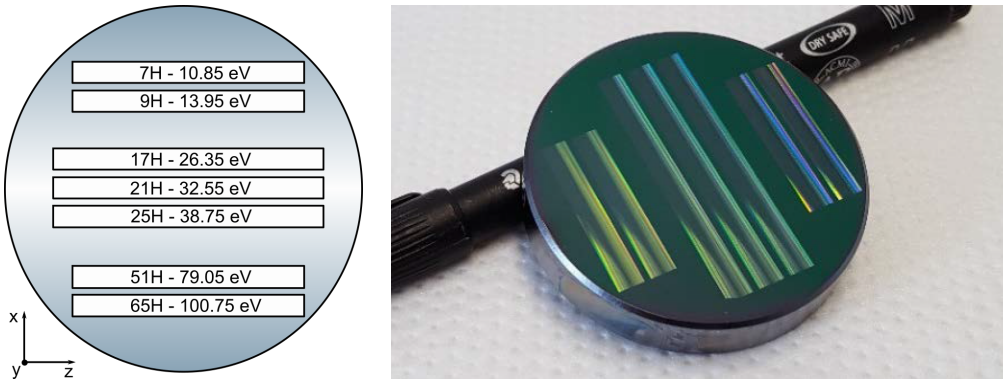

FIGURE 4.8: A schematic and image of the patterned silicon substrate of the 7-element reflection zone plate array designed for the HHG beamline in the TRPES setup. The right image was provided by Alexander Firsov.

TABLE 4.1: The geometrical and energy resolution parameters of the reflective ZP monochromator as well as the calculated meridional line periods and the optical refraction efficiency in the center of each ZP array.

ZP Array	HH Order	E / eV	α°	β°	ΔE / meV	E/ΔE / eV	d / μm	η / %
1	7	10.85	9.75	10.25	132	82.2	75.4	28.5
2	9	13.95	9.75	10.25	164	85.2	58.7	27.4
3	17	26.35	9.6	10.4	199	132.6	19.4	27.6
4	21	32.55	9.6	10.4	235	138.6	15.7	28.2
5	25	38.75	9.6	10.4	271	143.1	13.2	27
6	51	79.05	9.5	10.5	408	193.7	6.5	23.8
7	65	100.75	9.5	10.5	500	201.5	4.1	24.4

resolution parameters (E, ΔE) of the reflective ZP monochromator, the calculated central meridional line periods (d), and the optical diffraction efficiency into the $+1^{st}$ order (η) in the center of each ZP array using the HZB ray tracing program RAY-UI, which is built upon the RAY and REFLEC packages [378]. Since the time resolution in TRPES experiments is determined by the duration of the pump and probe pulses, the temporal broadening of the spectrally selected EUV probe pulse should be minimal. From the calculated values of the spectral resolving power of the reflective ZP monochromator ($E/\Delta E$), presented in the Table 4.1, the output pulse duration at the exit of the slit can be estimated as $\Delta t = \lambda^2/(\Delta\lambda c)$. For the photon energy of the 21^{st} harmonic employed in TRPES experiments in this dissertation, $\Delta t \simeq 45$ fs.

4.4.2 Optimisation of High Harmonic Generation Beamline Efficiency

For the TRPES experiments presented in this dissertation, macroscopic phase matching conditions were optimised to maximise a monochromatised harmonic intensity. The optimisation procedure included varying the gas cell length, position of the driving laser focus, generating gas pressure, and driving laser energy. The driving laser pulse duration was fixed to its minimum value in the HHG cell, 28 fs (FWHM). Two gas cells with a lengths of 4 mm and 8 mm were examined during the three dimensional optimisation. Under the given experimental conditions (see Section 4.4), the most efficient harmonic generation was achieved while placing the focus slightly outside the gas cell.

Figure 4.9 shows the change in the position of the focus, z_f, relative to the exit of the gas cell, highlighting the interaction region where the strong field ionisation and HHG can happen. Here, $z_f = 0$ is the position of the focus centered at the exit of the gas cell, which was defined using

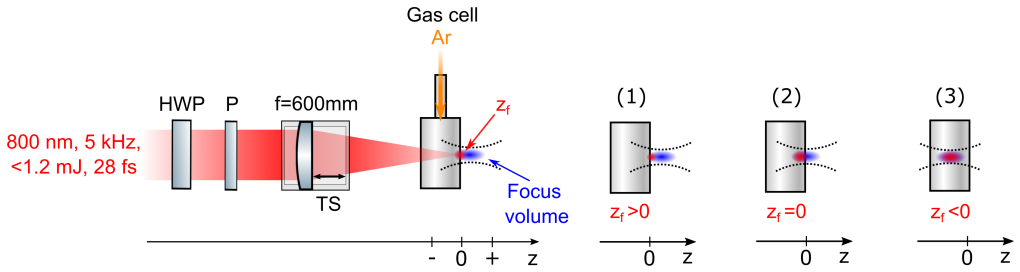

FIGURE 4.9: Schematic view of the optimisation of HHG source efficiency in the TRPES setup. z_f is the focus position relative to the gas cell, where the interaction region (red) and the laser focus volume (blue) highlighted. Three focus positions relative to the gas cell exit are outlined: focus placed beyond the gas cell (1), focus centered at the cell exit (2), and focus contained within the gas cell (3).

separate measurements using an attenuated fundamental laser beam in air and the reflection of a pickoff mirror and glass wedge placed after the focusing lens, while reflecting the focused laser beam to a CCD camera. The energy of the fundamental beam was varied from 0.76 mJ pulse^{-1} to 1.08 mJ pulse^{-1} by a half-wave plate (HWP) combined with a thin-film polariser (P). The intensity in the cell and the degree of the ionisation was further varied by moving the lens, which was mounted on a linear translational stage (TS). The collimated fundamental laser beam with a 1/e^2 beam diameter of 12 mm (FWHM), propagated on axis in the z direction. After the laser beam was focused by the 600 mm focal length lens, the resulting beam diameter was 60 μm (FWHM) with a Rayleigh range of z_R = 3.5 mm. The Ar gas inlet pressure in the cell was adjusted over a range of 5 to 50 mbar using a dosing valve. The HHG photon flux was maximised by detecting the photodiode (PD) photocurrent of a monochromatised harmonic using a Keithley picoammeter, Series 6400 (see Figure 4.5 for more details of the HHG setup design) and optimising the HHG parameters. Sequentially, the steady-state PES spectra of the generated harmonic were recorded using the ionisation of Ar gas (with the gas stagnation pressure set to produce an average sample-chamber pressure of 10^{-3} mbar) wide-angle mode (WAM) of the TOF spectrometer. In this section, the exemplary optimisation of the 17^{th} harmonic efficiency is presented.

- **8 mm Argon-filled Gas Cell Target**

The 17^{th} harmonic optimisation for the 8 mm gas cell is shown in the Figure 4.10, where the 2D colour maps represent the dependence of the TOF photoemission signal as a function of the 800-nm-laser focus position and gas cell pressure for five driving laser energies. The recorded data show that with reducing laser pulse energy, the optimum focus position decreases, and the phase matching pressure increases. The maximum yield of the 17^{th} harmonic is achieved when the focus position is placed slightly outside the gas cell ($z_f \approx 1.5$ mm, assuming the focus position is not shifted in the vacuum chamber when the Ar-filled HHG cell is pressurised), the driving laser energy is the highest value applied (1.08 mJ pulse^{-1}) and over a relatively broad range of gas cell pressures from 20 to 50 mbar. As the laser energy decreases, it is still, in principle, possible to reach the optimum harmonic yield by moving the focus into the gas cell ($z_f \leq 0$). However, the further into the cell the focus is shifted ($z_f < 0$), the less efficient the HHG process becomes. This can be attributed to reabsorption by the generating gas cell medium (see Section 3.2.3.2). An increase in the focus position, z_f, generally results in an increased HHG efficiency, while when the focus is placed inside the gas cell, the propagation length in the absorbing medium enlarges for harmonics generated before the focal spot, and they suffer from absorption. The maximisation of the harmonic yield is just a part of the whole HHG optimisation process. Notably, for the lower-order harmonics, such as the 17^{th} harmonic, and when a high driving laser peak intensity and/or gas pressure is applied, spectral

broadening, splitting, and blueshift effects are also present. This results in a significant reduction of the spectral flux density. These effects were further investigated throughout the HHG optimisation procedure, as discussed below.

The spectral splitting, broadening, and blueshift effects associated with the 17^{th} harmonic, as recorded via the photoemission spectrum of Ar gas, are shown for the 8-mm-long gas cell in Figure 4.11. The figure highlights two focus position cases, when the nominal focus is placed outside the gas cell ($z_f > 0$) at 1.5 mm (left panel), and when the focus is within the gas cell $z_f \approx$ - 4.5 mm, relative to the exit of the cell (right panel). Since the focus position was determined at low power and in air, self-focusing of the mJ-level, 28 fs 800 nm pulses in and around the Ar gas cell is expected to reduce the focal length in the HHG optimisation experiments performed in the vacuum chamber, bringing the focus into the gas cell. As demonstrated in Figure 4.11, when the focus is placed outside the gas cell (left panel), a slight spectral broadening and blueshift are observed for higher phase matching pressures, whereas it is strengthened as the focus moves into the cell (right panel).

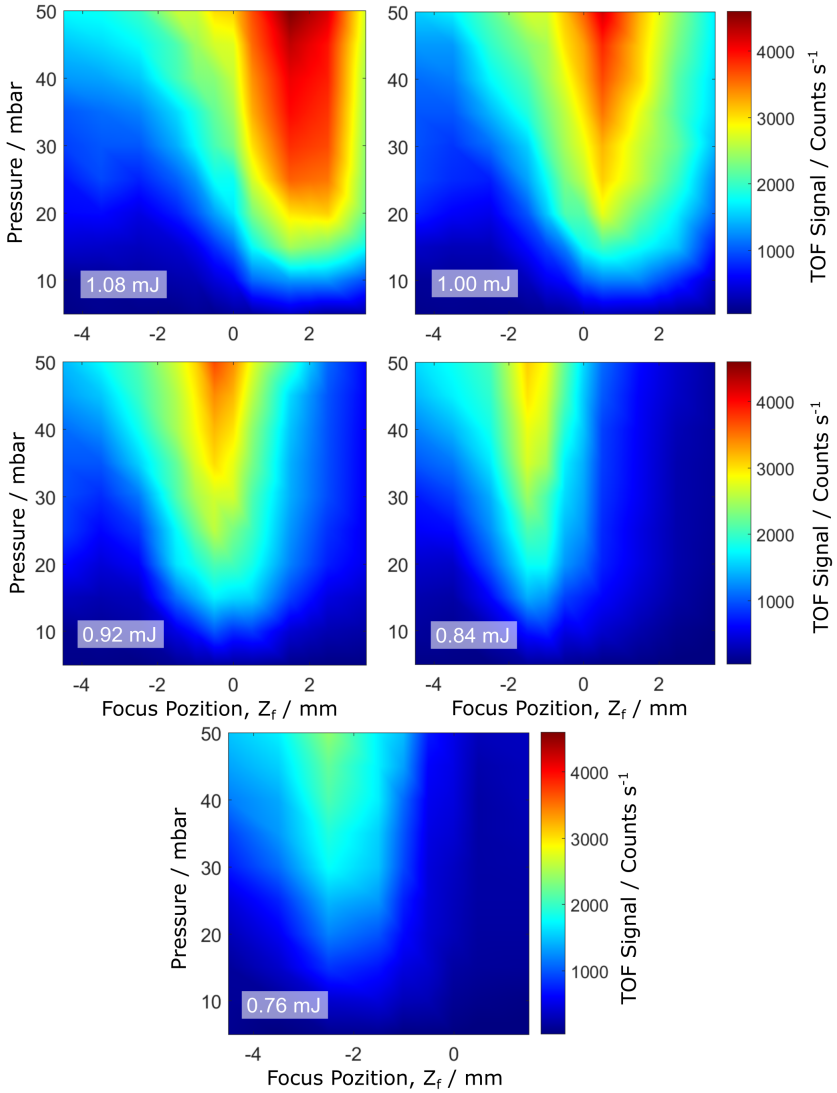

FIGURE 4.10: TOF photoemission signal of the 17^{th} harmonic produced via the photoionisation of Ar atoms. The high harmonics were generated in Ar gas for with 8-mm-long Al-foil-sealed gas cell. The data is presented as a function of driving laser energy, focus position, and gas cell pressure and was produced using an effusive Ar gas source and the WAM mode of the TOF spectrometer.

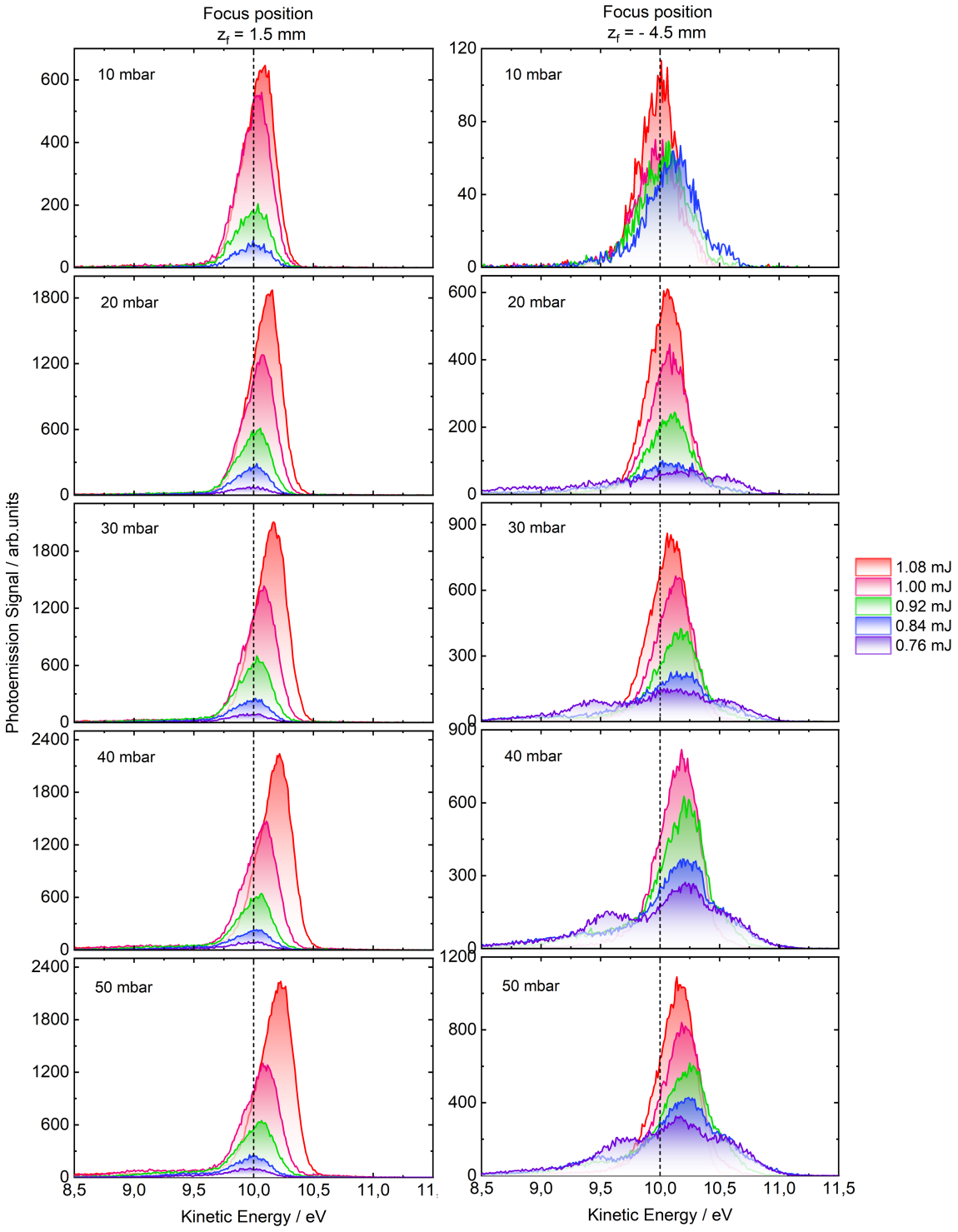

FIGURE 4.11: The adiabatic 17^{th} harmonic spectral effects observed when varying the gas cell pressure and driving laser pulse energies in a 8-mm-long, Al-foil-sealed gas cell. The displayed photoemission spectra were recorded in the WAM of the TOF spectrometer using an effusive Ar gas source.

Furthermore, with increasing driving laser pulse energy, these effects become more pronounced. In addition, the harmonic generated within the gas cell exhibits a significant spectral splitting, which is prominent at lower pulse energies. The observed spectral features can be assigned with either non-adiabatic [379–382] or adiabatic effects [383–386] in the HHG process, due to the interaction of the strong ultrashort laser pulses within the non-linear medium. The non-adiabatic effect depends on a constantly evolving laser pulse envelope that causes a time-dependent atomic phase for different electron trajectories in the total harmonic field. Thus, for laser pulses with durations less than 100 fs, non-adiabatic spectral splitting occurs. The adiabatic effect, also known as transient phase matching, is based on the impact of the varying phase contribution from the free electrons which occurs in ionising media when intense driving pulses are applied. At the rising edge of the pulse, the medium is strongly ionised, as a result, the density of free electrons depends on time and increases with every half-cycle of the driving laser. Through the monotonically changing free electrons phase, different high-frequency components are generated. Consequently, the harmonic emission is strongly chirped, leading to a spectral splitting and blueshift due to the temporal selection by transient phase matching.

While the adiabatic spectral splitting is determined by the atomic density, the non-adiabatic spectral splitting arises from the single-atomic response, which is not directly dependent to the gas pressure. The gas pressure and laser driving intensity defines the density of the free electrons, thereby affecting the phase contribution of the free electrons. Thus, the gas pressure and focus position dependence of the spectral features observed in the optimisation of the harmonic yield (Figure 4.11) can be attributed to the adiabatic effect. Zhong *et al.* [386] performed calculations on the harmonic spectra generated in ionised noble gases, supporting that the harmonic spectral lines broaden and split into a number of peaks. They assigned these spectral features to the transient phase matching effect, when the laser intensity is strong enough to ionise the noble gas.

- **4 mm Argon-filled Gas Cell Target**

The optimisation of the HHG yield for the 4 mm gas cell was carried out under the same experimental conditions as for the 8 mm cell. Figure 4.12 shows the 2D colour maps of the photoemission signal for the generated 17^{th} harmonic in the 4-mm-long, Ar-filled gas cell, depending on the driving laser focus position and gas cell pressure when changing the pulse energy of the driving laser. Similar to the optimisation with the 8 mm gas cell, by placing the nominal focus (i.e. the gas-free, low-input-pulse energy focus position) outside the gas cell ($z_f > 0$), the yield of the 17^{th} harmonic was the highest. In contrast, the further the focus shifts into the gas cell ($z_f < 0$), the more challenging it is to generate the 17^{th} harmonic. However, the region in which the 17^{th} harmonic output is most efficient narrows at high gas pressures and widens at lower pressures in comparison to the 8 mm gas cell length. That potentially allows efficient 17^{th} harmonic generation at lower gas cell pressures. At the same time, since the gas cell length was halved, the potential harmonic yield within the cell ($z_f < 0$) diminishes. However, it is found to at least equal the yield from the 8 mm cell, due to re-absorption and potential temporal walk-off effects in the longer gas cell. The optimised high harmonic photon flux of the 17^{th} harmonic generated in a 4-mm-long, Al-foil-sealed gas cell and measured in the interaction chamber in front of the electron spectrometer entrance aperture yields 4 x 10^6 photons pulse $^{-1}$. The obtained value of the photon flux per pulse is reasonable for carrying out time-resolved photoemission experiments, which allow one electron per EUV probe pulse to be detected, thus avoiding the space-charge effect (see Section 3.3.4) caused by the EUV pulse, as was previously reported in the literature [334, 387]. Therefore, the 4 mm long gas cell was chosen for HHG in the present TRPES experiments.

Although the most efficient HHG can be achieved at the rather high gas cell pressures and driving laser energies, as described earlier, this is not a criterion for the optimal spectral shape of the generated harmonics. For this reason, the HHG cell was usually operated with moderate gas pressure and driving laser energy at the optimal focus position. Analogous to the spectral features observed during optimisation of the 8 mm long gas cell, photoemission spectra of the 17^{th} harmonic, recorded in

an argon target gas, for the 4-mm-long cell exhibited similar characteristics. Figure 4.13 shows the effects of spectral splitting, broadening, and blueshift of the 17^{th} harmonic, emphasising the influence of the intense laser pulses on the ionised gaseous media. For a focus position of +1.5 mm (upper left panel), placed outside the gas cell ($z_f > 0$), there is a significant spectral blueshift at high driving laser pulse energies. At the lower pulse energies, the blueshift vanishes, although a spectral broadening signature retains. As displayed on the left panel of the Figure 4.13, for driving laser energies of 0.92 mJ pulse^{-1}, all adiabatic spectral effects are minimised. When the harmonic is generated within the gas cell ($z_f < 0$) at a focus position of -2.5 mm, a notable spectral splitting occurs at higher pulse energies (upper right panel). Apparently, for this focus position geometry and with $<$ 0.84 mJ pulse^{-1} laser pulse energies, the spectral features caused by such transient phase matching effects are minor.

In summary, in order to fulfill the conditions for both transverse spatial and transient longitudinal phase matching, it is necessary to optimise the HHG yield by varying the focus position, gas cell pressure, and driving laser pulse energy for a gas cell of optimum length for each specific HHG

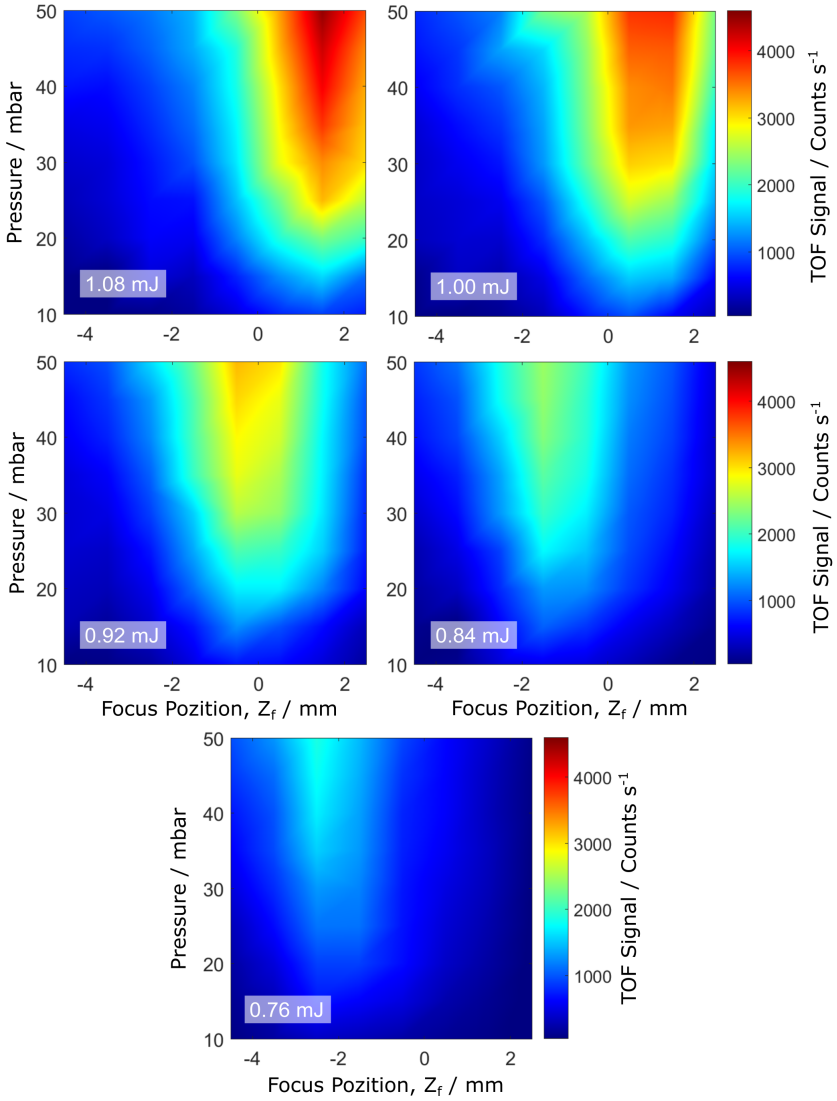

FIGURE 4.12: Ar 3p photoemission signal of the 17^{th} harmonic generated in an Ar-gas-filled 4 mm Al-foil-sealed gas cell length as a function of driving laser energy, focus position, and gas cell pressure, recorded from an effusive Ar gas source using the WAM mode of the TOF spectrometer.

setup. Previously published HHG phase-matching considerations [278] allow the optimum gas cell length to be estimated. By testing HHG cell performances with approximately these lengths and for specific harmonic emission, the properties of the harmonic radiation can be optimised for a given application. In the present HHG setup, the optimum HHG output was achieved for the 17^{th} harmonic

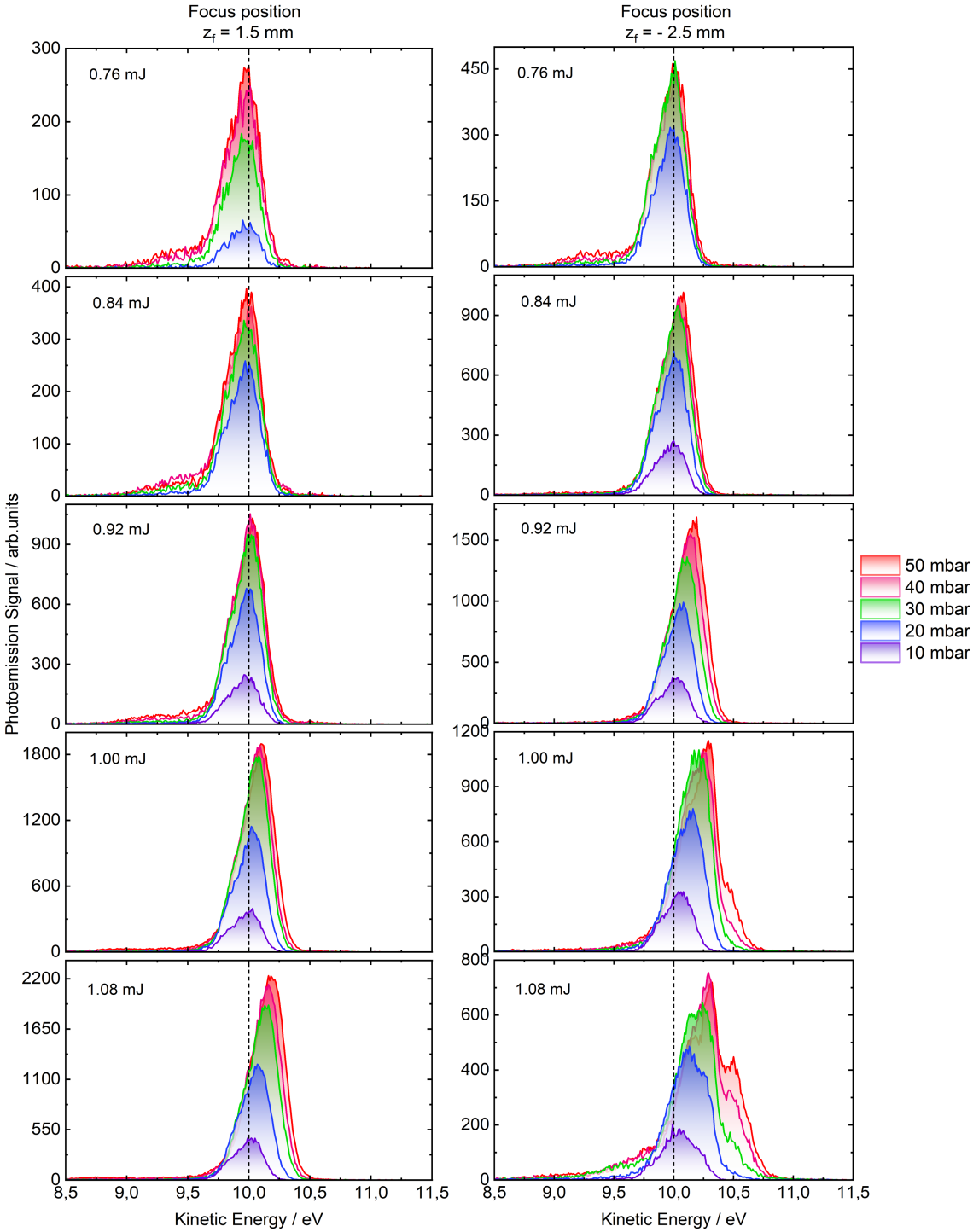

FIGURE 4.13: The driving-laser-induced adiabatic spectral effects on the 17^{th} harmonic photoemission spectra as a function of driving laser pulse energy and gas cell pressure, as generated in a 4 mm argon-filled gas cell. The displayed photoemission spectra were recorded in the WAM of the TOF spectrometer using an effusive Ar gas.

when utilising the 4 mm gas cell and focusing 0.92 mJ pulse^{-1} energies at 1.5 mm distances after the gas cell exit with 50 mbar Ar gas cell pressures. Further enhancement of the HHG process can be realised, for example, by using softer laser foci and shorter gas cells to potentially reduce the harmonic spectral bandwidth and reabsorption effects, respectively. Furthermore, higher photon energies can be accessed with higher ionisation-energy gases, such as Ne or He. The main disadvantage of using Ne and He gases with higher ionisation potentials of 21.56 eV and 24.59 eV compared to Ar, is that higher gas cell pressures are used to achieve efficient HHG [388] and the associated HHG process is significantly less efficient [389]. As a result, the higher pressures in the gas cell can overload vacuum pumps, if appropriate differential pumping setups are not engineered, and lower harmonic fluxes are generally generated compared to Ar, unless photon energies beyond $\sim$ 50 eV are required with an 800 nm HHG laser driver.

4.4.3 Photon Energy Calibration and Spectral Bandwidth of the EUV Probe Beam

The central photon energy and the spectral bandwidth of the EUV beam, as well as the total experimental energy resolution, were inferred from the steady-state EUV photoemission spectra of gas-phase argon (Ar), recorded by the TOF electron spectrometer prior to each data collection run. Here it was assumed that the natural linewidths of the valence Ar photoemission lines are negligible compared to the experimental energy resolution. Figure 4.14 shows typical results of these measurements recorded with the 21st monochromatised harmonic of the laser in the electron spectrometer drift mode (DM), the wide-angle mode (WAM), and the low-angular dispersion mode (LADM). The spectra were fitted to a sum of two Gaussian envelopes corresponding to the formation of the residual Ar^+ ion in the two lowest-energy spin-orbit cation states, 3p $^2P_{3/2}$ and 3p $^2P_{1/2}$, which have ionisation potential energies of 15.759 eV and 15.937 eV, respectively [258]. In the fit routine, the energy separation between the Gaussian peaks was fixed to the literature value of 177.5 meV of the spin-orbit splitting of the Ar^+ ground state [390], whereas their peak widths were considered to be equal. The Gaussian peak width, the peak amplitudes, and the kinetic energy position of the peak attributed to the formation of Ar^+ in the 3p $^2P_{3/2}$ state represented the fit parameters.

In the spectrometer‘s DM, a typical Ar^+ 3p individual peak width of 180 meV (FWHM) was obtained from the fit. This value is representative of the spectral bandwidth of the EUV beam, since the spectrometer resolution in the DM is of the order of 25 meV at an electron kinetic energy of 20 eV. In the LADM, the finite spectrometer resolution results in a broadening of the peak width to a value of 200 meV (FWHM), and in the WAM to 240 meV (FWHM). The extracted EUV peak width in the LADM and WAM represents the total spectral energy resolution of the TRPES experiments that implemented these lens modes. The central photon energy of the EUV beam was calibrated taking into account the following factors. First of all, the measured arrival time of the EUV pulse at the spectrometer orifice was determined through an EUV reflection to the detector from a thin Au wire and the known distance-of-flight to the detector in the spectrometer (see Equation 4.8). Secondly, since in the DM, the spectrometer operates in a field-free regime (the electrostatic lenses are switched off), the spectrometer calibration factor can be ascertained via photoemission spectral measurements with multiple gas targets with known ionisation potentials. Thereby, the gas-phase He 1s peak was used as a second gas target, in addition to the Ar 3p and 3s photoemission lines to calibrate the steady-state EUV photoemission spectra. As a result, central photon energy of 32.55 $\pm$ 0.08 eV could be determined for the 21st harmonic EUV beam by adding the literature value for the Ar ionisation potential and the kinetic energy position of the measured photoemission peak associated with the Ar^+ 3p $^2P_{3/2}$ final state. Similar calculations were performed for the Ar^+ 3p $^2P_{1/2}$ and He^+ 1s $^2S_{1/2}$ peak positions, yielding similar photon energies and defining the uncertainty on the photon energy.

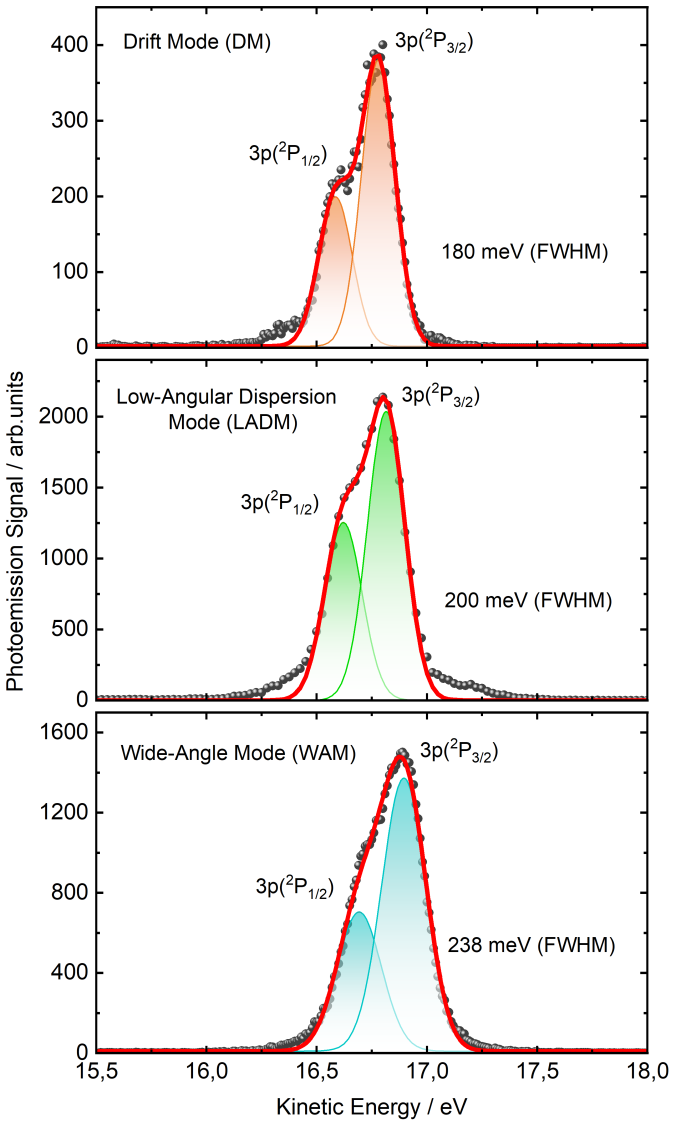

FIGURE 4.14: Steady-state EUV photoemission spectra of gas-phase argon recorded for the 21st harmonic in the drift mode (DM), low-angular dispersion mode (LADM), and wide-angle mode (WAM) of the TOF spectrometer.

4.4.4 Temporal Overlap: Cross-Correlation between Pump and Probe Pulses

The temporal overlap between the optical pump and EUV probe pulses, as well as the time resolution of the TRPES experiments, were defined from the reference cross-correlation (CC) measurements conducted with a gas-phase (Ar beam) or solid-phase (Au wire) target prior to each experiment. The CC signal is a result of the laser-assisted photoelectric effect (LAPE), which was first discovered and studied on gas-phase targets [391, 392], and was later observed in solid-phase targets [393, 394] and then extended to liquid-phase targets [395]. In this process, the simultaneous irradiation of an atom, molecule, or material by both the optical pump and EUV probe pulses alters the photoemission spectrum in the range of the photoelectrons associated with the EUV pulse only. The LAPE can be considered as the simultaneous two-color multiphoton absorption or emission of laser photons, when an electron is photoionised simultaneously by a short-wavelength EUV photon and additional long-wavelength pump pulse photons, due to a dressing of the emitted photoelectrons by the pump laser field. This leads to the appearance of side bands in the EUV photoemission spectrum, with an energy separation equivalent to the pump laser photon energy and a height determined by the intensity of the

dressing field during ionisation, which is dependent on the relative time delay. For optical pump and EUV probe pulses with a Gaussian envelope, the CC function corresponds to the spectrally integrated photoemission yield over the side bands region, recorded as a function of time delay.

In the present experiments, the CC measurements were carried out either using a Ar gas target or a 100-µm-thin Au wire, which was introduced into the interaction region and adjusted in front of the skimmer in a vacuum chamber using a high-precision 3D translation stage. The typical beam size of the pump beam was more than twice the EUV probe beam, providing a consistent spatial overlap of the two beams, and thus enabling temporal overlap and CC measurements with a high side band generation contrast. Moreover, to initiate a multiphoton transition in the CC measurements, the pump laser field intensity should be sufficiently high. Hence, pump pulse peak intensities of approximately 5×10^{12} W cm^{-2} were applied. Additionally, the CC measurements can be used to determine the pulse duration of the EUV probe beam for a given pump pulse duration. This was accomplished with the OPA, which was used to tune the fundamental wavelength of the laser output for the pump beam to 500 nm wavelength for the autocorrelation measurements. Thus, the pump pulse duration of 30 fs was measured before the interaction chamber using an autocorrelator (APE PulseCheck), equipped with a non-linear crystal and a photodiode operating in the visible spectral range.

Figure 4.15 shows exemplary cross-correlation measurements recorded for the 500 nm wavelength pump pulse and the 21st harmonic EUV probe pulse with the use of the Ar gas (upper panels) and the Au wire (bottom panels) targets, using the WAM of the spectrometer. The photoemission spectra were

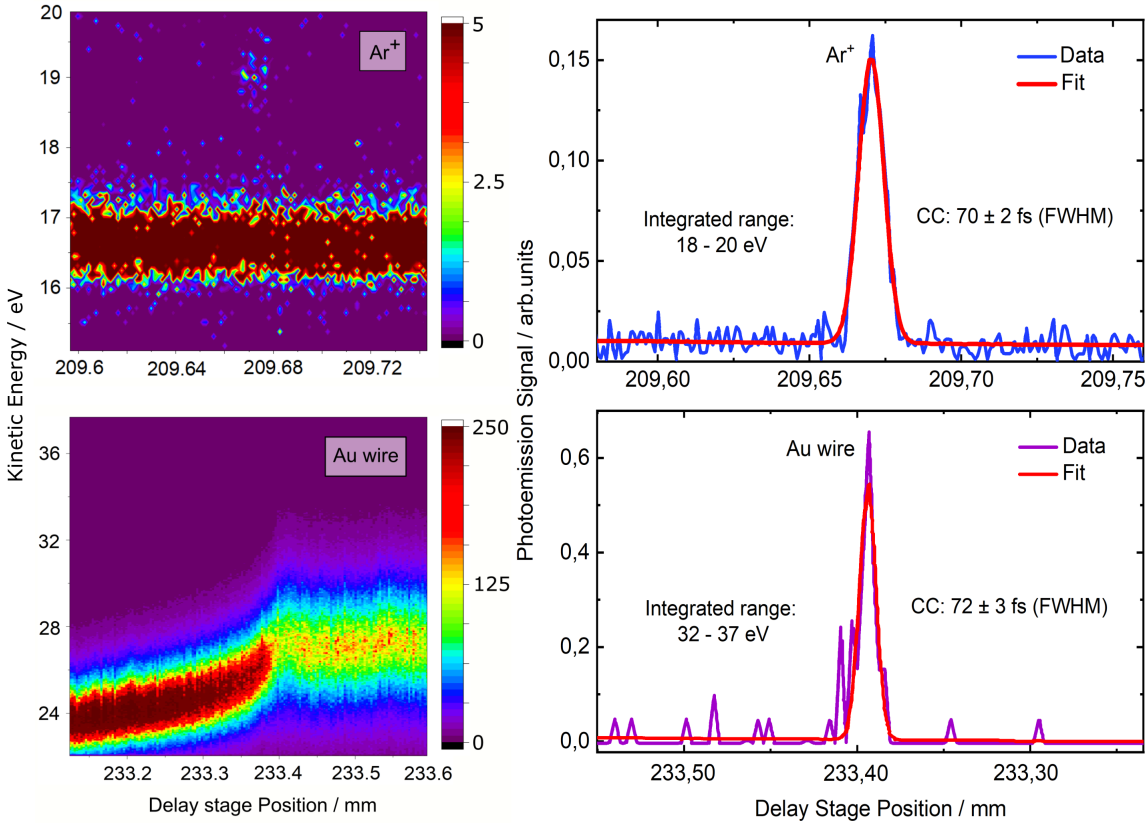

FIGURE 4.15: Cross-correlation measurements recorded for the 500 nm wavelength pump pulse and the 21st harmonic EUV probe pulse with the use of the Ar gas (upper panels) and the Au wire (bottom panels) in the WAM of the spectrometer. The pump-probe CC signal was fitted by a Gaussian function.

recorded as a function of the delay time between the pump and probe pulses. For the Ar gas target, a +1 side band occurs at a kinetic energy of 19 eV, when the two pulses overlap in time, giving rise to the CC signal of the pump and probe pulses (upper right panel). Considering that both the pump and EUV probe pulses have a Gaussian envelope, the CC signal was fitted by a Gaussian function, and by integrating the kinetic energy range between 18 – 20 eV, the CC of 70 $\pm$ 2 fs (FWHM) and the zero time position were obtained (bottom right panel). The result of the CC measurement with the use of the Au wire as a solid target was similar to the result obtained with the use of Ar gas. The temporal overlap between pump and probe pulses on the conductive Au wire additionally induces a charging, however. Thus, the zero time position and CC can be determined by mapping the charging curve at various delay time positions and integrating the photoemission signal in the kinetic energy range at the position where the slope of the charging curve reaches its maximum (upper right panel). For better visualisation of the CC signal, the kinetic energy range of 32 – 37 eV was integrated, resulting in the CC value of 72 $\pm$ 3 fs (FWHM) (bottom left panel). Taking into account the CC values obtained and the autocorrelation measurement of the pump pulse duration, the estimated EUV probe pulse duration was determined to be 42 $\pm$ 4 fs (FWHM).

4.5 Time-of-Flight Electron Spectrometer

In the TRPES experiments, the photoemission kinetic energy spectra were recorded using a commercial angle-resolved time-of-flight (TOF) electron spectrometer (THEMIS 600 EP, SPECS GmbH) equipped with a three-dimensional (x, y, t) delay-line detector (3D-DLD). The spectrometer is best suited to ultrafast spectroscopy measurements with high repetition rate pulsed light sources. The main principle of the TOF spectrometer is based on the measurement of the kinetic energy of the 3D charge cloud of photoelectrons emitted from a sample by a pulsed source and subsequently determining their precise arrival time and position at a D electron detector. The TOF spectrometer has the following advantages: single-shot measurements, simple arrangement in comparison with a concentric hemispherical analyser or cylindrical mirror analyser, possible angle-resolved PES measurements, and high energy and angular resolution [396].

In a field-free environment, the TOF electron detection technique is based on the measurement of a transit time, t, of an electron that passes a distance, l, in a differentially-pumped time-of-flight tube, free from a magnetic field, between the sample and electron detector. The electron kinetic energy is expressed as:

$$E_{kin} = \left(\frac{m}{2}\right)\left(\frac{l}{t}\right)^2, \tag{4.5}$$

where m is the mass of electron. The relative energy resolution depends on the time resolution Δt and the flight distance uncertainty Δl:

$$\frac{\Delta E_{kin}}{E_{kin}} = \left[\left(\frac{2\Delta t}{t}\right)^2 + \left(\frac{2\Delta l}{l}\right)^2\right]^{1/2}, \tag{4.6}$$

The time resolution also depends on the incident photoelectron pulse width and the electron detector performance. Generally, the absolute energy resolution depends on the measured kinetic energy of the electron and the flight distance:

$$\Delta E_{kin} = 2\left(\frac{m}{2}\right)^{-1/2} l^{-1} E_{kin}^{3/2} \Delta t, \tag{4.7}$$

The THEMIS 600 EP time-of-flight spectrometer is composed of a conical skimmer, the deferentially pumped TOF tube, a cylindrical multi-element electrostatic lens, an auxiliary (AUX) grid, the electron 3D-DLD detector equipped with two multi-channel plates (MCP), and the iris apertures with

external rotary feedthroughs. All elements must be kept under high vacuum conditions, to operate the MCPs in the electron detection system and avoid the collision of the generated photoelectrons with gas-phase atoms and molecules, changing their energy and momentum on the way to the detector. A schematic view of the analyser, including typical electron flight trajectories is shown in the Figure 4.16. The sample is placed at a distance of 663.5 mm from the 3D-DLD in front of the skimmer with an entrance aperture of 0.4 mm, which acts as the primary differential pumping aperture of the spectrometer. The TOF tube is surrounded by two layers of 2 mm thick μ-metal foil to shield the external magnetic fields down to an uncritical level, via a shielding factor of 250. The μ-metal shielding has an appreciable effect on stray magnetic fields, such as a naturally occurring magnetic field (the Earth's magnetic field). In order to compensate magnetic fields in the interaction region, three pairs of Helmholtz coils are attached to the setup and around the sample and the TOF spectrometer entrance, with the aim of reducing the magnetic field at the sample position down to $\pm$ 0.5 μT / $\pm$ 5 mG. The ten electrostatic lenses (T1 – T10) in the drift tube serve to collect photoelectrons emitted from the sample surface within the acceptance angle of the spectrometer, with the sample being at the focal plane of the lens system and imaged onto the 3D-DLD placed at the end of the lens assembly. As a result, the analyser can be operated in different lens modes that are characterised by different angular and energetic windows and associated resolutions.

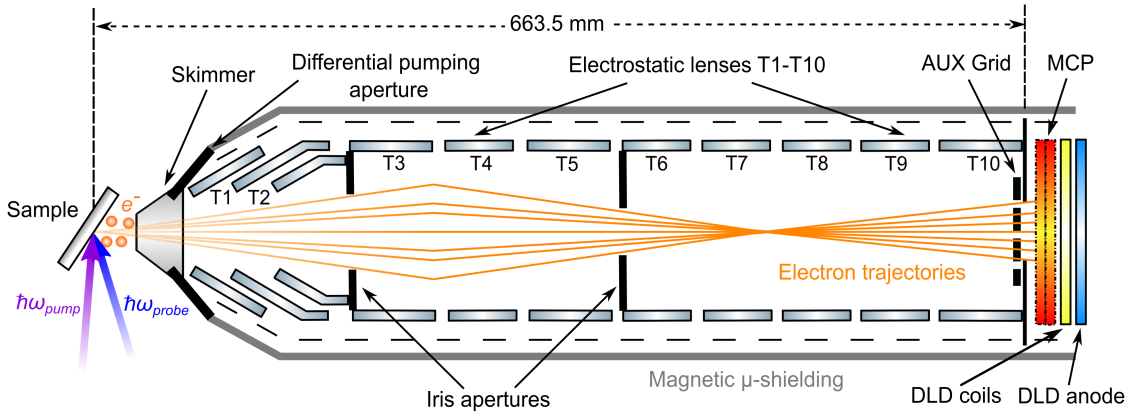

FIGURE 4.16: Schematic view of the THEMIS 600 EP TOF electron spectrometer. Adapted figure from https://www.specs-group.com/ instrument manual.

The THEMIS 600 EP TOF spectrometer can be operated with a maximum acceptance angle of $\pm$ 15° and a minimum of $\pm$ 1°. In the present TRPES experiments, the spectrometer was operated in three modes. The drift mode (DM) was applied to record steady-state (i.e. ground state) PES spectra in a wide kinetic energy range with an electron acceptance angle of $\pm$ 1° and an energy resolution of 180 meV (FWHM) at a photon energy of 32.55 eV, which includes and is limited by the EUV spectral bandwidth. The wide-angle mode (WAM) was used for high signal-to-noise ratio spectral acquisition over a narrower kinetic energy range that was sufficient to reveal the high-kinetic-energy EUV ionisation signal from the sample in the ground and transient excited states. The WAM provides a higher electron acceptance angle of $\pm$ 15°, but the kinetic energy scale in this mode is limited to a certain pass energy range and the energy resolution is typically decreased to 240 meV (FWHM). The low-angular dispersion mode (LADM), with an acceptance angle of $\pm$ 7°, as an alternative to the WAM, was used to record the ground and transient excited states spectra with the possibility of doubling the kinetic energy range in comparison to the WAM and offers an energy resolution of 200 meV (FWHM) under the implemented conditions. The switching between the different spectrometer operational modes was electronically controlled in the acquisition software associated with the analyser.

After passing through the drift tube of the spectrometer, the electrons are projected onto a position- and time-sensitive 3D-DLD (Surface concept GmbH) to amplify and detect the photoemission signal. The 3D-DLD is made up of a chevron MCP pair that amplifies the incoming pulse and an in-vacuum readout unit, which is made up of two crossed delay lines, forming a grid-like structure. It is also equipped with a low-energy cut-off filter, which consists of an AUX grid placed in front of the DLD. When negatively biased, the grid prevents a large number of slow electrons reaching the detector and exceeding the total count rate of the detection system, roughly equivalent to the laser repetition rate of 5 kHz, depending on the kinetic energy and angular distribution of the measured photoelectron distribution maximum. After amplification in the MCP pair, the electron cloud hits the delay lines at a certain position (x, y), inducing an electronic pulse that transmitted along the delay line. The pulsed signal spreads in both directions for each dimension and reaches the ends of each line with a certain delay (x_1, y_1, x_2, y_2) that depends on the electron impact position. Consequently, kinetic energies and angular distributions of photoelectrons can be determined from the arrival time and the position of electron impact at the 3D-DLD.

To measure the arrival time of the electrons with respect to the arrival time of the laser pulse in the interaction region, each end of each delay line is linked to an amplifier, a constant fraction discriminator (CFD) and a time-to-digital converter (TDC). The external start DLD signal is supplied to the TDC and data acquisition software from the laser system timing electronics. To convert the measured x,y,t-data into θ, ϕ, E_{kin} data (where θ and ϕ are orthogonal Cartesian electron emission angles), the acquisition program simulates the electron trajectories when the electrostatic lens fields are applied, enabling the conversion of the arrival time and position of the detected electrons. The raw data is correspondingly directly converted to a photoemission kinetic energy spectrum, and potentially an angular distribution, taking into account an associated ionising-laser-arrival time-zero calibration. To calibrate the time-zero of the spectrometer and to determine the electron birth times, t_0, the following procedure is applied: the distribution of arrival time of scattered EUV photons from the sample is measured at the detector, t_{photon}, taking the fixed travel time defined by the spectrometer length, l_{TOF}, and the speed of light, c, into account:

$$t_0 = t_{photon} - \left(\frac{l_{TOF}}{c}\right), \tag{4.8}$$

$$\Delta t_0 = \sqrt{(\Delta t_{photon})^2 + \left(\frac{\Delta l_{TOF}}{c}\right)^2}, \tag{4.9}$$

where Δt_{photon} and Δl_{TOF} are the uncertainties in the arrival time and scattered-photon travel length, respectively.

4.6 Overview of the UV-Vis Transient Absorption Spectroscopy Setup

For the experiments discussed in this dissertation, the TAS setup was used in a diffuse reflectance geometry. A schematic overview of the TAS setup is shown in Figure 4.17. The pump and probe pulses in the TAS experiments were generated utilising femtosecond NIR pulses from a Ti:Sapphire CPA laser system as described in detail in Section 4.1. Similar to the TRPES setup, a central fundamental wavelength of 800 nm of the laser output was divided by a beam splitter (BS) into two parts, where 0.3 mJ pulse^{-1} energies were used to generate ultrashort pump pulses at 400 nm wavelength by frequency doubling of the fundamental wavelength in a BBO non-linear crystal (see Section 4.3). The half-wave plate (HWP1) placed in front of the BBO crystal was used for optimisation of the SHG conversion efficiency by rotating the polarisation axis of the fundamental laser pulse. Subsequently, the generated 400 nm wavelength was reflected by dichroic mirrors (DM), blocking the transmitted remaining fundamental beam using beam dumps (BD).

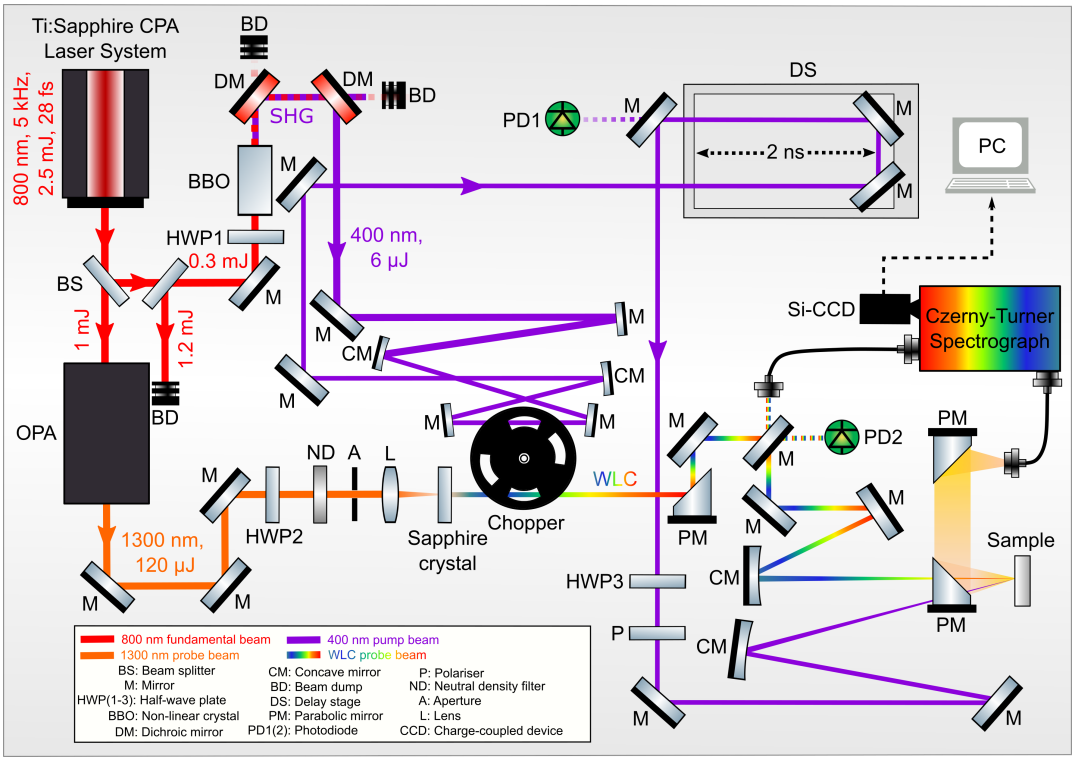

FIGURE 4.17: Schematic overview of the UV-Vis TAS setup.

The generated approximately 6 μJ pulse^{-1} energies at 400 nm were directed by mirrors (M) towards a mechanical chopper based on a brushless DC motor along with a programmable motion controller (MC2000, Thorlabs Inc.). The chopper was positioned in the path of both the pump and probe beams to ensure synchronisation of pump-probe cycles, thereby suppressing the flip-over-effect that occurs when the pump and probe phases are inadvertently mixed. The chopper unit consists of a home-built chopper wheel with 3 phases (operates with 17 duty cycles passing the chopper blades and 27 duty cycles interrupting the beam path) to detect either the pump or probe pulse, or both pulses in the TAS setup, that was operated with the 5 kHz repetition rate laser. The rotation frequency of the chopper of 41 Hz was synchronized to the trigger signal output of the laser oscillator. The spectra were recorded by the detector at a rate of 62 Hz, which receives every 81 signals from the 5 kHz laser. To ensure that the pump beam passes through the chopper wheel without contacting adjacent wheel segments, the pump beam was reduced in size by focusing it before and after the chopper using two 500 mm focal length spherical concave mirrors (CM), which acted as an optical telescope.

After passing the chopper, the pump beam traveled along a motorised-optical-delay linear translation stage (DS) (FMS300PP, Newport Corp.) that was used to vary the time delay between the pump and probe pulses in the TAS experiments with a maximum possible delay range of 2 ns and a minimum step motion of 3.3 fs. A photodiode (PD1) positioned after the DS and a partially transmissive mirror was used to monitor the presence of pump pulses at a given time. Thereafter, the pump beam was focused with a 500 mm focal length CM at a distance of 400 mm into the 2.2 mm thick, 10×10 mm^2 size solid sample, resulting in a focal spot size of 600 μm (FWHM). The pump beam intensity was varied by a half-wave plate (HWP3) and a polariser (P) placed before focusing the pulses into the interaction region. Since one of the main objectives of the TAS experiments was to study the pump-pulse-excitation-fluence dependence of the TA signal decay kinetics, the pump pulse energy was gradually changed from 0.6 μJ to 0.02 μJ pulse^{-1} at the sample focus.

The second part of the ultrashort NIR pulses delivered from the Ti: Sapphire CPA laser system output, 1 mJ pulse^{-1}, was used to generate white-light continuum (WLC) probe pulses. For this purpose, a commercial femtosecond optical parametric amplifier (OPA, Coherent OPerA Solo) was employed

to produce a pump wavelength of 1300 nm with 120 μJ pulse energies. The 1300 nm wavelength beam was sent through a half-wave plate (HWP2) and, using a neutral density filter (ND) in conjunction with an aperture (A), was focused with a 100 mm focal length lens (L) into a 3 mm-thick sapphire crystal to produce WLC probe light in a spectral range spanning 550 - 920 nm. Subsequently, after passing through the chopper, the generated supercontinuum probe pulses were directed to a parabolic mirror (PM), which focused the beam onto a photodiode (PD2) and an optical fiber that was coupled to the spectrograph. This allows continuous detection and monitoring of the probe pulses at a given time. The probe beam was focused with a 200 mm CM into the interaction region of the sample with a beam focal spot size of 300 μm (FWHM).

When the pump and probe pulses were spatially overlapped at the sample surface, the diffusely reflected probe light from the sample was routed via two parabolic mirrors (PM) that focused the beam into an optical fiber, which delivered the signal to the entrance slit of the spectrograph (Shamrock 303i, Andor, 150 l/mm grating blazed at 500 nm). The spectrograph is based on a Czerny-Turner optical design and consists of two toroidal mirrors and a diffraction grating. Thus, the incident light was collimated by the first mirror from the entrance slit to the diffraction grating, splitting it into its wavelength components, so that the second mirror focused the dispersed probe beam onto a detector. The detector is a fast silicon (Si) charge-coupled device camera (CCD, Newton DU920P, Andor, 1024$\times$256 pixels, pixel size 26$\times$26 μm) attached to the spectrometer. The camera recorded the resulting spectrum. Consequently, the diffuse reflectance spectrum of the probe pulse was recorded for every measurement. The intensity of the pump or probe pulses, as well as the background signal when both pulses are blocked by the chopper, were monitored by the data acquisition computer software (PC) in addition, while the chopper was synchronised with the detector. The change in optical density $\Delta OD\,(t,\,\lambda)$ was determined by integrating the intensities adding successive 51 shots of probe-only or pump-probe pulses for each recorded spectrum. The time-resolved measurements yielded multidimensional data sets, $\Delta OD\,(t,\,\lambda)$, with 200 acquisitions as a function of the pump-probe delay time (10 s for each delay stage position) and wavelength of the probe light.

Chapter 5

Relaxation Dynamics of Electronically Photoexcited $[Fe(CN)_6]^{3-}$ Ion Dissolved in Ionic Liquid [emim][DCA]

"I was gratified to be able to answer promptly, and I did. I said I didn't know."

— Mark Twain, Life on the Mississippi, 1883

The following people and institutions contributed to the work presented in Chapter 5. **N. Kuzkova** prepared the samples, co-designed and performed the PES, TRPES and UV-Vis absorption spectroscopy experiments, analysed the data, interpreted the results, wrote the description of results and discussion, and summary. **L. Puskar** (Helmholtz-Zentrum Berlin) performed the ATR-FTIR spectroscopy experiments. **S. Bokarev** (University of Rostock) performed the theoretical TDDFT calculations and contributed to the data interpretation. **I. Kiyan** (Helmholtz-Zentrum Berlin) conceived the PES and TRPES experiments, co-supervised the project, contributed to the data interpretation and proof-reading of the work. **I. Wilkinson** (Helmholtz-Zentrum Berlin) contributed to the preparation of the PES and TRPES experiments, supervised the data analysis and interpretation of the results.

In this chapter, the results obtained from TRPES experiments performed with the $[Fe(CN)_6]^{3-}$ transition metal complex dissolved in the [emim][DCA] ionic liquid are presented and discussed. As described in Section 2.1.5, the relaxation dynamics of the lowest-lying, electronically photoexcited ^{2}LMCT state of the $[Fe(CN)_6]^{3-}$ complex, particularly when dissolved in various molecular solvents, is much debated in the literature. Therefore, the goal of this study was the revelation of the changes of the $[Fe(CN)_6]^{3-}$ ion ultrafast photodynamics in different solvents, following 400 nm excitation. The environmentally benign 1-Ethyl-3-methylimidazolium dicyanamide [emim][DCA] ionic liquid ($C_8H_{11}N_5$) solvent was chosen as a medium to investigate the influence of the solvation environment on the $[Fe(CN)_6]^{3-}$ deactivation pathways. Since only a limited number of studies have been carried out to examine photoinduced processes in ILs so far, this study reflected several essential characteristics of ILs compared to the more frequently studied aqueous environment.

The electronic ground state configuration of the $[Fe(CN)_6]^{3-}$ complex was determined with respect to the local vacuum level using steady-state PES. The ultrafast kinetics of $[Fe(CN)_6]^{3-}$ dissolved in [emim][DCA] solution following 400 nm photoexcitation were investigated as a function of electron binding energy and pump-probe time delay using TRPES. From the TRPES experimental data analysis, aided by TDDFT calculations, it was confirmed that an intermediate quartet ligand-field, ^{4}LF, state is involved in the ^{2}LMCT relaxation. In addition, the intersystem crossing transition rates of $[Fe(CN)_6]^{3-}$ were found to be considerably faster, in comparison to in water, when the complex was dissolved in the IL environment. The experiments accordingly tackled an ongoing debate about the role of the ^{4}LF electronic excited state in the ferricyanide photocycle [91–93].

The chapter is divided into three sections. Section 5.1 is dedicated to the sample preparation and characterisation procedures, providing information on vibrational and electronic transitions in the sample using optical ATR-FTIR and UV-Vis absorption spectroscopy, respectively. Section 5.2 presents the steady-state PES results. There, the $[Fe(CN)_6]^{3-}$ valence-shell structure in the ionic liquid [emim][DCA] and the binding energy of the lowest ionisation channel - appended to electron removal from the Fe 3d (t_{2g}) molecular orbital - were determined. Section 5.3 describes the results obtained from subsequent TRPES experiments and the global analysis procedure based on the kinetic modelling of the experimental data, as well as the computational details associated with the TDDFT-based spectral simulations, describing the population of electronic excited states in the $[Fe(CN)_6]^{3-}$ / IL solution. A discussion of the influence of the solvent on the electron relaxation dynamics, based on the experimental and theoretical findings, and the key findings reported in this chapter are presented in Section 5.4.

5.1 Sample Preparation and Characterisation

The $[Fe(CN)_6]^{3-}$ ions dissolved in the [emim][DCA] ionic liquid solution were prepared using potassium hexacyanoferrate (III) $[K_3Fe(CN)_6]$ powder ($\geq$99% purity with $\leq$0.05% ferro compounds, utilised as purchased from Sigma Aldrich) and ionic liquid [emim][DCA] (>98% purity, purchased from IoLiTec). Due to the low solubility of $[Fe(CN)_6]^{3-}$ in ionic liquids containing imidazolium, a highly concentrated 0.8 M aqueous solution was prepared first by dissolving 2.6 g of $[K_3Fe(CN)_6]$ powder in 10 ml of water. Subsequently, 1 ml of this ferricyanide-water ($[Fe(CN)_6]^{3-}_{(aq)}$) solution was mixed with 2 ml of [emim][DCA] using an ultrasonic bath until a homogeneous dissolution was achieved. The water content from the mixed solution was evaporated by placing the sample mixture into a vacuum chamber at a base pressure of 10^{-5} mbar for twelve hours. As a result, $[Fe(CN)_6]^{3-}$ was dissolved in the [emim][DCA] at a 400 mM concentration. Potential residual water content and any solute-water interactions in the evaporated sample of $[Fe(CN)_6]^{3-}$ / [emim][DCA] solution were examined using the attenuated total reflection Fourier transform infrared spectroscopy technique (see Section 5.1.1). In the PES experiments, a 1 μl droplet of 400 mM $[Fe(CN)_6]^{3-}$ / [emim][DCA] solution was held within a 200-μm-thick-cooper-wire loop at room temperature, exploiting the surface tension of the highly viscous solution. The associated droplet remained uniform and did not exhibit precipitation during the experiments, due to the solution's high viscosity and the nonvolatility of the IL. The ion sample and wire loop was placed inside an interaction chamber, maintained at a high vacuum pressure of 10^{-7} mbar, and was attached to a high-precision three dimensional translation stage, enabling the precise adjustment of the droplet position in front of the electron spectrometer orifice. The sample and the spectrometer were in electrical contact with each other and were both grounded.

5.1.1 ATR-FTIR Spectra of Bare IL [emim][DCA], $[Fe(CN)_6]^{3-}_{(aq)}$ / [emim][DCA] and $[Fe(CN)_6]^{3-}$ / [emim][DCA] Solution

To confirm whether complete evaporation of the water content occurs from the initially prepared $[Fe(CN)_6]^{3-}_{(aq)}$ / [emim][DCA] mixture in a vacuum environment, measurements were performed to probe the microhydration of the vacuum dried $[Fe(CN)_6]^{3-}$ / [emim][DCA] sample. Specifically, the attenuated total reflection Fourier transform infrared (ATR-FTIR) spectroscopy technique was implemented. The measurements were carried out and the results provided by Dr. Ljiljana Puskar (Helmholtz-Zentrum Berlin). The ATR-FTIR spectra of three samples - bare IL [emim][DCA], $[Fe(CN)_6]^{3-}_{(aq)}$ / [emim][DCA] and 400 mM $[Fe(CN)_6]^{3-}$ / [emim][DCA] solution (resulted from the aqueous sample that was mixed with the IL and exposed to a vacuum environment for twelve hours) - were recorded with a Bruker Vertex 80v FTIR spectrometer in the mid-IR spectral region using the internal IR source, a KBr beam-splitter and a liquid-nitrogen-cooled MCT detector. An in-house-built sample cell, comprising a single bounce ZnSe ATR crystal, was positioned inside the spectrometer

vacuum chamber (10^{-4} mbar). A drop of sample (50 μL) was placed onto the central part of the ATR crystal and the cell was covered with the lid. The gas cell inlets and outlets were left open to the spectrometer vacuum to allow for a slow evacuation of the sample cell. The ATR-FTIR spectra were collected at 6 cm^{-1} (0.74 meV) spectral resolution over 128 individual sample scans. Corresponding background measurements were measured with the ATR clean crystal, prior to the sample measurements. The FTIR delay scanner frequency was 40 kHz, which corresponds to 22 s between the measurements.

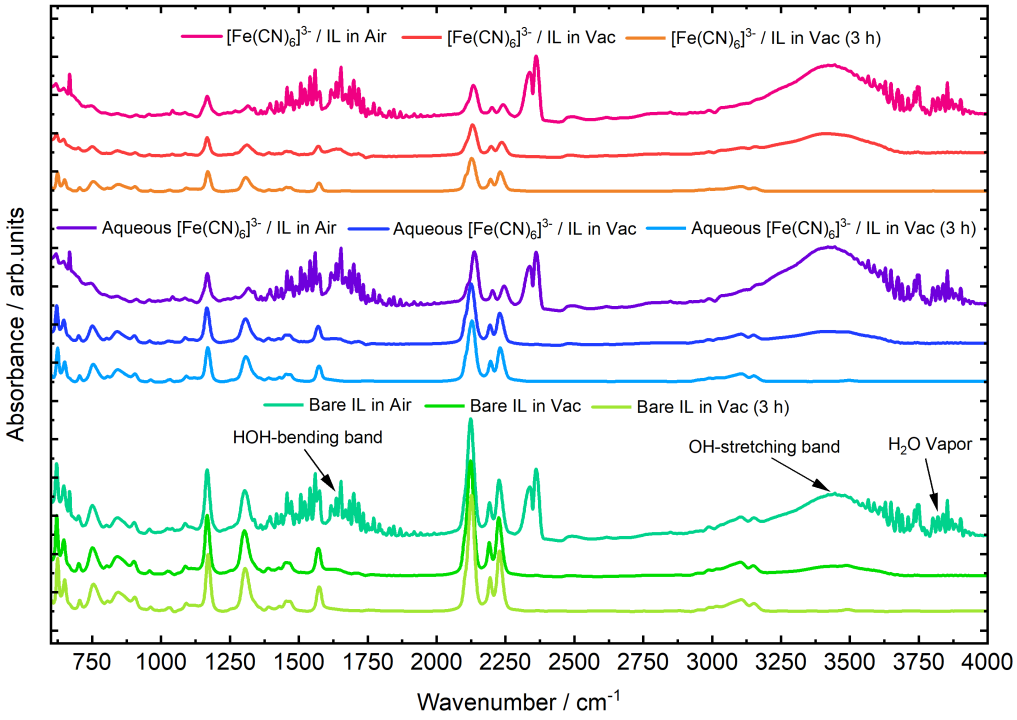

FIGURE 5.1: ATR-FTIR spectra of the $[Fe(CN)_6]^{3-}$ / IL and aqueous $[Fe(CN)_6]^{3-}$ / IL solution as well as the bare IL [emim][DCA] recorded in air, immediately after sample cell evacuation (vac), and after three hours under vacuum.

Figure 5.1 shows the room temperature ATR-FTIR spectra of the $[Fe(CN)_6]^{3-}$ / IL ([emim][DCA]) and $[Fe(CN)_6]^{3-}_{(aq)}$ / IL solution as well as the bare IL [emim][DCA] recorded in air, immediately after cell evacuation, and after three hours in vacuum. For each sample, the first spectrum was measured in air, prior to evacuating the sample cell. This measurement was used as a reference to determine the initial quantity of water in the samples of the $[Fe(CN)_6]^{3-}$ / IL (pink), $[Fe(CN)_6]^{3-}_{(aq)}$ / IL (violet) and bare IL (dark green) solution, respectively. These reference spectra display intense spectral features that appear in the regions of 1375 – 1875 cm^{-1} (0.17 – 0.23 eV) and 3625 – 4000 cm^{-1} (0.45 – 0.49 eV), associated with the absorption of water vapor. This indicates that non-evacuated samples contain a fairly large amount of water, even in the case of the bare IL sample. The bands centered around 1602 cm^{-1} (0.2 eV) and 3496 cm^{-1} (0.43 eV) in the spectra are associated with HOH-bending and OH-stretching modes of liquid water [397, 398], respectively. Other bands in the spectra correspond to the characteristic peak positions of the bare IL [emim][DCA], which are highlighted in Figure 5.2 and will be discussed in detail in the following.

From Figure 5.1 it can be clearly seen that the spectral features associated with adsorbed water vapor diminished significantly immediately after the sample cells were evacuated, with the liquid water HOH-bending and OH-stretching bands in the ATR-FTIR spectra of the $[Fe(CN)_6]^{3-}$ / IL (red), $[Fe(CN)_6]^{3-}_{(aq)}$ / IL (blue) and bare IL [emim][DCA] (green) samples all being significantly diminished. After three hours in vacuum, the exposure to the vacuum environment led to the disappearance of the OH-stretching band signal and a 100-fold reduction of the HOH-bending band, shown in the

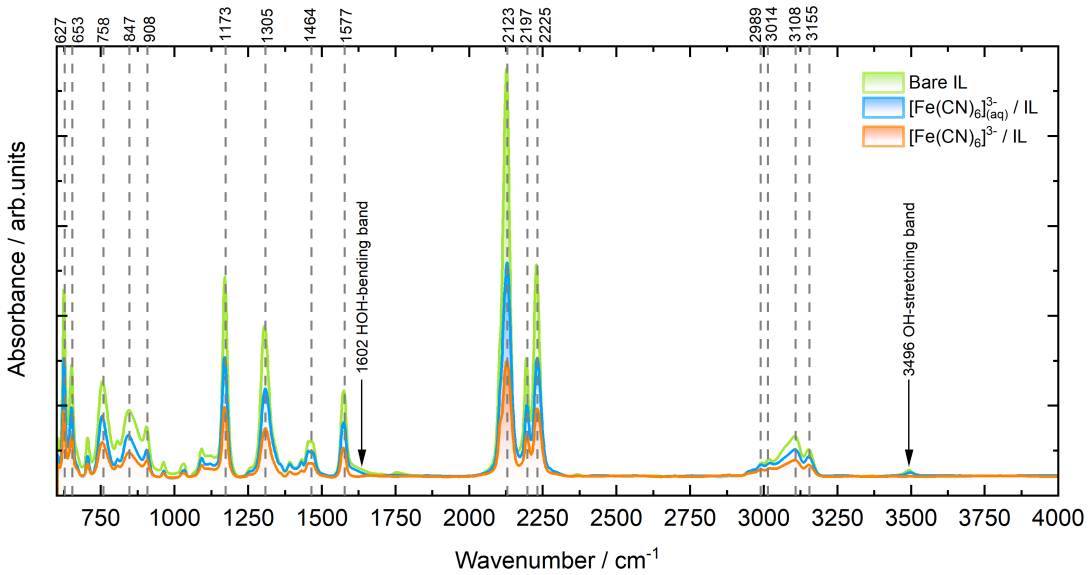

FIGURE 5.2: ATR-FTIR spectra of the bare IL [emim][DCA], $[Fe(CN)_6]^{3-}_{(aq)}$ / IL and $[Fe(CN)_6]^{3-}$ / IL solution recorded after three hours in vacuum environment. The peak positions associated with the bare IL (grey dashed lines) as well as the HOH-bending and OH-stretching modes of liquid water (arrows) are indicated in the figure.

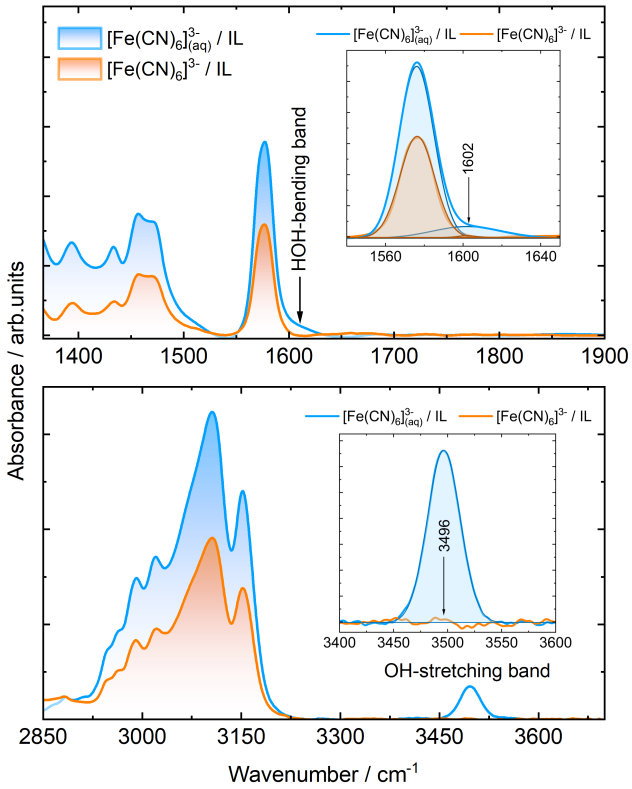

FIGURE 5.3: Magnified two regions in the ATR-FTIR spectra of the $[Fe(CN)_6]^{3-}_{(aq)}$ / IL and $[Fe(CN)_6]^{3-}$ / IL solution recorded after three hours in a vacuum environment, highlighting the suppression of the HOH-bending and OH-stretching modes of liquid water in the $[Fe(CN)_6]^{3-}$ / IL sample, which was used in the TRPES experiments. The bands associated with HOH-bending and OH-stretching modes fitted to a superposition of Gaussian envelopes are shown in the insets.

spectra in Figure 5.1. The effect of water content evaporation from the ILs in vacuum environment of $\leq 10^{-4}$ mbar is in accordance with previous temperature programmed desorption and high vacuum distillation studies in other wet materials [399]. For comparison and better visualisation, the ATR-FTIR spectra of the bare IL, $[Fe(CN)_6]^{3-}_{(aq)}$ / IL (i.e. the mixed sample solution containing water) and $[Fe(CN)_6]^{3-}$ / IL (i.e a similar sample, that had previously been placed under vacuum for twelve hours) solutions, recorded after three hours in the ATR-FTIR spectrometer vacuum environment, are presented in Figures 5.2 and 5.3. The characteristic peak positions associated with the vibrational groups of the IL [emim][DCA] (DCA anion, imidazole, alkyl group, etc.) are indicated by dashed lines in Figure 5.2, in accord with previous literature reports [400, 401].

The bands associated with the HOH-bending and OH-stretching modes of liquid water, marked with arrows, are suppressed in the $[Fe(CN)_6]^{3-}$ / IL sample (orange colour), as highlighted in the upper and bottom panels of Figure 5.3. The evaporation of water content from the sample solution and suppression of the HOH-bending and OH-stretching modes of liquid water were assessed by comparing the recorded ATR-FTIR absorbance signals of the mixed solution sample before and after it was exposed to the spectrometer vacuum environment for three hours. The absorbance peaks of the HOH-bending and OH-stretching bands of liquid water were fitted to a superposition of Gaussian envelopes to compare the water absorbance signal area between the $[Fe(CN)_6]^{3-}_{(aq)}$ / IL and $[Fe(CN)_6]^{3-}$/IL samples, as shown in the insets in Figure 5.3. As can be seen from the inset in the bottom panel, the peak associated with the OH-stretching band (3496 cm^{-1}) is completely suppressed in the $[Fe(CN)_6]^{3-}$/IL sample. In the case of the HOH-bending band centered around 1602 cm^{-1}, the signal area suppression of this band has reduced to approximately 1% relative signal area after three hours of vacuum pumping, in comparison to the signal areas associated with the initially prepared solution. Although some IR-absorption signal persists at the liquid-water bending-mode resonance, this signal cannot be associated with liquid water, specifically because no such signal remains at the less-spectrally congested, liquid-water stretching-mode resonance. In the stretching mode case, any liquid-water signal area has reduced by at least a factor of 1000 compared to the non-evacuated sample, suggesting that any residual water content, after three hours under vacuum, is at the < 30 mM level; the water concentration in the initially prepared ferricyanide/IL samples was 55 M / 2 = 27.5 M, resulting in a < 27.5 M/1000 residual water concentration after three hours of evacuation. Clearly, with the 400 mM ferricyanide, < 30 mM water, and > 10 M IL concentrations in the evacuated ATR-FTIR and PES samples, the majority of the ferricyanide molecules cannot be in contact with water and, on average, containment of ferricyanide in aqueous micelles within the IL is not possible, due to the relatively limited water content. Correspondingly, the ATR-FTIR experiments foster the conclusion that the samples used in the PES experiments, to be described below, are essentially free from residual water contributions. Additionally, one can speculate that if the evaporation of water content from the prepared sample of $[Fe(CN)_6]^{3-}$ / [emim][DCA] solution was not complete, the steady-state EUV photoemission spectrum would contain characteristic spectral features arising from water-ferricyanide micelles, which would be expected to have similar photoemission spectral signatures to aqueous ferricyanide [93, 402]. As shown in Section 5.2, this is clearly not the case.

5.1.2 Steady-state UV-Vis Absorption Spectrum of $[Fe(CN)_6]^{3-}$ / [emim][DCA]

The electronic transitions that can be photoinduced in the $[Fe(CN)_6]^{3-}$ ion dissolved in [emim][DCA] solvent were inferred from steady-state UV-Vis absorption spectroscopy measurements. Figure 5.4 shows the measured room temperature UV-Vis absorption spectrum of such solutions, as well as the associated TDDFT calculated spectrum. The experimental spectrum was measured with a potassium ferricyanide concentration of 400 mM in the [emim][DCA] solvent, using a quartz cell with a liquid path length of 0.1 mm. The spectrum was recorded using a Perkin Elmer - Lambda 950 UV/Vis/NIR spectrometer over a photon energy range of 2.2 – 4.8 eV, adopting a 4.1 meV photon energy step size.

The computed spectrum was obtained by broadening the discrete calculated absorption lines with a Gaussian temporal envelope of 0.25 eV (FWHM) for the first bright line at about 3 eV and 0.5 eV

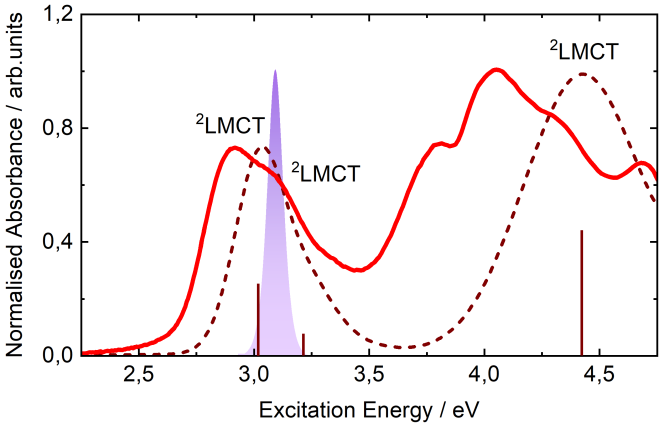

FIGURE 5.4: UV-Vis absorption spectrum of $[Fe(CN)_6]^{3-}$ dissolved in [emim][DCA] ionic liquid (red). The dashed lines represent the spectra predicted by the TDDFT calculations. The central wavelengths and amplitudes of the calculated LMCT transitions are illustrated by vertical lines. The spectral profile of the pump pulse with a central excitation energy of 3.1 eV is depicted by a violet Gaussian envelope.

(FWHM) for the two other lines at 3.2 eV and 4.4 eV photon energy. The simulated transitions associated with the three optically "bright" doublet LMCT states in the given energy range are also observed in the experimental absorption spectrum. The four absorption bands associated with ^{2}LMCT transitions in $[Fe(CN)_6]^{3-}$ dissolved in [emim][DCA] solution occur at 2.87 eV, 3.06 eV, 4.05 eV and 4.72 eV central photon energies. Vibrational sub-bands of the ^{2}LMCT transition centred around 4.04 eV, as well as two other electronic absorption bands centred around 3.82 eV and 4.30 eV that can be assigned to LF transitions, have not been computed and are therefore not present in the theory results shown in Figure 5.4. The energetic positions of the spectral bands extracted from the experimental UV-Vis absorption spectrum, corresponding to allowed electronic transitions in $[Fe(CN)_6]^{3-}$ dissolved in [emim][DCA], are summarised in Table 2.1 and are discussed in detail in Section 2.1.3.

5.2 Steady-state EUV Photoemission Study of Bare IL [emim][DCA] and $[Fe(CN)_6]^{3-}$ Dissolved in [emim][DCA] Solution

The steady-state EUV photoemission spectra of the bare [emim][DCA] ionic liquid as well as the $[Fe(CN)_6]^{3-}$ dissolved in [emim][DCA] solution were recorded with the 25^{th} harmonic in the DM of the electron spectrometer by applying the EUV probe beam alone. The central photon energy of 38.54 ± 0.02 eV and the spectral bandwidth of 210 ± 2 meV of the 25^{th} harmonic were defined by the HHG conditions, as described in Section 4.4.3.

Figure 5.5 shows the steady-state EUV photoemission spectra obtained for the 400 mM $[Fe(CN)_6]^{3-}$ dissolved in [emim][DCA] solution and bare IL [emim][DCA]. The electron binding energy scale in Figure 5.5 was calculated as the difference between the EUV photon energy and the kinetic energy of the detected photoelectrons and presented relative to the local vacuum level. The spectra display a hardly distinguishable contribution of the $[Fe(CN)_6]^{3-}$ ion to the emission yield of the $[Fe(CN)_6]^{3-}$ / [emim][DCA] solution as a result of the dominant ionisation signal from the bare IL. In particular, the HOMO band of the ferricyanide ion, associated with the occupied Fe 3d (t_{2g}) orbital, is indistinct from the spectrum of the bare IL. In contrast to the aqueous ferricyanide solution, where the Fe 3d peak is well-resolved at a 7.62 eV binding energy [83], in the IL solution, it is obscured at binding energies lower than 9 eV. Thus, the photoemission patterns from the solute ($[Fe(CN)_6]^{3-}$) can only be obtained by the subtraction of the bare [emim][DCA] solvent photoemission spectrum.

In the inset in Figure 5.5, the corresponding contributions of $[Fe(CN)_6]^{3-}$ are shown in more detail. The energy positions of the peaks corresponding to the electronic ground state configuration

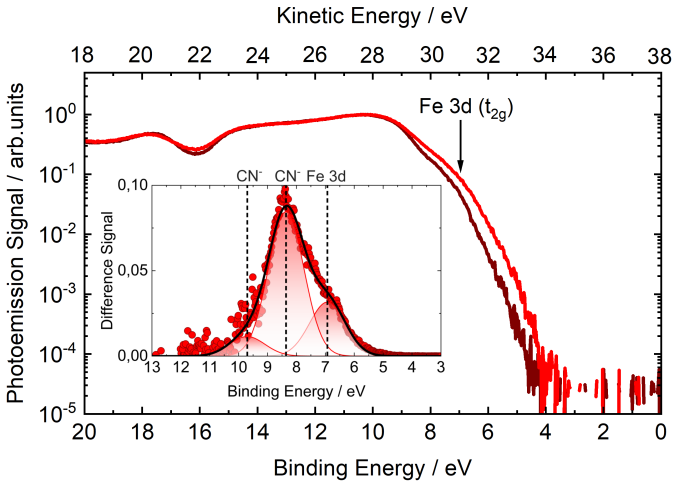

FIGURE 5.5: Steady-state EUV photoemission spectrum of $[Fe(CN)_6]^{3-}$ dissolved in [emim][DCA] solution (red line) and the bare IL [emim][DCA] solvent (brown line). The difference between the solvent and the solution spectra, highlighting the emission peaks of the Fe 3d orbital and CN^- ligands is shown in the inset. The binding energy scale is presented with respect to E_{vac}.

of $[Fe(CN)_6]^{3-}$ were obtained by fitting the solvent-subtracted signal to a superposition of three Gaussian envelopes, described by Equation 2.1. The fit result is presented by the black curve, the individual Gaussian envelopes are also indicated in Figure 5.5. As can be seen from the inset, the peak associated with the Fe 3d (t_{2g}) orbital is apparent at 6.93 $\pm$ 0.06 eV binding energy with a peak width of 1.47 $\pm$ 0.12 eV (FWHM). Two other peaks merged with the IL solute's Fe 3d peak at 8.36 $\pm$ 0.03 eV and 9.7 $\pm$ 0.13 eV binding energy are predominantly attributed to the π-orbitals of the cyanide ligands, CN^-. The corresponding widths of these peaks are 1.45 $\pm$ 0.05 eV (FWHM) and 1.45 $\pm$ 0.11 eV (FWHM), respectively. The position of the identified peaks associated with the Fe 3d and CN^- orbitals in $[Fe(CN)_6]^{3-}$ / [emim][DCA] solution will be correlated with the TDDFT calculations in Section 5.3.4.

It should also be noted that the solute peaks in the [emim][DCA] are shifted and broadened when compared to those observed in an aqueous solution [83], which can be attributed to a different effect of the IL environment on the molecular properties of the $[Fe(CN)_6]^{3-}$ ion, with respect to that in water. In ILs, the main intermolecular interactions are governed by the attractive Coulomb force between two ions of opposite charge, which generally forms ionic bond. The van der Waals and hydrogen bonding type forces are generally less involved, contrary to more ordinary molecular liquids (e.g., water). Consequently, the solvation dynamics and the electronic transition rates of the $[Fe(CN)_6]^{3-}$ ion when dissolved in the IL [emim][DCA] are expected to be different. In addition, although the steady-state as well as time-resolved PES experiments were performed with a $[Fe(CN)_6]^{3-}$ concentration that was close to the solubility limit, the Fe 3d orbital contribution to the photoemission spectra is comparatively low. The ratio of the maximum peak value of the CN^- ligands to the Fe 3d orbital ionisation yield is found to be $\sim$3 in the $[Fe(CN)_6]^{3-}$ / [emim][DCA] solution. This effect has previously been observed in the ruthenium tris-bipyridine transition metal complex dissolved in an imidazolium ionic liquid [403], where the ligand-donated π-orbitals of the metal complex had a greater contribution to the photoemission yield in the IL compared to conventional molecular solvents. Due to the low ionisation yield of the $[Fe(CN)_6]^{3-}$ ion in [emim][DCA], reported in this work, the acquisition time in the TRPES experiments had to be significantly increased by sweeping through a delay time range 20 times, with the aim of improving the signal-to-noise level of the transient signal.

5.3 Time-resolved EUV Photoemission Study of $[Fe(CN)_6]^{3-}$ Dissolved in [emim][DCA] Solution

The time-resolved EUV photoemission spectra of $[Fe(CN)_6]^{3-}$ dissolved in [emim][DCA] solution were recorded in the WAM of the electron spectrometer by applying pump and probe pulses at well-defined times. The lowest-lying doublet ligand-to-metal charge-transfer (^{2}LMCT) electronic transition occurring at a central energy of 3.06 eV in $[Fe(CN)_6]^{3-}$ / [emim][DCA] solution was excited by pump pulses of 400 nm wavelength (3.1 eV photon energy), 45 fs (FWHM) durations, 0.5 μJ pulse^{-1} energies with a corresponding pump photon flux of 10^{12} photons pulse^{-1}. The focal spot size of the pump beam was 100 μm (FWHM) at the sample. The spatial peak intensity of the pump pulse at the focus was attenuated to 1.3×10^{11} W cm^{-2} in order to prevent significant multiphoton ionisation of the sample and, thus, to reduce the vacuum space-charge effect that perturbs the photoemission spectra, as described in Section 3.3.4. After the pump-pulse-induced dynamics, the 21st harmonic of the fundamental frequency generated via the HHG process was applied at varying time delays to probe the electron density distribution. These EUV probe pulses, with a central photon energy of 32.55 $\pm$ 0.05 eV, had a spectral bandwidth of 250 $\pm$ 3 meV. The monochromatised EUV probe beam had a 80 μm (FWHM) focal spot size, a 50 fs (FWHM) pulse duration, and a photon flux of 10^6 photons pulse^{-1} in the sample interaction region. This corresponded to a probe pulse spatial peak intensity of 2×10^6 W cm^{-2}. The orientation of the linearly polarised pump and probe pulses were both set to be collinear to the electron spectrometer time-of-flight axis. The time delay between the pump and probe pulses in the interaction region was scanned between – 400 fs to + 2.5 ps with a step size of 13 fs by tuning the optical delay stage in the pump beam path.

5.3.1 Transient Photoemission Spectra of $[Fe(CN)_6]^{3-}$ / [emim][DCA] Solution

The 2D colour map representing the transient photoemission signal from the 400 mM $[Fe(CN)_6]^{3-}$ dissolved in [emim][DCA] solution, recorded as a function of electron binding energy and time delay between the pump and probe pulses, is shown in Figure 5.6. The colour bar in the figure highlights the relative magnitude of the photoemission yield. The electron binding energy scale in Figure 5.6 is energy referenced to the local vacuum level. For better visualisation of the excited state ionisation signal from the $[Fe(CN)_6]^{3-}$ solute, the EUV-only photoemission spectrum recorded at negative time delays and averaged over the range between – 400 fs and – 200 fs was subtracted as a background spectrum from the pump-probe photoemission spectra. Due to a shift of the time zero position during the measurements, the corrected time delay axis of the background subtracted transient photoemission spectrum spans the range between – 215 fs and + 2.1 ps. The transient photoemission spectrum is presented over the binding energy range of 4.1 – 8.5 eV. In addition, the photoemission spectra recorded at the beginning and end of the time-resolved measurement sets are presented in Figure B.1 (Appendix B) to demonstrate that the $[Fe(CN)_6]^{3-}$ dissolved in [emim][DCA] solution was not chemically altered by the optical pump and EUV probe pulses on the timescales of the TRPES measurements. In Figure 5.6, the background subtraction gives rise to negative values of the transient signal at positive time delays, that are associated with a partial depletion of the electronic ground state population of $[Fe(CN)_6]^{3-}$, as induced by the pump pulse. Since ionisation from both the Fe 3d and CN^- ligand molecular orbitals of $[Fe(CN)_6]^{3-}$ contributes to the photoemission yield, the negative transient signal can be seen at binding energies above 5 eV (see Figure 5.5). However, as shown in Figure 5.6, such a negative transient signal is compensated by the positive signal from ionisation of the transient excited states at binding energies and time delays where these states significantly contribute to the total photoemission yield.

At short time delays in the $\pm$ 100 fs range, there is a distinct feature in the transient photoemission spectra over the entire binding energy range that is attributable to a strong contribution from the cross-correlation (CC) signal. As described in Section 4.4.4, this temporal overlap between the pump

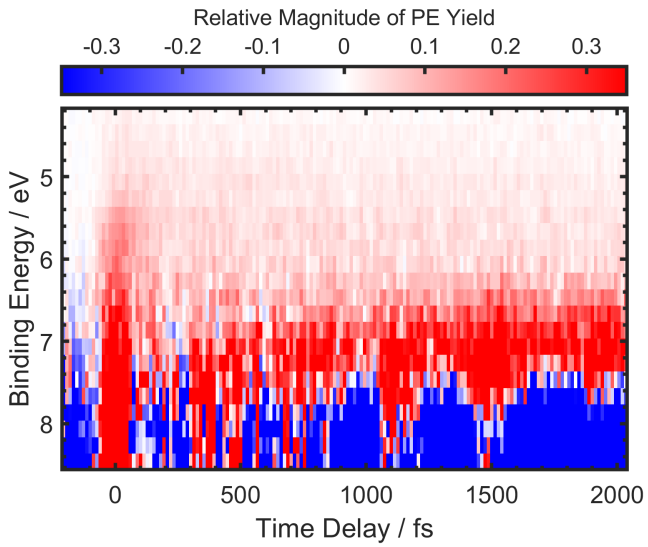

FIGURE 5.6: 2D colour map of the transient photoemission signal as a function of the electron binding energy and pump-probe time delay for $[Fe(CN)_6]^{3-}$ dissolved in [emim][DCA] solution. The time-independent background signal recorded at negative pump-probe delays has been subtracted from the measured data.

and EUV probe pulses, as well as the EUV pulse durations, can be determined using a gas- or solid-phase target. In the present work, a 100 µm-thin Au wire was introduced into the interaction region instead of the sample prior to TRPES experiments to define the zero time-delay and time resolution of the experiment. Thus, the experimental time zero position and the CC signal were determined by recording the transient photoemission spectra of the Au wire at negative and positive time delays within the - 300 fs to + 300 fs delay time range. By integrating the recorded signal across the binding energy axis where the pump and probe pulses overlap in time, and fitting the result by a Gaussian envelope, the CC width was obtained. Figure 5.7 shows the time dependence of the transient signal recorded for the 2^{nd} harmonic pump pulse and 21^{st} harmonic probe pulse with the conductive Au wire target, as recorded in the WAM of the spectrometer. The yielded symmetric CC width of 89 $\pm$ 6 fs (FWHM) constituted a high time resolution in the TRPES experiments performed with the $[Fe(CN)_6]^{3-}$ / [emim][DCA] solution.

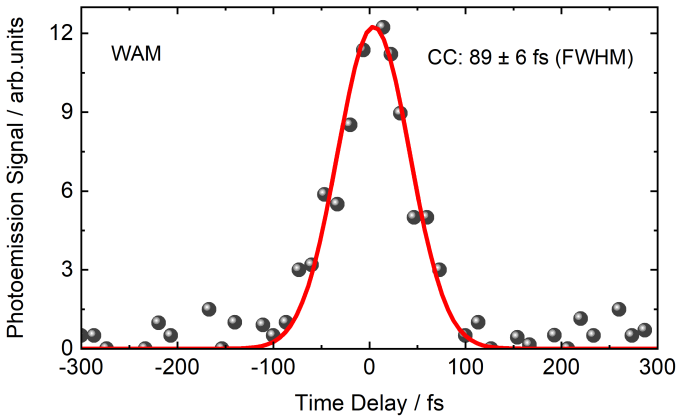

FIGURE 5.7: Transient photoemission signal recorded as a function of pump-probe delay and integrated over 4 – 5 eV binding energy range (grey circles), recorded from an Au wire in the WAM of the spectrometer. The fit to the CC trace with a Gaussian envelope yielded a CC FWHM of 89 $\pm$ 6 fs (black line).

The transient signal in Figure 5.6 - which is prominent immediately after the CC at positive time delays and is present in the sub-picosecond delay and lower binding energy region (5.2 – 6.2 eV) - dissipates within a few hundred femtoseconds. In the higher binding energy ranges, 6.5 – 7.5 eV, a distinct long-lived positive transient signal persists for much longer time delays, appearing as a band with a central binding energy of approximately 7.2 eV. In addition, the clearly-displayed negative transient signal (ground-state bleach) remains constant with increasing pump-probe time delay. This is apparent in the 7.5 – 8.5 eV binding energy range, where photoemission from the excited states is not visible. This feature indicates that the total lifetime of the electronically excited states is long with respect to the interrogated delay ranges, and that the relaxation to the ground state is relatively slow in $[Fe(CN)_6]^{3-}$ / [emim][DCA] solution. This perspective is supported by the presence of the long-lived 7.2 eV band. It is noted that the positive feature appearing on top of the negative transient signal, specifically after the CC in the higher binding energy 7.5 – 8.5 eV range, is an artifact caused by the applied auxiliary grid voltage at the MCP detector, which is necessarily applied during the TRPES experiments performed with the WAM of the spectrometer to avoid saturating the 3D-DLD.

5.3.2 Kinetic Model and Global Fitting

The transient signal shown in Figure 5.6, was analysed using global fitting to a kinetic model that describes the population of the involved electronic states. Prior knowledge of the photocycle of the involved electronic transitions in the studied system is a necessity for the correct modeling and interpretation of the experimental TRPES data. Based on previous studies [93, 402] and TDDFT calculations, which will be discussed in detail in Section 5.3.4, the kinetics of $[Fe(CN)_6]^{3-}$ dissolved in [emim][DCA] solution following 400 nm optical excitation was interpreted using a four-state kinetic model with sequential population of the electronic states. According to this model, the following description of the photoinduced electron dynamics was proposed. 400 nm optical excitation leads to population of the two lowest ^{2}LMCT states by a dipole-allowed transition from the doublet ground state (GS). The major population resides in the lowest-lying ^{2}LMCT state due to the larger associated oscillator strengths. Subsequently, the lowest-lying ^{2}LMCT state undergoes ultrafast intersystem crossing process and populates the quartet ligand-field (^{4}LF) state followed by electronic relaxation to the vibrationally-hot excited ground state or its adjacent low-lying degenerate doublet ligand-field (^{2}LF) states, from which, slower vibrational cooling occurs. These transitions are collectively referred to as leading to GS*, as they cannot be distinguished because of the similarity of their electronic structure and proximity in energy.

The corresponding photocycle of $[Fe(CN)_6]^{3-}$ dissolved in [emim][DCA] solution, represented in terms of a four-state kinetic model with the sequential population of the involved states, can be expressed as:

$$\mathrm{GS} \xrightarrow{P(t)} {}^2\mathrm{LMCT} \xrightarrow{k_1} {}^4\mathrm{LF} \xrightarrow{k_2} \mathrm{GS}^* \xrightarrow{k_3} \mathrm{GS}, \tag{5.1}$$

where k_{1-3} denote the rate constants that characterise the sequential transitions to the ^{4}LF state, GS*, and GS, respectively. *P(t)* is the time-dependent excitation rate of the ^{2}LMCT state from the GS, described by a Gaussian temporal envelope of the pump pulse, $P(t) \propto \exp(-t^2/\sigma_{pump}^2)$, where σ_{pump} is the pump pulse width.

The corresponding system of differential equations describing the electron population dynamics has the form:

$$\begin{aligned}
\frac{d[\mathrm{GS}]}{dt} &= -P(t)\cdot[\mathrm{GS}] + k_3\cdot[\mathrm{GS}^*] \\
\frac{d[^2\mathrm{LMCT}]}{dt} &= P(t)\cdot[\mathrm{GS}] - k_1\cdot[^2\mathrm{LMCT}] \\
\frac{d[^4\mathrm{LF}]}{dt} &= k_1\cdot[^2\mathrm{LMCT}] - k_2\cdot[^4\mathrm{LF}] \\
\frac{d[\mathrm{GS}^*]}{dt} &= k_2\cdot[^4\mathrm{LF}] - k_3\cdot[\mathrm{GS}^*]\,, \qquad (5.2)
\end{aligned}$$

where $[Q]$ denotes the population of state Q (Q = ^{2}LMCT, ^{4}LF, GS*, or GS) and k_{1-3} are the kinetic rate constants, which were treated as fit parameters.

Figure 5.8 shows the 2D colour maps representing the transient photoemission signal data from the 400 mM $[Fe(CN)_6]^{3-}$ dissolved in [emim][DCA] solution. The data is shown in the upper panel, the result of the global analysis is shown in the middle panel (see Section 3.5.1) and the corresponding residuals are shown in the lower panel. To compare the fit result with the background-signal-subtracted experimental data (Figure 5.6), the fitted photoemission spectrum of the ground state, $S_{GS}(E)$, was subtracted from the $TS(E,t)$ matrix at each data vector on the time delay axis. The residual 2D colour map (lower panel in Figure 5.8) was calculated via the global fit routine, which minimised the reduced χ^2 value between the 2D array of the experimental transient data and the fit result. Within the implemented model, the global fit procedure finds the best-fit parameters that describe the kinetics of the involved states through a least equal quality fit. The optimised, extracted reduced χ^2 value was 0.503.

In Figure 5.8, it is possible to select two binding energy regions (indicated by black dashed lines), where the positive transient signal can be assigned to the fast and slow kinetics of the electron population in $[Fe(CN)_6]^{3-}$ / [emim][DCA] solution. The time dependence of the transient signal was binding energy integrated over different ranges associated with the fast (5.2 – 6.2 eV) and slow (6.5 – 7.5 eV) dynamics and is presented in Figure 5.9. The figure shows experimental data and fit results of the transient signal decomposed into the individual contributions from the involved electronic states, which was obtained from the global fit to the kinetic model described by Equation 5.2. Panel (a) shows the transient photoemission signal integrated over the 5.2 – 6.2 eV binding energy range, where after the CC signal (yellow dashed line), the fast relaxation of the initially populated lowest-lying ^{2}LMCT (red line) and ^{4}LF (purple line) states occur on a sub-picosecond time scale. The ultrafast biexponential decay of the excited electronic state population was previously reported in an aqueous solvent by Engel *et al.* [93], which was assigned to the intersystem crossing transition from the photoexcited ^{2}LMCT state to the ^{4}LF state within 170 fs, with a subsequent decay on the order of 730 fs.

In Figure 5.9, panel (b) highlights the buildup of population in the long-lived GS* (green line), which results in a positive transient signal at a higher 6.5 – 7.5 eV binding energy range, and is observed up to the 2.1 ps maximum measured pump-probe delay time applied in the experiments. This result is in agreement with the transient mid-IR absorption spectroscopy studies in water, D_2O and ethylene glycol environments reported by Ojeda *et al.* [91], where the population of a vibrationally excited level of the ground state of $[Fe(CN)_6]^{3-}$ was found to occur within approximately 10 ps. Panel (c) in Figure 5.9 shows the transient population densities of the excited electronic states, $[Q^*(t)]$ (Q = ^{2}LMCT, ^{4}LF, GS*, GS), described by the kinetic model (see Equation 5.2) as function of pump-probe time delay. The curves associated with each of the rate constants, k_{1-3}, as obtained from the global fitting and the cumulative temporal profile, are shown. The population of the GS (blue line) is given relative to its initial value, at large negative time delays. Because of the depletion of the initial state population, the GS population in Figure 5.9 is of negative value at positive time delays. The global fitting results reproduced in Figure 5.8, in conjunction with the energy-integrated transient

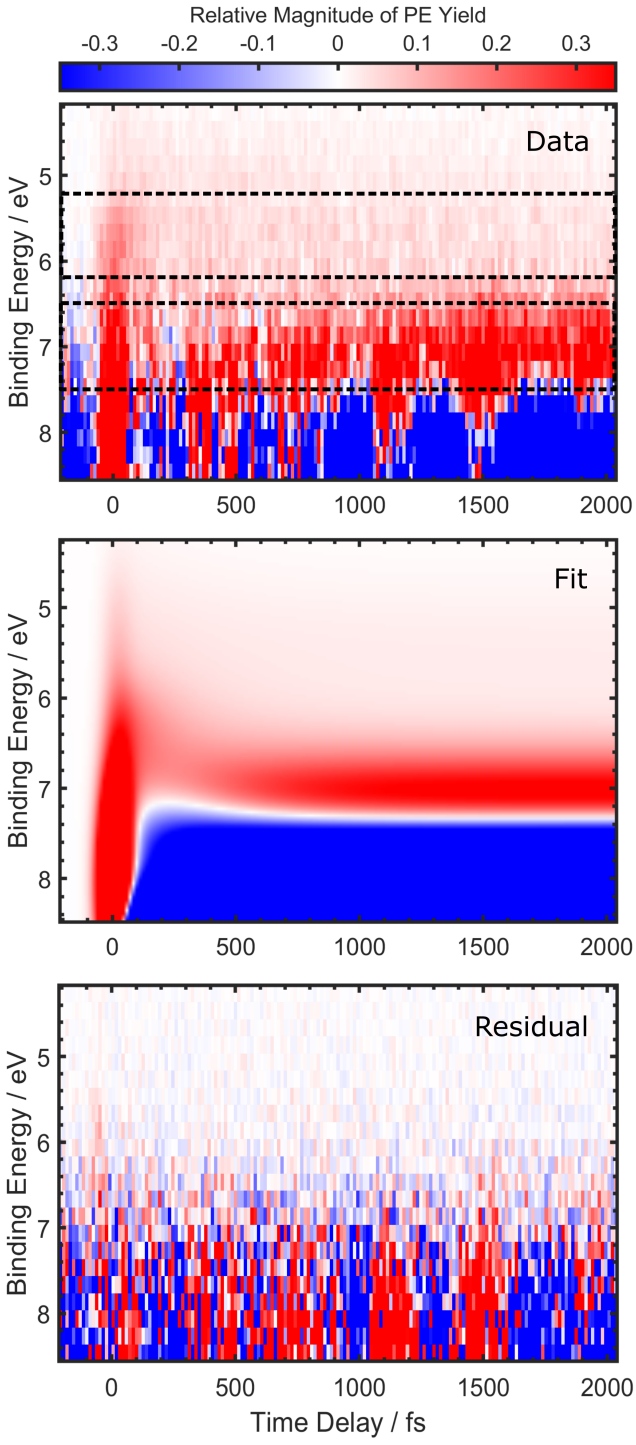

FIGURE 5.8: Data and global fitting reproduction of the experimental transient photoemission spectra for the 400 mM $[Fe(CN)_6]^{3-}$ anion dissolved in [emim][DCA] solution, as obtained with the use of the kinetic model described by Equation 5.2. The residual data was extracted from the converged result of the global fitting procedure.

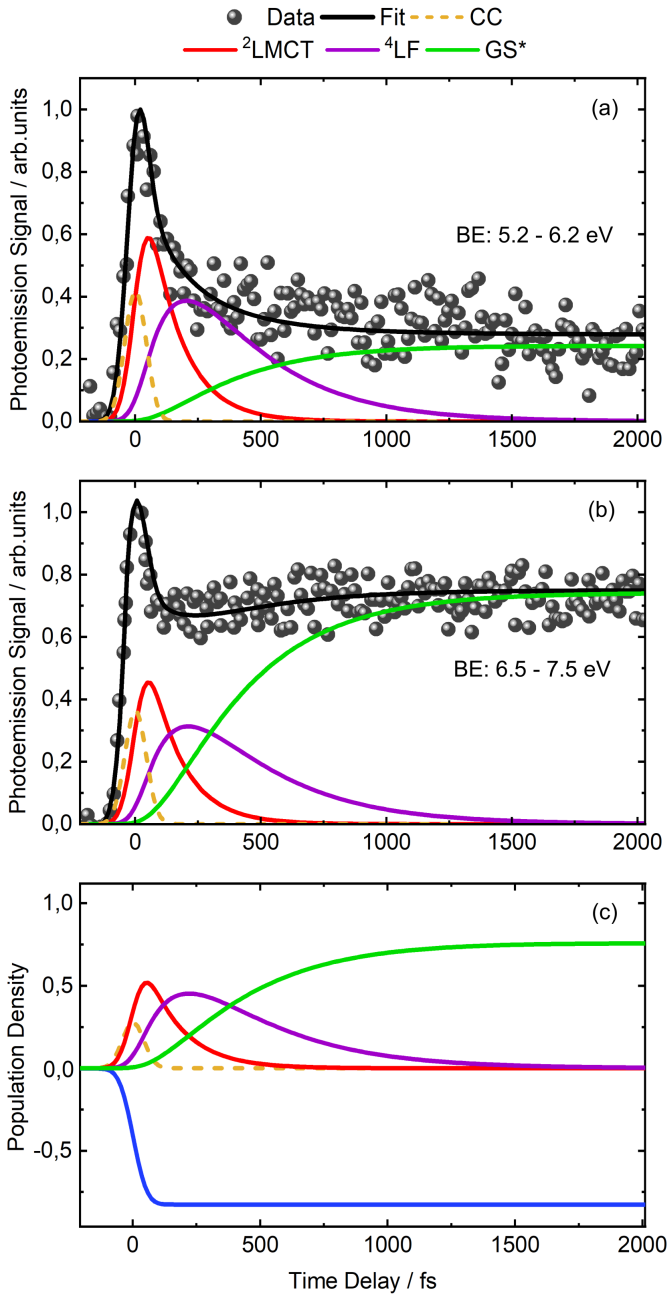

FIGURE 5.9: The time dependence of the transient signal integrated over the 5.2 – 6.2 eV binding energy range, encompassing the fast dynamics, is shown in panel (a) and the analogous results integrated over 6.5 – 7.5 eV binding energy range, encompassing the slow dynamics, is shown in panel (b). The negative contribution to the transient signal, due to depletion of the ground state, is not presented in panels (a) and (b). Panel (c) shows the transient population densities of all four electronic states involved in the kinetic model described by Equation 5.2, including the negative GS depletion, as extracted from the global analysis.

signals shown in Figure 5.9, demonstrate a good agreement between the experimental data when the four-state sequential population kinetic model is implemented.

Table 5.1 summarises the kinetic parameters for $[Fe(CN)_6]^{3-}$ dissolved in [emim][DCA] solution, as obtained from the global fitting. The inverse values of the rate coefficients, k_{1-3}, are presented as the decay time constants, $\tau_{1-3} = 1/k_{1-3}$. The decay time constants correspond to the sequential decay from ^{2}LMCT $\rightarrow$ ^{4}LF (τ_1), ^{4}LF $\rightarrow$ GS* (τ_2), and GS* $\rightarrow$ GS (τ_3), respectively. The error bars given in the table refer to the numerical results extracted from the global fitting. The GS* $\rightarrow$ GS transition, assigned to the time constant τ_3, occurs on a much longer time scale than probed in the transient photoemission experiments. Therefore, in Table 5.1, the lowest limit of the fit results, which corresponds to the maximum measured time delay range applied in the experiments, is presented. The exact value of the time constant τ_3 could be determined through extension of the delay time span to a range of approximately 100 ps in the time-resolved photoemission experiments. Since the present work was focused on revealing the early-time ultrafast dynamical processes of $[Fe(CN)_6]^{3-}$ dissolved in [emim][DCA] solution, the long-time dynamics of this molecular system would be the subject of separate studies.

TABLE 5.1: Kinetic parameters obtained from the global fitting of the transient photoemission spectra of 400-nm-excited $[Fe(CN)_6]^{3-}$ dissolved in the [emim][DCA] ionic liquid.

Parameter	Value
τ_1 (^{2}LMCT $\rightarrow$ ^{4}LF)	$142\ ^{+8}_{-7}$ fs
τ_2 (^{4}LF $\rightarrow$ GS*)	$332\ ^{+47}_{-50}$ fs
τ_3 (GS* $\rightarrow$ GS)	> 2.1 ps
P(t)	0.14 ± 0.01
σ_{pump}	50 ± 3 fs
σ_{probe}	43 ± 2 fs

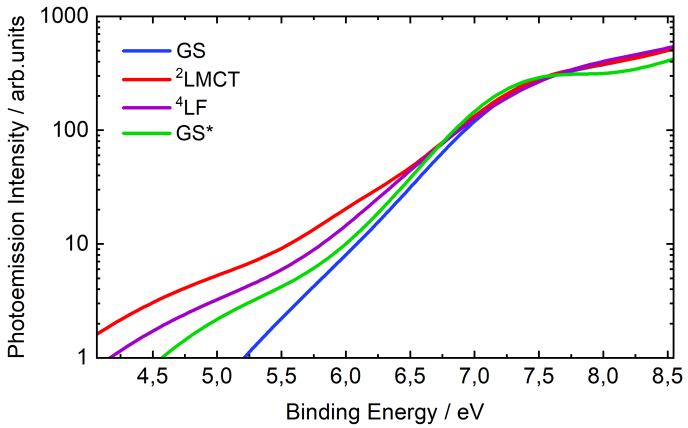

FIGURE 5.10: State-associated photoemission spectra of the electronic states extracted from global analysis of the photoemission spectra for $[Fe(CN)_6]^{3-}$ dissolved in [emim][DCA] solution, following excitation at 3.1 eV photon energy.

The state-associated spectra, $S_Q(E)$, of the involved electronic states, extracted from the global analysis to the photoemission spectra, are shown in Figure 5.10. The fit parameters of the Gaussian temporal envelopes used to represent the binding energy amplitudes in the global fitting are listed in Table A.1 in Appendix A. These fit parameters were obtained using Equation 3.74. As can be seen from Figure 5.10, the state-associated photoemission spectra exhibit a similar spectral distribution of the involved ground and excited states. For better visualisation of the signals, the vertical axis in

the state-associated spectra is presented on a logarithmic scale. The photoemission spectrum of the GS obtained from global analysis highlights the ionisation of the HOMO band of the $[Fe(CN)_6]^{3-}$ ion, associated with the occupied Fe 3d (t_{2g}) orbitals as well as the CN^- ligand orbitals above 7 eV. This result coincides with the $[Fe(CN)_6]^{3-}$ valence-shell electronic energetics determined from the experimental steady-state PES spectra in Section 5.2. The excitation with a pump pulse at 3.1 eV photon energy produces transient features associated with the excited ^{2}LMCT, ^{4}LF and GS* at lower binding energies compared to the GS signals. The spectral contributions from the ^{2}LMCT and ^{4}LF states, with sub-ps lifetimes, are dominant at binding energies of approximately 4.5 – 6.5 eV, as observed in the experimental transient data. The long-lived transient component associated with the GS* contributions is less pronounced at lower binding energies as compared to the ^{2}LMCT and ^{4}LF states. However, a spectral band of the GS* becomes prominent at the binding energy of $\sim$ 7 eV. According to the global fit results, this state has a lifetime > 2.1 ps. The solvent-dependent lifetime of GS* is in the range of a few to tens ps and has previously been reported in the UV pump – mid-IR probe TAS and UV pump – EUV probe TRPES studies of Zhang *et al.* [92] and Ojeda *et al.* [91].

5.3.3 F-test Validation of Kinetic Modelling

The role of the intermediate ^{4}LF state in the relaxation dynamics of the $[Fe(CN)_6]^{3-}$ anion following 400 nm optical excitation to the lowest-lying ^{2}LMCT state has been actively discussed [91–93]. Hence, the results obtained from the kinetic modelling should be validated. Thus, in addition to the global analysis of the transient photoemission data, an F-test [404] of the kinetic modelling was performed. In order to confirm the presence of two fast decay time constants, τ_1 and τ_2, associated with the population and subsequent decay of the ^{4}LF state, a simplified 3-state kinetic model was introduced, where the photoexcited ^{2}LMCT state decays directly to the GS*. By comparing the global fitting results using the kinetic model described by Equation 5.2 (named as the extended model below) with the simplified model, the statistical goodness of fits can be determined.

The photocycle of $[Fe(CN)_6]^{3-}$ dissolved in [emim][DCA] solution, represented in terms of a simplified 3-state kinetic model, can be expressed as:

$$\mathrm{GS} \xrightarrow{P(t)} {}^2\mathrm{LMCT} \xrightarrow{k_1^s} \mathrm{GS}^* \xrightarrow{k_2^s} \mathrm{GS}, \tag{5.3}$$

where k_1^s and k_2^s are the rate constants that characterise the sequential transition to GS*, and the decay of GS* to GS, respectively.

The three-state system of differential equations describing the electron population dynamics has the following form:

$$\begin{aligned} \frac{d[\mathrm{GS}]}{dt} &= -P(t)\cdot[\mathrm{GS}] + k_2\cdot[\mathrm{GS}^*] \\ \frac{d[{}^2\mathrm{LMCT}]}{dt} &= P(t)\cdot[\mathrm{GS}] - k_1\cdot[{}^2\mathrm{LMCT}] \\ \frac{d[\mathrm{GS}^*]}{dt} &= k_1\cdot[{}^2\mathrm{LMCT}] - k_2\cdot[\mathrm{GS}^*]\,, \end{aligned} \tag{5.4}$$

where $[Q]$ denotes the population of state Q (Q = ^{2}LMCT, GS*, or GS).

The two models - with number of data points n and number of fit parameters p_s and p_e corresponding to the simplified and extended kinetic models, respectively - can be statistically validated by calculating the F-test value:

$$F = \frac{(\mathrm{RSS}_s - \mathrm{RSS}_e)}{\mathrm{RSS}_e}\frac{(n-p_e)}{(p_e-p_s)}, \tag{5.5}$$

where RSS_s and RSS_e are the residual sums of squares obtained from the fit to the simple and extended models, respectively.

The improvement of the extended model can be tested by calculating the F-test value and comparing it to the critical value of the F-distribution:

$$F_c = F(p_e - p_s, n - p_e), \tag{5.6}$$

The F-test validation was performed using the implicit global analysis procedure (Section 3.5.1) with the fit function, described by Equation 3.75. For a given set of rate constants k_i, the matrix $[Q]^*$ is defined by the numerical solution of the differential equations 5.2 and 5.4, respectively describing the population dynamics of involved states for the extended and simplified models. The fit procedure checks if the 2D array of the experimental transient signal, TS_{exp}, matches the population by minimising the χ^2 value:

$$\chi^2 = \| TS_{exp} - S_Q \times ([Q]^*)^T \|^2 , \tag{5.7}$$

Each element of the matrix S, apart from the transition rate constants and the cross-correlation width, σ_{CC}, was treated as a fit parameter. Thus, four fit parameters k_1, k_2, k_3, σ_{CC}, and the $4 \times N$ elements of matrix S were applied in the global fitting procedure using the extended model. In the simplified model, three fit parameters k_1, k_2, σ_{CC}, and the $3 \times N$ elements of matrix S were correspondingly used. The difference in the number of fit parameters was $p_e - p_s = 1 + N$.

Figure 5.11 shows the fit results of the transient photoemission signal from the $[Fe(CN)_6]^{3-}$ dissolved in [emim][DCA] solution, as obtained using the extended 4-state kinetic model (panel (a)) and

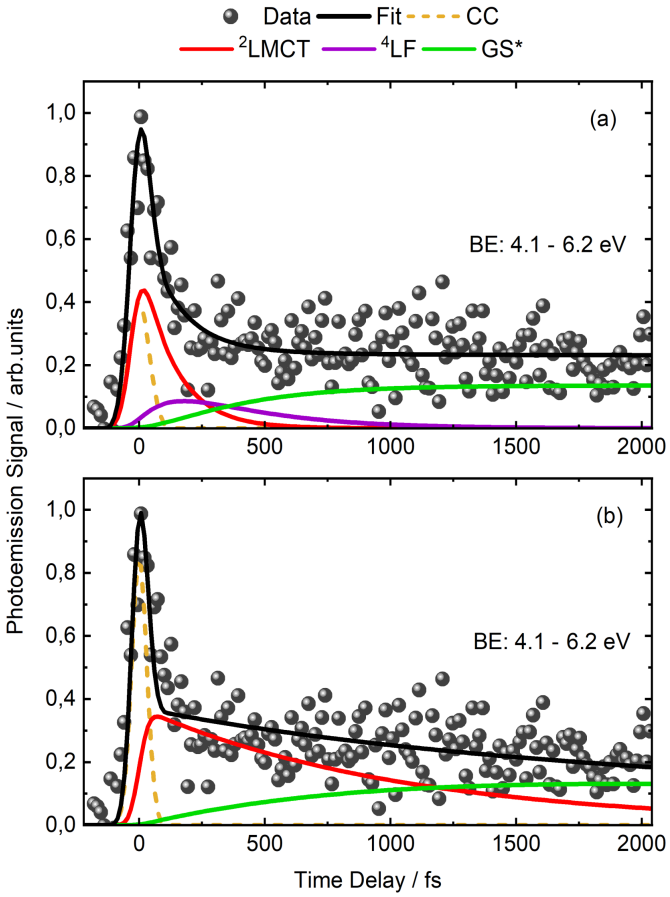

FIGURE 5.11: The time dependence of the transient signal integrated over the 4.1 – 6.2 eV binding energy range, as obtained by employing the matrix formalism of the global analysis, as used in the F-test procedure. The population dynamics of the excited states involved in the extended, panel (a), and simplified, panel (b), kinetic models are described by the differential Equations 5.2 and 5.4, respectively.

simplified 3-state kinetic model (panel (b)). Both kinetic models employed the matrix formalism of the global analysis, integrated over the binding energy range $4.1 - 6.2$ eV, associated with the fast dynamics of the excited states. The transient signal fit results were decomposed into the individual contributions from the electronic states considered in the models and are shown in the figures. The number of experimental data points, N, on the energy scale is 77, whereas the total number, $N \times M$, of data points in the fitted range is 12777. From Equation 5.5, an F-test value of 2.038 was obtained. The smaller value of the residual sums of squares extracted for the extended model is statistically significant if the F-statistics exceed a critical value, F_c. For a confidence factor of 99.9%, with the use of Equation 5.6, the critical value F_c (78, 12777) = 1.5714 was calculated. The F-statistics exceed the critical value and, thus, the simplified model can be rejected with a statistical confidence $> 99.9\%$.

5.3.4 TDDFT Calculations and Discussion

To assist with the analysis of the TRPES experimental data, time-dependent density functional theory (TDDFT) calculations were implemented using an implicit solvation model. The calculations were performed and provided by Dr. Sergey Bokarev (University of Rostock). For comparison with the $[Fe(CN)_6]^{3-}$ dissolved in [emim][DCA] solution data, the quantum-chemistry calculations were also carried out for the $[Fe(CN)_6]^{3-}_{(aq)}$ solution data presented in the studies of Raheem [402].

The TDDFT calculations were performed using the optimally-tuned, range-separated LC-BLYP functional [405] with the aug-cc-pVTZ basis set [406, 407]. The use of such density functionals allows the reliable prediction of the energies of CT transitions in transition metal complexes [408]. The range-separation parameter was determined prior to the inclusion of implicit solvation to avoid respective errors. [409] In the calculations given here, the same value of 0.27 bohr^{-1} for the range-separation parameter was used as implemented in the work of Engel *et al.* [93]. The solvent environment was accounted for by using the implicit SMD solvation model [410], which is also critical for stabilising the complex ion's high negative charge. The standard parameters [410] were chosen for the water solvent. The following parameters were used to simulate the [emim][DCA] IL system: static and optical dielectric constants of $\varepsilon = 11.00$ [411] and $\varepsilon_\infty = 2.3498$ [412], surface tension 66.07 $\text{cal}\cdot\text{mol}^{-1}\text{Å}^{-2}$ [412], and the H-bond acidity and basicity, as well as carbon aromaticity and electronegative halogenicity were set to 0.229, 0.265, 0.2308, and 0.0, [413] respectively. The values of the H-bond acidity and basicity for the "generic" IL [413] were adopted in this work.

As discussed in Ref. [93], the geometry for the doublet ground state of $[Fe(CN)_6]^{3-}$ (low-spin d^5 system) was optimised, resulting in the D_{3d} point group symmetry. The lowest quartet state equilibrium geometry has D_{4h} symmetry. All calculations were performed using the GAUSSIAN 16 package [414]. Consequently, the electronic structure calculations for $[Fe(CN)_6]^{3-}$ in the ground and lowest excited doublet and quartet states, as well as for the ionised species, $[Fe(CN)_6]^{2-}$, in the singlet, S, triplet, T, and quintet, Q, states, in both the [emim][DCA] and H_2O solvents, were carried out using an implicit solvation model. This model cannot capture all of the features of [emim][DCA] solvation, such as inhomogeneity and domain-formation in the ionic liquid [122, 123]. However, it provides valuable guidance for evaluating the associated solvent effects at the most basic level.

The TDDFT calculations presented in this work, follow on from and further strengthens the aqueous-phase interpretation suggested by Engel *et al.* [93]. To estimate the shifts of the potential energy surfaces along the vibrational coordinates, in addition to the Fe–CN symmetric stretching, Huang-Rhys factors [415] for the lowest singlet, triplet, and quintet states of the ionised aqueous-phase species ($[Fe(CN)_6]^{2-}$) were determined, as shown in Figure 5.12. These factors, especially for the quintet states, are very large (>15), emphasising that the implemented shifted harmonic oscillator model is not applicable in these cases. However, the results still allow an estimation of which vibrational modes are involved in the reorganisation upon photoionisation. In fact, the largest contributions are observed from modes 4 – 6 (NC–Fe–CN scissor deformation modes, frequencies 131, 139, and 154 cm^{-1}), 10 – 12 (asymmetric and symmetric Fe–CN stretching 388, 388, and 393 cm^{-1}) and mode 21 (CN wagging 519 cm^{-1}). According to the Huang-Rhys factor analysis within a shifted harmonic

oscillator model, as well as symmetry considerations, a number of fully-symmetric a_{1g} tuning and e_g coupling modes have been identified [93]. The most prominent shift of the potential energy minima is observed along the "breathing" (symmetric stretching) Fe–CN vibrational mode. Therefore, the qualitative interpretation presented here is exclusively based on this mode.

Figure 5.13 shows the computed 1D cuts through the potential energy surfaces of $[Fe(CN)_6]^{3-}$ along the a_{1g} Fe–CN stretching mode with ground state harmonic vibrational frequencies of 387 cm^{-1} and 393 cm^{-1} for the [emim][DCA] and H_2O solvation cases, respectively. Here, the states of the unionised species are classified into four main groups:

(1) Doublet ground, $^2A_{1g}$, and close-lying, ^2E_g, states, which are very similar in nature and belong to the *doublet ligand-field*, ^{2}LF, states. They result from an originally triply degenerate state split due to a trigonal Jahn-Teller distortion.

(2) Other ^{2}LF states, which are located at much higher energies and have longer equilibrium Fe–CN distances than in the ground state. Direct dipole transitions between ^{2}LF states are forbidden by the parity selection rule.

(3) *Doublet charge-transfer* states, ^{2}LMCT, which have shorter equilibrium Fe–CN distances than in the ground state. Only the potentials of the lowest "bright" ^2A_u and ^2E_u states are plotted in the graph. The associated transitions from the ground state correspond to the first absorption peaks on the red side of absorption spectrum, as shown in Figure 2.1, with there ^{2}LMCT states being directly populated in the course of excitation.

(4) *Quartet ligand-field* states, ^{4}LF, having potential curves similar to those of the ^{2}LF states.

Upon ionisation from a doublet state, the residual ion can be formed in a singlet or triplet state; for the case of ionisation from a quartet state, the ion resides in a triplet or quintet state. The respective potential energy curves of the ionised species along the Fe–CN stretching mode are also shown in Figure 5.13. The curves in this figure corresponding to ^{2}LF, ^{4}LF, and ^{2}LMCT states are coloured black, red, and blue, respectively. The singlet, triplet, and quintet potential curves of the ionised species are coloured orange, brown, and green, respectively. Solid lines refer to the aqueous solution and dashed lines to the [emim][DCA] ionic liquid solution potential energy curves. Slightly different overall shifts of +1.52 eV and +1.41 eV for H_2O and IL, were respectively applied to the ionised state manifolds to reproduce the peak positions in the experimental $[Fe(CN)_6]^{3-}_{(aq)}$ solution photoemission spectra reported in Ref. [402] and in this work. In the former case, the experimental Fe 3d peak binding energy at 7.62 eV was assigned to the GS$\rightarrow$ T_1 (^{3}Ion) ionisation transition. In the later

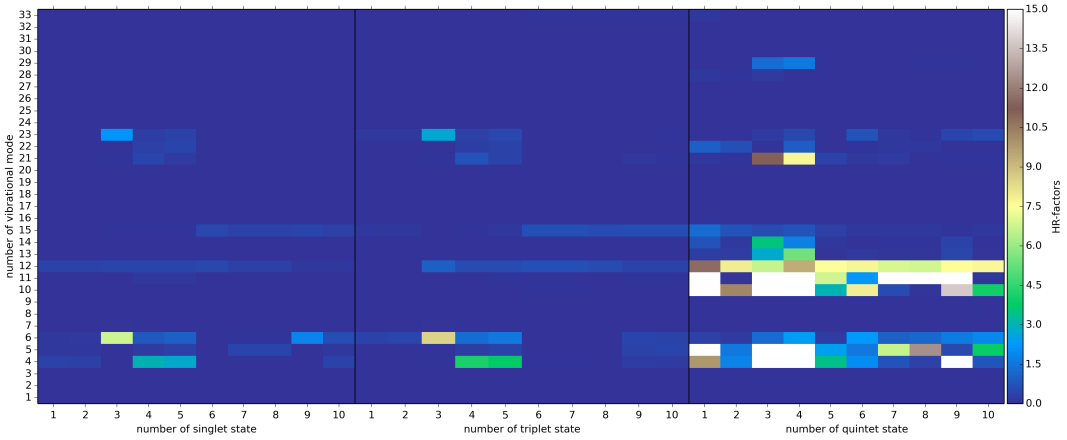

FIGURE 5.12: Huang-Rhys factors of the lowest singlet (left panel), triplet (central panel), and quintet (right panel) states of the ionised complex ($[Fe(CN)_6]^{2-}$) in water. Note that for convenience, the colour bar is truncated up to a value of 15. The figure was provided by Sergey Bokarev.

case, the predominantly ligand-centered peak at 8.32 eV was used as a reference for the GS→ S_1 (^{1}Ion) transition. These experimental band energies, denoted by *, were used to adjust the calculated energies to those measured in the experiments (see Table 5.2). The reason for this choice is that the ligand-centered peak is more pronounced and its position in the IL spectrum is more reliably extracted than that of the Fe 3d peak, as described in Section 5.2.

The implicit solvation model cannot provide quantitative results for the solvation energy shifts in all of their intrinsic complexity. However, it includes the most prominent solute-solvent interactions and effects and may be used to deduce qualitative trends. The comparison of the results obtained for H_2O and [emim][DCA], demonstrates that the shape of the potential energy surfaces remains almost unchanged. The ^{2}LMCT potentials are minutely up-shifted when going from water to [emim][DCA], which can be explained by the lower dielectric constant of the latter, resulting in less stabilisation. Both the ^{2}LF and ^{4}LF curves shift downwards more or less uniformly by up to 0.15 eV. These two trends lead to slight changes in the intersection positions between the potential energy surfaces and the corresponding barrier heights.

As demonstrated in Figure 5.13, the positions of the potential curves of the ionised states of different multiplicities - singlet (^{1}Ion), triplet (^{3}Ion), and quintet (^{5}Ion) - give insights into how the binding energies change for the transitions originating from the transient ^{2}LF, ^{4}LF, and ^{2}LMCT states, as compared to the doublet ground state, ^{2}GS. The lowest energy transition in the steady-state photoemission spectrum is from the ^{2}GS state to the group of close-lying ^{3}Ion states. The next major feature at about 10 eV for the aqueous solution and 9 eV for the IL solution corresponds to the transitions to the d singlet and triplet states. Ionisation from the quartet states can in turn result in triplet and quintet ionised states. Provided the original excitation is at 3.1 eV and vibrational cooling is negligible on the timescale of τ_1 and τ_2, one expects the lowest binding energy for the ^{2}LMCT state to appear at 4.5 – 5.0 eV. If a ^{4}LF or ^{2}LF state is populated in the course of non-radiative relaxation, then, depending on the actual position of the nuclear wavepacket, the lowest binding energy can change in a rather broad range of 5 – 8 eV. In fact, one could expect this transient signal to represent a broad low-intensity feature, compare with Figure 5.12. This is due to the fact that the direction of the wavepacket's momentum on the quartet potential surface is opposite to the energy gradient (force) in the ^{3}Ion state, which should lead to a fast decay of the wavepacket's autocorrelation function. The characteristic feature in the photoemission spectrum of the ^{4}LF states, i.e. quartet-to-quintet ionisation, is unfortunately overlaid with multiple quartet-to-triplet transitions and cannot be used to unequivocally identify contributions from ^{4}LF states.

As summarised in Table 5.1, the dynamic relaxation pathway of the electronically photoexcited ^{2}LMCT state of $[Fe(CN)_6]^{3-}$ upon 400 nm excitation in the [emim][DCA] ionic liquid solution involves fast early-time transition rates. In particular, the intersystem crossing transition time constant from the initially excited ^{2}LMCT state to the ^{4}LF state is found to be $142\,(^{+8}_{-7})$ fs. The subsequent transition from the ^{4}LF state to the vibrationaly-hot excited ground state or its adjacent low-lying degenerate ^{2}LF states, collectively referred to as GS*, occurs within $332\,(^{+47}_{-50})$ fs. Comparing these decay time constants with those obtained in aqueous solution (170 fs and 730 fs), as previously reported [93, 402], it can be concluded that the $[Fe(CN)_6]^{3-}$ deactivation pathway is affected by the IL solvation environment, particularly the associated lower-energy doublet-quartet potential energy surface crossings, leading to faster transition rates. Consequently, the acceleration of the first two steps in the adopted kinetic scheme (see Equation 5.2) may be attributed to the purely electronic solvent response, mainly due to a different dielectric constant, as predicted by the implicit solvation model. As can be seen from Figure 5.13, the slight positive energetic shift of the ^{2}LMCT state and down-shift of the ^{4}LF states, when changing from H_2O to [emim][DCA], lead to the lower energies of the intersection points between the ^{2}LMCT and ^{4}LF states, and between the ^{4}LF and ^{2}LF potential curves. This likely results in the decrease of transition time constants τ_1 and τ_2 in the IL compared to the H_2O solution.

Note that the above discussion provides only approximate qualitative arguments. The implicit solvation theoretical model applied here includes only the ultrafast electronic response of the solvent,

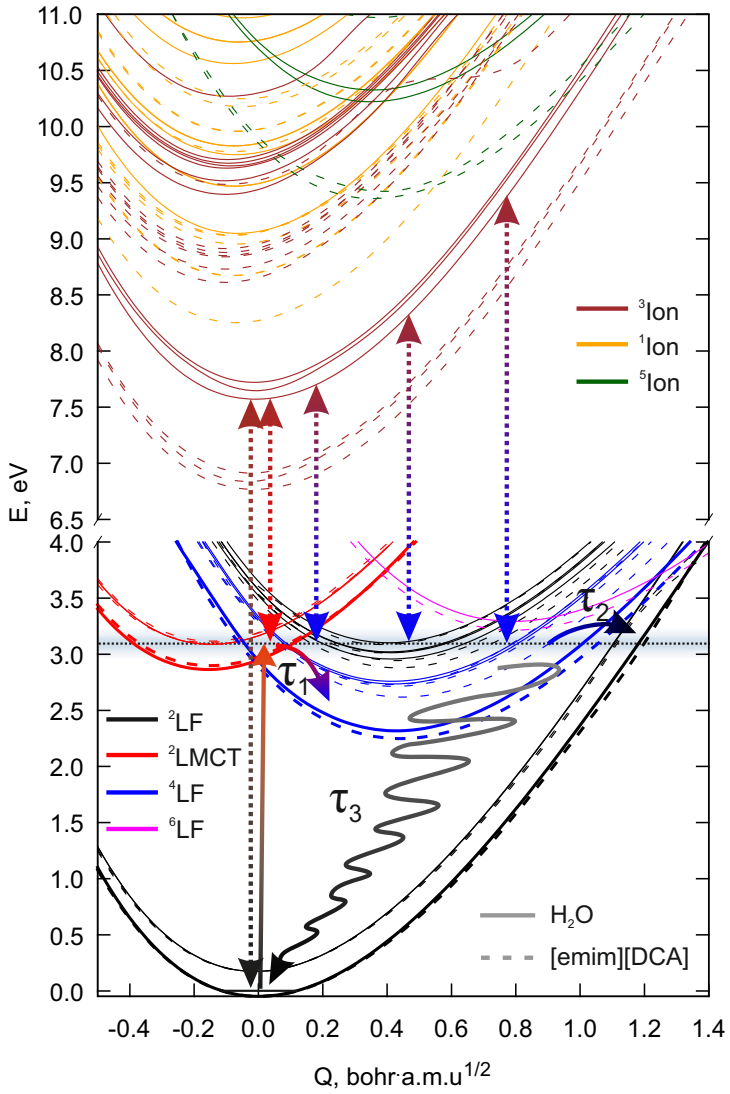

FIGURE 5.13: Calculated 1D cuts through the potential energy surfaces of $[Fe(CN)_6]^{3-}$ along the a_{1g} Fe–CN stretching mode with ground-state harmonic vibrational frequencies of 393 cm^{-1} (H_2O) and 387 cm^{-1} ([emim][DCA]). The lowest doublet and quartet electronic states of $[Fe(CN)_6]^{3-}$, as well as the singlet, triplet, and quintet states of the ionised system, $[Fe(CN)_6]^{2-}$, are presented. Black lines correspond to the doublet ligand-field states (^{2}LF), red – doublet charge-transfer states (^{2}LMCT), blue – quartet ligand-field states (^{4}LF), orange – singlets (^{1}Ion), brown – triplets (^{2}Ion), and green – quintets (^{5}Ion). The potential curves of $[Fe(CN)_6]^{3-}$ in H_2O and [emim][DCA] solutions are presented by solid and dashed lines, respectively. The pump pulse excitation energy of 3.1 eV is marked by a horizontal dotted line; its width corresponds to a shaded area. The three main states involved in the dynamics (see Section 5.3.2) are highlighted with thicker lines. The curves of the ionised states are shifted by +1.52 eV for H_2O and +1.41 eV for [emim][DCA], based on the steady-state EUV PES results. Solid arrows correspond to optical excitation and non-radiative relaxation; dashed double-sided arrows denote vertical ionisation potentials for different states and geometries.

TABLE 5.2: Assignment of the lowest ionisation energy transitions corresponding to the ionic states shown in Figure 5.13. Colour code: black – metal-centered ionization, blue – ligand-centered, red – shake-up states. For the lowest state of each multiplicity, the reference electronic configuration is given. The excitation characters of the states are provided relative to these lowest-state configurations. The vertical IP is shifted by 1.41 eV for [emim][DCA] ionic liquid to match the GS band positions in the experimental photoemission spectrum. For the H_2O case, the vertical IP value is shifted by 1.52 eV to match the previously reported experimental results of Ref. [402].

State	Electronic configuration / Excitation	Vertical IP / eV	
		[emim][DCA]	H_2O
Triplets			
T_1	$(d_{x^2-y^2})^2(d_{xy})^1(d_{z^2})^1(d_{yz})^0(d_{xz})^0$	6.82	7.62*
T_2	$d_{x^2-y^2} \rightarrow d_{xy}$	6.90	7.69
T_3	$d_{x^2-y^2} \rightarrow d_{z^2}$	6.97	7.77
T_4	$\pi(CN) \rightarrow d_{xy}$	8.71	9.48
T_5	$\pi(CN) \rightarrow d_{z^2}$	8.82	9.60
T_6	$\pi(CN) \rightarrow d_{xy}$	8.93	9.71
T_7	$\pi(CN) \rightarrow d_{xy}$ (64%) $\pi(CN) \rightarrow d_{z^2}$ (32%)	8.94	9.72
T_8	$\pi(CN) \rightarrow d_{xy}$ (30%) $\pi(CN) \rightarrow d_{z^2}$ (62%)	8.97	9.75
T_9	$\pi(CN) \rightarrow d_{z^2}$	9.00	9.79
T_{10}	$\pi(CN) \rightarrow d_{xy}$ (77%) $\pi(CN) \rightarrow d_{z^2}$ (19%)	9.57	10.34
T_{11}	$\pi(CN) \rightarrow d_{xy}$	9.59	10.37
Singlets			
S_1	$(d_{x^2-y^2})^2(d_{xy})^2(d_{z^2})^0(d_{yz})^0(d_{xz})^0$	8.32*	9.11
S_2	$\pi(CN)+d_{xy} \rightarrow d_{z^2}$	8.75	9.54
S_3	$d_{x^2-y^2} \rightarrow d_{z^2}$	8.75	9.54
S_4	$\pi(CN) \rightarrow d_{z^2}$	9.02	9.81
S_5	$\pi(CN) \rightarrow d_{z^2}$	9.11	9.89
S_6	$\pi(CN) \rightarrow d_{z^2}$	9.11	9.89
Quintets			
Q_1	$(d_{x^2-y^2})^2(d_{xy})^1(d_{z^2})^1(d_{yz})^1(d_{xz})^0$	9.90	10.74
Q_2	$d_{yz} \rightarrow d_{xz}$	9.95	10.80

whereas the slower component related to the reorganisation of the solvent molecules is computed only for the ground state and is frozen for other electronic states (so-called non-equilibrium solvation). Without explicit representation of the solvent molecules, the nanoscale heterogeneity of the IL due to the formation of micelle-like domains [123] cannot be reproduced. But the photophysics of the highly-charged $[Fe(CN)_6]^{3-}$ should notably depend on the distribution of the solute between the polar or non-polar domains and at interfaces between them. Notably, $[Fe(CN)_6]^{3-}$ in the LMCT and LF states cannot be considered as a classical CT complex within Marcus' theory of CT reactions. The excessive negative charge is evenly distributed over all six CN^- ligands and, when an LMCT state is excited, the outer portion of the charge is decreased and concentrates moves towards the center of the complex. Thus, the solvent response should primary resemble the partial oxidation when the radial distribution of charge within $[Fe(CN)_6]^{3-}$ is changed, leading to more efficient screening of the reduced metal center by the ligands. For the LMCT $\rightarrow$ LF transition, the opposite process occurs. Note again, that implicit solvation can only be used to deduce the qualitative trends, but not the quantitative behavior. For a more conclusive investigation, the explicit solvent QM/MM simulations would be warranted, allowing access to time scales of vibrational relaxation of the GS*. However, this represents a separate and further subject of study, and such a discussion is not pursued here.

5.4 Summary

In Chapter 5, the relaxation dynamics of the lowest-lying electronically photoexcited ^{2}LMCT state of the ferricyanide anion, $[Fe(CN)_6]^{3-}$, following 400 nm excitation was investigated by means of sub-100 fs time resolution TRPES in the [emim][DCA] ionic liquid environment. The TRPES method allowed the transient populations of the involved excited states to be monitored on a binding energy scale referenced to the local vacuum level. The relaxation dynamics of $[Fe(CN)_6]^{3-}$ dissolved in [emim][DCA] solution was described by a four-state kinetic model with the sequential population of the involved electronic states. The interpretation of the results was assisted by TDDFT calculations, implementing the optimally-tuned range-separated functionals in the [emim][DCA] and reference H_2O solvents using an implicit solvation model.

Based on the theoretical calculations and experimental observations, the previously suggested ultrafast biexponential decay of the first, optically excited ^{2}LMCT state population was confirmed [93, 402], which is believed to be associated with a sequence of intersystem crossings between doublet and quartet states. Specifically, low-lying ^{4}LF states are evidenced to play a role of the intermediate state in the relaxation dynamics of $[Fe(CN)_6]^{3-}$. From the results of the global analysis, using a kinetic model, and their further validation through a F-test, two fast decay time constants of 142 $^{+8}_{-7}$ fs and 332 $^{+47}_{-50}$ fs were precisely determined and associated with the population and subsequent decay of the ^{4}LF state for the solvated $[Fe(CN)_6]^{3-}$ ions in the [emim][DCA] IL solvent. The transient population of this state was shown to be associated with geometrical distortions due to vibronic interactions (Jahn-Teller effect) in the excited electronic state, instead of the transient electron hole localisation suggested by Zhang *et al.* [150]. The proposed mechanism also differs from the interpretation of Ojeda *et al.* [91], where a direct transition from the initially excited LMCT state to the vibrationally excited ground state was considered.

The intramolecular electron dynamics of ligand-to-metal charge-transfer excited $[Fe(CN)_6]^{3-}$ was found to be solvent dependent. A comparison between the [emim][DCA] and H_2O [93, 402] solvents demonstrates a clear difference in the values of the rates and the corresponding timescales of the elementary steps. The ionic liquid environment yields considerably faster intersystem crossing transition rates of $[Fe(CN)_6]^{3-}$ as compared to H_2O. This difference is ascribed on the basis of theoretical calculations to the opposite energetic shifts of the potential energy surfaces of charge-transfer and ligand-field states, primarily due to the different dielectric constants of the considered solvents. Nevertheless, the employed implicit solvation model can provide only qualitative evidence and should be considered with caution, as the heterogeneity of the IL structure cannot be reproduced.

Since only a limited number of studies have been carried out to examine photoinduced processes in ILs so far, this study has reflected several essential characteristics of ILs compared to the more frequently studied aqueous environment. This work can stimulate further studies, such as considering the explicit complexity of the IL structure together with the intricacy of the excited state electronic and vibrational relaxation processes of embedded solutes.

Chapter 6

Photoinduced Electron Dynamics in Bulk, Mesoporous and Porous Ultrathin Nanosheets of Polymeric Carbon Nitrides

> "Nature is the source of all true knowledge. She has her own logic, her own laws, she has no effect without cause nor invention without necessity."
>
> — *Leonardo da Vinci*

The following people and institutions contributed to the work presented in Chapter 6. **N. Kuzkova** prepared and characterised the solid thin film samples, co-designed and performed the PES, TRPES, UV-Vis TAS, and UV-Vis absorption spectroscopy experiments, analysed the data, interpreted the results, wrote the description of results and discussion, and summary. **A. Thomas** (Technische Universität Berlin) and **B. Zhang** (Tianjin University) synthesised and provided four sample powders. **C. Merschjann** (Helmholtz-Zentrum Berlin) co-designed and participated in the UV-Vis TAS experiments, contributed to the development of the data analysis, interpretation of the results and proof-reading processes. **I. Kiyan** (Helmholtz-Zentrum Berlin) co-supervised the project, contributed to the data interpretation and proof-reading of the work. **I. Wilkinson** (Helmholtz-Zentrum Berlin) assisted during the PES and TRPES experiments, supervised the research, data analysis and interpretation.

This chapter presents and discusses results obtained from TRPES and UV-Vis TAS experiments performed with PCN thin films. The photoinduced electron dynamics of the PCN thin films was studied upon 400 nm excitation at the surface-vacuum interface in the time range from hundreds of femtoseconds to several picoseconds using TRPES and at the surface-bulk interface, with deeper probing depths and on time scales up to several nanoseconds, by applying UV-Vis TAS. In this work, through TRPES, the ultrafast kinetics was probed in a nm-thickness layer of the solid sample. This approach was implemented, to the best of our knowledge, with PCN samples for the first time. By means of steady-state PES, the valence electronic structure of the PCN thin films was interrogated on an absolute binding energy scale with respect to the system Fermi level at the solid-vacuum interface. For this study, it was also of interest to investigate the relative vacuum-condensed-phase interfaces energetics between the PCN photocatalysts and $TEOA_{(aq)}$ solution, which is used as a sacrificial agent in an enhanced photocatalytic water splitting reaction. An accurate determination of the catalyst-sacrificial-agent interfacial energetics on the same energy scale allows direct comparison of the two (separated) systems associated with the solid-liquid interface. Thus, the valence electronic structure of the $TEOA_{(aq)}$ solution as well as the TEOA solute were determined on an absolute binding energy scale with respect to the local vacuum and Fermi levels at the liquid-vacuum interface using steady-state liquid jet PES.

The chapter is organised in five sections. Section 6.1 describes the PCN thin film preparation procedure as well as microscopic and optical characterisation of the prepared solid samples, employing

scanning electron microscopy and UV-Vis diffuse reflectance spectroscopy techniques. Section 6.2 focuses on steady-state PES results, from which the interfacial electronic structure properties and energetic information of the PCN thin films and aqueous TEOA solution were extracted, respectively. A comparison between PCN samples and aqueous TEOA solution energetics is presented with respect to the Fermi level on a combined band energy level diagram. Section 6.3 presents results obtained from ultrafast TRPES experiments recorded in two different modes of the electron spectrometer and the introduction of the kinetic model and global fitting procedure used to describe the early-time photoinduced dynamics of the PCN thin films at the surface-vacuum interface. The relationship between the spectral and kinetic TRPES information and the time-dependent changes in the electronic structure of the PCN samples is discussed in detail. Section 6.4 describes the results obtained from femtosecond UV-Vis TAS experiments, from which interfacial photoinduced electron transfer processes in the surface-bulk region of PCN thin films were investigated. The observed time-dependent spectral changes in the TAS spectra were simulated using a kinetic model and global analysis procedure, taking into account the existing spectroscopic observations from TRPL and TAS studies and on the basis of the TRPES results obtained in this work. As a result, the lifetimes of the relaxation processes associated with the population of photoexcited electronic states in the PCN thin films were determined, and the corresponding spectral distributions of transient signals from the involved electronic states are discussed. In addition, the effect of the excitation pulse fluence on the relaxation dynamics in photoexcited PCN thin films was investigated. A summary of the key findings described throughout this chapter is presented in Section 6.6.

6.1 Sample Preparation and Characterisation

Solid samples of thin films of polymeric carbon nitrides (PCNs) were prepared by depositing aqueous PCN dispersions onto the surface of a transparent low-iron sodalime–silica glass substrate with an electrically conductive fluorine-doped tin oxide (FTO) coating. The 2.2 mm-thick 1×1 cm^2 glass substrate, with a 7 Ω sq^{-1} FTO coating on one side, was purchased from Solaronix S.A. 10 mg of the mesoporous (sg-CN), bulk (CNB), 2D porous ultrathin nanosheets of oxygen-containing (CNPS-O) or amino co-functional group (CNPS-NH_2) polymeric carbon nitride powder were separately dispersed in 5 ml of distilled water (18 MΩ cm), followed by a sonication treatment at a 35 kHz ultrasonic frequency for two hours to obtain PCN dispersions with a concentration of 2 mg ml^{-1} for thin film deposition. The FTO-coated glass substrates were sequentially cleaned for 15 minutes using the same ultrasonic bath with isopropanol and the 70° C distilled water solvents. The sg-CN, CNB, CNPS-O, and CNPS-NH_2 thin films were deposited onto the pre-cleaned FTO substrates by drop-casting 20 μl of the PCN dispersions and dried at room temperature. As a result, four types of solid samples of sg-CN, CNB, CNPS-O, and CNPS-NH_2 thin films were produced (see Figure 6.1). The additionally studied aqueous triethanolamine (TEOA) solution of 750 mM concentration was prepared at room temperature by dissolving the TEOA solute ($\geq$99% purity, purchased from Carl Roth) in milli-Q water (18.2 MΩ cm resistivity at 25 °C). Sodium chloride (NaCl) salt of 50 mM concentration was admixed to this solution to suppress the effects of extrinsic potentials, such as the streaming potential and ionisation-induced sample charging that are commonly encountered in liquid jet PES [416].

Correct and reproducible solid sample preparation and its deposition on the substrate was one of the technical challenges in the time-resolved photoemission spectroscopy studies. Since the pulsed and high intensity light sources used in PES experiments generate dense clouds of ionised electrons, the photoemitted electrons can experience energy redistribution during and after their escape from the sample surface, due to the so-called space-charge effect (see Section 3.3.4). This can cause positive or negative time-dependent electron kinetic energy shifts and broadening of the spectral components, and often represents a limiting factor in PES experiments. Consequently, pump pulse intensities had to be reduced to minimise this effect and decrease the probability of multiphoton ionisation of

a sample (the major cause of pump-pulse-induced space-charge). By applying a smaller amount of sample on a substrate, one can decrease the space charge effect and increase the pump pulse power. On the other hand, an ultrathin or sparse sample deposition over a surface has a weaker contribution to the overall photoemission spectra, which makes the sample signal identification with respect to the substrate signals very difficult. Therefore, the thicknesses of the deposited sg-CN, CNB, CNPS-O, and CNPS-NH_2 thin films were optimised prior to each PES experiment by preparing thin film samples with different thickness and monitored using the scanning electron microscopy technique, as discussed in detail below.

6.1.1 Scanning Electron Microscopy (SEM) Images

To characterise the surface morphology and the thickness of the deposited PCN thin films, scanning electron microscopy (SEM) images were recorded in the sample plane and orthogonal cross-sectional view in the transverse sample-sample depth plane. The images were collected through detection of reflected secondary electrons, as collected by an objective lens field, as shown in Figure 6.1. The SEM measurements were carried out on a Zeiss Leo 1530 instrument equipped with an In-Lens secondary electron detector, yielding 1 nm spatial resolution with a 20 keV applied electron source. The SEM images were obtained by analysing secondary electrons with kinetic energies of 5 keV or 10 keV, with a primary electron current of 249 μA.

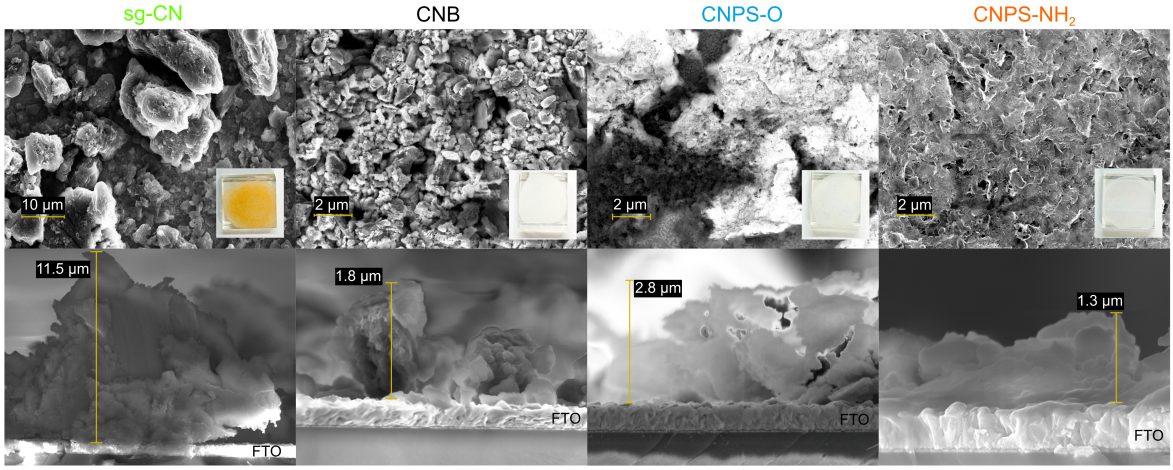

FIGURE 6.1: High resolution top-view (upper panels) and cross-sectional view (bottom panels) SEM images of the sg-CN, CNB, CNPS-O, and CNPS-NH_2 thin films (top images) deposited on the FTO-coated glass substrate.

The upper panels in Figure 6.1 show the top-view SEM images of the drop-casted sg-CN, CNB, CNPS-O, and CNPS-NH_2 thin films (top images), deposited on FTO-coated glass substrates. The plane view SEM images demonstrate that the obtained CNPS-NH_2 thin film has a homogeneous and porous nanosheet-like structure, which is dissimilar to the bulk CNB and mesoporous sg-CN thin films that show a regular inhomogeneously-distributed PCN nonporous layer structure that is composed of solid agglomerates. A high-magnification SEM image of the CNPS-O thin film highlights the multi-pore structure associated with the process of producing CNPS-O powder from CNB by oxidation and etching, as previously reported [175]. The cross-sectional view SEM images of the PCN thin films are presented in Figure 6.1 (bottom panels). The images display the transparent glass substrate with an electrically conductive FTO coating over which thin layers of the PCN dispersions were deposited. The thickness of the deposited layer of the sg-CN, CNB, CNPS-O, and CNPS-NH_2 thin films (indicated by the yellow lines) was estimated to be 11.5 μm, 1.8 μm, 2.8 μm, and 1.3 μm, respectively. It was found that this amount of the PCN material deposited on the surface of the FTO-coated glass substrate was optimal for sample photoemission spectra collection with reduced pump

pulse intensities. As a result, in the present work, these samples were employed in time-resolved photoemission and transient absorption spectroscopy studies. The cross-sectional view SEM images demonstrate that the CNPS-O and CNPS-NH_2 thin films have a macroscopic ultrathin structure. This confirms that the two-step thermal treatment, implemented in the preparation of the PCN powders by Meng *et al.* [175] lead to a reduction of the thickness and size of the layers, yielding porous and loose lamellar structures.

6.1.2 Steady-state UV-Vis Absorption Spectra of PCN Thin Films

The electronic energy gap between the HOMO and the LUMO, as related to the electronic excitations from the electronic ground to excited states, in the PCN samples were determined using UV-Vis diffuse reflectance and transmittance spectroscopy. Room temperature UV-Vis diffuse reflectance and transmittance spectra of the sg-CN, CNB, CNPS-O, and CNPS-NH_2 thin films deposited on the FTO coated glass substrate were recorded using a Perkin Elmer - Lambda 950 UV/Vis/NIR spectrometer, equipped with an integrating-sphere detector module. The integrating sphere was calibrated versus ceramic diffuse reflectance standards [417]. The UV-Vis absorption spectra of the PCN thin films are shown in Figure 6.2 and were obtained from the recorded diffuse reflectance and transmittance spectra by calculating the absorbance, A, as A = 1 - R - T, where R is the reflectance and T is the transmittance of the sample.

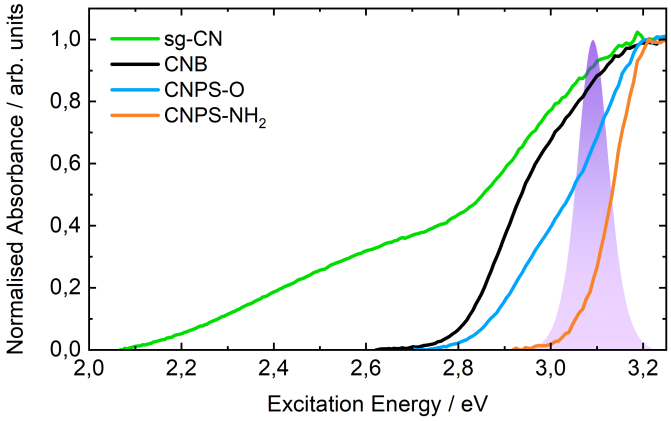

FIGURE 6.2: UV-Vis absorption spectra of the mesoporous (sg-CN), bulk (CNB), porous ultrathin nanosheets of oxygen-containing (CNPS-O) and amino co-functional groups (CNPS-NH_2) PCN thin films deposited on an FTO-coated glass substrate. The spectra are normalised at the 3.2 eV excitation energy. The spectral profile of the pump pulse is depicted in the figure.

The UV-Vis absorption spectra of the PCN thin films shown in Figure 6.2 exhibit a sharp increase in the UV spectral region with maximum absorption at a 3.2 eV photoexcitation energy (388 nm wavelength). The well-pronounced and higher intensity absorption bands of the PCN thin films, appearing at photon energies > 2.8 eV, can be assigned to $\pi \rightarrow \pi^{\star}$ transitions of the heterocyclic aromatic constituents in the conjugated ring systems, which provide the main contribution to the photocatalytic activity of the photoproducts in the UV-Vis range [418–421]. The CNPS-O and CNPS-NH_2 samples show blue-shifted absorption edges corresponding to larger HOMO-LUMO energy gaps as compared to the CNB. This can be possibly attributed to the quantum confinement effect [422], where the energy difference between HOMO and LUMO becomes larger with decreasing particle size. This suggests that the obtained atomically-thin 2D structures of CNPS-O and CNPS-NH_2 consist of nanosheets. In addition, the blue-shift in the absorption edge is prominent in the colouration of the PCN samples, progressing from yellow (CNB) to pale yellow (CNPS-NH_2). This colour change is affected by the reduction of polymer condensation during cross-linking and the restoration of the co-functional amino groups. The shoulder in the sg-CN sample, which appears at about 2.5 eV, is

caused by the increased synthesis temperature of the sg-CN powder (650 °C compared to 520 °C in the CNB, CNPS-O, CNPS-NH_2 powders) [418, 423], and can be interpreted as being due to n $\rightarrow \pi^\star$ transitions involving lone pairs on the N atoms of the triazine/heptazine rings [418, 424]. More recent theoretical studies indicate that such transitions may also be of $\pi \rightarrow \pi^\star$ character [425]. Both transitions are dipole-forbidden for perfectly symmetric and planar s-triazine or heptazine units, but they become weakly allowed due to vibronic intensity borrowing from higher-lying bright states, and due to the structures developing distortions during layer condensation, including effects from both layer buckling and deviation of the ring units from a trigonal symmetry [424, 425].

For a quantitative assessment of the energetic positions of the spectral bands corresponding to allowed electronic transitions from the electronic ground state to the excited states in the PCN samples, the experimental UV-Vis absorption spectra presented in Figure 6.2 were analysed by a fitting procedure, using a superposition of Gaussian envelopes (see Equation 2.1). It is noted that a Gaussian envelope is only an approximation for the true vibronic envelope of a condensed-phase transition. The minimum number of fitted Gaussian envelopes to describe the experimental absorption spectra was used, which are each deemed to correspond to the contributions of the individual electronic transitions. It is not excluded that two electronic transitions, which cannot be clearly distinguished in the present spectra without the use of theoretical calculations, are described by a single Gaussian envelope here. The electronic structure and the corresponding electronic transitions in PCNs are typically represented in a form of a band diagram of a semiconductor, where energy levels are inhomogeneously broadened as well as interact and split. By employing MO theory and considering the PCNs as molecular solids [143] the observed spectroscopic features may be more accurately modeled.

TABLE 6.1: Fit parameters of the Gaussian envelopes used to describe the absorption bands of the PCN samples, as obtained by Equation 2.1.

Sample	Label	E / eV	FWHM / eV	A / cts
sg-CN	1	2.57 ± 0.01	0.53 ± 0.01	0.09 ± 0.01
	2	3.21 ± 0.01	0.63 ± 0.01	0.42 ± 0.01
CNB	1	2.97 ± 0.01	0.19 ± 0.01	0.04 ± 0.01
	2	3.21 ± 0.01	0.39 ± 0.02	0.26 ± 0.02
CNPS-O	1	2.97 ± 0.01	0.17 ± 0.01	0.02 ± 0.01
	2	3.23 ± 0.01	0.33 ± 0.01	0.22 ± 0.01
CNPS-NH_2	1	3.22 ± 0.01	0.18 ± 0.01	0.13 ± 0.01

Figure 6.3 shows the aforementioned UV-Vis absorption spectra of the PCN thin films fitted to a superposition of Gaussian envelopes using Equation 2.1. In sg-CN, two absorption bands, associated with electronic transitions between the frontier molecular orbitals, occur at 2.57 eV and 3.21 eV central photon energies. The first absorption band, presumably associated with the lowest, i.e. the HOMO-LUMO transition, is blue-shifted in the CNB and CNPS-O samples compared to sg-CN, where the transition seemingly appears at a central photon energy of 2.97 eV. The second absorption band is also apparent in the CNB, CNPS-O and CNPS-NH_2 sample spectra, centred around 3.21 eV, 3.23 eV, and 3.22 eV, respectively. It should be noted that the widths of the sg-CN absorption bands are broader in comparison to the other three samples. This suggests that the two different synthesis methods, the thermal polymerisation and the sol–gel/thermal condensation used to produce sg-CN, CNB, CNPS-O, and CNPS-NH_2 powders (see Section 2.2.3 for details), have an effect not only on the morphology but also on the electronic structure of the PCNs. In addition, for the CNPS-NH_2 sample, which was synthesised by treating CNPS-O with ammonia to form -NH_2 groups in porous ultrathin nanosheets, only one band (or a merged band) is observed in the experimental absorption spectrum over the 2.00 – 3.25 eV photon energy range. It is correspondingly assumed that the first allowed electronic transition that can be photoinduced in CNPS-NH_2 is centered at a 3.22 eV photon energy. Taking this into account, a pump pulse photon energy of 3.1 eV (400 nm wavelength) was chosen to initiate the photoinduced electron dynamics in the PCN thin films in the present studies.

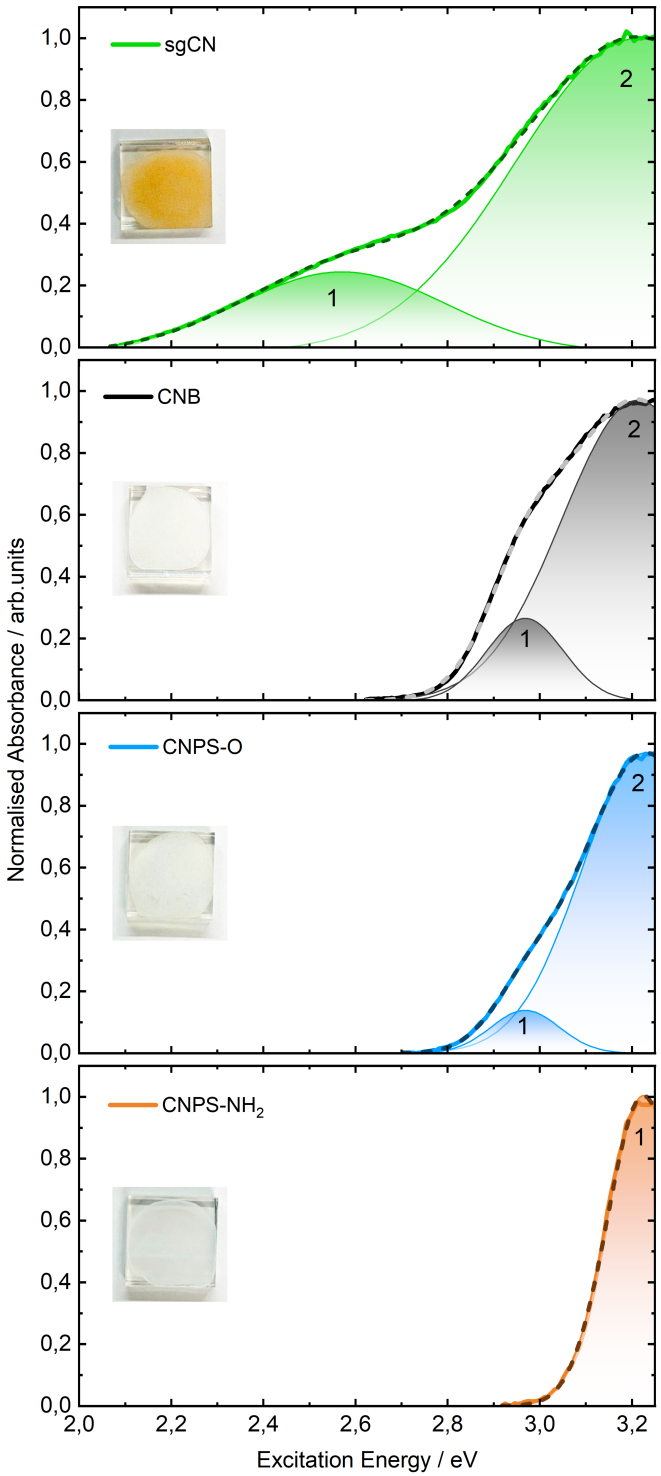

FIGURE 6.3: UV-Vis absorption spectra of the PCN thin films fitted to a superposition of Gaussian envelopes. The dashed lines represent the cumulative fit results. The numbers 1–2 are assigned to the decomposed absorption bands of the samples obtained from the fits. The fit parameters are summarised in Table 6.1. The images of the PCN samples deposited on an FTO-coated glass substrate are also shown.

As described in Section 2.2.1, the electronic structure of PCN is typically described within a semiconductor band structure framework. The band gap energy, E_g, of crystalline, amorphous as well as disordered semiconductors is most widely determined from UV-Vis diffuse reflectance spectra using Kubelka-Munk theory [426] in combination with the Tauc method [427]. The Tauc method is based on the relationship between E_g and the optical absorption coefficient, α:

$$(\alpha h\nu)^{1/n} = C(h\nu - E_g), \tag{6.1}$$

where C is a proportionality constant and $h\nu$ is the photon energy. The n factor depends on the nature of the electronic transition, where $n = 1/2$ for a direct or $n = 2$ for a indirect allowed electronic transitions, and $n = 3/2$ for a direct or $n = 3$ for a indirect forbidden electronic transitions, respectively [428].

By employing the Tauc method, the E_g can be determined from absorption spectra at the intersection point of the tangent of the region associated with the optical absorption edge and the horizontal $h\nu$-axis in the corresponding $(\alpha h\nu)^{1/n}$ *versus* $h\nu$ plot (Tauc plot). The experimental absorption spectra can be expressed in terms of the optical absorption coefficient, α, with the assumption that the Kubelka-Munk or reemission function, $f(R)$, is proportional to α as:

$$\alpha \propto f(R) = \frac{(1-R)^2}{2R}, \tag{6.2}$$

where R is the reflectance of an infinitely thick sample.

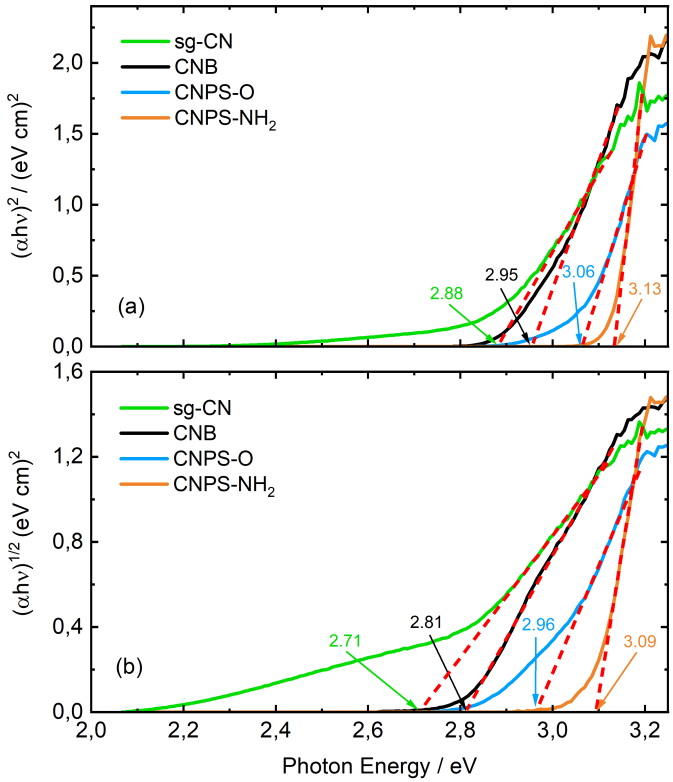

FIGURE 6.4: Tauc plots obtained from the UV-Vis absorption spectra of the PCN thin films. The E_g determined at the intersection of the tangent with the x-axis (red dashed line) in panel (a) corresponds to the direct allowed electronic transitions and in panel (b) to the indirect allowed electronic transitions, are summarised in Table 6.2.

To date, it is unclear whether the E_g values for PCN materials should be extracted as a direct or indirect allowed electronic transition, so values for both assumptions can be found in the literature. In the following, the E_g values were determined for both direct and indirect allowed electronic transitions. Figure 6.4 shows Tauc plots of the data transformed according to Equation 6.1. The UV-Vis

TABLE 6.2: Band gap energies of the PCN samples for the direct and indirect allowed electronic transitions, as determined from the Tauc plots.

Sample	E_g Direct / eV	E_g Indirect / eV
sg-CN	2.88 ± 0.02	2.71 ± 0.03
CNB	2.95 ± 0.03	2.81 ± 0.01
CNPS-O	3.06 ± 0.01	2.96 ± 0.02
CNPS-NH_2	3.13 ± 0.02	3.09 ± 0.01

absorption spectra of the PCN thin films are correspondingly used to determine the band gap energies of the samples. Using the tangent approach (see Equation 6.3), the E_g values for the *direct allowed* electronic transitions in the sg-CN, CNB, CNPS-O and CNPS-NH_2 samples are determined to be 2.88 eV, 2.95 eV, 3.06 eV and 3.13 eV, respectively (panel a). For the *indirect allowed* transitions, the extracted E_g values for the sg-CN, CNB, CNPS-O and CNPS-NH_2 samples are 2.71 eV, 2.81 eV, 2.96 eV and 3.09 eV, respectively (panel b). Table 6.2 summarises the determined E_g values. It is noted that the absorption edge and band gap energy of the CNPS-O and CNPS-NH_2 porous ultrathin nanosheets is blue-shifted in comparison with the bulk CNB and mesoporous sg-CN thin films. This may limit their use as photocatalysts in the visible spectral region (see Section 2.2.2). However, for instance, in the water-splitting reaction, the efficiency of a photocatalyst depends, to a large extent on the position of the VBM and CBM with respect to the redox potentials of water. It was previously reported that the CNPS-NH_2 sample, which exhibits a wide band gap, has 11 times higher visible light activity in the HER of water splitting than CNB [175].

6.2 Steady-state EUV Photoemission Studies of Polymeric Carbon Nitride Thin Films and $TEOA_{(aq)}$ Solution

The photoemission spectroscopy experiments were conducted with the *ex situ* prepared solid samples of PCN thin films inside an interaction chamber maintained at a high vacuum pressure of 10^{-7} mbar. The samples were placed in a vacuum compatible stainless steel sample holder, which was in electrical contact with the electron spectrometer. The position of the sample in the interaction chamber was adjusted in front of the electron spectrometer entrance aperture using a high-precision 3D manipulator, forming an angle of 45° between the EUV beams at the sample surface and the spectrometer electron collection axis.

The steady-state photoemission spectroscopy experiments on the aqueous TEOA ($TEOA_{(aq)}$) solution were carried out inside the interaction chamber, where the chamber was maintained at base pressures between 10^{-4} and 10^{-5} mbar using liquid nitrogen cold traps, the chamber's turbo molecular pump, and differential pumping techniques [429]. The 750 mM $TEOA_{(aq)}$ solution sample was introduced into the interaction vacuum chamber as a vertical, free-flowing liquid jet. The solution was injected at 1 ml min^{-1} flow rate through a 24 μm orifice diameter glass capillary nozzle, forming a liquid jet that maintained a laminar flow over a length of a few millimeters. Following interaction with the EUV laser pulses, the sample broke down into a droplet train, which was condensed, and was ultimately frozen at a nitrogen-cooled cryogenic trap further downstream. The jet was electrically grounded to the interaction chamber. A cooling system, connected to the liquid jet rod allowed the stabilisation of the solution sample temperature to 7 °C prior to delivery to the interaction chamber. The position of the laminar region of the jet in the vacuum chamber was adjusted in front of the spectrometer entrance aperture using the high-precision 3D manipulator.

The steady-state EUV photoemission spectra of the sg-CN, CNB, CNPS-O and CNPS-NH_2 thin films, as well as the $TEOA_{(aq)}$ solution, were recorded using the high-energy-resolution drift mode (DM) of the TOF spectrometer in a wide kinetic energy range (0.1 eV up to >100 eV, $\pm$ 1° electron acceptance angle from the interaction region). The spectra were recorded using the 25^{th} harmonic,

which was spectrally selected from the EUV light, using the zone plate monochromator. By recording steady-state, valence photoemission spectra of Ar gas with well-known ionisation potential under field-free conditions, a central EUV photon energy of 39.11 ± 0.02 eV and a spectral bandwidth of 275 ± 5 meV of the 25^{st} harmonic were exctracted. The electron binding energy scale of PCN samples was referenced with respect to the Fermi level, E_F, of the samples and spectrometer, which involves additional steps beyond the local vacuum level, E_{vac}, energy referencing.

The Fermi-level referencing can be introduced utilising a metallic reference sample, which is in electrical equilibrium with the grounded sample and the analyser. By recording steady-state EUV photoemission spectra of the metallic reference sample followed by the subsequent PES measurements on the sample under the same experimental conditions, the binding energy scale of the PCN thin films and the $TEOA_{(aq)}$ solution was assigned relative to the E_F. For the Fermi-level measurements, a gold wire with a thickness of 100 µm was implemented. The metal wire was in good electrical contact and in close proximity to the solid samples of PCN thin films in the solid-state PES experiments. In those cases, both the samples and the gold wire were mounted together on the same manipulator assembly allowing the PES spectra from the metal reference wire and the sample to be successively measured by slight relocation of the whole sample-holder assembly in front of the TOF spectrometer entrance aperture. In the LJ-PES experiments, the spectrum of the metallic reference sample was measured with the liquid jet running after moving the assembly to bring the gold wire target, instead of the liquid jet, in front of the analyser entrance aperture. The electron binding energy scale was determined with respect to the E_{vac} as the difference between the central EUV photon energy and the kinetic energy of the detected photoelectrons. By defining the Fermi-edge position of the gold reference sample with respect to the E_{vac}, the binding energy scale was subsequently calibrated with respect to E_F.

6.2.1 Steady-state EUV Photoemission Spectra of PCN Thin Films

The electronic structure of the PCN thin films was determined on an absolute binding energy scale at the solid-vacuum interface using solid-state PES. Figure 6.5 shows the steady-state EUV photoemission spectra of the sg-CN, CNB, CNPS-O, and CNPS-NH_2 thin films as well as the bare FTO-coated substrate presented with respect to the Fermi level. The steady-state PES spectrum of the gold reference sample was recorded first to determine the Fermi edge, allowing definition of the zero point position of the E_F scale with respect to the gold wire's local E_{vac} level. Subsequently, the steady-state PES spectra of the PCN thin films were recorded under the same conditions to calibrate the binding energy scale with respect to E_F, as defined from the metal sample.

The photoemission spectra presented in Figure 6.5 were fitted to a superposition of four Gaussian envelopes using Equation 2.1 to roughly extract the energetic positions of the spectral bands associated with the valence molecular orbitals of the PCN samples (see Table 6.3 for the fit results). Because the PE spectra exhibit a broad spectral structure, it is possible that several individual emission bands of PCN samples are represented by a single Gaussian envelope. For the deconvolution of the PES spectra, the minimum number of fitted Gaussian envelopes was used. Three emission bands centered at 3.61 eV (peak 1), 5.37 eV (peak 2) and 7.66 eV (peak 3) binding energies are present in the lower binding energy range of the photoemission spectra of the PCN thin films. The broad emission bands occurring at 11.90 eV, 10.89 eV, 12.78 eV, and 10.73 eV (peak 4) in sg-CN, CNB, CNPS-O, and CNPS-NH_2 thin films, respectively, gives the main, high-binding-energy contributions. With the low binding energy spectral features of the PCN samples being less pronounced. However, the CNPS-NH_2 sample displays a similar electronic structure to the bare FTO-coated substrate, where the underlying photoemission signal from the FTO substrate is interfering with the analysis of the low-signal-level CNPS-NH_2 data. Thus, the widths and amplitudes of the emission peaks 1–3 are larger for the CNPS-NH_2 porous ultrathin nanosheets when compared to the sg-CN, CNB, and CNPS-O thin films, as summarised in Table 6.3.

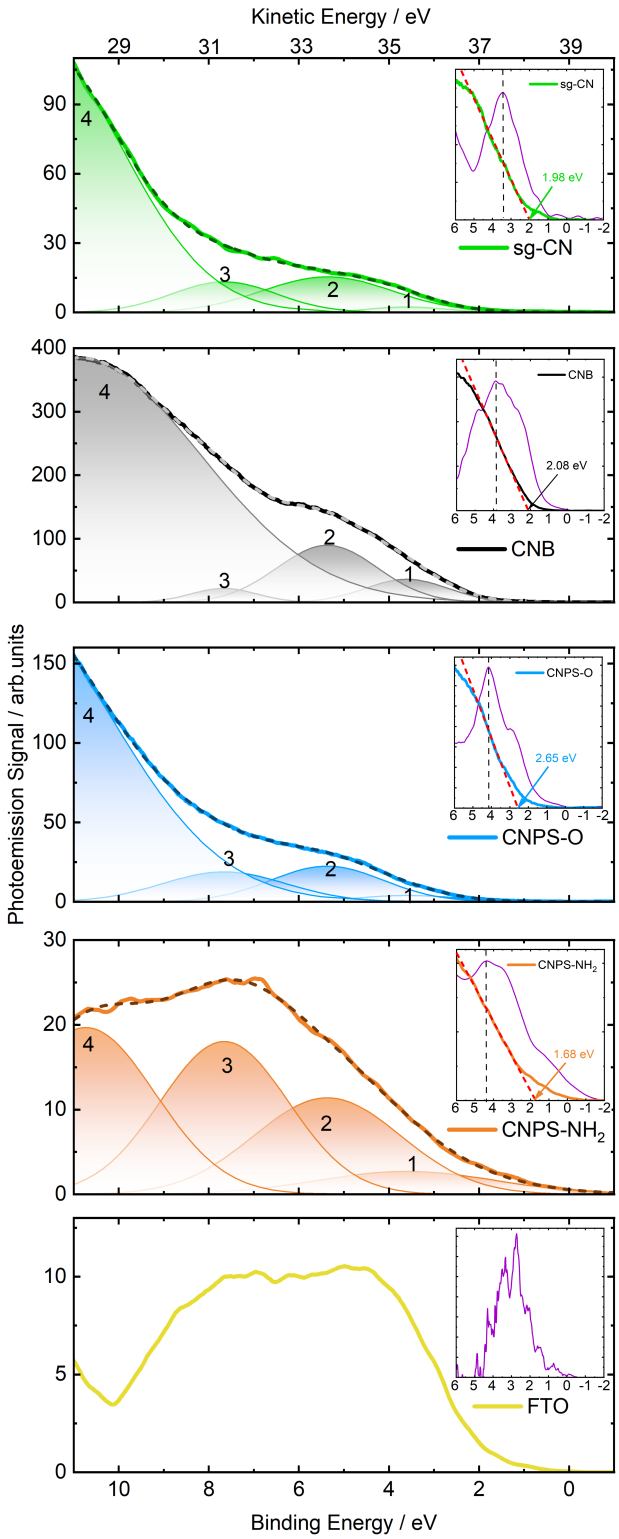

FIGURE 6.5: Steady-state EUV photoemission spectra of the sg-CN, CNB, CNPS-O, and CNPS-NH_2 thin films as well as the bare FTO-coated substrate. The sample spectra were fitted to a superposition of Gaussian envelopes. The numbers 1–4 are assigned to the decomposed emission bands of PCNs (Table 6.3). The VBM positions were determined for each sample, as extracted from the tangents and the low binding energy x-axis crossing points are shown in the associated figure panel insets. The electron binding energy scales are presented with respect to E_F.

Inoki *et al.* [430] observed similar emission bands to peaks 1–3, centered at around 3.5 eV, 4.5 eV and 7 eV binding energies, in their UPS studies on melon-based parvus carbon nitride thin films. In the present studies, the spectral bands of the PCN thin films are significantly broader compared to the previously reported results, which leads to less pronounced emission bands in the valence spectra of PCNs. This may be due to the fact that the electronic structure of PCN thin films depends on the local synthetic conditions of the obtained powdered PCN product. It was also found that the energetic position and width of the emission bands in the valence spectra of the carbon nitrides depend on the nitrogen content concentration [431]. Suoto *et al.* [432] attempted to assign the origin of the main features of the valence photoemission spectra of the amorphous carbon nitride films. According to this assignment, two emission bands centered around 3.61 eV and 7.66 eV binding energies can be associated with π-bonding and σ-bonding states, respectively, due to delocalised C $2p$ electrons. The peak arising at 5.37 eV can be attributed to C-C π-bonding states as well as localised nitrogen lone pair electrons. The broad emission bands arising at higher binding energies, $>$10 eV, originates from the C-N σ-bonding states.

TABLE 6.3: Fit parameters of the Gaussian envelopes used to describe the emission bands of PCN thin films in the photoemission spectra.

Sample	Label	E vs. E_F / eV	FWHM / eV	A / cts
sg-CN	1	3.61 ± 0.38	2.09 ± 0.07	4.98 ± 0.71
	2	5.37 ± 0.37	3.41 ± 0.06	55.72 ± 1.73
	3	7.66 ± 0.31	2.73 ± 0.05	38.44 ± 1.93
	4	11.90 ± 0.04	4.62 ± 0.06	576.47 ± 11.68
CNB	1	3.61 ± 0.39	2.16 ± 0.08	82.30 ± 19.21
	2	5.37 ± 0.34	2.62 ± 0.14	250.27 ± 20.51
	3	7.66 ± 0.30	1.71 ± 0.09	39.91 ± 7.28
	4	10.89 ± 0.29	6.33 ± 0.08	2595.03 ± 33.63
CNPS-O	1	3.61 ± 0.37	2.60 ± 0.06	11.10 ± 0.51
	2	5.37 ± 0.34	2.95 ± 0.03	70.39 ± 0.83
	3	7.66 ± 0.29	3.23 ± 0.03	64.90 ± 0.64
	4	12.78 ± 0.31	5.98 ± 0.22	1253.38 ± 1.17
CNPS-NH_2	1	3.61 ± 0.38	4.67 ± 0.22	13.43 ± 1.68
	2	5.37 ± 0.39	3.84 ± 0.14	46.58 ± 3.29
	3	7.66 ± 0.32	3.35 ± 0.04	64.38 ± 2.26
	4	10.73 ± 0.02	3.62 ± 0.06	75.87 ± 1.32

In addition to the MO decomposition of the photoemission spectra, the valence band maximum (VBM) positions of the samples were extracted within a semiconductor band structure framework. The VBM values of the PCN thin films were obtained from the experimental photoemission spectra using a tangent derivative-based method, as demonstrated in the insets in Figure 6.5. In this method, the first derivative of the data was computed (violet line), followed by a slight smoothing of the noisy derivative data using the Savitzky-Golay smoothing function (20 ppt) to identify the correct maximum of the derivative peaks. The center of the first peak of the derivative curve (dashed black line), corresponding to the inflection point with maximum change in slope in the data, determined the tangent anchor point and its slope (red dashed line). The position of the VBM was determined at the tangent intersection point with the binding-energy-axis and calculated from the point-slope tangent equation, which is given by:

$$y - f(a) = m(x - a), \tag{6.3}$$

where m is the slope of the tangent line to a curve, which is described by equation $y = f(x)$ and is the derivative of $f(x)$ at a point a.

The obtained VBM values of sg-CN, CNB, CNPS-O, and CNPS-NH_2 thin films are 1.98 ± 0.35 eV, 2.08 ± 0.32 eV, 2.65 ± 0.34 eV, and 1.68 ± 0.29 eV respectively. For application in photocatalytic water splitting, the position of the VBM of the PCNs should be low and correspond to a more positive

potential than the redox potential of the desired oxidation process. Based on the valence band spectroscopic results, a schematic diagram of the band edge potentials of the PCN samples, in comparison to standard water redox potentials, can be introduced. The corresponding diagram will be presented in Section 6.2.2.

6.2.2 Steady-state EUV Photoemission Spectra of $TEOA_{(aq)}$ Solution

The valence electronic structure of the TEOA sacrificial agent, which is used as a hole scavenger for polymeric carbon nitride photocatalysts to achieve a high H_2 evolution rate in the water splitting reaction, was mapped at the liquid-vacuum interface using LJ-PES. The electronic structure fingerprints arising from the TEOA solute, as well as the $TEOA_{(aq)}$ solution in the valence spectral region, were identified from steady-state PES spectra.

Figure 6.6 shows the steady-state EUV photoemission spectra of a reference 50 mM aqueous NaCl solution ($NaCl_{(aq)}$) and sample 750 mM $TEOA_{(aq)}$ solution. The binding energy scale presented in Figure 6.6 is energy-referenced with respect to E_{vac} and was calibrated to reproduce the $1b_{1,liq}$ binding energy of neat liquid water with respect to the local vacuum level at 11.33 eV [433]. The reference $NaCl_{(aq)}$ solution spectrum (upper panel in Figure 6.6) displays the photoemission peaks predominantly arising from the three outer molecular orbitals of the H_2O molecular subunits, labeled $1b_1$, $3a_1$ and $1b_2$. The spectrum was fitted to a superposition of Gaussian envelopes associated with the liquid-phase *(liq)* and residual, evaporating gas-phase *(g)* contributions to the spectra, which represent the liquid water molecular orbital binding energies at the solution-vacuum interface.

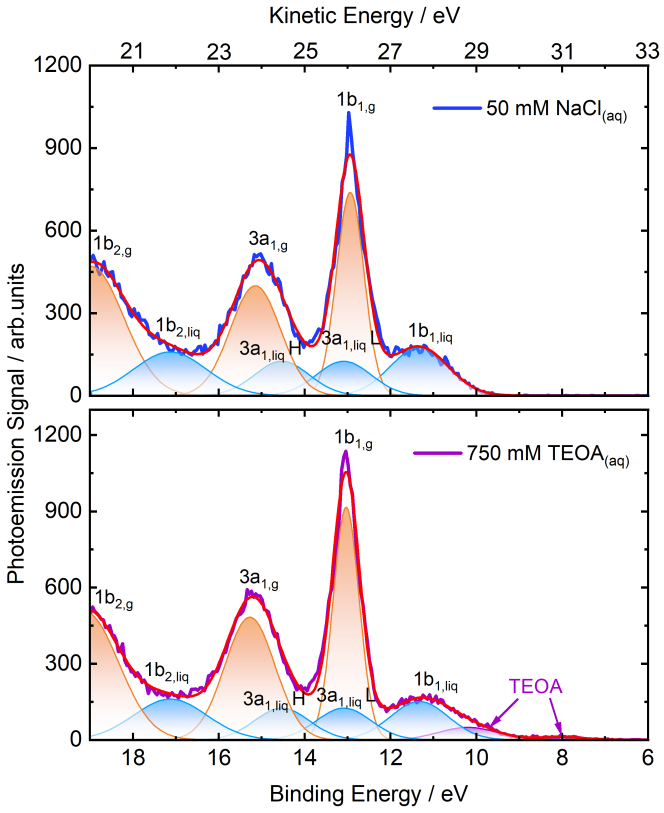

FIGURE 6.6: Steady-state EUV photoemission spectrum of the reference 50 mM $NaCl_{(aq)}$ solution (upper panel) and the 750 mM $TEOA_{(aq)}$ solution (lower panel). The labels are assigned to the decomposed emission bands of the neat-water liquid- (light blue) and gas-phase (orange) molecular orbitals, as well as the TEOA solute (violet) obtained from the multi-component Gaussian fit (Table 6.4). The binding energy scales are presented with respect to E_{vac}.

The four emission bands $1b_{1,liq}$, $3a_{1,liq}$L, $3a_{1,liq}$H and $1b_{2,liq}$ associated with the liquid-phase orbitals occur at 11.33 ± 0.31 eV, 13.09 ± 0.29 eV, 14.53 ± 0.32 eV, and 17.13 ± 0.41 eV binding energies in neat water, respectively. The three observed emission bands at 12.93 ± 0.29 eV, 15.15 ± 0.29 eV and 18.97 ± 0.30 eV binding energies are accordingly attributed to the $1b_{1,g}$, $3a_{1,g}$ and $1b_{2,g}$ gas-phase orbitals (which are notably recorded under the influence of extrinsic and intrinsic LJ potentials and are offset with respect to there known binding energy values). The assignment and energetic positions of the emission bands in neat liquid water are in agreement with previous reports [416, 434, 435]. The $TEOA_{(aq)}$ solution spectrum (lower panel in Figure 6.6) highlights the presence of two additional emission bands in the lower binding energy range centred at 8.02 ± 0.54 eV and 10.19 ± 0.39 eV, which can be attributed to the contribution from the TEOA solute. The spectrum was fitted to a superposition of Gaussian envelopes with the peak positions and widths obtained for the reference $NaCl_{(aq)}$ solution being fixed in the fit to the TEOA solution data. The energetic positions of the decomposed emission bands of the neat water molecular orbitals and the TEOA solute obtained from the fit are summarised in Table 6.4.

TABLE 6.4: Fit parameters of the Gaussian envelopes used to describe the emission bands of the neat-water molecular orbitals and the TEOA solute in the photoemission spectra. The electron binding energies are presented with respect to E_{vac} and E_F.

Peak Origin	Label	E vs. E_{vac}/ eV	E vs. E_F / eV	FWHM / eV	A / cts
TEOA	1	8.02 ± 0.54	3.35 ± 0.54	1.11 ± 0.59	14.58 ± 6.79
TEOA	2	10.19 ± 0.39	5.44 ± 0.42	1.59 ± 0.30	84.21 ± 16.31
H_2O $1b_{1,liq}$	3	11.33 ± 0.31	6.66 ± 0.34	1.59 ± 0.24	256.08 ± 15.65
H_2O $1b_{1,g}$	4	12.93 ± 0.29	8.26 ± 0.32	0.76 ± 0.01	596.65 ± 6.28
H_2O $3a_{1,liq}$L	5	13.09 ± 0.29	8.42 ± 0.32	1.50 ± 0.07	200.12 ± 7.25
H_2O $3a_{1,liq}$H	6	14.53 ± 0.32	9.86 ± 0.35	1.50 ± 0.05	200.08 ± 21.36
H_2O $3a_{1,g}$	7	15.15 ± 0.29	10.45 ± 0.32	1.37 ± 0.04	585.37 ± 9.06
H_2O $1b_{2,liq}$	8	17.13 ± 0.41	12.46 ± 0.44	2.05 ± 0.15	338.32 ± 12.04
H_2O $1b_{2,g}$	9	18.97 ± 0.30	14.30 ± 0.33	1.78 ± 0.14	901.37 ± 16.24

Since the electronic structure of the PCN thin films were interrogated from the steady-state PES spectra on an absolute binding energy scale with respect to E_F, such energy referencing of the $TEOA_{(aq)}$ solution must also be adopted to enable related valence band determination (with respect to the Fermi level) and a solid-liquid comparison. With the help of the Fermi edge position of the gold reference sample, solute and solvent binding energies can be determined without the commonly used local-vacuum-energy referencing of the LJ-PES spectra to the lowest-energy $1b_{1,liq}$ of neat liquid water. Figure 6.7 shows the steady-state EUV photoemission spectra of 750 mM $TEOA_{(aq)}$ solution and 50 mM $NaCl_{(aq)}$ solution presented with respect to the E_F energy scale. Based on the aforementioned energy referencing procedure utilising the metallic reference sample, the local vacuum and E_F energy scales were approximately related to each other. The steady-state PES spectrum of the gold (Au) reference sample, sequentially recorded under the same experimental conditions, was used to determine the Fermi edge. The Fermi edge was fitted to a Fermi-Dirac distribution function [288] to define the zero binding energy point position for the reference $NaCl_{(aq)}$ solution and $TEOA_{(aq)}$ solution LJ-PES spectra with respect to the E_F. The Fermi edge of the measured Au reference spectrum (multiplied by a factor of 30 for better visualisation) is presented in Figure 6.7. Following peak height normalisation to the $1b_{1,liq}$ emission peak position and binding-energy-shifting to overlap the positions of the water $1b_{1,liq}$ peaks in the two solutions, the reference 50 mM $NaCl_{(aq)}$ solution spectrum was subtracted as a background to extract the solute-related signal from the $TEOA_{(aq)}$ data.

Figure 6.8 shows the difference between the water solvent and the $TEOA_{(aq)}$ solution spectra. The solvent-subtracted signal was fitted to a superposition of two Gaussian envelopes, described by Equation 2.1, to extract the energy positions of the peaks corresponding to the removal of an electron from the HOMO and HOMO-1 of the TEOA solute within the photoionisation process. The fit result is presented as the black curve, the individual Gaussian envelopes are also highlighted in the figure

as violet-filled Gaussian profiles. After such a subtraction, two emission bands of the TEOA solute are resolved at 3.35 ± 0.54 eV and 5.44 ± 0.42 eV binding energies with respect to E_F (Table 6.4). By applying the tangent method (using Equation 6.3), the VBM of the sample was also extracted from the recorded LJ-PES difference spectrum. The inset in Figure 6.8 shows the VBM of the TEOA solvent with the tangent (red dashed line) used to determine the edge position. The extracted VBM value of the TEOA solute is 2.31 ± 0.38 eV. This value differs from the previously reported cyclic and differential pulse voltammetry studies [436–438], where the irreversible oxidation potential for the $TEOA_{(aq)}$ solution was found to vary between 0.5 V and 1.07 V (or eV) *versus* SHE depending on both the TEOA concentration and the pH of the solution. It is important to highlight the fact that no PES studies of the TEOA solute have been performed to date. The results of this work go beyond previous reports, showing that a high-resolution spectroscopic technique, such as LJ-PES can provide binding-energy-resolved spectral information on the valence electronic structure of the $TEOA_{(aq)}$ solution and TEOA solute.

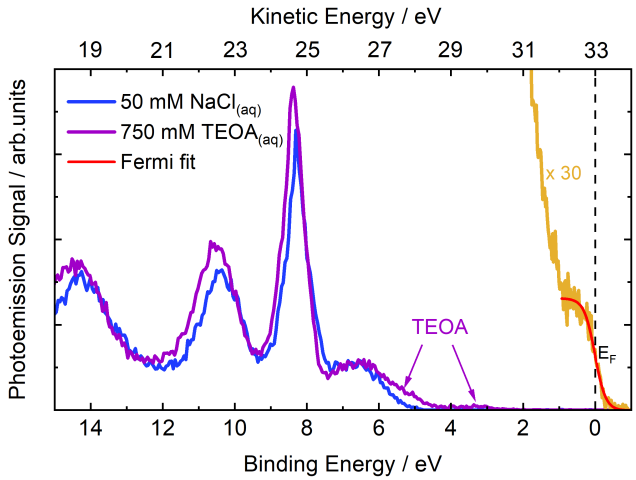

FIGURE 6.7: Steady-state EUV photoemission spectrum of the reference 50 mM $NaCl_{(aq)}$ solution and the 750 mM $TEOA_{(aq)}$ sample solution, binding energy referenced with respect to the Fermi level, E_F. The Fermi edge of the gold reference sample (yellow line) used to calibrate the energy scale is depicted in the figure.

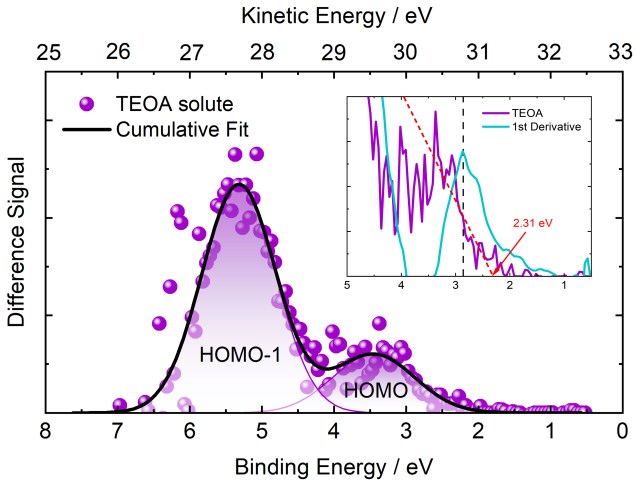

FIGURE 6.8: The difference between the water solvent and the $TEOA_{(aq)}$ solution spectra, with a focus on the low binding energy region, highlighting two low binding energy emission peaks of the TEOA solvent as well as the VBM position determined from the tangent intersection with the binding-energy-axis, as highlighted in the inset.

In accordance with the values obtained for the VBM position of the PCN thin films and TEOA solute from the steady-state EUV photoemission spectra, the VBM and CBM potentials were compared to the standard redox potentials of water. An accurate determination of the band edge potentials of the PCN thin films and the TEOA sacrificial agent allows an estimation of the catalyst-sacrificial agent interfacial energetics and to evaluate the maximum redox potentials of the photogenerated electron-hole pairs in the photocatalyst, which plays a major role in efficiently driving photocatalytic water splitting reaction (see Section 2.2.2). Note the assumption that the interfaces are unaltered by their interactions in a real water-splitting system is considered here.

Figure 6.9 shows a schematic diagram of the band edge alignment of the PCN thin films and TEOA solute within a semiconductor band structure framework, as well as the redox electrochemical potentials of the HER (H^+/H_2) and OER (O_2/H_2O). The energy scale is presented relative to the electrochemical potential in a solution containing a redox couple, equivalent to the Fermi level, $E_{\mathrm{F,redox}}$, in eV, when E_{F} in a solid sample and $E_{\mathrm{F,redox}}$ are in equilibrium. The absolute potential of SHE in water $E_0^{SHE}(\mathrm{H^+/H_2})_{\mathrm{H_2O}} = 4.44 \pm 0.02\,\mathrm{eV}$ (or V) at 298 K [155], relative to the electron in vacuum close to the solution surface, was set as zero of the energy scale. Since in photocatalytic water splitting reaction, solid-state PCN compounds are dispersed in a pH-dependent aqueous electrolyte solution (e.g. $\mathrm{TEOA}_{(aq)}$, pH = 7.0), electrochemical potentials of the two systems must be compared to the reference electrode, whose potential depends on the pH of the solution. Thus, the VBM energy positions, E_{VBM}, obtained for the PCN thin films from the solid-state PES experiments and presented as electron binding energies relative to E_F, were used to calculate the electrochemical potentials of the samples relative to the RHE at pH 7.0. Based on Equation 2.4, the calculated E_{VBM} values for the sg-CN, CNB, CNPS-O, and CNPS-NH_2 thin films *versus* RHE are 1.56 $\pm$ 0.37 eV, 1.66 $\pm$ 0.34 eV, 2.24 $\pm$ 0.36 eV, and 1.26 $\pm$ 0.31 eV, respectively. Taking into account the band gap energy, E_g, values, for the *direct allowed* electronic transitions in the PCN thin films, as determined from the Tauc plots (Section 6.1.2), the CBM energy positions, E_{CBM}, for the solid samples *versus* RHE are estimated to be - 1.32 $\pm$ 0.39 eV, - 1.29 $\pm$ 0.37 eV, - 0.82 $\pm$ 0.37 eV, and - 1.87 $\pm$ 0.33 eV, respectively. The associated E_g values and the E_{VBM} energetic positions relative to the E_F are summarised in Table 6.5.

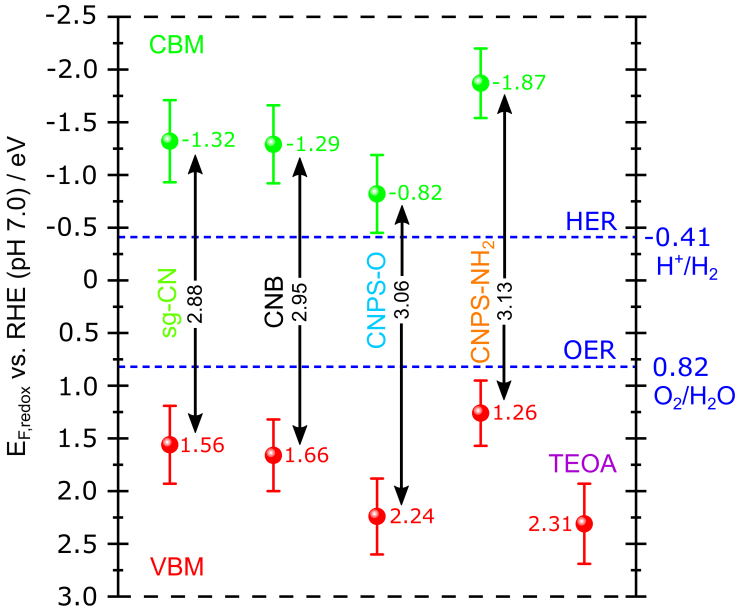

FIGURE 6.9: A schematic diagram of the band edge alignment of the PCN thin films as compared to the TEOA solute within a semiconductor band structure framework. The respective water redox potentials are shown by the blue dashed lines. The energy scale is presented relative to the electrochemical potential versus the RHE. The obtained E_{VBM}, E_{CBM} and E_{g} values are summarised in Table 6.5.

TABLE 6.5: The E_g values and the E_{VBM} energetic positions relative to E_F, used to determine the E_{VBM} and E_{CBM} values *versus* RHE for the PCN thin films.

Sample	E_g / eV	E_{VBM} vs. E_F / eV	E_{CBM} vs. E_F / eV	E_{VBM} vs. RHE / eV	E_{CBM} vs. RHE / eV
sg-CN	2.88 ± 0.02	1.98 ± 0.35	-0.90 ± 0.37	1.56 ± 0.37	-1.32 ± 0.39
CNB	2.95 ± 0.03	2.08 ± 0.32	-0.87 ± 0.35	1.66 ± 0.34	-1.29 ± 0.37
CNPS-O	3.06 ± 0.01	2.65 ± 0.34	-0.41 ± 0.35	2.24 ± 0.36	-0.82 ± 0.37
CNPS-NH_2	3.13 ± 0.02	1.68 ± 0.29	-1.45 ± 0.31	1.26 ± 0.31	-1.87 ± 0.33

As can be seen from Figure 6.8, for all four PCN samples the thermodynamic condition for driving a single-step, overall water-splitting reaction is satisfied for both HER and OER. Specifically, the mesoporous, sg-CN, and bulk, CNB, polymeric carbon nitride samples, with the moderate E_g values of 2.88 eV and 2.95 eV, respectively, similarly possess sufficiently large thermodynamic driving force for H_2 (0.91 eV for sg-CN and 0.88 eV for CNB) and O_2 (0.74 eV for sg-CN and 0.84 eV for CNB) evolution. The electronic band structure of the porous oxygen-rich carbon nitride nanosheets, CNPS-O, suggests that the presence of an oxygen-containing group provides a greater driving force for the OER (1.42 eV vs O_2/H_2O) and an inferior one for the HER (0.41 eV vs H^+/H_2). The potential of the CBM of the amino functional group, atomically-thin porous carbon nitride nanosheets, CNPS-NH_2, is notably higher than those of the other samples (1.46 eV vs H^+/H_2), which can provide a relatively large thermodynamic driving force for the HER.

6.3 Time-resolved EUV Photoemission Studies of Polymeric Carbon Nitride Thin Films

The time-resolved EUV photoemission spectra of the sg-CN, CNB, CNPS-O, and CNPS-NH_2 thin films were recorded in the wide-angle mode (WAM) and the low-angular dispersion mode (LADM) of the electron spectrometer following application of the pump and probe pulses. The WAM was used to record the ground and transient excited states spectra over a narrow kinetic energy range (≈ 7 eV) with a higher signal-to-noise ratio, allowing to map the photoinduced electron dynamics of the PCN samples near the Fermi level. The LADM was used to expand the kinetic energy range of the recorded ground and transient excited states spectra to ≈ 15 eV, enabling detection of the transient signal in a wider energy range, but with a lower signal-to-noise ratio. The pump pulses of 400 nm wavelength (3.1 eV photon energy) and 55 fs pulse durations (FWHM) were applied to initiate the electronic transitions centered at a photon energy around 3.21 eV in the PCN thin films. Utilising the PES experimental setup and the high-harmonic monochromator, the 21^{st} harmonic of 800 nm was used as the probe beam to photoionise the system and, thus, to monitor the changes in the relaxing system at various time delays of the pump with respect to the probe pulses.

Central photon energies of 32.52 ± 0.05 eV or 32.43 ± 0.08 eV with spectral bandwidths of 265 ± 7 meV and 200 ± 5 meV were applied in the WAM and LADM TRPES experiments, respectively. The EUV probe beam was focused into the interaction chamber resulting in a focal spot size of 60 μm (FWHM) at the sample surface. The produced monochromatised EUV probe pulses with 45 fs (FWHM) pulse durations and a photon flux of 10^6 photons pulse^{-1} yielded spatial peak intensity of 2×10^6 W cm^{-2} in the interaction region. The pump beam was sent through a variable optical delay linear translation stage and was focused into the interaction region, resulting in a focal spot size of 150 μm (FWHM). The spatial peak intensity of the pump pulse at the focus was attenuated by a half-wave plate to suppress the multiphoton ionisation as well as to avoid photochemical degradation of the sample. As a result, the pump pulse energies of approximately 50 nJ pulse^{-1} were applied in

the TRPES experiments on the PCN thin films. This corresponded to spatial peak pump pulse intensities of 5×10^9 W cm^{-2} in the sample interaction region. The pump and probe beam polarisation alignment were parallel to each other and to the spectrometer time-of-flight axis. The TRPES spectra were recorded by scanning the pump-probe time delay over a range from - 400 fs to + 2500 fs with a high-temporal resolution of 20 fs. To improve the signal-to-noise levels the delay range was swept through 15 – 25 times.

6.3.1 Transient Photoemission Spectra of PCN Thin Films

The early-time electron dynamics of the PCN thin films following 400 nm wavelength photoexcitation were studied at the surface-vacuum interface using TRPES. Figure 6.10 shows the 2D colour maps representing the transient photoemission signal from the sg-CN, CNB, CNPS-O, and CNPS-NH_2 thin films recorded as a function of the electron binding energy and the time delay between the pump and probe pulses in the WAM and LADM of the spectrometer. The relative magnitude of the photoemission yield (individually normalised) is presented by the colour bar in the figures. The electron binding energy scale in Figure 6.10 is energy referenced with respect to E_F, as determined from the steady-state PES measurements on the reference metal sample. To enhance the visibility of the transient signal, the EUV emission spectrum of the unpumped sample, recorded at negative time delays and averaged over the range between - 400 fs and - 200 fs, was subtracted as a background spectrum from the pump-probe photoemission spectra at each time delay. The time zero position was corrected in each separate delay time scan, resulting in slightly different time delay axes for the background subtracted transient photoemission spectra. Due to the 5 kHz repetition rate laser source employed in the present experiments, the acquired photoemission signals exhibit a low signal-to-noise ratio. For this reason, the 2D colour maps in Figure 6.10 show rebinned transient data over the binding-energy-axis with a bin size of 0.25 eV and 0.35 eV for the WAM and LADM, respectively. However, the integration of the transient signal over the different binding energy ranges gives much better statistics, as shown in Figure 6.14 and Figure 6.17. To confirm that the PCN thin film samples were chemically stable during the TRPES measurements, the photoemission spectra obtained at the beginning and end of the time-resolved measurements are also presented in Appendix B (Figure B.2).

The left panels in Figure 6.10 show the transient photoemission spectra of the PCN samples recorded in the WAM of the spectrometer. The background-subtracted transient spectra are presented over the binding energy range of -3.6 – 3.3 eV, -4.9 – 2.1 eV, -5.0 – 1.9 eV, and -4.3 – 2.7 eV for the sg-CN, CNB, CNPS-O, and CNPS-NH_2 thin films, respectively. The time delay axes correspondingly span the ranges from - 376 fs to + 2444 fs, - 426 fs to + 2313 fs, - 273 fs to + 2387 fs, and - 284 fs to + 2395 fs, respectively. The negative bleach signal (blue colour), which appears after the background subtraction in the transient data at positive time delays, is due to the depletion of the electronic ground state population of the PCN samples, as induced by the pump beam. The PCN thin films' ionisation contributions to the photoemission yield are prominent at positive electron binding energies. The transient signal shown in the left panels in Figure 6.10 includes a strong negative binding energy feature at short time delays within the $\pm$ 100 fs range. This signal is attributed to the cross-correlation (CC) signal from the PCN samples when the pump and probe pulses are temporally overlapped. The experimental time zero positions as well as the time resolutions of the TRPES experiments were determined by using an Ar gas target prior to each experiment and integrating the transient signal in the binding energy range where the pump and probe pulses overlap in time (Section 4.4.4).

Figure 6.11 (upper panel) shows the time dependence of the transient signal recorded with the 400 nm pump pulse and the 38 nm (21^{st} harmonic) probe pulse from Ar gas, recorded in the WAM of the spectrometer. The transient signal was fitted to a Gaussian envelope to determine the CC width. The obtained CC width of 80 $\pm$ 16 fs (FWHM) represented the time resolution in the TRPES experiments conducted in the WAM of the electron spectrometer. The short CC width allows the revelation of the early-time electron dynamics on a sub-100 fs time scale. Besides the prominent CC signal, there is a clear indication (left panels in Figure 6.10) of an enhanced photoemission transient signal at the

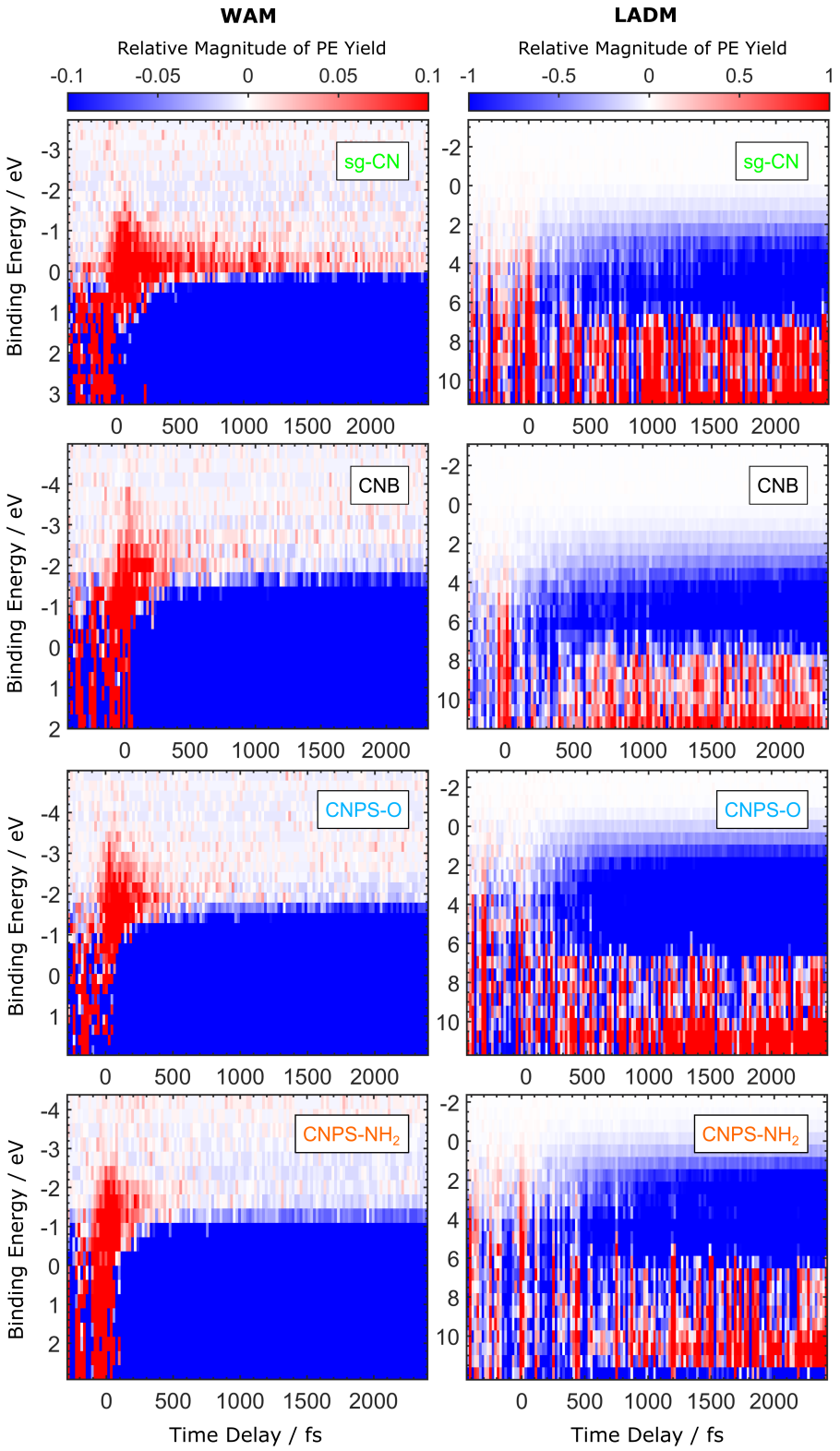

FIGURE 6.10: 2D colour maps of the transient photoemission signal as a function of the electron binding energy and pump-probe time delay for the PCN samples recorded in the WAM (left panels) and LADM (right panels) of the spectrometer. For better visualisation of the transient signal, the time-independent background signal recorded at negative pump-probe delays has been subtracted from the measured data. The binding energy scale is energy-referenced with respect to the spectrometer E_F.

positive time delays in the lower (i.e. negative) binding energy range. The short-lived transient signal is apparent in the binding energy ranges -2 – 1 eV, -3 – 0 eV, -4 – -1 eV and -4 – -1 eV in the sg-CN, CNPS-NH_2, CNB and CNPS-O samples, respectively. In these binding energy ranges, the transient signal dissipates within 1 ps. However, a persistent negative transient signal intensity arising in the higher binding energy range suggests that the lifetime of the excited states is long and the relaxation to the ground state is comparatively slow. Due to the predominant photoemission signal from the ground state, the photoemission features from the excited states are generally not directly visible in the binding energy range below 0 eV.

The right panels in Figure 6.10 show the transient photoemission spectra of the PCN samples recorded in the LADM of the spectrometer. The extended binding energy range in the LADM revealed the long-lived transient signal in the higher binding energy range. Here, the background subtracted transient spectra are presented over binding energy ranges of -3.05 – 10.93 eV, -2.20 – 11.00 eV, -1.95 – 11.45 eV, and -1.9 – 11.4 eV for the sg-CN, CNB, CNPS-O, and CNPS-NH_2 thin films, respectively. The time delay axis spans the range of - 265 fs to + 2335 fs, - 472 fs to + 2447 fs, - 428 fs to + 2411 fs and - 480 fs to + 2420 fs, respectively. Analogously to the WAM results, the negative values at positive time delays in the background-subtracted signal spectra originate from the depletion of the sample ground states upon photoexcitation by the 400 nm pump laser pulses. Note that for better visualisation of the positive signal from ionisation of the transient excited states, the relative magnitude of the colour scale of the photoemission yield differs in the 2D colour maps presented for the WAM and LADM. Therefore, the negative values of the transient signal at positive time delays seemingly but artificially emerge at different binding energy ranges in the left and right panels in Figure 6.10. Due to the lower collection efficiency, the positive transient signal in the LADM is less readily identified in the electron binding energy range below about 2 eV in comparison to that

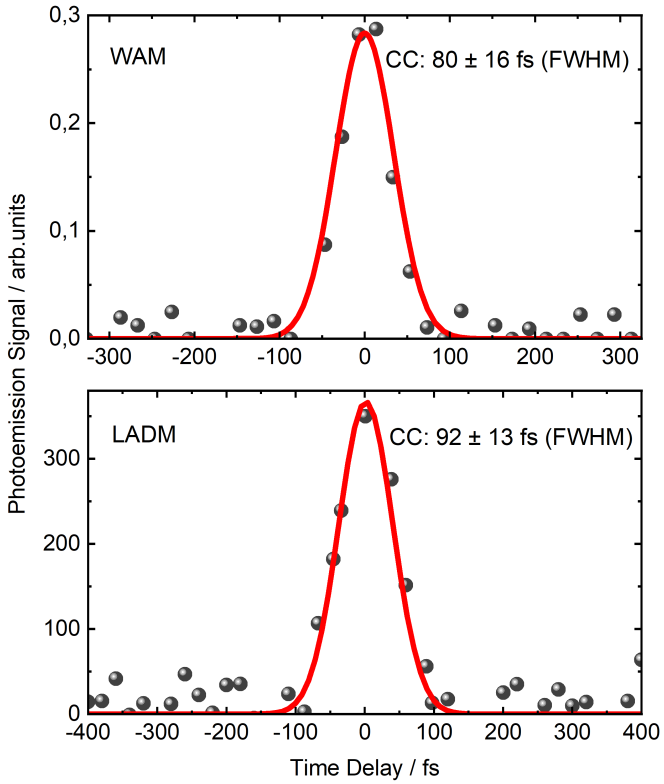

FIGURE 6.11: Transient photoemission signal as a function of pump-probe delay (grey circles) recorded with the use of Ar gas in WAM and LADM. The FWHM of the CC signal fitted to a Gaussian envelope (red curve) represents the time resolution of TRPES experiments conducted in the two modes of the TOF spectrometer.

collected in WAM. This also has an impact on the strength of the positive feature associated with the CC signal from the PCN samples in the vicinity of zero time delay. The energetic position of the CC signal in the transient photoemission spectra recorded in the LADM extends over a range from approximately 11 eV to 0 eV binding energy, which is most prominent in the higher binding energy range. Figure 6.11 (lower panel) shows the time dependence of the transient signal recorded with the use of an Ar gas target in the LADM of the spectrometer, integrated over the binding energy range of temporally overlapped pump-probe pulses. The signal fitted to a Gaussian envelope was used to determine the CC width. The obtained symmetric CC width of 92 $\pm$ 13 fs (FWHM) represents the time resolution in the TRPES experiments using LADM of the spectrometer. Apart from the CC signal, there is a clearly visible buildup of positive transient signal within the first few hundred femtoseconds in the binding energy range above $\approx$ 6 eV (right panels in Figure 6.10). This long-lived transient signal remains constant until the maximum delay time applied in the experiment and strongly contributes to the emission signal in the binding energy range centered around 10 eV.

6.3.2 Kinetic Model and Global Fitting of the Ultrafast Kinetics at the Surface-Vacuum Interface

The analysis of the transient photoemission spectra, which reveals the ultrafast kinetics of the photoexcited PCN samples at the surface-vacuum interface, was based on solving sets of kinetic equations that are used to model the time-dependent population of electronic states using a global fitting procedure. According to the previously reported PCN time-resolved photoluminescence and absorption spectroscopy studies [419–421, 439], the decay of the initially populated state upon 400 nm excitation in PCN powders and colloids occurs within about 200 fs. The dynamics that occurs on this timescale is also present in the transient photoemission spectra of the PCN thin films, specifically as a prominent transient signal in the low binding energy range; this is apparent in the transient photoemission spectra recorded in the WAM of the spectrometer. Also, there is a clear indication of the subsequent population of an excited electronic state that decays within 1 ps, which was not previously observed.

The transient signal prevailing in the photoemission spectra recorded in the LADM of the spectrometer indicates a further buildup of population in a long-lived electronic state at higher binding energy range. The long-lived dynamics in the PCN colloids after light excitation has previously been attributed to the formation of a charge-transfer (CT) or a singlet exciton (SE) state [419–421]. Thus, based on the observed spectroscopic features as well as previously reported results, the early-time electron dynamics of PCN thin films following 400 nm optical excitation can be represented in terms of a 4-state kinetic model, with sequential population of the involved electronic states, as further discussed in in the following pages. The proposed photocycle is schematically depicted in Figure 6.12. The kinetic model includes the minimum number of electronic states required to describe the population dynamics and transition channels in the PCN samples, as based on a global analysis of the measured multidimensional data in both the WAM and LADM of the spectrometer.

From the experimental observations, as well as the associated kinetic modeling, the following description of the photoinduced electron dynamics of the PCN thin films at the surface-vacuum interface is proposed. The optical excitation with a 400 nm wavelength leads to electron transfer from the electronic ground state (GS) to a first excited state (ES1), corresponding to a dipole-allowed electronic transition at 3.21 eV central photon energy (see Table 6.1) . The excited ES1 state undergoes a fast relaxation process and populates a short-lived intermediate state (ES2). The sequential relaxation of the intermediate ES2 state leads to the formation of a long-lived metastable state (ES3) followed by the further electronic relaxation processes on a timescale that significantly exceeds the time delay range used in the TRPES experiments. This kinetic model describing the early-time electron population dynamics of the PCN thin films will be extended later based on the results of TAS experiments, which can reveal kinetics on much longer time scales.

The early-time electron population dynamics of the sg-CN, CNB, CNPS-O and CNPS-NH_2 thin films at the surface-vacuum interface can be described by a 4-state (ES1, ES2, ES3, and GS) kinetic

model with the sequential population of the involved states as:

$$\mathrm{GS} \xrightarrow{P(t)} \mathrm{ES1} \xrightarrow{k_1} \mathrm{ES2} \xrightarrow{k_2} \mathrm{ES3} \xrightarrow{k_3} \mathrm{X}, \tag{6.4}$$

where k_{1-3} denote the rate constants that characterise the sequential transitions to the intermediate state ES2, to the metastable state ES3, and to the subsequent excited electronic states referred to as X, respectively. *P(t)* is the time-dependent excitation rate of the initially populated state ES1 from the ground state GS, which is described by a Gaussian temporal envelope of the pump pulse, $P(t) \propto \exp(-t^2/\sigma_{pump}^2)$, where σ_{pump} is the pump pulse FWHM.

The system of differential equations applied to describe the electron population dynamics has the following form:

$$\begin{aligned}
\frac{d[\mathrm{GS}]}{dt} &= -P(t)\cdot[\mathrm{GS}] \\
\frac{d[\mathrm{ES1}]}{dt} &= P(t)\cdot[\mathrm{GS}] - k_1\cdot[\mathrm{ES1}] \\
\frac{d[\mathrm{ES2}]}{dt} &= k_1\cdot[\mathrm{ES1}] - k_2\cdot[\mathrm{ES2}] \\
\frac{d[\mathrm{ES3}]}{dt} &= k_2\cdot[\mathrm{ES2}] - k_3\cdot[\mathrm{ES3}]\ ,
\end{aligned} \tag{6.5}$$

where $[Q]$ denotes the population of state Q (Q = GS, ES1, ES2, or ES3) with the initial condition [ES1] = 0, [ES2] = 0 and [ES3] = 0 at $t \to -\infty$ and [GS] = 1.

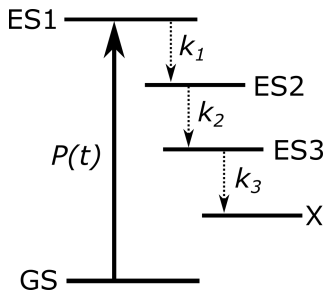

FIGURE 6.12: Schematic depiction of the PCN thin film photocycle at the surface-vacuum interface following 400 nm optical excitation. The rate parameters described in Equation 6.5 are used to label the diagram.

The transient signals shown in Figures 6.13 and 6.16 were analysed using a global fitting procedure with the fit function described by Equation 3.70. Based on the global analysis procedure described in Section 3.5.1, the system of differential Equations 6.5 which represents the state population dynamics of the PCN samples was solved numerically to extract a transition rate constants k_{1-3}. For the transient signal recorded in the LADM, the photoemission spectrum, S_Q, of each state Q (see Equation 3.76) was additionally modeled and fitted implicitly by a superposition of Gaussian envelopes, allowing the energetic positions of the photoemission spectral bands of the studied samples to be extracted, as described in detail in Section 3.5.

- **Global Analysis of the Transient Photoemission Spectra Recorded in WAM**

Figure 6.13 shows the 2D colour maps associated with and representing the transient photoemission signal from the PCN thin films, as recorded in the WAM of the spectrometer. The experimental results (left panels) were obtained after probe-only background subtracting the measured pump-probe data. Global fit results are also shown (middle panels). Analogously to the experimental data, the GS photoemission spectra of the PCN samples, as obtained from the respective fit, were subtracted from

the modeled transient spectra. The residual maps were determined via subtraction of the experimental data from the corresponding global fitting results. Systematic errors are seen in the residual maps, especially in the regions of the bleach signal, resulting from the inaccuracies of the mathematical modeling of the background-subtracted data. Within the measured binding energy range in the WAM, Figure 6.13 shows a population of short-lived transient electronic states in the PCN thin films on an ultrafast timescale. The ultrafast dynamics of the electronic population, which appears as a prominent transient signal at a lower binding energy range, is highlighted with dashed black lines.

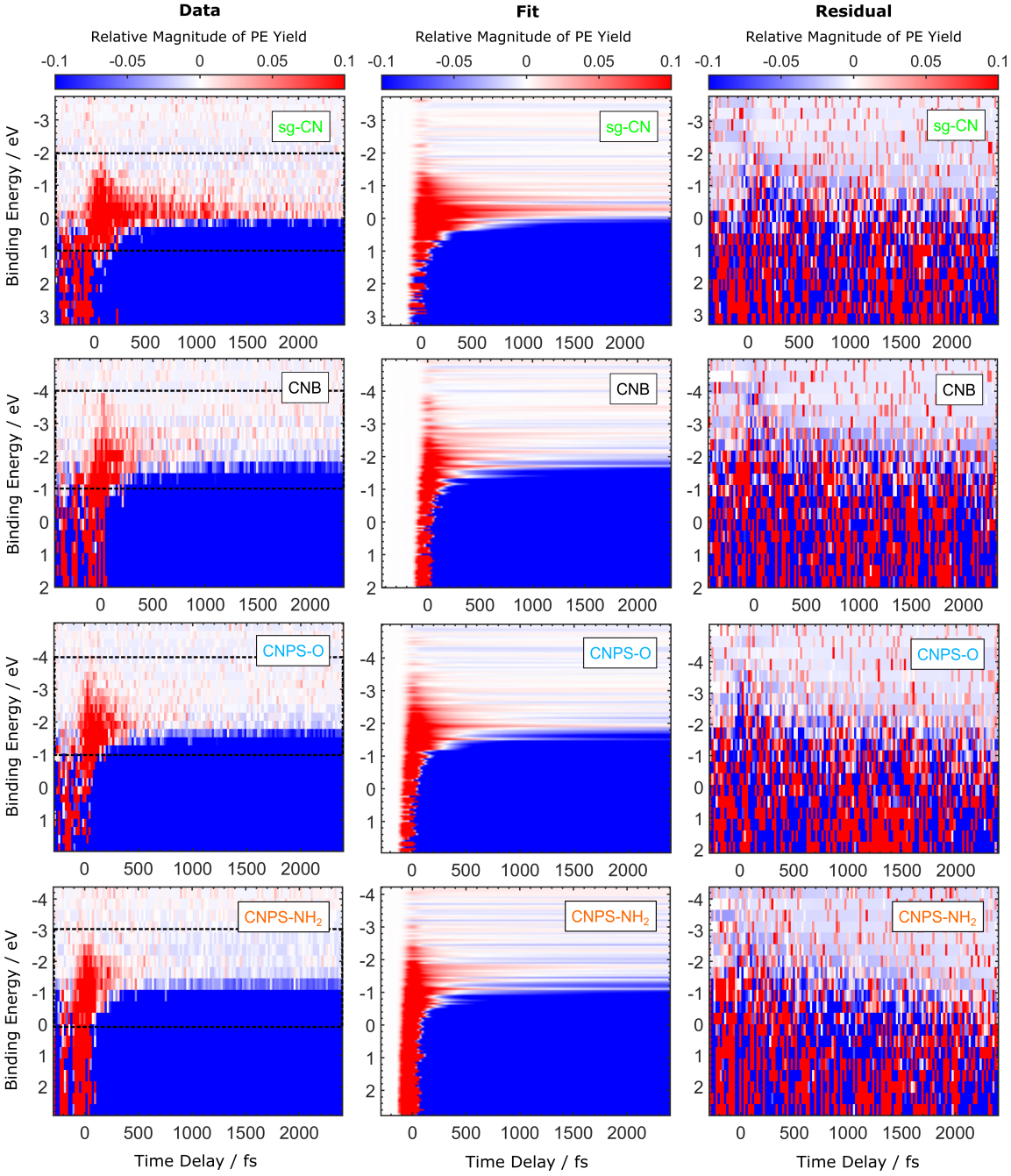

FIGURE 6.13: Global fitting reproduction of the experimental transient photoemission spectra for the PCN thin films recorded in the WAM of the spectrometer with the use of the kinetic model described by Equation 6.5. The residual 2D colour maps were determined by subtracting the experimental data and the corresponding fit results. The data is energy-referenced with respect to E_F of the spectrometer.

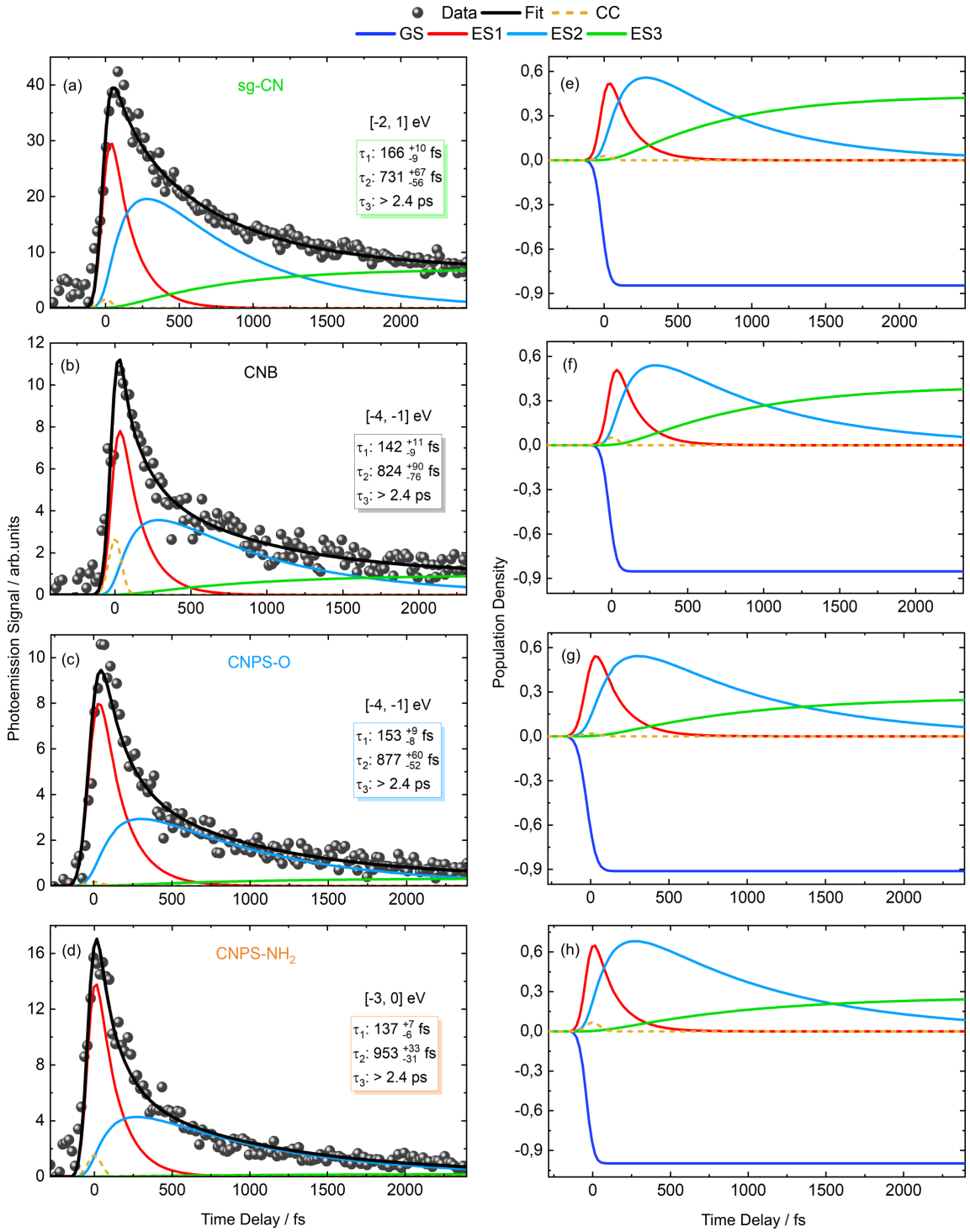

FIGURE 6.14: The time dependence of the transient signal integrated over the lower binding energy ranges encompassing the population of the short-lived excited states in the PCN thin films. The corresponding transient population densities of the ground and excited electronic states involved in the kinetic model, as described by Equation 6.5 and extracted from the global fit analysis are shown in panels (e) – (h). The fit component of the negative transient signal associated with the depletion of the ground state was subtracted from cumulative fit results and is not presented in panels (a) – (d). The decay time constants, τ_{1-3}, obtained from the fit results are shown in the inset.

The transient photoemission yields, which are obtained by binding energy integration of the experimental transient spectra and from the global analysis results for a given delay time, are presented in Figure 6.14. Panels (a) – (d) in Figure 6.14 show the decomposition of the transient signal into individual contributions from the involved ground and excited electronic states, as well as the CC signal, which was obtained from the global fit using the kinetic model described by Equation 6.5. The decomposition is presented for selected binding energy ranges, -2 – 1 eV, -4 – -1 eV, -4 – -1 eV, and -3 – 0 eV for the sg-CN, CNB, CNPS-O, and CNPS-NH_2 thin films, respectively, where the photoemission yields of the short-lived excited states ES1 and ES2 are the highest, according to the global fitting results. The dominant, negative-intensity time-independent transient signal associated with the depletion of the ground state is subtracted from the spectra in these figures. Panels (e) – (h) in Figure 6.14 show transient population densities obtained from the fits for the ground and excited states of the sg-CN, CNB, CNPS-O, and CNPS-NH_2 thin films, respectively. Taking into account the initial condition of ground state population, [GS] = 1 (blue line), after depletion of the initial state population, the GS population appears with negative-intensity values at positive time delays.

Figure 6.14 demonstrates that apart from the CC signal (yellow dashed line), the three components associated with the ES1 (red), ES2 (cyan), and ES3 (green) excited electronic states contribute to the energy-integrated transient photoemission signal, which survives over the full 2.5 ps probed time delay range. The initially populated ES1 state, appears to undergo ultrafast relaxation to an intermediate ES2 state within 166 $^{+10}_{-9}$ fs, 142 $^{+11}_{-9}$ fs, 153 $^{+9}_{-8}$ fs, and 137 $^{+7}_{-6}$ fs in the sg-CN, CNB, CNPS-O, and CNPS-NH_2 thin films, respectively. Afterwards, the population is transferred from the ES2 state to a metastable ES3 state, where a slower relaxation takes place on a 731 $^{+67}_{-56}$ fs, 824 $^{+90}_{-76}$ fs, 877 $^{+60}_{-52}$ fs, and 953 $^{+33}_{-31}$ fs timescale in the sg-CN, CNB, CNPS-O, and CNPS-NH_2 thin films, respectively. The sequentially populated metastable ES3 state relaxes on much longer timescales than the maximum measured pump-probe delay time applied in the TRPES experiments. The decay time constants, τ_{1-3}, obtained from the fit results represent the inverse values of the transition rates, k_{1-3}, and are summarised in Table 6.6. The error bars given in the table refer to the global fitting numerical results. The lowest boundary of the time constant associated with the ES3 $\rightarrow$ X transition, corresponding to the time delay span in the transient measurements, is presented in Table 6.6.

TABLE 6.6: Kinetic parameters obtained for the ES1, ES2, and ES3 states from the global fitting of transient photoemission spectra of the PCN thin films recorded in the WAM of the spectrometer.

Parameter	sg-CN	CNB	CNPS-O	CNPS-NH_2
τ_1 (ES1 $\rightarrow$ ES2)	166 $^{+10}_{-9}$ fs	142 $^{+11}_{-9}$ fs	153 $^{+9}_{-8}$ fs	137 $^{+7}_{-6}$ fs
τ_2 (ES2 $\rightarrow$ ES3)	731 $^{+67}_{-56}$ fs	824 $^{+90}_{-76}$ fs	877 $^{+60}_{-52}$ fs	953 $^{+33}_{-31}$ fs
τ_3 (ES3 $\rightarrow$ X)	$>$ 2.4 ps	$>$ 2.4 ps	$>$ 2.4 ps	$>$ 2.4 ps
P(t)	0.048 $\pm$ 0.003	0.045 $\pm$ 0.008	0.032 $\pm$ 0.009	0.014 $\pm$ 0.005
σ_{pump}	57 $\pm$ 8 fs	55 $\pm$ 4 fs	56 $\pm$ 7 fs	57 $\pm$ 7 fs
σ_{probe}	45 $\pm$ 3 fs	42 $\pm$ 2 fs	44 $\pm$ 3 fs	46 $\pm$ 4 fs

The state-associated spectra for the PCN samples extracted from the global fits to the high kinetic energy photoemission spectra recorded in the WAM are shown in Figure 6.15. For better visualisation, the vertical axes in the figures are presented on a logarithmic scale. The global fit results imply that the shape of the photoemission spectra of all four involved electronic states is similar. The photoexcitation induced by the pump pulse, with the central photon energy of 3.1 eV, causes the appearance of the transient features associated with the ES1 and ES2 excited states at lower binding energies, shifted by the excitation energy with respect to the GS state. The contribution from the short-lived excited states is dominant in the low binding energy range, while it is absent from the long-lived ES3 state, as demonstrated from the transient data. The photoemission spectra of the ES2 state are shifted to

higher binding energies, which indicates a different nature of this state compared to ES1 and ES2. Additionally, the shift becomes more prominent for the CNPS-O and CNPS-NH_2 thin films, which may be related to the morphology and their microscopically ultrathin structure.

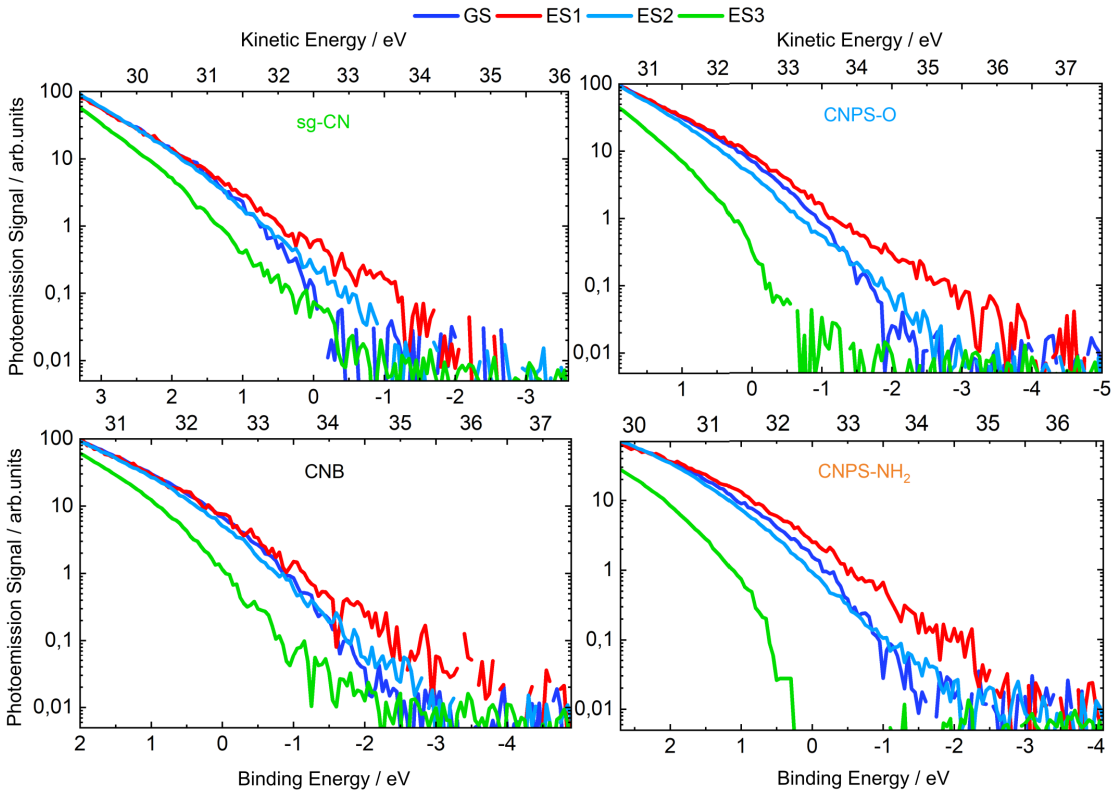

FIGURE 6.15: State-associated spectra of the electronic states extracted from global fits to the photoemission spectra for the PCN thin films recorded in the WAM following photoexcitation at 3.1 eV. The binding energy scale is energy-referenced with respect to the spectrometer E_F.

- **Global Analysis of the Transient Photoemission Spectra Recorded in LADM**

The 2D colour maps of the transient photoemission spectra data of the PCN thin films recorded in the LADM of the spectrometer and the global fit results, which were extracted with the use of the kinetic model described by Equation 6.5, are shown in Figure 6.16. The modeled photoemission spectra are presented after subtraction of the ground state spectrum of the PCN samples at a negative time delay. The negative-time delay fits were subtracted and the probe-only background subtracted data and ground state subtracted fit results are shown in the left and middle panels, respectively. The difference between the experimental photoemission spectra and the corresponding fit results are shown as residual 2D colour maps, demonstrating that the global fitting procedure reproduces the experimental data. The LADM data allows the mapping of the long-lived transient population dynamics and population build-up of excited electronic states in the PCN thin films. Such dynamics arises as a distinct positive transient feature in the high binding energy range, which is highlighted with dashed black lines in the left panels in Figure 6.16. The data is presented in more detail in Figure 6.17, where the time dependence of the transient signal is binding energy integrated over a range associated with a population of the long-lived dynamics (i.e. 7 – 11 eV). The decomposition of the transient signal into individual contributions from the involved electronic states and the CC signal is shown in panels (a) – (d) in Figure 6.17. The negative contribution to the transient signal, due to the depletion of the ground state, was subtracted from cumulative fit results (black curves) and is not present in these panels. The decomposed, integrated traces are shown in the binding energy ranges, 6.9 – 10.9 eV,

7 – 11 eV, 7.45 – 11.45 eV, and 7.4 – 11.4 eV for the sg-CN, CNB, CNPS-O, and CNPS-NH_2 thin films, respectively, to visualise the longed-lived population dynamics. The corresponding transient population densities obtained from the global fitting results for the ground and excited states of the sg-CN, CNB, CNPS-O, and CNPS-NH_2 thin films are presented in panels (e) – (h), accordingly.

Similar to the fit results obtained for the WAM data, the population of the ES1, ES2, and ES3 excited electronic states can be observed over the binding-energy-integrated transient signal covering the 0 – 2.5 ps time delay range using the LADM, shown in Figure 6.17. Following the population of

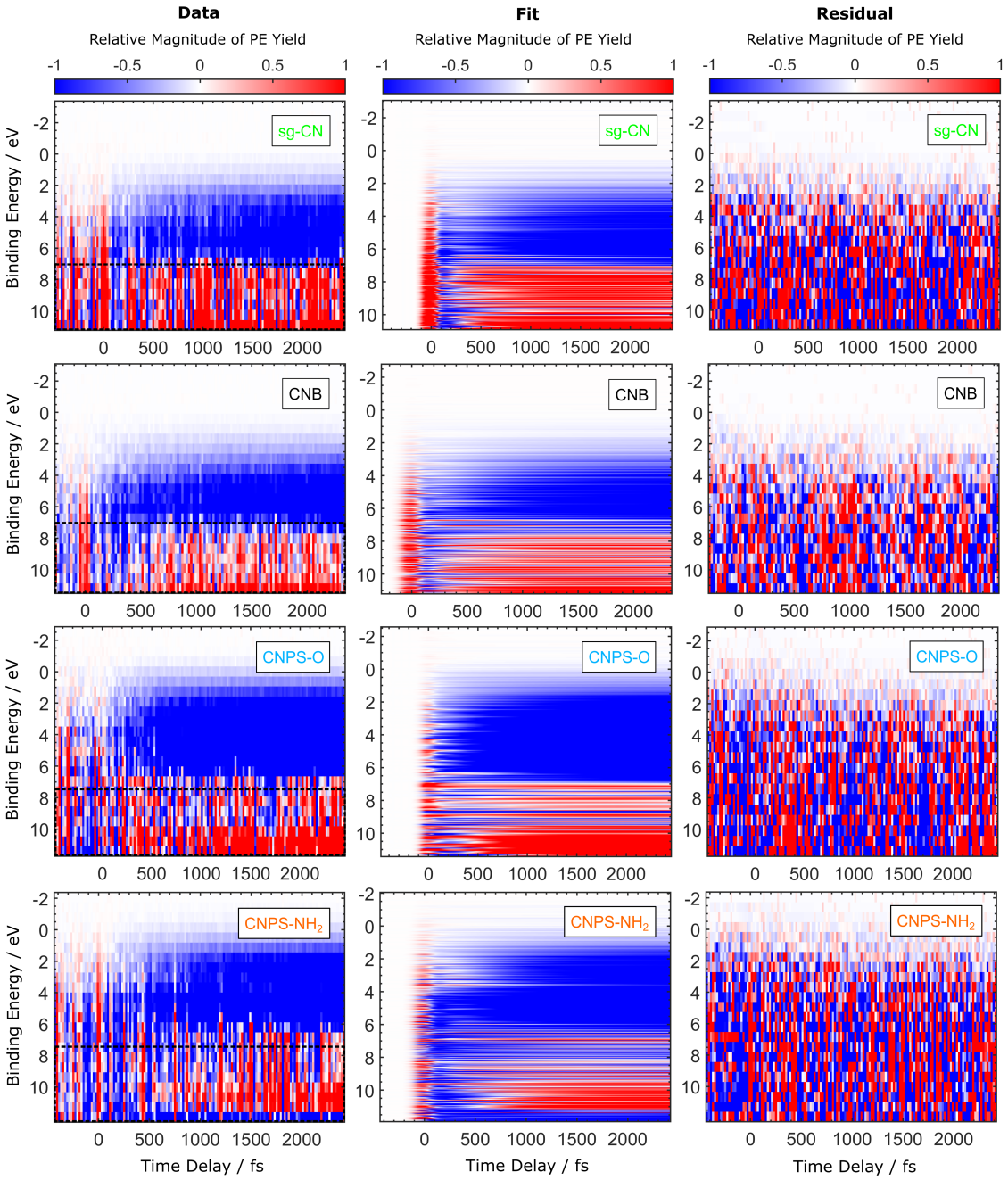

FIGURE 6.16: Global fitting reproduction of the experimental transient photoemission spectra for the PCN thin films recorded in the LADM of the spectrometer with the use of the kinetic model described by Equation 6.5. The residual data was extracted from the converged result of the global fitting procedures from the negative-time delay probe-only background subtracted data. The binding energy scale is energy-referenced with respect to the spectrometer E_F.

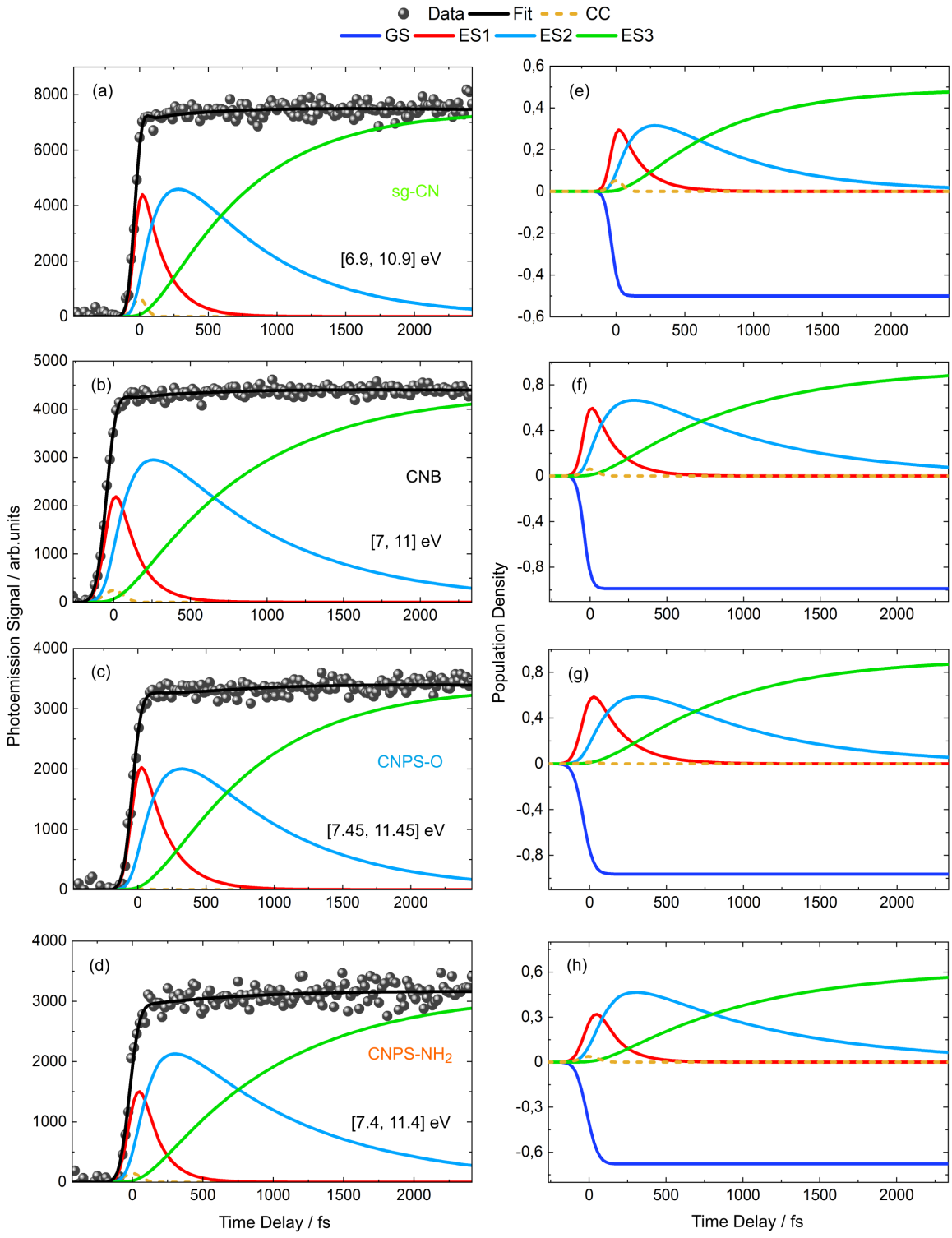

FIGURE 6.17: The time dependence of the transient signal recorded using LADM and integrated over the higher binding energy ranges encompassing the long lifetime state population dynamics in the PCN thin films. Panels (e) – (h) show the corresponding transient population densities obtained from the fits for the ground and excited states of PCN samples. The negative contribution to the transient signal due to depletion of the ground state was subtracted from the data (grey circles) and the cumulative fit results (black curves) and is not presented in panels (a) – (d).

the initially-excited ES1 state upon 400 nm excitation, the excited systems undergo ultrafast relaxation processes to populate the intermediate ES2 state. Based on the data recorded in the WAM, it was found that the ES1 state decays on a sub-150 fs time scale, which, within the error values obtained from the global fitting numerical results, is in agreement with the corresponding decay time constants obtained from the LADM data: 165 $^{+10}_{-9}$ fs, 138 $^{+8}_{-7}$ fs, 146 $^{+13}_{-11}$ fs, and 135 $^{+8}_{-7}$ fs for the sg-CN, CNB, CNPS-O, and CNPS-NH_2 thin films, respectively. The sequential relaxation of the ES2 state, leading to a formation of a metastable ES3 state, occurs within 709 $^{+39}_{-35}$ fs, 830 $^{+38}_{-35}$ fs, 903 $^{+75}_{-53}$ fs, and 960 $^{+39}_{-28}$ fs in the PCN samples, respectively. This result is also consistent with the one obtained from the WAM data. As can be clearly seen from Figure 6.17, the constant increase of the population of the metastable ES3 state within a given delay time range indicates a build-up of a long-lived state population, which is followed by further longer-time relaxation processes. The decay time constant associated with the relaxation of the populated ES3 state, obtained from the global analysis, is presented only as a lower boundary, based on the time-limited delay range applied in the TRPES experiments in the LADM, analogous to the WAM results. The decay time constants obtained for the ES1, ES2, and ES3 excited states from the global fitting procedure to the transient photoemission spectra of the PCN thin films recorded in the LADM of the spectrometer are summarised in Table 6.7.

TABLE 6.7: Kinetic parameters obtained for the ES1, ES2, and ES3 states from the global fitting of the transient photoemission spectra of the PCN thin films, as recorded in the LADM of the spectrometer.

Parameter	sg-CN	CNB	CNPS-O	CNPS-NH_2
τ_1 (ES1 $\rightarrow$ ES2)	165 $^{+10}_{-9}$ fs	138 $^{+8}_{-7}$ fs	146 $^{+13}_{-11}$ fs	135 $^{+8}_{-7}$ fs
τ_2 (ES2 $\rightarrow$ ES3)	709 $^{+39}_{-35}$ fs	830 $^{+38}_{-35}$ fs	903 $^{+75}_{-53}$ fs	960 $^{+39}_{-28}$ fs
τ_3 (ES3 $\rightarrow$ X)	$>$ 2.4 ps	$>$ 2.4 ps	$>$ 2.4 ps	$>$ 2.4 ps
P(t)	0.030 $\pm$ 0.006	0.031 $\pm$ 0.009	0.055 $\pm$ 0.003	0.055 $\pm$ 0.004
σ_{pump}	55 $\pm$ 4 fs	59 $\pm$ 6 fs	53 $\pm$ 7 fs	54 $\pm$ 4
σ_{probe}	42 $\pm$ 2 fs	38 $\pm$ 3 fs	44 $\pm$ 5 fs	40 $\pm$ 4 fs

The state-associated spectra for the PCN samples extracted from the global fits to the photoemission spectra recorded in the LADM are shown in Figure 6.18 on a logarithmic y-scale. The associated extended binding energy range demonstrates that there appears to be an additional transient signal that immediately emerges in the 6 – 11 eV spectral range and slowly grows when compared to the WAM data. Likewise, the photoemission spectra of the excited states reproduce the shape of the spectrum of the GS. The contribution from the short-lived ES1 and ES2 states at lower binding energies is barely visible due to a predominant photoemission signal arising at higher binding energies. Nonetheless, the characteristic shift of the photoemission signal associated with the long-lived ES3 state to higher energies is shown to occur analogously to that observed in the WAM data.

To roughly extract the energetic positions of the photoemission bands associated with the PCN thin films, the state-associated spectra derived from the implicit global fitting, presented in Figure 6.18, were fitted to a superposition of Gaussian envelopes using Equation 3.74. Figure 6.19 shows fit results for the state-associated spectra of the PCN samples associated with the ground and the excited states. In contrast to Figure 6.18, the data in Figure 6.19 is shown on a linear y-scale. The Gaussian fit parameters associated with the envelopes of the sg-CN, CNB, CNPS-O, and CNPS-NH_2 samples, as recorded in the LADM of the spectrometer, are summarised in Tables A.2, A.3, A.4 and A.5 in Appendix A, respectively. The deconvolved photoemission spectra of the ground state, GS (blue curves in Figure 6.19), show a contribution from the three emission bands centred at 3.61 eV, 5.37 eV and 7.66 eV binding energies, which were previously observed in the steady-state PE spectra (see Figure 6.5). The predominant fourth photoemission band, occurring at higher binding energies, is also present. However, in comparison to the ground state photoemission spectra recorded in the

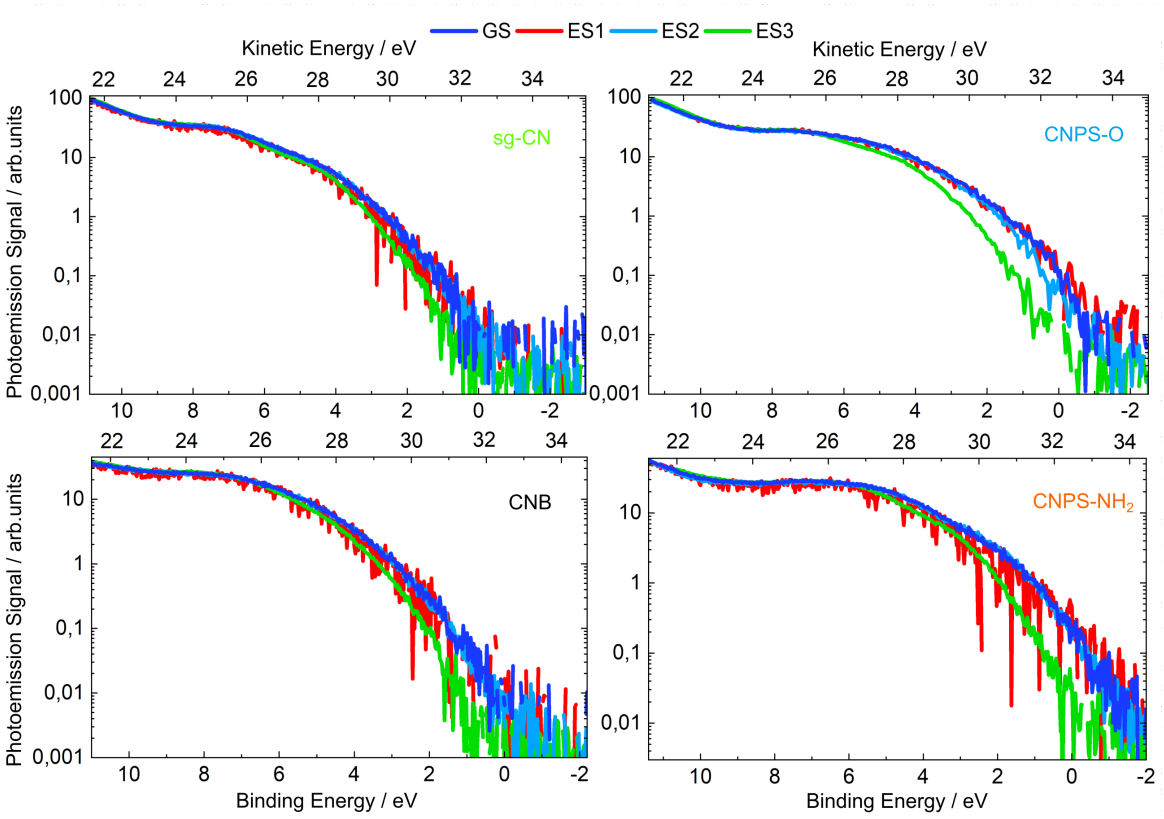

FIGURE 6.18: State-associated spectra of the electronic states extracted from global fits to the photoemission spectra for the PCN thin films recorded in the LADM following photoexcitation at 3.1 eV. The binding energy scale is energy-referenced with respect to the spectrometer E_F.

DM, the amplitude of the third photoemission peak is much higher in the LADM, which leads to more pronounced features in the structure of the spectra. The energetic positions of the emission bands used to decompose the photoemission spectra of the excited states ES1 (red curves) and ES2 (magenta curves) are nearly the same as in the ground state spectrum. The fit results for the Gaussian decomposition of the photoemission spectra of the excited state ES3 (green curves) demonstrates that the first emission peak is shifted to higher binding energies at approximately 4.2 eV.

Over the different electron binding energy ranges analysed from the separate data sets recorded in the WAM and LADM, the lifetimes obtained for the initially populated excited ES1 state and long-lived ES3 state in the TRPES experiments are in agreement with previous transient absorption and photoluminescence studies of PCN samples [419–421, 439]. In the UV-pump-Vis/NIR-probe femtosecond TAS studies on aqueous PCN dispersions by Zhang *et al.* [420] and Godin *et al.* [421], the decay of the ES1 state, within the first few hundreds of femtoseconds (within the TAS instrument response of $\sim$ 200 fs), was attributed to the direct formation of a CT state. Based on their results, the authors concluded that under UV excitation, direct photogeneration of dissociated changes occurs without any indication of the presence of excitonic states. The ultrafast femtosecond UV-Vis TAS studies reported by Merschjann *et al.* [419] suggest a different interpretation of the initial charge separation process in PCN colloids. These authors assigned the primary photoexcitations to SE, which dissociate into singlet polaron pairs within the time resolution of their experiment, in the time range of 200 fs. Such dissociation may be driven by the so-called hot excitons [440] or be based on entropic effects [441]. Similarly, in the TAS studies of Corp *et al.* [439] the observed ultrafast decay upon UV excitation was attributed to exciton dissociation, which occurs in PCN colloids on time scales of 200 fs or faster. In accordance with the present TRPES experimental observations, the ultrafast relaxation

of the short-lived ES1 state is most likely due to the internal thermalisation of the electronic system caused by the relatively high flux of the pump pulse applied to excite the system [442]. Considering the organic, molecular nature of PCNs [143], the optical excitation of the heptazine units, i.e. the building blocks of PCN materials, does not only involve purely electronic transitions but is generally

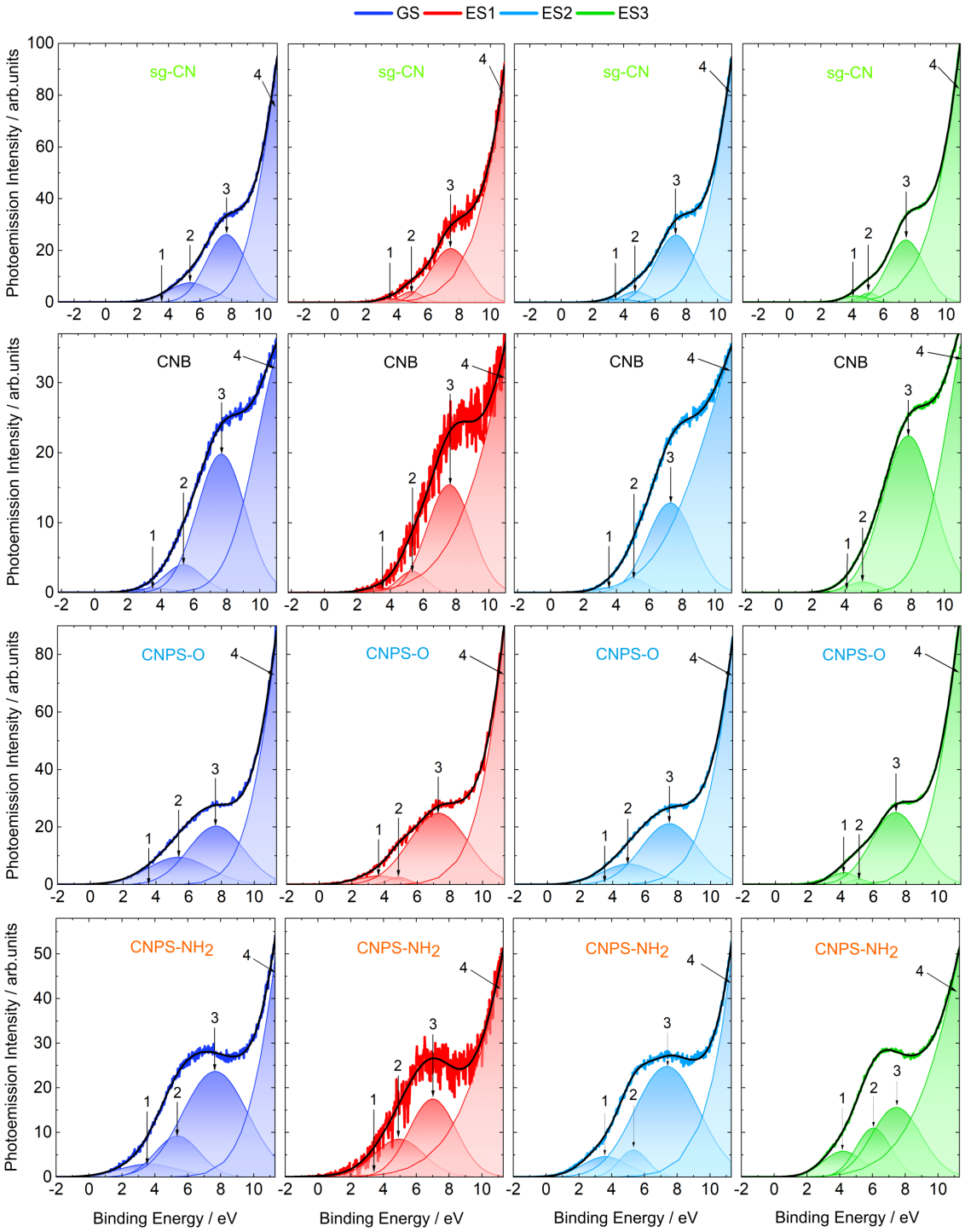

FIGURE 6.19: State-associated spectra of the electronic states extracted from global fits to the photoemission spectra for the PCN samples, as recorded in the LADM. The results of fits to a superposition of Gaussian profiles are shown by black solid lines. The numbers (1) – (4) are assigned to the decomposed emission bands obtained from the fit. Tables A.2, A.3, A.4 and A.5 summarise the fit parameters.

accompanied by vibrational excitation. The linear excitation of electronically excited states with different equilibrium nuclear configuration leads to a rapid relaxation resulting in a vibrational energy relaxation of the initially excited ES1 state. The subsequently populated ES2 state, which was not observed and considered in references [419–421, 439], indicates that an energetic relaxation of the hot electrons and fast cooling of the system occurs to reach thermal equilibrium with the lattice on <1 ps time scale. The observed sub-1 ps relaxation in the PCN thin films is similar to that taking place in conjugated polymer films, which is often attributed to fast interchain energy transfer, due to the short distances between the chains and a great number of available pathways, as compared to transfer along a single chain in solution [443]. Once the cooling of the ES2 state has ceased, the population of the long-lived metastable ES3 state occurs, encompassing the transfer of the population to the potentially formed CT or SE states (generically denoted here as X state), as suggested in references [419–421, 439]. The photodynamics of the ES3 $\rightarrow$ X transition and the energy relaxation pathways on longer time scales will be explored in greater detail in Section 6.4.2

6.4 UV-Vis Transient Absorption Studies of Polymeric Carbon Nitride Thin Films

The UV-Vis transient diffuse reflectance spectra of the sg-CN, CNB, CNPS-O, and CNPS-NH_2 thin films were collected by recording the diffusely reflected probe light from the solid samples when the applied pump and probe pulses were spatially overlapped at the sample surface. Analogous to the TRPES experiments, pump pulses of 400 nm wavelength (3.1 eV photon energy), 65 fs (FWHM) pulse durations were applied to induce the PCN thin film electronic transition with peak absorption cross-section at a wavelength of 385 nm (3.21 eV photon energy) (see Section 6.1.2). White-light continuum (WLC) probe pulses were used to map the subsequent population dynamics of the excited states (introduced in Section 6.3.2) in a spectral range of 550 – 920 nm. The WLC probe beam was focused into the interaction region, resulting in a focal spot size diameter of 300 μm (defined at $1/e^2$) at the sample surface. The generated WLC probe pulses of 80 fs pulse duration (FWHM) and 2 nJ pulse^{-1} energy corresponded to a spatial peak intensity of 7×10^7 W cm^{-2} in the interaction region. The pump beam was focused into the sample with a focal spot size diameter of 600 μm ($1/e^2$). The pump pulse energy density was varied from 424 μJ cm^{-2} to 42 μJ cm^{-2} for the sg-CN, CNB, and CNPS-O and from 2.12 mJ cm^{-2} to 424 μJ cm^{-2} for the CNPS-NH_2 thin films at the sample focus. This allowed the dependence of the transient diffuse reflectance signal decay kinetics on the pump pulse fluence to be monitored. The associated spatial peak pump pulse intensities are estimated to be 3.26×10^9 W cm^{-2} – 3.26×10^8 W cm^{-2} and 1.63×10^{10} W cm^{-2} – 3.26×10^9 W cm^{-2}, respectively. The relative polarisation of the probe and pump pulses was set parallel with respect to the reflection angle to the sample surface. The diffuse reflectance spectra of the PCN thin films were recorded by scanning the pump-probe time delay over a range of - 20 ps to + 1.8 ns.

6.4.1 Transient Diffuse Reflectance Spectra of PCN Thin Films

Diffuse reflectance TAS studies were performed to gain detailed insight into interfacial electron transfer processes and to track the ultrafast photodynamics of the PCN thin films at 400 nm excitation on time scales ranging from femtoseconds to nanoseconds. Figure 6.20 shows the 2D colour maps associated with chirp-corrected transient diffuse reflectance signals from the PCN thin films for the applied pump pulse fluence of 424 μJ cm^{-2}, as recorded as a function of wavelength and pump-probe time delay. The colour bar represents the relative magnitude of the $\Delta OD\,(t, \lambda)$ induced by the pump pulse (see Equation 3.69). The transient diffuse reflectance spectra are presented over the wavelength range of 550 – 920 nm and were recorded from - 20 ps to + 1.8 ns with four different time delay step size ranges. The first time delay axis spans over the range of - 20 ps to - 2 ps with a step size of 1.29 ps, the second range between - 2 ps and 4 ps has the smallest time steps of 40 fs, the third range

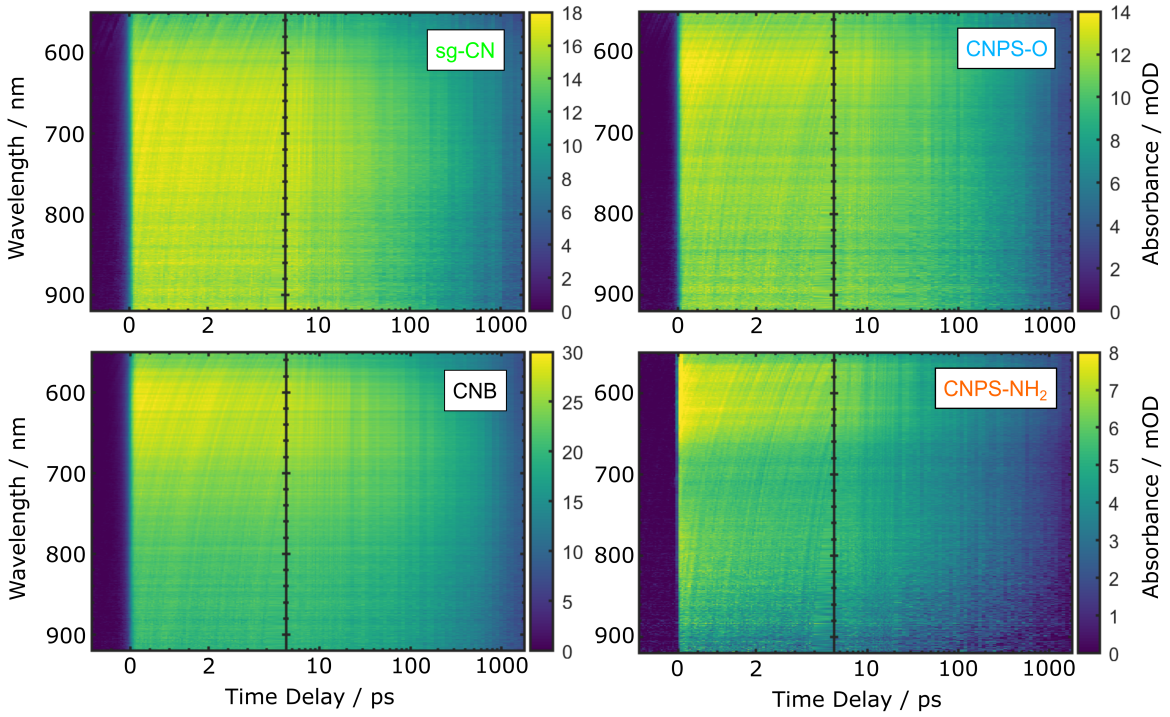

FIGURE 6.20: 2D colour maps of the chirp-corrected transient diffuse reflectance signal from the PCN samples after applying a pump pulse fluence of 424 μJ cm^{-2}, as recorded as a function of wavelength and pump-probe time delay. The colour bar represents the relative magnitude of the absorbance signal.

spans between 4 ps and 20 ps with a step size of 163 fs. The fourth interval between 20 ps and 1.8 ns is logarithmically increasing with a starting value of 1.054 ps. For better visualisation of the transient signal in Figure 6.20, the time delay axis from 4 ps to 1.8 ns is presented on a logarithmic scale.

Typically, in raw 2D transient absorption or diffuse reflectance spectra, there is a strong curvature that emerges around the time zero position, when the pump and probe pulses overlap in time, and at the beginning of the appearance of the transient signal. This feature arises from the temporally-chirped WLC probe pulses caused by the group velocity dispersion during the propagation of ultrashort pulses through air and optical components (see Sections 3.1.2 and 3.2.2). The frequency-dependent chirping effect is associated with a non-zero temporal and spectral phase of the propagating pulse and limits the time resolution in TAS experiments. Accordingly, the raw transient data should be compensated for the chirp. This can only be done if the dispersion curve of the WLC is defined. In the present work, the chirp correction was implemented in the global analysis procedure by the simultaneous fitting of the wavelength-dependent time zero offset using a second-order polynomial [371]. The obtained dispersion curve is then used for numerical correction of the time zero shift of the measured data and fit results. Thereby, the chirp correction determines a single corrected time zero position and the wavelength dependence of the pump-probe temporal overlap, i.e cross-correlation signal, which is displayed as a sharp positive feature at zero time delay in the 2D maps in Figure 6.20. The determined CC width of 103 $\pm$ 26 fs (FWHM) represents the time resolution in the TAS experiments.

Following the CC, the transient signal appears at positive time delays, which is apparent over the entire wavelength range (550 – 920 nm) measured in the TAS experiments. This transient signal is shown to build within the first few hundred femtoseconds, to produce a long-lived transient signal, which remains unchanged until a pump-probe delay time of approximately 100 ps. Furthermore, the prominent bands, corresponding to the highest $\Delta OD\,(t,\,\lambda)$ values in the recorded diffuse reflectance

spectra, are found to emerge at different wavelength ranges for each sample. The maximum absorbance signal is observed in the wavelength range of 600 – 800 nm, 575 – 700 nm, 575 – 650 nm and 550 – 650 nm for the sg-CN, CNB, CNPS-O and CNPS-NH_2 thin films, respectively. From the 2D maps shown in Figure 6.20, a slow dissipation of the transient signal from 100 ps to the maximum 1.8 ns delay time measured in the TAS experiments is noted. To follow further details of this relaxation process, the time delay range in TAS experiments needs to be extended to the ms range, which requires currently unavailable infrastructure and is beyond the scope of this work.

6.4.2 Kinetic Model and Global Fitting of the Photoinduced Electron Dynamics at the Surface-Bulk Interface

Transient diffuse reflectance spectra shown in Figure 6.20, were analysed using global fits to different kinetic models, that were setup to describe the population and depopulation of the potentially excited electronic states of the PCN samples at the surface-bulk interface. The model used to describe the time-dependent spectral changes in the TAS spectra incorporates the information obtained from the TRPES results on the early-time electron population dynamics at the surface-vacuum interface, which were well-described by Equation 6.5. To simulate the population of the prevailing long-lived dynamics in the PCN thin films, observed in the TAS studies, it was necessary to implement a more complex kinetic scheme.

In light of the existing kinetic models proposed on the basis of TRPL and TAS studies of the photoinduced electron dynamics in PCN powders or colloids [150, 419–421, 439, 444–446], there are two additional processes that potentially contribute to the long-lived population dynamics in PCN materials. The first process is the result of spontaneous photon emission after excitation and is referred to as prompt fluorescence. Upon photoexcitation, the aforementioned studies determined that prompt fluorescence in PCN samples occurs within hundreds of ps up to several ns following photoexcitation and depopulates the excited electronic states. The second process is the so-called delayed fluorescence, which exhibits a spectral distribution similar to prompt fluorescence, but with emission occurring on distinctly longer timescales. Wang *et al.* attributed the observed contribution of delayed fluorescence in the PCN polymer matrix to the P-type delayed fluorescence associated with the triplet–triplet annihilation (TTA) process and associated strong excitonic effects [444]. Taking into account the existing spectroscopic observations from the TRPL and TAS studies and on the basis of TRPES results presented in Section 6.3.2, the interfacial dynamics of PCN thin films following 400 nm excitation can be cumulatively represented using a 5-state kinetic model. This model includes the early-time sequential population of excited electronic states, as introduced previously (see Equation 6.5), and assumes a parallel transfer of the population to the metastable CT and SE states with corresponding dissipation channels. The proposed kinetic model and justification for it is described in more detail below.

Initially, the first excited state, ES1, is populated by a dipole-allowed transition from the ground state, GS, upon 400 nm optical excitation. The ES1 state undergoes sequential electronic/vibrational relaxation leading to the formation of the intermediate ES2 state. Afterwards, the population is transferred from the intermediate, ES2, to the metastable, ES3 and ES4, states, presumably respectively corresponding to the CT and SE states, as the system approaches electrical and thermal equilibrium. The transition from the ES3 state to the CT and SE states was previously generically referred to as the X state in the kinetic model introduced to describe the TRPES results (see Equation 6.4). The formed ES3 (CT) state undergoes sequential transition to the ES4 (SE) state and further relaxation processes (denoted as X*), which appear as delayed fluorescence signals, on timescales much longer than those measured in the TAS experiments. Successively, the population of the ES4 state is followed by relaxation to the GS, which corresponds to the prompt or delayed fluorescence signal. A schematic depiction of the PCN thin film photocycles at the bulk-surface interface is presented in Figure 6.21.

Accordingly, the kinetic rate equations, describing transitions between the electronic states in the PCN thin films, can be expressed as:

$$\begin{aligned}
\frac{d[\mathrm{GS}]}{dt} &= -P(t)\cdot[\mathrm{GS}] + k_5\cdot[\mathrm{ES4}] \\
\frac{d[\mathrm{ES1}]}{dt} &= P(t)\cdot[\mathrm{GS}] - k_1\cdot[\mathrm{ES1}] \\
\frac{d[\mathrm{ES2}]}{dt} &= k_1\cdot[\mathrm{ES1}] - k_2\cdot[\mathrm{ES2}] - k_3\cdot[\mathrm{ES2}] \\
\frac{d[\mathrm{ES3}]}{dt} &= k_2\cdot[\mathrm{ES2}] - k_4\cdot[\mathrm{ES3}] - k_6\cdot[\mathrm{ES3}] \\
\frac{d[\mathrm{ES4}]}{dt} &= k_3\cdot[\mathrm{ES2}] + k_4\cdot[\mathrm{ES3}] - k_5\cdot[\mathrm{ES4}],
\end{aligned} \tag{6.6}$$

where $[Q]$ denotes the population of state Q (Q = GS, ES1, ES2, ES3, or ES4) with the initial condition that all involved excited states were unpopulated at $t \to -\infty$ and only the ground state is initially occupied ([GS] = 1). Here, k_{1-6} are the kinetic rate constants, and *P(t)* is the time-dependent population rate, which is proportional to the time-dependent pump pulse, σ_{pump}, intensity as $P(t) \propto \exp(-t^2/\sigma_{pump}^2)$.

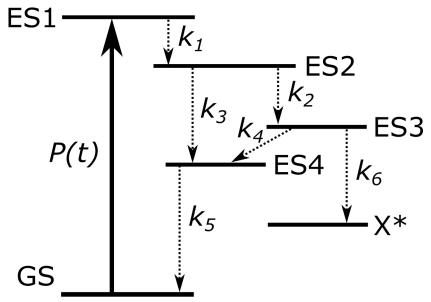

FIGURE 6.21: Schematic depiction of the total PCN thin film photocycle at the surface-bulk interface following 400 nm optical excitation. The rate parameters described in Equation 6.6 are used to label the diagram.

Following the global fitting procedure described in detail in Section 3.5.1, the system of differential Equations 6.6 was solved numerically for a given set of transition rate constants k_{1-6}. Time-dependent absorbance changes of the excited ES1, ES2, ES3, and ES4 states and their lifetimes were extracted using the global fitting and are summarised in Table 6.8. Figure 6.22 shows associated 2D colour map data and fits to the transient diffuse reflectance signal from the PCN thin films recorded for pump pulse fluence of 424 μJ cm^{-2}, where the later were obtained from the global analysis results using the kinetic model described by Equation 6.6. The right panels in Figure 6.22 display the difference between the measured transient diffuse reflectance data and the global fit results (residuals), demonstrating a good reproduction of the measured spectra using the corresponding fit results.

The time-dependent diffuse reflectance signal traces of the PCN thin films integrated over the entire wavelength range 550 – 920 nm are shown in Figure 6.23. The transient signal is presented on a linear scale for time delays up to 4 ps and on a logarithmic scale from 4 ps to 1.8 ns. Figure 6.23 shows the transient signal, decomposed into individual contributions from the involved excited electronic states, for the PCN thin films. The time-independent contribution to the transient signal, due to photoinduced depletion of the GS, is not shown in the figures. As can be seen from the figures, the evolution of the transient signal spanning the delay time range from fs to ns incorporates two relaxation processes associated with the short and long-lived population dynamics of the excited electronic states. In accordance with the results obtained from the TRPES experiments, rapid relaxation of the initially populated excited ES1 state (red curve) occurs on a time scale of less than 200 fs. The lifetimes of the ES1 state extracted in the TAS experiments are 200 $^{+10}_{-9}$ fs, 102 $^{+16}_{-14}$ fs, 103 $^{+13}_{-12}$ fs, and

101 $^{+15}_{-13}$ fs in the sg-CN, CNB, CNPS-O, and CNPS-NH_2 thin films, respectively. The sequentially populated intermediate ES2 state (cyan curve), is experimentally found to be involved in the subsequent parallel population of the long-lived ES3 (green curve) or ES4 (purple curve) states. Due to the shorter pump-probe delay measurements in the TRPES experiments, compared to the TAS experiments, parallel relaxation channels leading to the formation of the long-lived excited states could not be identified. However, the TAS data shows that two decay time constants, instead of one, affect the lifetime of the ES2 state. The first associated decay time constant, τ_2, is linked to the ES2 $\rightarrow$ ES3 transition and is found to be 877 $^{+79}_{-65}$ fs, 392 $^{+94}_{-81}$ fs, 1.56 $^{+0.17}_{-0.15}$ ps and 2.66 $^{+0.37}_{-0.25}$ ps in the sg-CN, CNB, CNPS-O and CNPS-NH_2 thin films, respectively. The ES2 $\rightarrow$ ES3 transition, which corresponds to the τ_3 decay time constant, occurs within 2.87 $^{+0.89}_{-0.68}$ ps, 1.37 $^{+0.38}_{-0.36}$ ps, 2.88 $^{+0.92}_{-0.78}$ ps and 5.35 $^{+1.64}_{-1.43}$ ps, respectively. It is noted that the lifetime of the ES2 state is lower than that determined from the TRPES data fit results, especially for the CNPS-O and CNPS-NH_2 thin films. The longer relaxation processes of the porous oxygen-rich carbon nitride nanosheets (CNPS-O) and the amino functional group carbon nitride porous sheets (CNPS-NH_2) identified in the TAS measurements, can be attributed to the morphology of the samples, i.e. the large BET surface area in comparison to the bulk polymeric carbon nitride (CNB) (see Section 2.2.3).

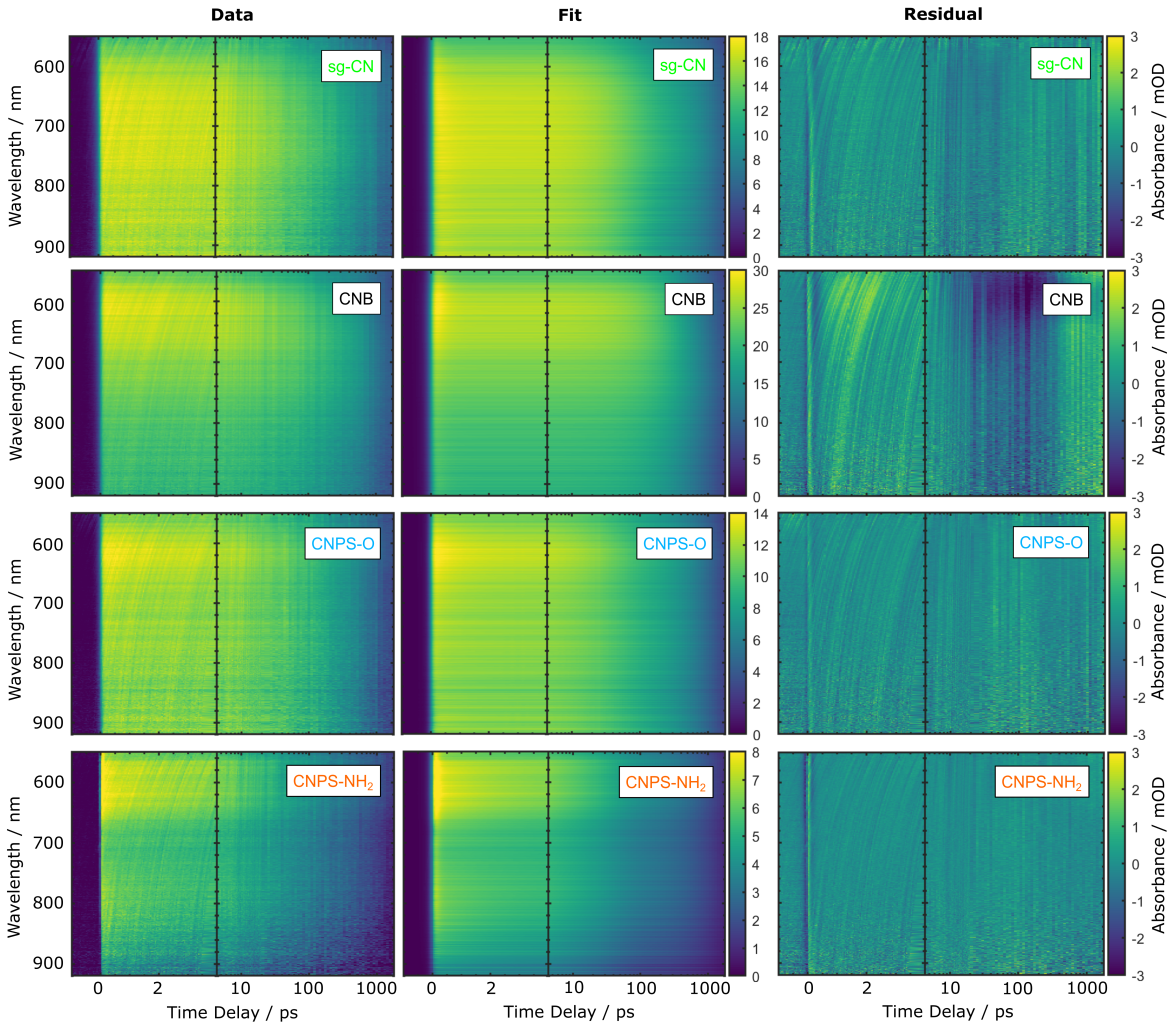

FIGURE 6.22: Global fitting reproduction of the experimental chirp-corrected diffuse reflectance spectra for the PCN thin films recorded for pump pulse fluence of 424 μJ cm^{-2} with the use of the kinetic model described by Equation 6.6. The difference between the experimental and corresponding fit results (residual signals) are shown in the right panels.

TABLE 6.8: Kinetic parameters obtained from the global fitting of the transient diffuse reflectance spectra recorded for pump pulse fluence of 424 μJ cm^{-2} encompassing decay time constants for the ES1, ES2, ES3, and ES4 states for the PCN thin films following 400 nm excitation at the surface-bulk interface.

Parameter	sg-CN	CNB	CNPS-O	CNPS-NH$_2$
τ_1 (ES1 $\rightarrow$ ES2)	200 $^{+10}_{-9}$ fs	102 $^{+16}_{-14}$ fs	103 $^{+13}_{-12}$ fs	101 $^{+15}_{-13}$ fs
τ_2 (ES2 $\rightarrow$ ES3)	877 $^{+79}_{-65}$ fs	392 $^{+94}_{-81}$ fs	1.56 $^{+0.17}_{-0.15}$ ps	2.66 $^{+0.37}_{-0.25}$ ps
τ_3 (ES2 $\rightarrow$ ES4)	2.87 $^{+0.89}_{-0.68}$ ps	1.37 $^{+0.38}_{-0.36}$ ps	2.88 $^{+0.92}_{-0.78}$ ps	5.35 $^{+1.64}_{-1.43}$ ps
τ_4 (ES3 $\rightarrow$ ES4)	2.70 $^{+1.9}_{-1.8}$ ns	2.70 $^{+1.8}_{-1.7}$ ns	2.30 $^{+1.3}_{-1.3}$ ns	2.60 $^{+1.7}_{-1.6}$ ns
τ_5 (ES4 $\rightarrow$ GS)	50.00 $^{+15}_{-11}$ ps	40.00 $^{+13}_{-10}$ ps	43.00 $^{+14}_{-11}$ ps	40.00 $^{+12}_{-10}$ ps
τ_6 (ES3 $\rightarrow$ X*)	5.00 $^{+3.6}_{-3.5}$ ns	5.00 $^{+3.7}_{-3.3}$ ns	3.60 $^{+2.8}_{-2.3}$ ns	3.80 $^{+3.1}_{-2.8}$ ns
$P(t)$	0.60 $\pm$ 0.04	0.60 $\pm$ 0.05	0.80 $\pm$ 0.20	0.90 $\pm$ 0.10
σ_{pump}	65 $\pm$ 3 fs	67 $\pm$ 5 fs	65 $\pm$ 5 fs	64 $\pm$ 6
σ_{probe}	80 $\pm$ 5 fs	82 $\pm$ 6 fs	84 $\pm$ 5 fs	82 $\pm$ 7 fs

After the population is transferred to the metastable ES3 and ES4 states, the relaxation processes take place on much longer time scales, with lifetimes of tens of picoseconds to nanoseconds. Based on the TRPL and TAS studies reported so far [419–421, 439, 444–446], these relaxation processes are likely of radiative nature. Moreover, the current knowledge of the ultrafast photophysics of PCN

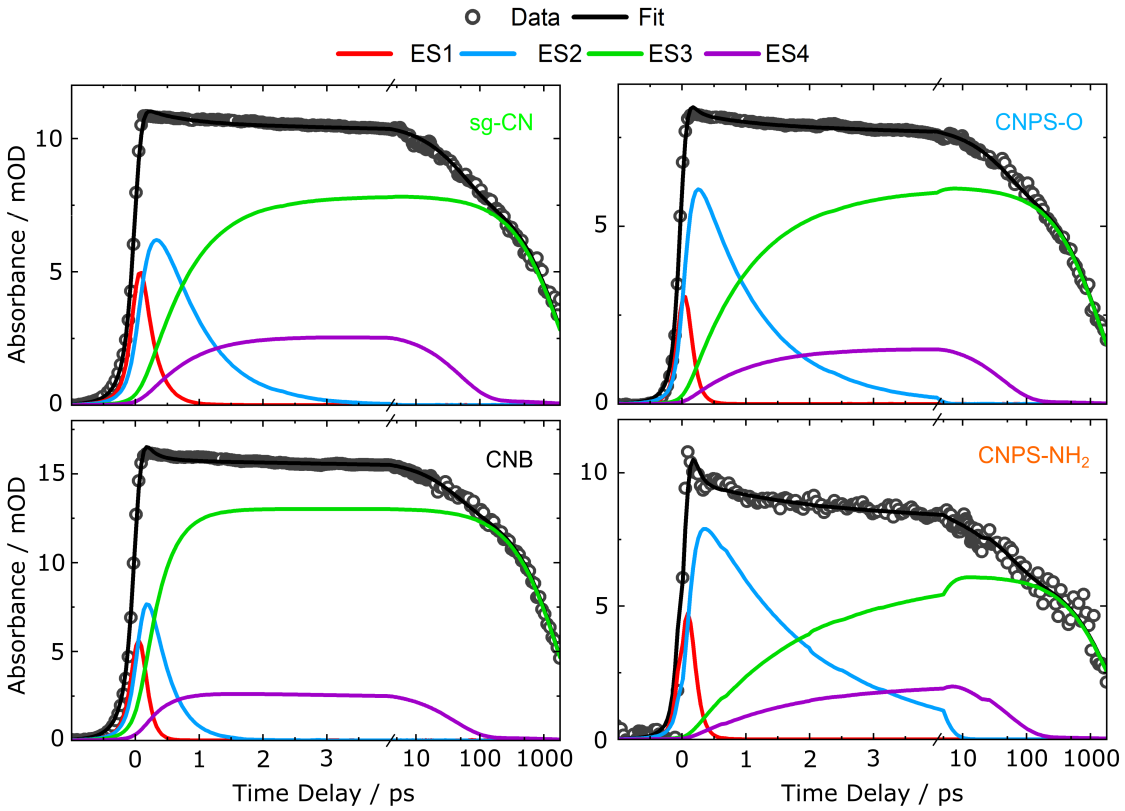

FIGURE 6.23: The time dependence of the transient diffuse reflectance signal integrated over the 550 – 920 nm wavelength range. This range encompasses the interfacial population dynamics of the 400 nm photoexcited states in the PCN thin films.

suggests that charge-transfer and/or singlet exciton states are potentially formed upon 400 nm photoexcitation. In the present TAS studies, it is assumed that both CT and SE states contribute to the photocycle of the PCN thin films at the surface-bulk interface. Specifically, the ES3 (CT) state can undergo sequential electronic transitions to the ES4 (SE) state, which is found to occur within $2.7\ ^{+1.9}_{-1.8}$ ns, $2.7\ ^{+1.8}_{-1.7}$ ns, $2.3\ ^{+1.3}_{-1.3}$ ns and $2.6\ ^{+1.7}_{-1.6}$ ns in the sg-CN, CNB, CNPS-O, and CNPS-NH_2 thin films, respectively. Further, the ES3 state can be involved in an additional relaxation process to the X* state with corresponding time constants of $5.0\ ^{+3.6}_{-3.5}$ ns, $5.0\ ^{+3.7}_{-3.3}$ ns, $3.6\ ^{+2.8}_{-2.3}$ ns and $3.8\ ^{+3.1}_{-2.8}$ ns, respectively. The last process was previously observed as the delayed fluorescence signal. Furthermore, the lifetimes of $50\ ^{+15}_{-11}$ ps, $40\ ^{+13}_{-10}$ ps, $43\ ^{+14}_{-11}$ ps and $40\ ^{+12}_{-10}$ ps for the ES4 (SE) state that have been respectively extracted from sg-CN, CNB, CNPS-O, and CNPS-NH_2 sample 2D data sets and are in agreement with the reported lifetime values for the prompt fluorescence signals detected from PCN powders and colloids.

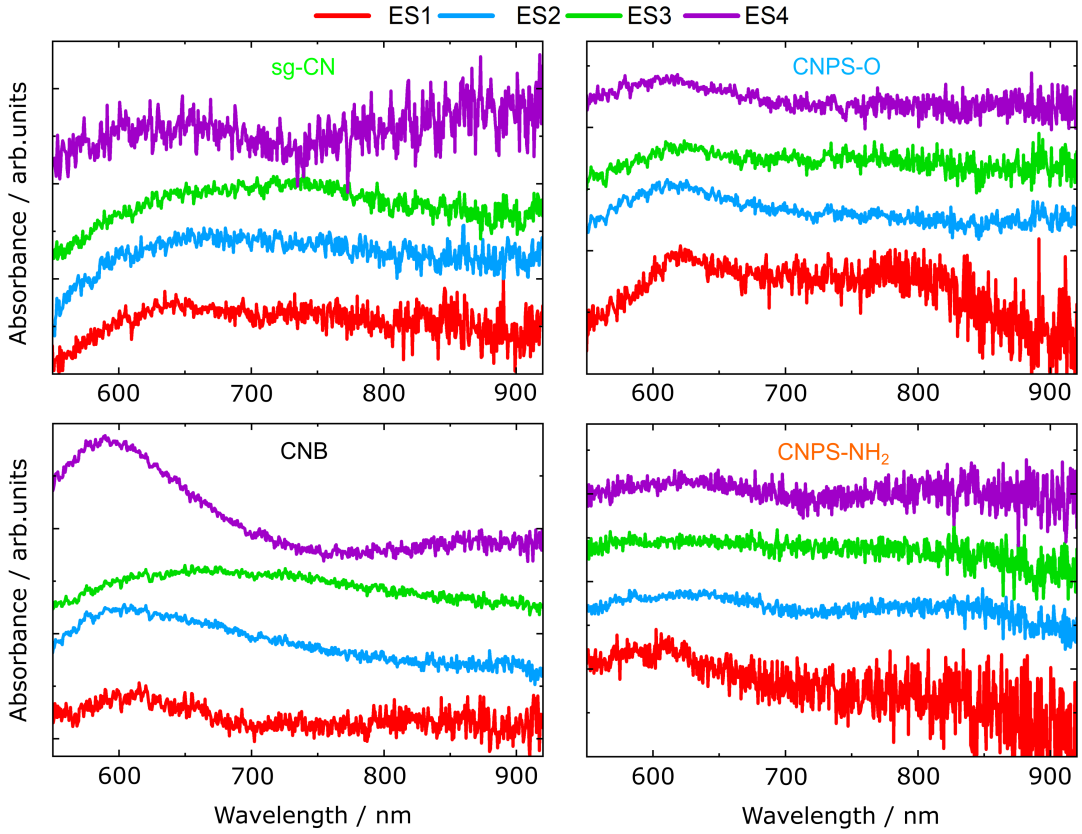

FIGURE 6.24: Species-associated diffuse reflectance spectra extracted from the global analysis results for the 400 nm photoexcited states of the PCN thin films.

The species-associated diffuse reflectance spectra (Figure 6.24), extracted from the global analysis results for the excited states of the PCN samples, were used to determine the spectral distribution of the transient signals from the involved electronics states. To enhance the visibility of the spectral components of the excited state signals, the spectrum of the ground state, GS, was set to zero in the implicit global fitting procedure (see Section 3.5.1) and therefore is not displayed in the figures. In Figure 6.24, it can be observed that the transient diffuse reflectance spectra, associated with the population of the excited states, recorded after 400 nm excitation have similar spectral distributions. In particular, an increase in the relative absorbance signal, $\Delta OD\,(t, \lambda)$, emerges in the spectral range spanning approximately 550 – 700 nm for all PCN samples. In addition, for the mesoporous sg-CN sample, which was prepared using a sol–gel/thermal condensation preparation process, the signal associated with the population of the long-lived ES4 state incorporates another absorption band between 750 – 920 nm. The three other samples, CNB, CNPS-O and CNPS-NH_2, prepared from the

thermal polymerisation of melamine, exhibit a slightly different spectral distribution for the excited states. The time-dependent absorbance changes of the initially excited ES1 state are the highest. The spectral distribution of the ES2, ES3 and ES4 states signals nearly overlap with each other for the CNPS-O and CNPS-NH_2 thin films. The signal associated with the population dynamics of the ES3 state for the CNB sample is somewhat shifted to the higher wavelengths. The spectral evolution of the ES4 state has a distinct absorption band, which is blue-shifted compared to other excited states.

6.4.3 Excitation Fluence-Dependent Transient Signal Decay Kinetics

To aid in the interpretation of the PCN thin film TRPES and TAS data sets, a 400 nm photoexcitation pump pulse fluence-dependent decay kinetic study of the transient diffuse reflectance signal was performed. The influence of pump fluence on the electronic relaxation dynamics in photoexcited PCN thin films was specifically monitored for excitation fluences of 42 μJ cm^{-2}, 141 μJ cm^{-2} and 424 μJ cm^{-2} for the sg-CN, CNB and CNPS-O samples. Due to the relatively low $\Delta OD\,(t, \lambda)$ values obtained for the transient diffuse reflectance signal recorded from the CNPS-NH_2 sample, higher excitation fluences of 424 μJ cm^{-2}, 1410 μJ cm^{-2} and 2120 μJ cm^{-2} were applied.

Figure 6.25 shows the normalised kinetic traces of the transient diffuse reflectance signal of the PCN thin films integrated over the 550 – 920 nm wavelength range as a function of pump fluence. Following the aforementioned fitting procedure (Section 6.4.2), the experimental data was analysed by global fitting to a kinetic model described by Equation 6.6. The initial amplitude of the raw diffuse reflectance signal of the PCN samples at zero time delay, t_0, is found to increase linearly with the pump fluence, as shown in the insets in Figure 6.25. This demonstrates that the efficiency of the initial generation of electrons is independent of the excitation fluence. However, the normalised traces of the diffuse reflectance transient signals of the PCN thin films show a clear dependence of

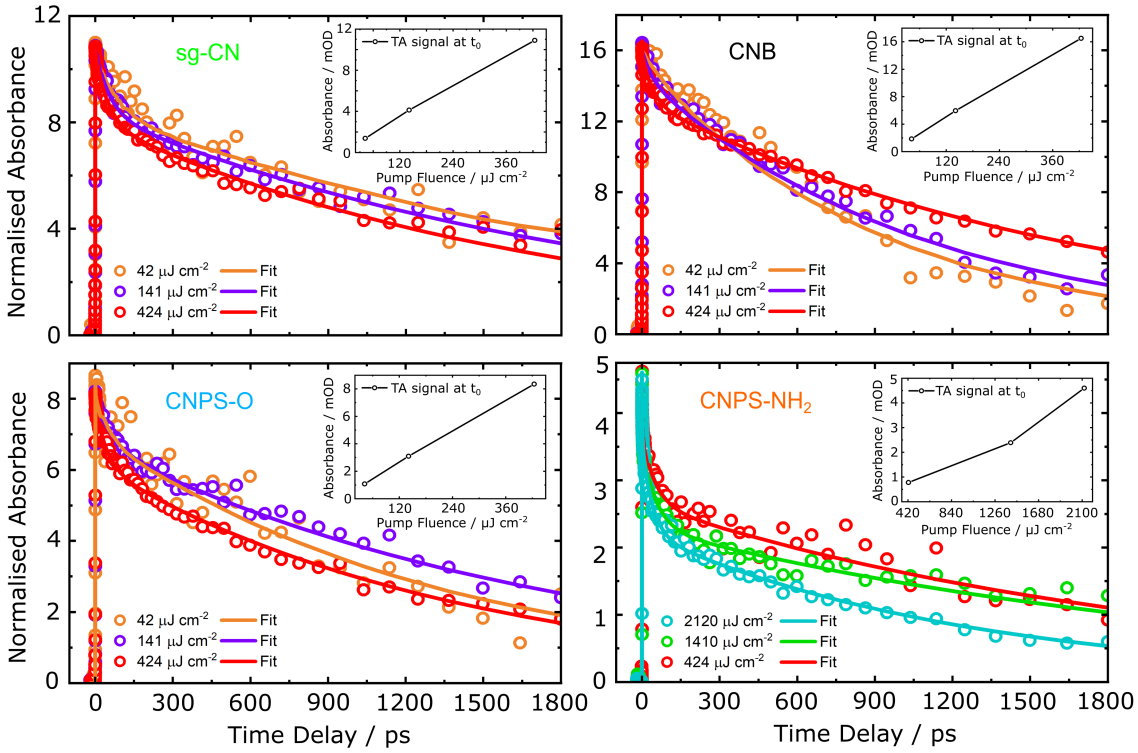

FIGURE 6.25: The decay kinetics of the normalised transient diffuse reflectance signal for the PCN thin films integrated over 550 – 920 nm wavelength range as a function of 400 nm pump fluence. The insets show the dependence of the initial amplitude of the raw transient signal on the excitation fluence at zero time delay.

the long-lived decay kinetics on the pump fluence. In particular, increasing the excitation density from 42 μJ cm^{-2} to 424 μJ cm^{-2} for the sg-CN, CNB and CNPS-O samples resulted in a relative decrease of the transient signal in the hundreds of picoseconds to nanoseconds delay time range. For the CNPS-NH_2 sample this change is even more pronounced, while applying the higher excitation fluences from 42 μJ cm^{-2} to 2120 μJ cm^{-2}.

The pump fluence-dependent transient signal decay kinetics in the PCN powders and colloids was previously observed in TRPL and TAS studies [419, 421, 439, 444, 445]. In their works, the kinetic decay traces were fitted by a power-law relationship of the form $I \propto t^{-\alpha}$, extracting the power law exponent parameter, α, associated with changes in the decay dynamics. Godin *et al.* [421] found that increasing the excitation fluence leads to an increase in the TA and TRRL signal amplitudes, I, and the α exponent of the power law decay. At their highest employed excitation laser fluences (784 μJ cm^{-2}), they observed α values of 0.2, whereas at the lowest excitation fluence (24.7 μJ cm^{-2}) α was near 0.11, on both fs – ns and μs – s time scales. According to the model describing photophysical processes in PCN colloids upon 355 nm excitation proposed by the same authors, similar to metal oxide semiconductors [447] and organic photovoltaic blends [448], the power law decays represent the electron trapping-detrapping processes and recombination of the formed trap states, which were assumed to be involved in the photocycle of PCN. In contrast to the aforementioned work, Merschjann *et al.* [419] reported in their TRPL studies that the decay kinetics following 388 nm excitation of the investigated PCN aqueous dispersions exhibit a non-exponential decay behavior that is independent of the excitation laser fluence on ms to tens of ns time scales. In this case the fluence was varied by a factor of 300 (0.73 – 220 μJ cm^{-2}) at the sample. Based on this observation, Merschjann *et al.* concluded that any bimolecular processes, i.e. exciton-exciton annihilation, which occur as concentration-dependent changes in the shape of decay kinetic traces of PCN, can be neglected on the time scale and the excitation fluence range applied in their experiments.

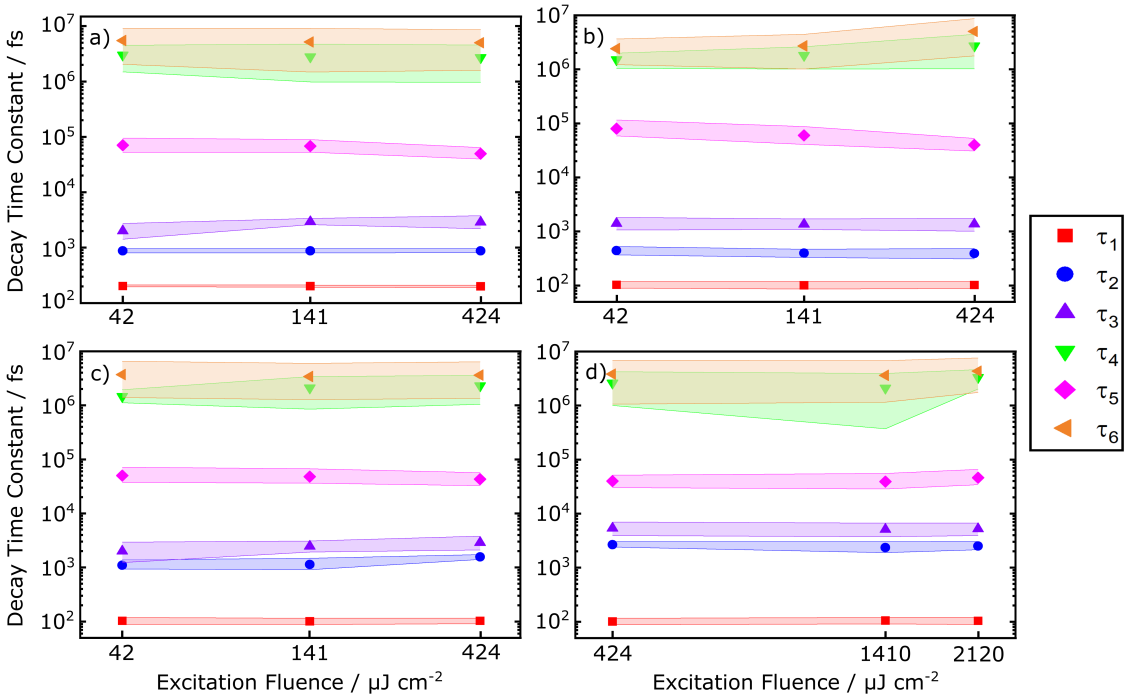

FIGURE 6.26: The decay time constants, τ_{1-6}, of the pump fluence-dependent transient diffuse reflectance signal for the sg-CN (a), CNB (b), CNPS-O (c), and CNPS-NH_2 (d) thin films obtained at various 400-nm pump excitation fluences, as summarised in Table 6.9. The error bars, which refer to the global fitting numerical results are depicted by the corresponding shading.

In the present studies, based on the global analysis and kinetic modelling, the decay time constants associated with electronic transitions between the involved excited states in the PCN thin films were used to determine the origin of the pump-pulse-fluence-induced changes to the decay dynamics. The corresponding decay time constants, τ_{1-6}, obtained from the global fitting results of the pump fluence-dependent transient diffuse reflectance spectra for the sg-CN, CNB, CNPS-O, and CNPS-NH_2 samples, as obtained using Equation 6.6, are summarised in Table 6.9. Figure 6.26 shows the decay time constants obtained from these modeled transient signals as a function of the 400-nm pump fluence. The associated reproducibility of the values of the decay time constants with the implemented pump fluences (within the error bars) confirms the reliability of the kinetic model used to describe the transient population of the excited electronic states in the PCN thin films at the surface-bulk interface. Based on those results, it can be concluded that the early timescale dynamics associated with the excited ES1, ES2 and ES3 states following 400 nm photoexcitation do not depend on the pump fluence.

TABLE 6.9: Decay time constants, τ_{1-6}, obtained from the global fitting results of the pump fluence-dependent transient diffuse reflectance spectra for the PCN samples.

sg-CN	$424\,\mu J\,cm^{-2}$	$141\,\mu J\,cm^{-2}$	$42\,\mu J\,cm^{-2}$
τ_1 (ES1 $\rightarrow$ ES2)	200^{+10}_{-9} fs	202^{+9}_{-8} fs	203^{+8}_{-7} fs
τ_2 (ES2 $\rightarrow$ ES3)	877^{+79}_{-65} fs	873^{+90}_{-75} fs	875^{+78}_{-65} fs
τ_3 (ES2 $\rightarrow$ ES4)	$2.87^{+0.89}_{-0.68}$ ps	$2.93^{+0.43}_{-0.32}$ ps	$2.00^{+0.72}_{-0.58}$ ps
τ_4 (ES3 $\rightarrow$ ES4)	$2.7^{+1.9}_{-1.8}$ ns	$2.8^{+2.0}_{-1.9}$ ns	$3.0^{+1.6}_{-1.5}$ ns
τ_5 (ES4 $\rightarrow$ GS)	50^{+15}_{-11} ps	68^{+22}_{-16} ps	71^{+25}_{-19} ps
τ_6 (ES3 $\rightarrow$ X*)	$5.0^{+3.6}_{-3.5}$ ns	$5.2^{+4.0}_{-3.8}$ ns	$5.5^{+3.7}_{-3.5}$ ns
CNB	$424\,\mu J\,cm^{-2}$	$141\,\mu J\,cm^{-2}$	$42\,\mu J\,cm^{-2}$
τ_1 (ES1 $\rightarrow$ ES2)	102^{+16}_{-14} fs	101^{+17}_{-15} fs	103^{+15}_{-13} fs
τ_2 (ES2 $\rightarrow$ ES3)	392^{+94}_{-81} fs	397^{+73}_{-65} fs	443^{+83}_{-74} fs
τ_3 (ES2 $\rightarrow$ ES4)	$1.37^{+0.38}_{-0.36}$ ps	$1.35^{+0.35}_{-0.26}$ ps	$1.40^{+0.42}_{-0.34}$ ps
τ_4 (ES3 $\rightarrow$ ES4)	$2.7^{+1.8}_{-1.7}$ ns	$1.80^{+0.81}_{-0.79}$ ns	$1.50^{+0.48}_{-0.46}$ ns
τ_5 (ES4 $\rightarrow$ GS)	40^{+13}_{-10} ps	60^{+28}_{-20} ps	80^{+36}_{-22} ps
τ_6 (ES3 $\rightarrow$ X*)	$5.0^{+3.7}_{-3.3}$ ns	$2.7^{+1.8}_{-1.7}$ ns	$2.4^{+1.3}_{-1.2}$ ns
CNPS-O	$424\,\mu J\,cm^{-2}$	$141\,\mu J\,cm^{-2}$	$42\,\mu J\,cm^{-2}$
τ_1 (ES1 $\rightarrow$ ES2)	103^{+13}_{-12} fs	101^{+14}_{-13} fs	103^{+16}_{-15} fs
τ_2 (ES2 $\rightarrow$ ES3)	$1.56^{+0.17}_{-0.15}$ ps	$1.13^{+0.35}_{-0.22}$ ps	$1.10^{+0.28}_{-0.16}$ ps
τ_3 (ES2 $\rightarrow$ ES4)	$2.88^{+0.92}_{-0.78}$ ps	$2.45^{+0.64}_{-0.53}$ ps	$2.00^{+0.94}_{-0.77}$ ps
τ_4 (ES3 $\rightarrow$ ES4)	$2.3^{+1.3}_{-1.3}$ ns	$2.1^{+1.4}_{-1.3}$ ns	$1.46^{+0.47}_{-0.35}$ ns
τ_5 (ES4 $\rightarrow$ GS)	43^{+14}_{-11} ps	48^{+19}_{-12} ps	50^{+22}_{-13} ps
τ_6 (ES3 $\rightarrow$ X*)	$3.6^{+2.8}_{-2.3}$ ns	$3.4^{+2.6}_{-2.2}$ ns	$3.7^{+2.9}_{-2.4}$ ns
CNPS-NH_2	$424\,\mu J\,cm^{-2}$	$1410\,\mu J\,cm^{-2}$	$2120\,\mu J\,cm^{-2}$
τ_1 (ES1 $\rightarrow$ ES2)	101^{+15}_{-13} fs	105^{+15}_{-14} fs	104^{+16}_{-15} fs
τ_2 (ES2 $\rightarrow$ ES3)	$2.66^{+0.37}_{-0.25}$ ps	$2.35^{+0.65}_{-0.45}$ ps	$2.50^{+0.57}_{-0.35}$ ps
τ_3 (ES2 $\rightarrow$ ES4)	$5.4^{+1.7}_{-1.5}$ ps	$5.1^{+1.6}_{-1.4}$ ps	$5.2^{+1.6}_{-1.3}$ ps
τ_4 (ES3 $\rightarrow$ ES4)	$2.6^{+1.7}_{-1.6}$ ns	$2.1^{+1.9}_{-1.8}$ ns	$3.3^{+1.4}_{-1.3}$ ns
τ_5 (ES4 $\rightarrow$ GS)	40^{+12}_{-10} ps	39^{+17}_{-11} ps	46^{+20}_{-12} ps
τ_6 (ES3 $\rightarrow$ X*)	$3.8^{+3.1}_{-2.8}$ ns	$3.6^{+3.2}_{-2.5}$ ns	$4.3^{+3.3}_{-2.6}$ ns

This supports the interpretation that the initial excitation process is mainly localised at the heptazine units, not involving band-like delocalisation. Thus, it is only through transport that individual excited species can be affected by an increase in their average bulk concentration. In contrast to the short lifetime population dynamics, the long lifetime population kinetics is found to be excitation-fluence dependent. In particular, the transition from the excited ES4 state to the ground GS state occurs faster at the higher excitation fluences. The decay time constant τ_4, which is appended to the relaxation channel from the excited ES3 (CT) state to the ES4 (SE) state, becomes shorter with increasing pump fluence. At the same time, the ES3 $\rightarrow$ X* transition, which occurs on a similar timescale, is lengthened. Thus, there is a competition between the two relaxation channels of the ES3 state. Due to the limited time delay range that can be applied in the present experiments (1.8 ns), the resulting decay time constants exceed the maximum measured time delay range and only corresponded to the numerical result obtained from the fit. By increasing the delay time span in the TAS experiments to the range of ms, the exact values of the time constants τ_4 and τ_6 can be determined, which would allow a mechanism underlying the two simultaneous relaxation processes to be further investigated and perhaps proposed.

6.5 Excited State Dynamics of Polymeric Carbon Nitride Thin Films

Based on the TRPES and TAS results obtained in this work, it is important to understand and describe the kinetic processes that occur in the PCN thin films upon 400 nm photoexcitation. In previous studies, various excitation wavelengths were employed, ranging from 355 nm to 400 nm, to presumably map the $\pi \rightarrow \pi^{\star}$ electronic transition, which occurs at approximately 3.2 eV [420, 421, 439]. It was found that the CT state emerged after ≈ 200 fs, and along with it, the SE state developed, which was responsible for the TRPL signals. The TAS studies conducted by Corp *et al.* [439] and Zhang *et al.* [420] estimated the efficiency of charge separation to be in the range of 5% to 65%, indicating a trend towards higher values as the photon energy increases. In the current study, the TRPES data revealed the existence of an intermediate state that undergoes progressive evolution towards the SE and CT states. The observation of the resulting state indicates that there is a sustained charge separation happening on a picosecond timescale, potentially generating hole-separated electrons with a broad range of binding energies. Based on the TAS results in this work, the efficiency of charge separation in the PCN thin films is determined to range from 65 ± 11 % to 78 ± 11 % via the ratio of rate constants k_2 to $(k_2 + k_3)$. Even though the confidence intervals allow only a rough estimate, one can still infer that the transient photoemission signals observed in the TRPES experiments, specifically for delay times exceeding 1 ps, are primarily affected by the CT state. Although there is generally a good agreement between the results of TRPES and TAS experiments when examining the excited state dynamics of PCN thin films, there are some minor discrepancies that could be considered significant. These discrepancies may be attributed to the lower temporal resolution of the TAS experiment. Furthermore, it is not clear how the differences between surface-sensitive (TRPES) and bulk-sensitive (TAS) techniques impact the observations of kinetics. Excited species located near the surface, such as surface excitons or polarons, tend to have a more two-dimensional nature than those in the bulk. Consequently, they may display distinct kinetic behaviors [449].

The TRPES results facilitated the derivation of the state-associated photoemission spectra for the PCN thin films. By assuming that the initial excited state dynamics primarily occur on the PCN-material building blocks, i.e. heptazine units, these results can be utilised to assign the early-time state-associated spectra of the electronic states extracted for the PCN thin films recorded in the WAM of the spectrometer (Figure 6.15) to specific heptazine photoexcited states. While there are no available experimental PES results for molecular heptazine, there are comprehensive reports on the valence excited and ionic states of molecular triazine, which include the assignments of associated electronic and vibrational state characters [450, 451]. Several theoretical works [132, 452–454] provide further confirmation on the experimental results, showing that the electronic states and transitions in triazine

and heptazine molecules are largely similar in nature and symmetry. However, the overall energetics of heptazine are lower due to its more extended aromatic system. These findings suggest the structural similarities between these two compounds, allowing a description of the early-time excited state dynamics and electronic transitions that are involved in the photocycle of PCN thin films upon 400 nm excitation.

In accordance with the terminology of Ehrmaier *et al.* [454], the PCN thin film photocycle following 400 nm optical excitation (Figure 6.12) may be described as follows: photons with an energy of 3.1 eV (400 nm) resonantly photoexcite the ground state, GS ($^1A_1'$, S_0), of a heptazine PCN subunit to reach the optically-bright ES1 state ($^1E'$, S_4) [454]. This state (S_4) is expected to undergo an ultrafast radiationless relaxation into ES2 ($^1A_2'$, S_1^*), which should be optically dark and would be populated with a high degree of vibrational excitation [453]. From here, the substantial vibrational excess energy (up to ≈ 1 eV) opens two possible relaxation paths to ES3, both of which occur on a sub-picosecond timescale. The system will then undergo intra-state vibrational relaxation (IVR) toward the vibrationally-cold S_1 state (corresponding to the SE state, ES4, in Fig. 6.21). Furthermore, Ehrmaier *et al.* [453] suggest that a transition can occur towards a CT state, in their case between molecular heptazine and a water molecule. One can speculate that a similar relaxation path is open between neighbouring heptazine motifs in the polymeric materials, thus leading to the population of the CT state, ES3, in the TAS photocycle shown in Figure 6.21. Regardless of whether IVR, CT, or a combination of the two relaxation processes occur, the resulting states are expected to have lifetimes well in excess of a few picoseconds, since they will exhibit minimal electric-dipole coupling to the S_0 ground state. Such a mechanism could be assessed, and further details about the initial stages of the heptazine and PCN photocycles could be investigated, via additional calculations that utilise the techniques applied by Ehrmaier *et al.* [454], albeit with a focus on the electronic structure and excited-state dynamics in PCN supercells.

By considering the molecular system of triazine, we can infer certain conclusions about the expected PES spectral signatures of the various excited states mentioned earlier. These conclusions can then be extended and applied to the heptazine molecule and PCN material systems that have been investigated here. In the specific case of triazine, photoexcitation and ionization are expected to lead to the following states and energetics [450, 451]. The optically bright $^1A_1' \rightarrow {}^1E'$ transition at 7.65 eV can be related to the $1e'' \rightarrow 2e''$ molecular orbital transition. The associated excited state will Koopmans correlate with the first excited state of the triazine cation, [455, 456] $(1e'')^{-1}$ or D_1, which has an electron binding energy of 11.69 eV with respect to vacuum, resulting in an expected excited-state binding energy of $11.79\,\text{eV} - 7.65\,\text{eV} = 4.04\,\text{eV}$, with respect to the vacuum level. [451] Upon internal conversion from this excited state to the vibrationally excited S_1 state, a $(6e')^{-1}(2e'')^1$ configuration is produced in comparison to the ground state. This state correlates with the ground state of the cation, $(6e')^{-1}$ or D_0, with a binding energy of 10.01 eV with respect to vacuum. [451] Following vibrational relaxation, this state is then expected to result in an approximate excited-state binding energy of $10.01\,\text{eV} - 3.70\,\text{eV} = 6.31\,\text{eV}$, [451] i.e., a more than 2 eV increase in binding energy following ultrafast internal conversion from the optically-bright state and subsequent IVR.

If the analogy between triazine and heptazine is applicable, it is reasonable to assume that this scenario will be comparable to the PCN case, although there may be variations in energy levels. That is, a similar optically bright $^1A_1' \rightarrow {}^1E'$ transition pervades in the heptazine and PCN cases to populate the S_4 state, ES1, in this case with lower peak absorption energies of around 4.4 eV [454]. Like in the triazine case – and generally for higher-lying, singly-excited states of molecular systems – the heptazine and PCN S_4 states will correlate with electronically-excited ionized states, which are here expected to produce low-binding-energy electrons, as observed in the ES1 state-associated spectra. Following the generally expected ultrafast internal conversion from the electronically excited singlet state (S_4) to vibrationally-excited levels of S_1, [457, 458] ES2 is formed and the related PCN state-associated-spectra exhibit a binding energy reduction of ≈ 1 eV, which together with the extracted time-constants are indicative of an electronic state switch.

Generally, when molecular excited states that are excited vibrationally undergo IVR, it is anticipated that the associated excited-state electron binding energies will increase. This phenomenon has been observed in the case of the PCN material as the system relaxes from vibrationally-excited levels of S_1, in going from ES2 to ES3, where a further electron-binding-energy reduction of $\approx 1\,\text{eV}$ is discerned in the PCN state-associated spectra. Similar relaxation processes, although energetically shifted, appear to occur in all of the PCN materials, resembling the behavior previously simulated in the triazine case [454]. Likewise, there appears to be a relaxation process in the PCN materials that is comparable to that observed in the triazine case, although it shows a slight variation in energy. It is important to note that conducting PES experiments, particularly femtosecond-time-resolved PES measurements, on molecular and solid heptazine samples would greatly assist in validating these considerations. Moreover, it would contribute significantly to a better comprehension of the ionisation mechanisms, early-time excited-state behaviors, and photocatalytic properties of PCN materials.

6.6 Summary

In Chapter 6, the electronic structure and photoinduced electron dynamics of the PCN thin films upon 400 nm excitation were investigated at the surface-vacuum and surface-bulk interfaces by performing femtosecond TRPES and UV-Vis TAS experiments, respectively. The combination of steady-state PES and LJ-PES experiments allowed the valence electronic structure of the PCN thin films and the $\text{TEOA}_{(aq)}$ solution to be probed in the solid and liquid phases, including the determination of the photocatalyst-sacrificial agent liquid-vacuum-interface energetics with respect to the Fermi level. The major findings obtained from TRPES and TAS experiments in conjunction with the steady-state UV-Vis absorption and EUV photoemission spectroscopy experiments are described in the following. The energetic positions of the spectral bands extracted from the steady-state UV-Vis absorption spectra indicate that the PCN photocatalysts are optically photoexcited at a central photon energy of ≈ 3.2 eV (388 nm wavelength). The band gap energy, E_g, values for the direct allowed electronic transitions in the PCN thin films were determined from the Tauc plots associated with the UV-Vis absorption data. The extracted E_g values in the PCN thin films suggest that, within a semiconductor electronic structure framework, these samples have a wide-band-gap-semiconductor-like electronic structure.

The outer valence electron binding energies of the PCN thin films, as determined at the surface-vacuum interface and with respect to E_F, were obtained from the steady-state EUV PES experiments. The valence band spectroscopic results of the PCN thin films were presented within MO and semiconductor band electronic structure frameworks, extracting the energetic positions of the spectral features associated with the valence MOs and VBM position of the samples, respectively. The steady-state LJ-PES experiments allowed the outer valence electronic structure of the $\text{TEOA}_{(aq)}$ solution to be determined relative to E_{vac} and E_F. Similarly to the PES results on the PCN thin films, the data was interpreted within MO and semiconductor band structure frameworks. The HOMO and HOMO-1 electron binding energies as well as the VBM position of the TEOA solute were determined from the photoionisation results. An experimentally-determined VBM and CBM diagram of the PCN thin films was produced and compared to the TEOA solute VBM within a semiconductor band structure framework. The diagram was energy referenced with respect to E_F and the RHE, with the latter allowing the catalyst and the sacrificial agent VBMs and the catalysts CBMs to be compared to the water OER and HER energetics, respectively. Accurately-determined valence band electron binding energies of the PCN samples and the TEOA solute give insights into the catalyst-sacrificial agent interfacial energetics in a photocatalytic water splitting reaction.

TRPES experiments performed with the PCN thin films revealed the sub-100 fs time resolution ultrafast kinetics of the photoexcited PCN samples at the surface-vacuum interface upon 400 nm excitation (3.1 eV photon energy). The time-dependent populations of electronic states in the PCN samples were tracked in the WAM and LADM of the electron spectrometer with respect to the E_F over the different electron binding energy ranges. To improve the accuracy and precision of the

data analysis, a global fitting procedure and an appropriate kinetic model was employed, providing spectral and kinetic information on time-dependent changes in the electronic structure of the PCN thin films. The temporal and spectral information obtained from the TRPES experiments was used to elucidate the charge and energy transfer mechanisms occurring on the sub-1 ps time scales in the photoexcited PCN samples. The results clearly show that optical excitation at a 3.1 eV photon energy leads to a short-lived excited state, ES1, from which a transition into a short-lived intermediate state, ES2, occurs within $<$ 150 fs. The comprehensive analysis of the transient data recorded in both the WAM and LADM of the spectrometer, demonstrates that a previously unidentified excited state, ES2, undergoes a sequential relaxation processes and populates a metastable state, ES3, with lifetimes of less than 1 ps. The observed sub-1 ps decay was attributed to interchain energy transfer in the PCN thin films, most likely between the heptazine units, which occurs similarly in conjugated polymer films, due to the short distances between the chains and a large number of available pathways [443]. The formation of the metastable ES3 state is followed by the build up of a long-lived population in the subsequent excited states on timescales $>$ 2 ps.

UV-Vis TAS experiments performed with the PCN thin films provided detailed insights into electron transfer processes at the bulk-surface interface and the long-lived photodynamics in the PCN thin films upon 400 nm excitation. The time-dependent spectral changes in the transient diffuse reflectance spectra of the PCN samples were monitored over the 550 – 920 nm wavelength range on time scales up to 1.8 ns. Analogous to TRPES, the TAS data was analysed using a global fitting procedure employing an optimised kinetic model, which included the early-time information obtained from the TRPES results and described the evolution of the transient signal at the surface-vacuum interface and the long-lived population dynamics of the excited electronic states with additional dissipation channels into the bulk of the PCN thin films. The lifetimes of the electronically excited states in the PCN thin films, extracted from the 3.1 eV photoexcitation energy TAS experiments, enabled the determination of the photoinduced relaxation processes in the PCN photocatalysts on longer nanosecond time scales and confirmation of the presence of the ultrafast kinetics detected via TRPES. A parallel transfer of the early-time excited state population to metastable CT and SE excited states was inferred to take place in the PCN samples, followed by delayed and prompt fluorescence relaxation processes within tens of ps to several ns. Variable pump pulse energy density PCN thin film TAS experiments allowed the dependence of the transient reflectance signal decay kinetics on the pump pulse fluence to be monitored. The obtained kinetic results confirmed a robustness of the applied kinetic model, describing the PCN thin film photocycle at the bulk-surface interface to pump pulse fluence.

Overall, the present TRPES and TAS experiments, in conjunction with previous TRPL and TAS results [419–421, 439, 444–446], have revealed the ultrafast photophysics in the PCN thin films upon 400 nm excitation at the bulk-surface-vacuum interface. The joint analysis of the TRPES and TAS data reported here and associated kinetic modeling is a powerful tool for extracting spectral and kinetic information on time-dependent changes in the electronic structure of the PCN thin films, which assisted in gaining an understanding the relationship between the electron dynamics and photocatalytic activity. These aspects are crucial for the development of general strategies that will lead to optimal PCN photocatalytic materials for various applications.

Chapter 7

Conclusions

> "It is not in what you succeed in doing that you get your joy, but in the doing of it."
>
> *— Jack London, Martin Eden, 1909*

The work presented in this thesis has demonstrated the immense potential of employing femtosecond time-resolved EUV photoemission (TRPES) and UV-Vis transient absorption spectroscopy (TAS) in the study of ultrafast photodynamics of catalytic molecular compounds for light-harvesting and energy transfer applications. Two different homogeneous and heterogeneous catalytic molecular and material systems - ferricyanide ($[Fe(CN)_6]^{3-}$) transition metal complex dissolved in the [emim][DCA] ionic liquid (IL) and polymeric carbon nitride (PCN) thin films - were investigated. The evolution of the electronic structure of these liquid and solid-phase molecular systems after photoexcitation has been examined in their applied or natural environment, respectively.

In Chapter 5, the focus was drawn to the relaxation dynamics of the lowest-lying electronically photoexcited ^{2}LMCT state of the $[Fe(CN)_6]^{3-}$ transition metal complex upon 400 nm excitation, which has been much debated in the literature. The revelation of the $[Fe(CN)_6]^{3-}$ ion ultrafast photodynamics following 400 nm optically induced excitation was performed in a liquid environment, the IL [emim][DCA], using the TRPES technique. In this work, the applicability of ILs to study the dynamics in the liquid-phase using PES and with $[Fe(CN)_6]^{3-}$ dissolved in [emim][DCA] were explored under high vacuum conditions. In those experiments, a low-vapour-pressure, viscous droplet of the sample was readily held inside a thin, grounded loop of copper wire throughout the TRPES experiments. The use of low pump and probe fluences and this non-conventional molecular solvent [emim][DCA] allowed the excited state dynamics of solvated $[Fe(CN)_6]^{3-}$ ions and through comparison to previous work in alternative solvents, the influence of the solvation environment on the $[Fe(CN)_6]^{3-}$ deactivation pathway to be studied. The steady-state PES experiments provided the necessary information to map the electronic ground state configuration of the $[Fe(CN)_6]^{3-}$ compound dissolved in the [emim][DCA] ionic liquid. The $[Fe(CN)_6]^{3-}$ valence-shell electronic structure, in particular, the Fe 3d (t_{2g}) and the CN^- ligands molecular orbital electron binding energies were determined with respect to the local vacuum level. The energetic positions of the $[Fe(CN)_6]^{3-}$ solute peaks in the [emim][DCA] were found to be shifted and broadened when compared to the well-studied aqueous solution. The reason for the different positions of the solute peaks was related to the properties of the IL environment, which were found to have an impact on the solvation dynamics and the electronic transition rates of the $[Fe(CN)_6]^{3-}$ compound.

The TRPES experiments revealed the $[Fe(CN)_6]^{3-}$ dissolved in [emim][DCA] solution excited state dynamics following 400 nm pump wavelength excitation. Spectro-temporal modeling was employed to evaluate the measured transient data using a global analysis procedure based on fitting a physical kinetic model to the TRPES signal. The kinetics of $[Fe(CN)_6]^{3-}$ dissolved in [emim][DCA] solution was described by a four-state kinetic model in this work, and confirmed the previously observed relaxation mechanism, assigned to the dynamics in the related aqueous solution: intersystem crossing from the initially excited ^{2}LMCT state to the ^{4}LF state [93, 402] as well as the sequential

population of the vibrationaly-hot excited GS or its adjacent low-lying degenerate ^{2}LF states. The intersystem crossing transition rates of $[Fe(CN)_6]^{3-}$ extracted from the global fitting were found to be much faster in the IL, as compared to other molecular solvents [91–93], which demonstrates that the solvation environment has a significant influence on the ultrafast deactivation processes. With the aid of TDDFT calculations, the potential energy surfaces of $[Fe(CN)_6]^{3-}$ along the a_{1g} Fe–CN stretching mode in the [emim][DCA] as well as aqueous solution were computed using an implicit solvation model. The lowest ionisation energy transitions, corresponding to the calculated ionic states, were further identified on the binding energy scale, highlighting the solvent-induced energy shifts between the ^{2}LMCT and ^{4}LF states potential curves. These energetic offsets were related to the accelerated transition time constants in the IL environment in comparison to H_2O. This observation was attributed to the electronic solvent response, where the much lower dielectric constant of the IL led to relative changes in the position of the intersections between the potential energy surfaces. Further analysis, based on explicit solvent simulations, is needed to gain a more detailed insight into the electronic and vibrational relaxation processes in the IL environment. Photoinduced changes in the electronic structure of different catalytic molecular compounds in ILs have yet to be broadly studied, such experiments would allow the behaviours of the electronic structures of the ground and excited state of catalytic compounds to be interrogated. The implementation of ILs as a nonvolatile solvent, as described here, provides a route to the ready realisation of PES and TRPES experiments with a broad range of solutes under high vacuum conditions.

In Chapter 6, the electronic structure and 400-nm-photoinduced electron dynamics of the sg-CN, CNB, CNPS-O, and CNPS-NH_2 thin films at the bulk-surface-vacuum interface were examined and discussed. By virtue of the combined TRPES and UV-Vis TAS studies, the photophysical processes occurring in the PCN thin films have been elucidated on time scales ranging from femtoseconds to nanoseconds. In this work, the TRPES technique was implemented as a spectroscopic tool for investigating the photodynamic processes in a nanometer-thick layer of a solid PCN sample for the first time. Thereby, the ultrafast sub-picosecond dynamics of the PCN thin films at the surface-vacuum interface were probed using TRPES, while the interfacial-to-bulk electron transfer processes occurring on time scales up to several nanoseconds were examined by UV-Vis TAS. The steady-state UV-Vis absorption spectroscopy experiments provided the necessary information about the HOMO-LUMO energy gap and direct allowed electronic transitions in the PCN samples. From the UV-Vis absorption spectra, it was found that the PCN thin films can be optimally optically photoexcited at a central wavelength of 388 nm. Within the semiconductor band electronic structure framework, the band gap energy, E_g, values in the PCN samples were extracted by employing the Tauc method.

A combination of the results from steady-state PES and LJ-PES experiments provided insights into the electronic structure of the PCN thin films and the $TEOA_{(aq)}$ solution, as well as allowed extraction of the relative vacuum-condensed-phase interface energetics between the photocatalyst and its sacrificial agent. The obtained valence band spectroscopic results of the two systems were interpreted within the molecular orbital and semiconductor band electronic structure frameworks, which facilitated the identification of spectral features of the samples and comparison of their energetic positions. The PCN thin film outer valence electron binding energies were determined on an absolute binding energy scale with respect to the system Fermi level at the solid-vacuum interface. The energetic positions of the four spectral bands associated with the valence molecular orbitals of the PCN samples were identified. The position of the VBM was also estimated for each sample using a tangent derivative-based approach. The extracted VBM values in combination with the E_g values indicate that for all four PCN thin films, the thermodynamic condition for driving a photocatalytic water splitting reaction is met. The outer valence electron binding energies of the $TEOA_{(aq)}$ solution as well as the TEOA solute were determined on an absolute binding energy scale with respect to the local vacuum and Fermi levels at the liquid-vacuum interface. Two emission bands of the TEOA solute associated with the HOMO and HOMO-1 were observed. As far as is known, no previous study has identified the valence photoelectron signatures of the TEOA solute. To compare the solid-liquid interface energetics of the PCN thin films and the TEOA solute on the same energy scale, the tangent method was also

used to roughly extract the VBM position of the TEOA solute. Within a semiconductor band structure framework, a schematic energy diagram of the band edge alignment of the PCN thin films as well as TEOA solute, relative to the electrochemical potentials of the water HER and OER and the Fermi level, was produced from the PCN sample and TEOA solute PES data. The approach proposed here has the potential to solve scientific-technical challenges when comparing the photocatalyst-sacrificial agent vacuum-condensed-phase interface energetics in a photocatalytic water-splitting reaction.

The TRPES and UV-Vis TAS experiments, performed with different probing depths of the PCN samples, at the surface-vacuum and surface-bulk interfaces, respectively, provided insight into associated ultrafast photodynamic processes. The evolution of the excited state electronic structure of the PCN thin films upon 400 nm excitation was analysed and modeled using the global fitting procedure, which yielded kinetic information (i.e., lifetimes) as well as spectra associated with the involved electronic states. The ultrafast kinetics of the photoexcited PCN samples at the surface-vacuum interface were monitored with sub-100 fs time resolution, which facilitated the determination of the short-lived excited electronic state lifetimes and energetics. By measuring time-dependent transient signals from the PCN thin films with respect to the system Fermi level over the different electron binding energy ranges and analysing separate data sets, the sequential population of the three excited states was inferred. The lifetime obtained for the initially populated excited state, ES1, of $\simeq$ 150 fs and overall early-time dynamics in the photoexcited PCN thin films is similar to those previously reported in TRPL and TAS studies on PCN powders and colloids [419–421, 439]. However, in comparison with the literature, the results of the TRPES data analysis clearly show that a second, previously undetermined excited state, ES2, is populated via the initially-excited ES1 state within $<$ 1 ps. In addition, the formation of a long-lived state, ES3, was also detected. Due to the limited data acquisition speed and time-span of 2.4 ps in the 5-kHz repetition rate TRPES experiments, the build-up of the long-lived population in the subsequent excited states was only revealed on time scales up to several nanoseconds using UV-Vis TAS.

The UV-Vis transient diffuse reflectance spectra of the PCN thin films recorded over the 550 – 920 nm wavelength range on time scales up to 1.8 ns allowed the electron transfer processes at the bulk-surface interface and long-lived population dynamics upon 400 nm excitation to be mapped. Based on the TAS data global fitting results, the early-time sequential population of the excited states observed in the TRPES studies was confirmed and further transfer of the long-lived population was found to occur with additional dissipation channels into the bulk of the PCN thin films. Specifically, two metastable states were found to be formed after the parallel transfer of the initial population of the excited states. In accordance with the reported TRPL and TAS observations [419–421, 439], it was inferred that these metastable states correspond to the potential formation of charge-transfer, CT, and singlet exciton, SE, states within several picoseconds. In addition, it was found that the CT state can undergo sequential electronic transitions to the SE state with a lifetime of $\approx$ 2.7 ns. Further, the UV-Vis TAS results demonstrate that the population of the metastable CT and SE states is followed by radiative relaxation processes, which correspond to delayed and prompt fluorescence signals, as suggested in references [419–421, 439]. The lifetimes of these signals obtained from the global analysis were found to be $\approx$ 50 ps and $\approx$ 5 ns, respectively. Additionally, the pump pulse fluence dependence of the decay kinetics of the TAS signal in the PCN thin films was revealed by performing the TAS experiments with variable 400 nm pump pulse energy. Based on the results of global fitting and kinetic modelling, it was found that the early-time 400-nm-pump-induced dynamics in the PCN samples occur in the time interval from hundreds of femtoseconds to several picoseconds and do not depend on the pump fluence. However, the long-lived dynamics, associated mainly with the delayed and prompt fluorescence relaxation processes, were found to be excitation-fluence dependent. The extracted decay time constants suggest that these two radiative relaxation channels compete with each other. Further studies on the competing relaxation channels of the involved states are required to draw a final conclusion about the mechanism underlying such behaviour. As a follow-up to the pump fluence-dependent TAS experiments, the delay times should also be extended to a range of

milliseconds, to allow further investigation and possibly determine the origin of the pump-pulse-fluence-induced changes to the decay dynamics.

Summarising, the femtosecond EUV-based TRPES and UV-Vis TAS experiments provide essential information on the microscopic electronic structure of photoexcited catalytic molecular systems as they evolve in time. The sensitivity of the TRPES technique to both electronic structure and electronic dynamics allows the determination of individual contributions from specific electronic states of a photoexcited catalytically-active molecular system on an absolute binding energy scale with high accuracy. The TAS technique gives insights into photogenerated excited state absorption energies and high-resolution kinetic profiles of the transient species formation and decay. This work has shown that, by combining TRPES and UV-Vis TAS studies, the kinetic and spectral information about electronic dynamic processes occurring at different stages of the photophysical pathway in catalytic molecular compounds can be accessed. The application of such information provides the means to correlate light-harvesting mechanisms and photophysicochemical behaviour of catalytically-active systems with electron and energy transfer processes, contributing to further optimisation and development of highly-efficient selective functional materials. This methodology would also be generally applicable to any other photo-sensitive molecular compound.

Future research should be devoted to the development of TRPES and TAS experiments using pulsed laser sources with much higher repetition rates (from several tens of kHz to a few MHz) to improve the signal-to-noise level of the transient data. In addition, replication of TRPES and TAS results on the PCN thin films over a wider range of electron binding energies and wavelengths, as well as over longer time scales, might prove an important area for futher studies. Furthermore, soft X-ray TAS and PES studies of PCN materials could fruitfully explore the electron dynamics across different chemical sites and are desirable for future work. Insights into the structural dynamics and energy transfer processes between aqueous solution and photoexcited PCN species in real water splitting reactions could be derived from time-resolved sum-frequency generation (TRSFG) spectroscopy studies. Prospective implementation of a quartz reactor device in such experiments would facilitate the *in situ* studies of interfacial dynamics at the PCN-photocatalyst/water interface. These experiments could be beneficial for the development of efficient and selective photocatalysts for water splitting as well as energy conversion and storage applications.

Appendix A

Fit Parameters Extracted from TRPES State-Associated Spectra

A.0.1 $[Fe(CN)_6]^{3-}$ Dissolved in [emim][DCA] Solution

Here, E denotes the binding energy of the central peak position, FWHM is the full-width at half-maximum of the peak width, and A is the peak amplitude.

TABLE A.1: Fit parameters of the Gaussian peaks used to represent the binding energy amplitudes in the global fitting to the $[Fe(CN)_6]^{3-}$ dissolved in [emim][DCA].

Assignment	Label	E / eV	FWHM / eV	A / cts
GS	1	10.75 ± 0.20	3.30 ± 0.02	861.13 ± 44.40
GS	2	10.01 ± 0.06	3.09 ± 0.07	505.67 ± 14.26
GS	3	7.60 ± 0.04	1.09 ± 0.05	133.34 ± 4.60
^{2}LMCT	1	10.03 ± 0.02	3.18 ± 0.12	916.81 ± 48.70
^{2}LMCT	2	7.59 ± 0.01	1.09 ± 0.03	125.37 ± 9.15
^{2}LMCT	3	6.31 ± 0.02	0.91 ± 0.01	6.69 ± 0.05
^{2}LMCT	4	5.53 ± 0.02	2.23 ± 0.41	5.09 ± 0.25
^{4}LF	1	10.00 ± 0.01	3.09 ± 0.04	909.23 ± 86.83
^{4}LF	2	7.74 ± 0.10	1.34 ± 0.05	127.17 ± 2.23
^{4}LF	3	6.62 ± 0.05	1.05 ± 0.06	4.51 ± 0.03
^{4}LF	4	5.53 ± 0.32	2.09 ± 0.63	3.08 ± 0.07
GS*	1	10.04 ± 0.02	3.06 ± 0.05	802.10 ± 41.40
GS*	2	7.49 ± 0.03	0.99 ± 0.01	167.67 ± 10.00
GS*	3	6.86 ± 0.01	1.05 ± 0.03	9.51 ± 2.28
GS*	4	5.52 ± 0.02	1.60 ± 0.11	2.34 ± 0.43
CC	1	8.34 ± 0.04	1.86 ± 0.05	2.55 ± 0.03
CC	2	7.17 ± 0.01	1.80 ± 0.05	0.39 ± 0.01
CC	3	5.46 ± 0.04	1.21 ± 0.01	0.09 ± 0.01

A.0.2 Polymeric Carbon Nitride Thin Films

TABLE A.2: Fit parameters of the Gaussian peaks used to represent the binding energy amplitudes in the state-associated spectra of sg-CN sample.

Assignment	Label	E / eV	FWHM / eV	A / cts
GS	1	3.61 ± 0.03	2.02 ± 0.06	0.28 ± 0.02
GS	2	5.37 ± 0.09	3.25 ± 0.05	26.13 ± 0.42
GS	3	7.66 ± 0.11	2.98 ± 0.03	82.98 ± 0.95
GS	4	12.87 ± 0.08	4.75 ± 0.07	766.04 ± 33.44
ES1	1	3.61 ± 0.06	1.84 ± 0.55	2.91 ± 0.9
ES1	2	4.95 ± 0.11	1.70 ± 0.36	7.71 ± 2.55
ES1	3	7.44 ± 0.04	3.05 ± 0.19	67.82 ± 6.25
ES1	4	18.90 ± 0.13	8.93 ± 0.16	7983.48 ± 526.96
ES2	1	3.61 ± 0.03	2.37 ± 0.38	3.42 ± 0.81
ES2	2	4.74 ± 0.08	1.96 ± 0.24	9.06 ± 2.28
ES2	3	7.34 ± 0.04	3.07 ± 0.14	85.21 ± 8.66
ES2	4	14.29 ± 0.95	6.08 ± 0.83	1450.49 ± 570.52
ES3	1	4.22 ± 0.06	1.91 ± 0.05	5.21 ± 0.17
ES3	2	5.07 ± 0.03	1.47 ± 0.04	5.71 ± 0.21
ES3	3	7.42 ± 0.03	2.75 ± 0.02	70.53 ± 0.11
ES3	4	17.06 ± 0.02	8.02 ± 0.72	4492.06 ± 2.57

TABLE A.3: Fit parameters of the Gaussian peaks used to represent the binding energy amplitudes in the state-associated spectra of CNB sample.

Assignment	Label	E / eV	FWHM / eV	A / cts
GS	1	3.61 ± 0.05	2.64 ± 0.42	1.77 ± 0.46
GS	2	5.37 ± 0.06	2.68 ± 0.18	11.35 ± 1.44
GS	3	7.66 ± 0.09	3.41 ± 0.06	71.97 ± 2.46
GS	4	11.82 ± 0.08	4.57 ± 0.14	182.42 ± 8.18
ES1	1	3.61 ± 0.07	2.46 ± 0.32	1.71 ± 0.76
ES1	2	5.32 ± 0.08	2.03 ± 0.43	6.65 ± 1.68
ES1	3	7.58 ± 0.06	3.18 ± 0.22	52.22 ± 6.67
ES1	4	16.09 ± 2.17	9.11 ± 1.51	811.56 ± 508.23
ES2	1	3.61 ± 0.04	1.56 ± 0.27	1.19 ± 0.41
ES2	2	5.08 ± 0.08	1.86 ± 0.23	3.96 ± 1.31
ES2	3	7.26 ± 0.03	3.28 ± 0.13	44.75 ± 3.87
ES2	4	13.38 ± 0.29	8.13 ± 0.43	383.79 ± 33.18
ES3	1	4.27 ± 0.11	2.76 ± 0.51	1.21 ± 0.20
ES3	2	5.07 ± 0.12	2.24 ± 0.20	3.69 ± 1.49
ES3	3	7.81 ± 0.08	3.64 ± 0.18	86.97 ± 8.75
ES3	4	12.14 ± 0.13	4.36 ± 0.42	201.13 ± 26.88

TABLE A.4: Fit parameters of the Gaussian peaks used to represent the binding energy amplitudes in the state-associated spectra of CNPS-O sample.

Assignment	Label	E / eV	FWHM / eV	A / cts
GS	1	3.61 ± 0.03	2.58 ± 0.56	0.23 ± 0.06
GS	2	5.37 ± 0.08	4.41 ± 0.07	44.64 ± 1.03
GS	3	7.66 ± 0.05	3.97 ± 0.05	85.96 ± 1.07
GS	4	14.00 ± 0.13	5.18 ± 0.02	982.77 ± 3.51
ES1	1	3.61 ± 0.04	3.05 ± 0.26	9.86 ± 2.47
ES1	2	4.85 ± 0.11	1.53 ± 0.41	4.12 ± 2.91
ES1	3	7.29 ± 0.17	4.24 ± 0.52	112.15 ± 21.65
ES1	4	15.85 ± 2.88	6.36 ± 2.07	2440.51 ± 298.35
ES2	1	3.61 ± 0.09	2.61 ± 1.09	0.15 ± 0.92
ES2	2	4.97 ± 0.26	3.79 ± 1.36	28.96 ± 6.62
ES2	3	7.47 ± 0.11	4.08 ± 1.13	92.00 ± 76.78
ES2	4	16.02 ± 0.45	6.65 ± 0.13	2341.71 ± 57.65
ES3	1	4.20 ± 0.10	2.03 ± 0.34	8.88 ± 0.20
ES3	2	5.13 ± 0.03	1.32 ± 0.08	2.55 ± 0.22
ES3	3	7.36 ± 0.01	3.54 ± 0.09	94.45 ± 0.16
ES3	4	14.40 ± 0.21	5.61 ± 0.82	1297.26 ± 0.97

TABLE A.5: Fit parameters of the Gaussian peaks used to represent the binding energy amplitudes in the state-associated spectra of CNPS-NH_2 sample.

Assignment	Label	E / eV	FWHM / eV	A / cts
GS	1	3.61 ± 0.02	4.14 ± 0.31	12.93 ± 4.45
GS	2	5.37 ± 0.06	3.14 ± 0.22	30.81 ± 2.32
GS	3	7.66 ± 0.08	4.67 ± 1.41	117.57 ± 5.8
GS	4	15.10 ± 2.97	5.90 ± 2.81	979.71 ± 126.62
ES1	1	3.61 ± 0.05	5.78 ± 0.36	2.61 ± 4.20
ES1	2	4.95 ± 0.34	3.55 ± 0.75	32.19 ± 5.25
ES1	3	7.00 ± 0.15	3.37 ± 0.68	62.83 ± 3.48
ES1	4	18.66 ± 7.29	10.16 ± 5.19	2359.28 ± 110.20
ES2	1	3.61 ± 0.10	3.22 ± 0.39	15.75 ± 0.97
ES2	2	5.32 ± 0.46	2.05 ± 2.24	13.24 ± 1.71
ES2	3	7.36 ± 0.17	4.64 ± 0.11	122.33 ± 3.50
ES2	4	18.25 ± 2.50	7.73 ± 0.08	3668.98 ± 112.85
ES3	1	4.20 ± 0.05	2.86 ± 0.16	17.68 ± 2.53
ES3	2	6.05 ± 0.07	2.48 ± 0.47	29.02 ± 4.51
ES3	3	7.45 ± 0.15	3.56 ± 1.38	59.13 ± 6.26
ES3	4	16.68 ± 2.72	9.12 ± 2.58	1297.25 ± 47.09

Appendix B

Chemical Stability of Samples During TRPES Measurements

B.0.1 $[Fe(CN)_6]^{3-}$ Dissolved in [emim][DCA] Solution

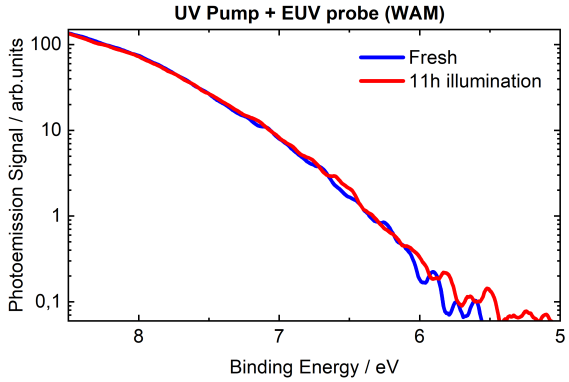

FIGURE B.1: Photoemission spectra of $[Fe(CN)_6]^{3-}$ dissolved in [emim][DCA] solution obtained in the beginning of TRPES data acquisition (fresh) and in the end (after 11 hours of illumination). The obtained spectra do not exhibit any spectral changes over the time span of TRPES measurements, indicating no damage to the sample.

B.0.2 Polymeric Carbon Nitride Thin Film Sample

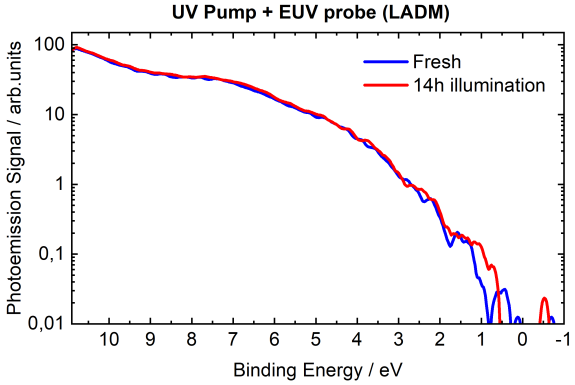

FIGURE B.2: Photoemission spectra of the sg-CN thin film sample recorded in the first hour of the data acquisition (fresh) and in the last hour (14 hours later) confirming the chemical stability of the PCN sample during the TRPES measurements.

Bibliography

1. Anastas, P. T. & Warner, J. C. *Green Chemistry: Theory and Practice* (Oxford University Press, 1998).
2. Anastas, P. T. & Zimmerman, J. B. *Innovations in Green Chemistry and Green Engineering* (Springer, 2012).
3. Armor, J. N. A history of industrial catalysis. *Catal.* **163,** 3–9 (2011).
4. Suib, S. L. *New and Future Developments in Catalysis: Batteries, Hydrogen Storage and Fuel Cells* (Elsevier, 2013).
5. Agbea, H., Nyankson, E., Raza, N., D.Dodoo-Arhin, Chauhan, A., Osei, G., Kumar, V. & Kim, K.-H. Recent advances in photoinduced catalysis for water splitting and environmental applications. *J. Ind. Eng. Chem.* **72,** 31–49 (2019).
6. Pereira, M. M. & Calvete, M. J. F. *Sustainable Synthesis of Pharmaceuticals: Using Transition Metal Complexes as Catalysts* (Royal Society of Chemistry, 2018).
7. Pasquarelli, A. *Catalytic Biosensors. In: Biosensors and Biochips. Learning Materials in Biosciences* (Springer, 2021).
8. Tucker, G. A. & Woods, L. F. J. *Enzymes in Food Processing* (Springer, 1995).
9. Grassian, V. H. *Environmental Catalysis* (CRC Press, 2005).
10. Bates, R. *Organic Synthesis Using Transition Metals* (Wiley & Sons, 2012).
11. Goswami, A. & Stewart, J. *Organic Synthesis Using Biocatalysis* (Elsevier, 2016).
12. Yang, X.-F., Wang, A., Qiao, B., Li, J., Liu, J. & Zhang, T. Single-Atom Catalysts: A New Frontier in Heterogeneous Catalysis. *Acc. Chem. Res.* **46 (8),** 1740—1748 (2013).
13. Imelik, B., Naccache, C. & Coudurier, G. *Catalysis by Acids and Bases* (Elsevier, 1985).
14. Van Leeuwen, P. W. N. M. *Supramolecular Catalysis* (Wiley-VCH, 2008).
15. Serp, P. & Philippot, K. *Nanomaterials in Catalysis* (Wiley-VCH, 2013).
16. Duca, G. *Homogeneous Catalysis with Metal Complexes: Fundamentals and Applications* (Springer, 2014).
17. Torok, B., Schaefer, C. & Kokel, A. *Heterogeneous Catalysis in Sustainable Synthesis* (Elsevier, 2021).
18. Kaur, P., Hupp, J. T. & Nguyen, S. T. Porous Organic Polymers in Catalysis: Opportunities and Challenges. *ACS Catal.* **1 (7),** 819—835 (2011).
19. Wang, X., Blechert, S. & Antonietti, M. Polymeric Graphitic Carbon Nitride for Heterogeneous Photocatalysis. *ACS Catal.* **2 (8),** 1596—1606 (2012).
20. Barbaro, P. & Liguori, F. *Heterogenized Homogeneous Catalysts for Fine Chemicals Production* (Springer, 2010).
21. Bommarius, A. S. & Riebel-Bommarius, B. R. *Biocatalysis: Fundamentals and Applications* (Wiley & Sons, 2007).
22. Kuznetrsov, A. M. *Charge Transfer in Physics, Chemistry and Biology* (CRC Press, 1995).

23. Gratzel, M. *Energy Resources through Photochemistry and Catalysis* (Elsevier, 1983).
24. Zewail, A. H. Femtochemistry: atomic-scale dynamics of the chemical bond. *J. Phys. Chem. A* **104,** 5660–5694 (2000).
25. Petek, H., Weida, M. J., Nagano, H. & Ogawa, S. Real-time observation of adsorbate atom motion above a metal surface. *Science* **288,** 5470 (2000).
26. Bovensiepen, U., Petek, H. & Wolf, M. *Dynamics at Solid State Surfaces and Interfaces* (Wiley & Sons, 2010).
27. Turro, N. J., Ramamurthy, V., Ramamurthy, V. & Scaiano, J. C. *Principles of Molecular Photochemistry: An Introduction* (University Science Books, 2009).
28. Schäfer, R. & Schmidt, P. C. *Methods in Physical Chemistry* (Wiley & Sons, 2012).
29. Peiponen, K.-E., Zeitler, A. & Kuwata-Gonokami, M. *Terahertz Spectroscopy and Imaging* (Springer, 2012).
30. Schrader, B. *Infrared and Raman Spectroscopy: Methods and Applications* (Wiley & Sons, 2008).
31. Diels, J.-C. & Rudolph, W. *Ultrashort laser pulse phenomena* (Oxford University Press, 2006).
32. Ding, T., Ott, C., Kaldun, A., Blattermann, A., Meyer, K., Stooss, V., Rebholz, M., Birk, P., Hartmann, M., Brown, A., Hart, H. V. D. & Pfeifer, T. Time-resolved four-wave-mixing spectroscopy for inner-valence transitions. *Opt. Lett.* **41,** 709–712 (2016).
33. Donaldson, P. M. Photon echoes and two dimensional spectra of the amide I band of proteins measured by femtosecond IR – Raman spectroscopy. *Chem. Sci.* **11,** 8862–8874 (2020).
34. Maiuri, M., Garavelli, M. & Cerullo, G. Ultrafast Spectroscopy: State of the Art and Open Challenges. *J. Am. Chem. Soc.* **142 (1),** 3–15 (2020).
35. Smith, G. D. & Palmer, R. A. *Handbook of Vibrational Spectroscopy, Fast Time-Resolved Mid-Infrared Spectroscopy Using an Interferometer* (Wiley & Sons, 2002).
36. Lakowicz, J. R. *Principles of Fluorescence Spectroscopy* (Springer, 2006).
37. Stolow, A., Bragg, A. E. & Neumark, D. M. Time-resolved photoelectron spectroscopy. *Chem. Rev.* **104(4),** 1719—1758 (2004).
38. Fielding, H. H. & Worth, G. A. Using time-resolved photoelectron spectroscopy to unravel the electronic relaxation dynamics of photoexcited molecules. *Chem. Soc. Rev.* **47,** 309–321 (2018).
39. Zhou, C., Ma, Z., Ren, Z., Wodtkeb, A. M. & Yang, X. Surface photochemistry probed by two-photonphotoemission spectroscopy. *Energy Environ. Sci.* **5,** 6833–6844 (2012).
40. Berera, R., van Grondelle, R. & Kennis, J. Ultrafast transient absorption spectroscopy: principles and application to photosynthetic systems. *Photosynth. Res.* **101,** 105–118 (2009).
41. Cerullo, G., Manzoni, C., Luer, L. & Polli, D. Time-resolved methods in biophysics. 4. Broadband pump-probe spectroscopy system with sub-20 fs temporal resolution for the study of energy transfer processes in photosynthesis. *Photochem. Photobiol. Sci.* **6,** 135–144 (2007).
42. Suga, S. & Sekiyama, A. *Photoelectron spectroscopy: bulk and surface electronic structures* (Springer Berlin Heidelberg, 2013).
43. Van Driel, T. B. *et al.* Atomistic characterization of the active-site solvation dynamics of a model photocatalyst. *Nat. Commun.* **7,** 1–7 (2016).
44. Twilton, J., Le, C., Zhang, P., Shaw, M. H., Evans, R. W. & MacMillan, D. W. C. The merger of transition metal and photocatalysis. *Nat. Rev. Chem.* **0052,** 1–18 (2017).

45. Kinzel, N. W., Werle, C. & Leitner, W. Transition Metal Complexes as Catalysts for the Electroconversion of CO_2: An Organometallic Perspective. *Angew. Chem. Int. Ed.* **60,** 11628—11686 (2021).
46. Brandsma, L., Verkruijsse, H. D. & Vasilevsky, S. F. *Application of Transition Metal Catalysts in Organic Synthesis* (Springer, Berlin, Heidelberg, United States, 1999).
47. Chergui, M. Ultrafast photophysics of transition metal complexes. *Acc. Chem. Res.* **48 (3),** 801–808 (2015).
48. Rondi, A., Rodriguez, Y., Feurer, T. & Cannizzo, A. Solvation-driven charge transfer and localization in metal complexes. *Acc. Chem. Res.* **48 (5),** 1432—1440 (2015).
49. Bertini, I., Gray, H. B., Lippard, S. J. & Valentine, J. S. *Bioinorganic Chemistry* (University Science Books , Mill Valley, 1994).
50. Warra, A. A. Transition metal complexes and their application in drugs and cosmetics. *J. Chem. Pharm. Res.* **3 (4),** 951—958 (2011).
51. Frezza, M., Hindo, S., Chen, D., Davenport, A., Schmitt, S., Tomco, D. & Dou, Q. P. Novel metals and metal complexes as platforms for cancer therapy. *Curr. Pharm. Des.* **16 (16),** 1813—1825 (2010).
52. Schmidt, S. B., Eisenhut, M. & Schneider, A. Chloroplast Transition Metal Regulation for Efficient Photosynthesis. *Trends Plant Sci.* **25 (8),** 817–828 (2020).
53. Hagfeldt, A. & Grätzel, M. Molecular Photovoltaics. *Acc. Chem. Res.* **33 (5),** 269—277 (2000).
54. Nazeeruddin, M. K. & Grätzel, M. *Transition Metal Complexes for Photovoltaic and Light Emitting Applications* (Springer, Berlin, Heidelberg, 2007).
55. Tsukerblat, B. S. *Group Theory and Chemistry and Spectroscopy: A Simple Guide to Advanced Usage* (Academic Press, 1994).
56. Griffith, J. S. & Orgel, L. E. Ligand-field theory. *Q. Rev. Chem. Soc.* **11,** 381–393 (1957).
57. Woolley, R. G. Ligand-Field Analysis of Transition-Metal Complexes. *Int. Rev. Phys.* **6,** 93–141 (1987).
58. Kettle, S. F. A. *Crystal field theory of transition metal complexes. In: Physical Inorganic Chemistry.* (Springer, Berlin, Heidelberg, 1996).
59. Condon, E. U. & Odabasi, H. *Atomic Structure* (Cambridge University Press, 1980).
60. Bersuker, I. B. *Electronic Structure and Properties of Transition Metal Compounds: Introduction to the Theory* (Wiley, 2010).
61. Groote, J.-Y. D., Jean, Y. & Hoffmann, R. *Molecular Orbitals of Transition Metal Complexes* (OUP Oxford, UK, 2005).
62. Clark, T. & Koch, R. *Linear Combination of Atomic Orbitals* (Springer, Berlin, Heidelberg, 1999).
63. Roundhill, D. M. *Photochemistry and Photophysics of Metal Complexes* (Springer US, Germany, 2013).
64. Gupta, V. P. *Principles and Applications of Quantum Chemistry* (Elsevier Science, Netherlands, 2015).
65. Franck, J. & Dymond, E. G. Elementary processes of photochemical reactions. *Trans. Faraday Soc.* **21,** 536–542 (1926).
66. Condon, E. U. Nuclear Motions Associated with Electron Transitions in Diatomic Molecules. *Phys. Rev.* **32 (6),** 858–872 (1928).
67. Yersin, H. *Transition metal and rare earth compounds* (Springer, Berlin, Heidelberg, 2004).

68. Daniel, C. Ultrafast processes: coordination chemistry and quantum theory. *Phys. Chem. Chem. Phys.* **23,** 43–58 (2021).

69. Montalti, M. & Murov, S. *Handbook of photochemistry* (CRC Press, Taylor Francis Group, Boca Raton, FL, 2006).

70. May, V. & Kühn, O. *Charge and energy transfer dynamics in molecular systems* (Wiley-VCH, Weinheim, 2011).

71. Lacowicz, J. R. *Principles of Fluorescence Spectroscopy* (Springer US, 2013).

72. Dunbar, K. R. & Heintz, R. A. *Chemistry of Transition Metal Cyanide Compounds: Modern Perspectives* (Wiley, 1996).

73. Karyakin, A. A., Gitelmacher, O. V. & Karyakina, E. E. Prusian Blue based first generation biosensor. A sensitive amperometric electrode for glucose. *Anal. Chem.* **67,** 2419–2423 (1995).

74. Rastogi, P. K., Ganesan, V., Gupta, R., Singh, P., Sonkar, P. K. & Yadav, D. K. Potassium ferricyanide-incorporated branched polyethylenimine as a potential scaffold for electrocatalytic reduction and amperometric sensing of nitrite. *J. Appl. Electrochem.* **47,** 95—104 (2017).

75. Arslan, F. & Beskan, U. An amperometric biosensor for glucose detection from glucose oxidase immobilized in polyaniline–polyvinylsulfonate–potassium ferricyanide film. *Artif. Cells Nanomed. Biotechnol.* **42 (4),** 284–288 (2014).

76. Song, K. & Chen, W. An electrochemical sensor for high sensitive determination of lysozyme based on the aptamer competition approach. *Open Chem.* **19,** 299—306 (2021).

77. Yamaoka, H. & Sode, K. A Disposable Electrochemical Glucose Sensor Using Catalytic Subunit of Novel Thermostable Glucose Dehydrogenase. *Open Biotechnol. J.* **1,** 26–30 (2007).

78. Prampolini, G., Yu, P., Pizzanelli, S., Cacelli, I., F. Yang, J. Z. & Wang, J. Structure and Dynamics of Ferrocyanide and Ferricyanide Anions in Water and Heavy Water: An Insight by MD Simulations and 2D IR Spectroscopy. *J. Phys. Chem. B* **118 (51),** 14899–14912 (2014).

79. Yu, P., Yang, F., Zhao, J. & Wang, J. Hydration Dynamics of Cyanoferrate Anions Examined by Ultrafast Infrared Spectroscopy. *J. Phys. Chem. B* **118 (11),** 3104–3114 (2014).

80. Engel, N., Bokarev, S. I., Suljoti, E., Garcia-Diez, R., Lange, K. M., Atak, K., Golnak, R., Kothe, A., Dantz, M. & Kühn, O. Chemical Bonding in Aqueous Ferrocyanide: Experimental and Theoretical X-ray Spectroscopic Study. *J. Phys. Chem. B* **118 (6),** 1555–1563 (2014).

81. Sando, G. M., Zhong, Q. & Owrutsky, J. C. Vibrational and Rotational Dynamics of Cyanoferrates in Solution. *J. Chem. Phys.* **121 (5),** 2158–2168 (2004).

82. Penfold, T. J., Reinhard, M., Rittmann-Frank, M. H., Tavernelli, I., Rothlisberger, U., Milne, C. J., Glatzel, P. & Chergui, M. X-ray Spectroscopic Study of Solvent Effects on the Ferrous and Ferric Hexacyanide Anions. *J. Phys. Chem. A* **118 (40),** 9411–9418 (2014).

83. Seidel, R., Thürmer, S., Moens, J., Geerlings, P., Blumberger, J. & Winter, B. Valence Photoemission Spectra of Aqueous $Fe^{2+/3+}$ and $[Fe(CN)_6]^{4-/3-}$ and Their Interpretation by DFT Calculations. *J. Phys. Chem. B* **115 (40),** 11671–11677 (2011).

84. Kunnus, K., Zhang, W., Delcey, M. G., Pinjari, R. V., Miedema, P. S., Schreck, S., Quevedo, W., Schroder, H., Föhlisch, A. & Gaffney, K. J. Viewing the Valence Electronic Structure of Ferric and Ferrous Hexacyanide in Solution from the Fe and Cyanide Perspectives. *J. Phys. Chem. B* **120 (29),** 7182–7194 (2016).

85. Hayakawa, K., Hatada, K., D'Angelo, P., Longa, S. D., Natoli, C. R. & Benfatto, M. Full Quantitative Multiple-Scattering Analysis of X-ray Absorption Spectra: Application to Potassium Hexacyanoferrat(II) and -(III) Complexes. *J. Am. Chem. Soc.* **126 (47),** 15618–15623 (2004).

86. March, A. M., Assefa, T. A., Bressler, C., Doumy, G., Galler, A., Gawelda, W., Kanter, E. P., Nemeth, Z., Papai, M. & et al., S. H. S. Feasibility of Valence-to-Core X-ray Emission Spectroscopy for Tracking Transient Species. *J. Phys. Chem. C* **119 (26),** 14571–14578 (2015).

87. Gray, H. B. & Beach, N. A. The Electronic Structures of Octahedral Metal Complexes. Metal Hexacarbonyls and Hexacyanides. *J. Am. Chem. Soc.* **85 (19),** 2922—2927 (1963).

88. Shirom, M. & Stein, G. The Absorption Spectrum of the Ferrocyanide Ion in Aqueous Solution. *Isr. J. Chem.* **7,** 405–412 (1969).

89. Gaynor, J. D., Courtney, T. L., Balasubramanian, M. & Khalil, M. Fourier Transform Two-Dimensional Electronic-Vibrational Spectroscopy Using an Octave-Spanning Mid-IR probe. *Opt. Lett.* **41 (12),** 2895–2898 (2016).

90. Courtney, T. L., Fox, Z., Slenkamp, K. M. & Khalil, M. Two-Dimensional Vibrational Electronic Spectroscopy. *J. Chem. Phys.* **143 (15),** 154201 (2015).

91. Ojeda, J., Arrell, C. A., Longetti, L., Chergui, M. & Helbing, J. Charge-Transfer and Impulsive Electronic-to-Vibrational Energy Conversion in Ferricyanide: Ultrafast Photoelectron and Transient Infrared Studies. *Phys. Chem. Chem. Phys.* **19 (26),** 17052–17062 (2017).

92. Zhang, W., Ji, M. & Z. Sund, K. J. G. Dynamics of Solvent-Mediated Electron Localization in Electronically Excited Hexacyanoferrate (III). *J. Am. Chem. Soc.* **134 (5),** 2581–2588 (2012).

93. Engel, N., Bokarev, S. I., Moguilevski, A., A. A. Raheem, R. A.-O., Möhle, T., Grell, G., Siefermann, K. R., Abel, B., Aziz, S. G., Kühn, O., Borgwardt, M., Kiyan, I. Y. & Aziz, E. F. Light-induced relaxation dynamics of the ferricyanide ion revisited by ultrafast XUV photoelectron spectroscopy. *Phys. Chem. Chem. Phys.* **19,** 14248–14255 (2017).

94. Anderson, N. A., Hang, K., Asbury, J. B. & Lian, T. Ultrafast Mid-IR Detection of the Direct Precursor to the Presolvated Electron Following Electron Ejection from Ferrocyanide. *Chem. Phys. Lett.* **329 (5,6),** 386–392 (2000).

95. Reinhard, M., Auböck, G., Besley, N. A., Clark, I. P., Greetham, G. M., Hanson-Heine, M. W., Horvath, R., Murphy, T. S., Penfold, T. J. & Towrie, M. Ultrafast Mid-IR Detection of the Direct Precursor to the Presolvated Electron Following Electron Ejection from Ferrocyanide. *J. Am. Chem. Soc.* **139 (21),** 37335–7347 (2017).

96. Reinhard, M., Penfold, T. J., Lima, F. A., Rittmann, J., Rittmann-Frank, M. H., Abela, R., Tavernelli, I., Rothlisberger, U., Milne, C. J. & Chergui, M. Photooxidation and Photoaquation of Iron Hexacyanide in Aqueous Solution: A Picosecond X-ray Absorption Study. *Struct. Dyn.* **1,** 024901 (2014).

97. Alexander, J. J. & Gray, H. B. Electronic structures of hexacyanometalate complexes. *J. Am. Chem. Soc.* **90 (16),** 4260–4271 (1968).

98. Naiman, C. S. Interpretation of the absorption spectra of $K_3Fe(CN)_6$. *J. Chem. Phys.* **35 (1),** 323–328 (1961).

99. Leal, J. M., Garcia, B. & Domingo, P. L. Outer-sphere hexacyanoferrate(III) oxidation of organic substrates. *Coord. Chem. Rev.* **173 (1),** 79–131 (1998).

100. Khoshtariya, D. E., Meusinger, R. & Billing, R. Optical and Thermal Outer-Sphere Electron Self-Exchange Reaction of the Hexacyanoferrate (II/III) Couple: Comparative Analysis of Band-Shape and Activation Parameters and Large Solvent Kinetic Isotope Effect. *J. Phys. Chem.* **99 (11),** 3592–3597 (1995).

101. Jay, R. M. *et al.* Disentangling Transient Charge Density and Metal–Ligand Covalency in Photoexcited Ferricyanide with Femtosecond Resonant Inelastic Soft X-ray Scattering. *J. Phys. Chem. Lett.* **9 (12),** 3538–3543 (2018).

102. Bersuker, I. *The Jahn-Teller Effect* (Cambridge University Press, 2006).

103. Hocking, R. K., Wasinger, E. C., de Groot, F. M. F., Hodgson, K. O., Hedman, B. & Solomon, E. I. Fe L-Edge XAS Studies of $K_4[Fe(CN)_6]$ and $K_3[Fe(CN)_6]$: A Direct Probe of Back-Bonding. *J. Am. Chem. Soc.* **128 (32),** 10442–10451 (2006).

104. Basu, G. & Belford, R. L. Nature of the Visible Charge-Transfer Bands of $K_3Fe(CN)_6$. *J. Chem. Phys.* **37 (9),** 1933—1935 (1962).

105. Gordon, C. M. New Developments in Catalysis Using Ionic Liquids. *Appl. Catal. A: Gen.* **222,** 101–117 (2001).

106. Chiappe, C. & Pieraccini, D. Ionic liquids: solvent properties and organic reactivity. *J. Phys. Org. Chem.* **18,** 275—297 (2005).

107. Walden, P. Molecular weights and electrical conductivity of several fused salts. *Bull. Acad. Imper. Sci. (St. Petersburg)* **8,** 405—422 (1914).

108. Rogers, R. D. & Seddon, K. R. Ionic Liquids–Solvents of the Future? *Science* **302,** 792—793 (2003).

109. Pham, T. P. T., Cho, C. W. & Yun, Y. S. Environmental fate and toxicity of ionic liquids: A review. *Water Res.* **44,** 352—372 (2010).

110. E Silva, F. A., Coutinho, J. A. P. & Ventura, S. P. M. *Aquatic Toxicology of Ionic Liquids (ILs)* (Springer Nature Singapore, 2019).

111. Seddon, K. R. *The International George Papatheodorou Symposium: Proceedings, Boghosian S. et al.* 131—135 (1999).

112. Hallett, J. & Kuzmina, O. *Application, Purification, and Recovery of Ionic Liquids* (Elsevier Science, Netherlands, 2016).

113. Cao, Y. & Mu, T. Comprehensive Investigation on the Thermal Stability of 66 Ionic Liquids by Thermogravimetric Analysis. *Ind. Eng. Chem. Res.* **53,** 8651—8664 (2014).

114. Hunger, J., Stoppa, A., Schrödle, S., Hefter, G. & Buchner, R. Temperature Dependence of the Dielectric Properties and Dynamics of Ionic Liquids. *Chem. Phys. Chem.* **10,** 723—733 (2009).

115. Weingärtner, H., Sasisanker, P., Daguenet, C., Dyson, P. J., Krossing, I., Slattery, J. M. & Schubert, T. The Dielectric Response of Room-Temperature Ionic Liquids: Effect of Cation Variation. *J. Phys. Chem. B* **111 (18),** 4775—4780 (2007).

116. Jiang, S., Hu, Y., Wang, Y. & Wang, X. Viscosity of Typical Room-Temperature Ionic Liquids: A Critical Review. *J. Phys. Chem.* **48,** 033101 (2019).

117. Hu, X., Zhang, S., Qu, C., Zhang, Q., Lu, L., Ma, X., Zhang, X. & Deng, Y. Ionic liquid based variable focus lenses. *Soft Matter* **7,** 5941–5943 (2011).

118. Lockett, V., Sedev, R., Bassell, C. & Ralston, J. Angle-resolved X-ray photoelectron spectroscopy of the surface of imidazolium ionic liquids. *Phys. Chem. Chem. Phys.* **10,** 1330–1335 (2008).

119. Lovelock, K. R. J., Villar-Garcia, I. J., Maier, F., Steinrück, H.-P. & Licence, P. Photoelectron Spectroscopy of Ionic Liquid-Based Interfaces. *Chem. Rev.* **110 (9),** 5158—5190 (2010).

120. Kanai, K., Nishi, T., Iwahashi, T., Ouchi, Y., Seki, K., Harada, Y. & Shin, S. Anomalous electronic structure of ionic liquids determined by soft X-ray emission spectroscopy: contributions from the cations and anions to the occupied electronic structure. *J. Chem. Phys.* **129 (22),** 224507 (2008).

121. Rodrigues, F., do Nascimento, G. M. & Santos, P. S. Studies of ionic liquid solutions by soft X-ray absorption spectroscopy. *J. Electron Spectrosc. Relat. Phenom.* **155,** 148—154 (2007).

122. Karmakar, R. & Samanta, A. Dynamics of Solvation of the Fluorescent State of Some Electron Donor-Acceptor Molecules in Room Temperature Ionic Liquids, [BMIM][$(CF_3SO_2)_2$N] and [EMIM][$(CF_3SO_2)_2$N]. *J. Phys. Chem. A* **107,** 7340–7346 (2003).

123. Ingram, J. A., Moog, R. S., Ito, N., Biswas, R. & Maroncelli, M. Solute Rotation and Solvation Dynamics in a Room-Temperature Ionic Liquid. *J. Phys. Chem. B* **107 (24),** 5926—5932 (2003).

124. Marquis, S., Ferrer, B., Alvaro, M., Garcia, H. & Roth, H. D. Photoinduced Electron Transfer in Ionic Liquids: Use of 2,4,6-Triphenylthiapyrylium as a Photosensitizer Probe. *J. Phys. Chem. B* **110,** 14956–14960 (2006).

125. Gordon, C. M. & McLean, A. J. Photoelectron transfer from excited-state ruthenium(II) tris (bipyridyl) to methylviologen in an ionic liquid. *Chem. Commun.,* 1395–1396 (2000).

126. Wang, X., Maeda, K., Thomas, A., Takanabe, K., Xin, G., Carlsson, J. M., Domen, K. & Antonietti, M. A metal-free polymeric photocatalyst for hydrogen production from water under visible light. *Nat. Mater.* **8,** 76–80 (2009).

127. Dai, L. *Carbon-Based Metal-Free Catalysts: Design and Applications* (Wiley & Sons, 2018).

128. Zhou, L., Zhang, H., Sun, H., Liu, S., Tade, M. O., Wang, S. & Jin, W. Recent advantages in non-metal modification of graphitic carbon nitride for photocatalysis: a historic review. *Catal. Sci. Technol.* **6,** 7002 (2016).

129. Wen, J., Xie, J., Chen, X. & Li, X. A review on g-C_3N_4-based photocatalysts. *Appl. Surf. Sci.* **391,** 72–123 (2017).

130. Ye, S., Wang, R., Wu, M. & Yuan, Y. A review on g-C_3N_4 for photocatalytic water splitting and CO_2 reduction. *Appl. Surf. Sci.* **358,** 15–27 (2015).

131. Xu, Y., Kraftacd, M. & Xu, R. Metal-free carbonaceous electrocatalysts and photocatalysts for water splitting. *Chem. Soc. Rev.* **45,** 3039 (2016).

132. Ehrmaier, J., Domcke, W. & Opalka, D. Mechanism of Photocatalytic Water Oxidation by Graphitic Carbon Nitride. *J. Phys. Chem. Lett.* **9 (16),** 4695—4699 (2018).

133. Marszewski, M., Cao, S., Yubc, J. & Jaroniec, M. Semiconductor-based photocatalytic CO_2 conversion. *Mater. Horiz.* **2,** 261–278 (2015).

134. Ilic, S., Zoric, M. R., Kadel, U. P., Huang, Y. & Glusac, K. D. Metal-free motifs for solar fuel applications. *Annu. Rev. Phys. Chem.* **68,** 305–331 (2017).

135. Ong, W. J., Tan, L. L., Ng, Y. H., Yong, S. T. & Chai, S. P. Graphitic carbon nitride (g-C_3N_4)-based photocatalysts for artificial photosynthesis and environmental remediation: are we a step closer to achieving sustainability? *Chem. Rev.* **116,** 7159–7329 (2016).

136. Darkwah, W. K. & Oswald, K. A. Photocatalytic applications of heterostructure graphitic carbon nitride: pollutant degradation, hydrogen gas production (water splitting), and CO_2 reduction. *Nanoscale. Res. Lett.* **14,** 234 (2019).

137. Paul, D. R. & Nehra, S. P. Graphitic carbon nitride: a sustainable photocatalyst for organic pollutant degradation and antibacterial applications. *Environ. Sci. Pollut. Res.* **28,** 3888—3896 (2021).

138. Liu, J., Wang, H. & Antonietti, M. Graphitic carbon nitride "reloaded": emerging applications beyond (photo)catalysis. *Chem. Soc. Rev.* **45,** 2308–2326 (2016).

139. Chan, M.-H., Liu, R.-S. & Hsiao, M. Graphitic carbon nitride-based nanocomposites and their biological applications: a review. *Nanoscale* **11,** 14993–15003 (2019).

140. Pandikumar, A., Murugan, C. & Vinoth, S. *Nanoscale Graphitic Carbon Nitride: Synthesis and Applications* (Elsevier Science, 2021).

141. Kroke, E., Schwarz, M., Horath-Bordon, E., Kroll, P., Nollc, B. & Norman, A. D. Tri-s-triazine derivatives. Part I. From trichloro-tri-s-triazine to graphitic C_3N_4 structures. *New J. Chem.* **26,** 508–512 (2002).

142. Lee, H. L., Sofer, Z., Mazanek, V., Luxa, J., Chua, C. K. & Pumera, M. Graphitic carbon nitride: Effects of various precursors on the structural, morphological and electrochemical sensing properties. *Appl. Mater. Today* **8,** 150–162 (2017).

143. Kessler, F. K., Zheng, Y., Schwarz, D., Merschjann, C., Schnick, W., Wang, X. & Bojdys, M. J. Functional carbon nitride materials — design strategies for electrochemical devices. *Nat. Rev. Mater.* **2,** 17030 (2017).

144. Yacobi, B. G. *Semiconductor Materials: An Introduction to Basic Principles* (Kluwer Academic Publishers, 2004).

145. Wang, Y., Zhang, Y., Li, B., Luo, K., Shi, K., Zhang, L., Li, Y., Yu, T., Hu, W., Xie, C., Wu, Y., Su, L., Dong, X., Zhao, Z. & Yang, G. Restacked melon as highly-efficient photocatalyst. *Nano Energy* **77,** 105124 (2020).

146. Seyfarth, L., Seyfarth, J., Lotsch, B. V., Schnick, W. & Senker, J. Tackling the stacking disorder of melon—structure elucidation in a semicrystalline material. *Phys. Chem. Chem. Phys.* **12,** 2227–2237 (2010).

147. Ye, M. & Wang, M. *Multifunctional Photocatalytic Materials for Energy* (Elsevier Science, 2018).

148. Guo, S., Deng, Z., Li, M., Jiang, B., Tian, C., Pan, Q. & Fu, H. Phosphorus-Doped Carbon Nitride Tubes with a Layered Micro-nanostructure for Enhanced Visible-Light Photocatalytic Hydrogen Evolution. *Angew. Chem. Int. Ed. Engl.* **55 (5),** 1830–1834 (2016).

149. Niu, P., Zhang, L., Liu, G. & Cheng, H. M. Graphene-Like Carbon Nitride Nanosheets for Improved Photocatalytic Activities. *Adv. Funct. Mater.* **22,** 4763—–4770 (2012).

150. Zhang, J. S., Zhang, M. W., Yang, C. & Wang, X. C. Nanospherical Carbon Nitride Frameworks with Sharp Edges Accelerating Charge Collection and Separation at a Soft Photocatalytic Interface. *Adv. Mater.* **26,** 4121—–4126 (2014).

151. Wu, W., Zhan, L., Fan, W., Song, J., Li, X., Li, Z., Wang, R., Zhang, J., Zheng, J., Wu, M. & Zeng, H. Cu–N Dopants Boost Electron Transfer and Photooxidation Reactions of Carbon Dots. *Angew. Chem. Int. Ed.* **54,** 6540—6544 (2015).

152. Jianga, L., Yuana, X., Pana, Y., Lianga, J., Zenga, G., Wua, Z. & Wang, H. Doping of graphitic carbon nitride for photocatalysis: A reveiw. *Appl. Catal. B* **217,** 388–406 (2017).

153. Schmickler, W. & Santos, E. *Interfacial Electrochemistry* (Springer, 2010).

154. Jerkiewicz, G. Standard and Reversible Hydrogen Electrodes: Theory, Design, Operation, and Applications. *ACS Catal.* **10 (15),** 8409—8417 (2020).

155. Trasatti, S. The Absolute Electrode Potential: an Explanatory Note (Recommendations 1986). *Pure Appl. Chem.* **58 (7),** 955–966 (1986).

156. Foster, R., Ghassemi, M. & Cota, A. *Solar Energy: Renewable Energy and the Environment* (US: CRC Press, 2009).

157. Mertens, K. *Photovoltaics: Fundamentals, Technology, and Practice* (UK: Wiley, 2018).

158. D'Accadia, M. D. *Solar Hydrogen Production: Processes, Systems and Technologies* (Elsevier Science, 2019).

159. Anpo, M. & Fu, X. *Current Developments in Photocatalysis and Photocatalytic Materials: New Horizons in Photocatalysis* (Elsevier Science, 2019).

160. Fujishima, A. & Honda, K. Electrochemical photolysis of water at a semiconductor electrode. *Nature* **238 (5358),** 37–38 (1972).

161. Ager, J. W., Shaner, M. R., Walczak, K. A., Sharpae, I. D. & Ardo, S. Experimental demonstrations of spontaneous, solar-driven photoelectrochemical water splitting. *Energy Environ. Sci.* **8,** 2811–2824 (2015).

162. Van de Krol, R. & Grätzel, M. *Photoelectrochemical Hydrogen Production* (Netherlands: Springer US, 2011).

163. Alfano, O. M., Bahnemann, D., Cassano, A., Dillert, R. & Goslich, R. Photocatalysis in water environments using artificial and solar light. *Catal. Today* **58 (2),** 199–230 (2000).

164. Liang, F., Sun, X., Hu, S., Ma, H., Wang, F. & Wu, G. Photocatalytic water splitting to simultaneously produce H_2 and H_2O_2 by two-electron reduction process over Pt loaded Na^+ introduced g-C_3N_4 catalyst. *Diam. Relat. Mater.* **108,** 107971 (2020).

165. Kumaravel, V., Imam, M. D., Badreldin, A., Chava, R. M., Do, J. Y., Kang, M. & Abdel-Wahab, A. Photocatalytic Hydrogen Production: Role of Sacrificial Reagents on the Activity of Oxide, Carbon, and Sulfide Catalysts. *Catalysts* **9 (3), 276,** 1–35 (2019).

166. Luo, B., Zhao, Y. & Jing, D. State-of-the-art progress in overall water splitting of carbon nitride based photocatalysts. *Front. Energy* (2021).

167. Zhou, H., Qu, Y., Zeida, T. & Duan, X. Towards highly efficient photocatalysts using semiconductor nanoarchitectures. *Energy Environ. Sci.* **5,** 6732–6743 (2012).

168. Marschall, R. Photocatalysis: Semiconductor Composites: Strategies for Enhancing Charge Carrier Separation to Improve Photocatalytic Activity. *Adv. Funct. Mater.* **24,** 2421 (2014).

169. Li, J. & Wu, N. Semiconductor-based photocatalysts and photoelectrochemical cells for solar fuel generation: a review. *Catal. Sci. Technol.* **5,** 1360–1384 (2015).

170. Chen, S., Huang, D., Xu, P., Xue, W., Lei, L., Cheng, M., Wang, R., Liu, X. & Deng, R. Semiconductor-based photocatalysts for photocatalytic and photoelectrochemical water splitting: will we stop with photocorrosion? *J. Mater. Chem. A* **8,** 2286–2322 (2020).

171. Lu, Q., Yu, Y., Ma, Q., Chen, B. & Zhang, H. 2D Transition-Metal-Dichalcogenide-Nanosheet-Based Composites for Photocatalytic and Electrocatalytic Hydrogen Evolution Reactions. *Adv. Mater.* **28,** 1917—1933 (2016).

172. Striegler, K. *Modified Graphitic Carbon Nitrides for Photocatalytic Hydrogen Evolution from Water: Copolymers, Sensitizers and Nanoparticles* (Germany: Springer Fachmedien Wiesbaden, 2015).

173. Sun, Y., Gao, S., Leia, F. & Xie, Y. Atomically-thin two-dimensional sheets for understanding active sites in catalysis. *Chem. Soc. Rev.* **44,** 623–636 (2015).

174. Tan, C., Cao, X., Wu, X.-J., He, Q., Yang, J., Zhang, X., Chen, J., Zhao, W., Han, S., Nam, G.-H., Sindoro, M. & Zhang, H. Recent advances in ultrathin two-dimensional nanomaterials. *Chem. Rev.* **117(9),** 6225—6331 (2017).

175. Meng, N., Ren, J., Liu, Y., Huang, Y., Petit, T. & Zhang, B. Engineering oxygen-containing and amino groups into two-dimensional atomically-thin porous polymeric carbon nitrogen for enhanced photocatalytic hydrogen production. *Energy Environ. Sci.* **11,** 566–571 (2018).

176. Martin, D. J., Qiu, K., Shevlin, S. A., Handoko, A. D., Chen, X., Guo, Z. X. & Tang, J. W. Highly efficient photocatalytic H_2 evolution from water using visible light and structure controlled graphitic carbon nitride. *Angew. Chem. Int. Ed.* **53 (35),** 9240–9245 (2014).

177. Wang, H., Zhang, X. D., Xie, J. F., Zhang, J. J., Ma, P., Pan, B. C. & Xie, Y. Structural distortion in graphitic-C_3N_4 realizing an efficient photoreactivity. *Nanoscale* **7,** 5152–5156 (2015).

178. Lau, V. W., Yu, V. W., Ehrat, F., Botari, T., Moudrakovski, I., Simon, T., Duppel, V., Medina, E., Stolarczyk, J., Feldmann, J., Blum, V. & Lotsch, B. V. Urea-Modified Carbon Nitrides: Enhancing Photocatalytic Hydrogen Evolution by Rational Defect Engineering. *Adv. Energy. Mater.* **7,** 1602251 (2017).

179. Yang, S., Zhou, W., Ge, C., Liu, X., Fang, Y. & Li, Z. Mesoporous polymeric semiconductor materials of graphitic-C_3N_4: General and efficient synthesis and their integration with synergistic AgBr NPs for enhanced photocatalytic performances. *RSC Adv.* **3,** 5631—5638 (2013).

180. Kailasam, K., Epping, J. D., Thomas, A., Losse, S. & Junge, H. Mesoporous carbon nitride–silica composites by a combined sol–gel/thermal condensation approach and their application as photocatalysts. *Energy Environ. Sci.* **4,** 4668–4674 (2011).

181. Indra, A., Acharjya, A., Menezes, P. W., Merschjann, C., Hollmann, D., Schwarze, M., Aktas, M., Friedrich, A., Lochbrunner, S., Thomas, A. & Driess, M. Boosting Visible-Light-Driven Photocatalytic Hydrogen Evolution with an Integrated Nickel Phosphide–Carbon Nitride System. *Angew.Chem. Int. Ed.* **56,** 1653—1657 (2017).

182. Indra, A., Menezes, P. W., Kailasam, K., Hollmann, D., Schroder, M., Thomas, A. & Driess, M. Nickel as a co-catalyst for photocatalytic hydrogen evolution on graphitic-carbon nitride (sg-CN): what is the nature of the active species? *Chem. Commun.* **52,** 104–107 (2016).

183. Hong, J., Wang, Y., Wang, Y., Zhang, W. & Xu, R. Noble-Metal-Free NiS/C_3N_4 for Efficient Photocatalytic Hydrogen Evolution from Water. *Chem. Sus. Chem.* **6,** 2263—2268 (2013).

184. Becker, W. *Advanced Time-Correlated Single Photon Counting Applications* (Springer International Publishing, 2016).

185. Sheetz, K. E. & Squier, J. Ultrafast optics: Imaging and manipulating biological systems. *J. Appl. Phys.* **105 (5),** 051101 (2009).

186. Malinauskas, M., Zukauskas, A., Hasegawa, S., Hayasaki, Y., Mizeikis, V., Buividas, R. & Juodkazis, S. Ultrafast laser processing of materials: from science to industry. *Light. Sci. Appl.* **5,** e16133 (2016).

187. Joachain, C. J., Kylstra, N. J. & Potvliege, R. M. *Atoms in Intense Laser Fields* (Cambridge University Press, 2012).

188. Iaconis, C., Wong, V. & Walmsley, I. A. Direct interferometric techniques for characterizing ultrashort optical pulses. *IEEE J. Sel. Top. Quantum Electron.* **4 (2),** 285–294 (1998).

189. Trebino, R. *Frequency-Resolved Optical Gating: The Measurement of Ultrashort Laser Pulses* (Springer, 2002).

190. Ristau, D. *Laser-Induced Damage in Optical Materials* (CRC Press, 2014).

191. Fork, R. L., Martinez, O. E. & Gordon, J. P. Negative dispersion using pairs of prisms. *Opt. Lett.* **9,** 150–152 (1984).

192. Treacy, E. Optical pulse compression with diffraction gratings. *IEEE J. Quantum Electron.* **9,** 454–458 (1969).

193. Matuschek, M., Kärtner, F. X. & Keller, U. Theory of double-chirped mirrors. *IEEE J. Sel. Top. Quantum Electron.* **4 (2),** 197–208 (1998).

194. Lenz, G., Eggleton, B. J. & Litchinitser, N. Pulse compression using fiber gratings as highly dispersive nonlinear elements. *J. Opt. Soc. Am. B* **15,** 1715–721 (1998).

195. Moulton, P. F. Spectroscopic and laser characteristics of Ti:Al_2O_3. *J. Opt. Soc. Am. B* **3,** 125–133 (1986).

196. Spence, D. E., Kean, P. N. & Sibbett, W. 60-fsec pulse generation from a selfmode-locked Ti:sapphire laser. *Opt. Lett.* **16,** 42–44 (1991).

197. Strickland, D. & Mourou, G. Compression of amplified chirped optical pulses. *Opt. Commun.* **56,** 219–221 (1985).

198. Danson, C. N. *et al.* Petawatt and exawatt class lasers worldwide. *High Power Laser Sci. Eng.* **7,** e54 (2019).

199. Ducasse, A., Rulliere, C. & Couillaud, B. *Methods for the Generation of Ultrashort Laser Pulses: Mode-Locking* (Springer, New York, 2005).

200. Moulton, P. Ti-doped sapphire: tunable solid-state laser. *Optics News* **6(9),** 9–9 (1982).

201. Fork, R. L., Greene, B. I. & Shank, C. V. Generation of Optical Pulses Shorter than 0.1 psec by Colliding Pulse Mode-Locking. *Appl. Phys. Lett.* **38(9),** 671–672 (1981).

202. Cerullo, G., Silvestri, S. D., Magni, V. & Pallaro, L. Resonators for Kerr-lens mode-locked femtosecond Ti:sapphire lasers. *Opt. Lett.* **19(11),** 807–809 (1994).

203. Sutter, D. H., Steinmeyer, G., Gallmann, L., Matuschek, N., Morier-Genoud, F., Keller, U., Scheuer, V., Angelow, G. & Tschudi, T. Semiconductor saturable-absorber mirror-assisted Kerr lens modelocked Ti:sapphire laser producing pulses in the two-cycle regime. *Opt. Lett.* **24 (9),** 631 (1999).

204. Ell, R., Morgner, U., Kärtner, F. X., Fujimoto, J. G., Ippen, E. P., Scheuer, V., Angelow, G., Tschudi, T., Lederer, M. J., Boiko, A. & Luther-Davies, B. Generation of 5-fs pulses and octave-spanning spectra directly from a Ti: sapphire laser. *Opt. Lett.* **26 (6),** 373–375 (2001).

205. Boyd, R. W. *Nonlinear optics* (Elsevier, 2008).

206. Boyd, R. W., Lukishova, S. G. & Shen, Y. R. *Self-focusing: Past and Present: Fundamentals and Prospects* (Springer, New York, 2010).

207. Fibich, G. & Gaeta, A. L. Critical power for self-focusing in bulk media and in hollow waveguides. *Opt. Lett.* **25,** 335–337 (2000).

208. Karlsson, M. Optical beams in saturable self-focusing media. *Phys. Rev. A* **46 (5),** 2726–2734 (1992).

209. Cheng, Z., Krausz, F. & Spielmann, C. Compression of 2 mJ kilohertz laser pulses to 17.5 fs by pairing doubleprism compressor: analysis and performance. *Opt. Commun.* **201 (1-3),** 145–155 (2002).

210. McPherson, A., Gibson, G., Jara, H., Johann, U., Luk, T. S., McIntyre, I. A., Boyer, K. & Rhodes, C. K. Studies of multiphoton production of vacuum-ultraviolet radiation in the rare gases. *J. Opt. Soc. Am. B* **4,** 595–601 (1987).

211. Ferray, M., L'Huillier, A., Li, X. F., Lompre, L. A., Mainfray, G. & Manus, C. Multiple-harmonic conversion of 1064 nm radiation in rare gases. *J. Phys. B: At. Mol. Opt. Phys.* **21,** L31 (1988).

212. Macklin, J. J., Kmetec, J. D. & Gordon, C. L. High-order harmonic generation using intense femtosecond pulses. *Phys. Rev. Lett.* **70 (6),** 766–769 (1993).

213. Corkum, P. B. Plasma perspective on strong field multiphoton ionization. *Phys. Rev. Lett.* **71 (13)** (1993).

214. Giordmaine, J. A. Mixing of light beams in crystals. *Phys. Rev. Lett.* **8 (1),** 19–20 (1962).

215. Dmitriev, V. G., Gurzadyan, G. G. & Nikogosyan, D. N. *Handbook of Nonlinear Optical Crystals* (Springer, Berlin, Heidelberg, 2013).

216. Alfano, R. R. & Shapiro, S. L. Emission in the region 4000–7000 A via four-photon coupling in glass. *Phys. Rev. Lett.* **24,** 584–587 (1970).

217. Alfano, R. R. & Shapiro, S. L. Observation of self-phase modulation and small scale filaments in crystals and glasses. *Phys. Rev. Lett.* **24,** 592–594 (1970).

218. Alfano, R. R. & Shapiro, S. L. Direct distortion of electronic clouds of rare-gas atoms in intense electric fields. *Phys. Rev. Lett.* **24,** 1219–1222 (1970).

219. Link, S., Duerr, H. A. & Eberhardt, W. Femtosecond spectroscopy. *J. Phys. Condens. Matter* **13,** 7873 (2001).

220. Bradler, M., Baum, P. & Riedle, E. Femtosecond continuum generation in bulk laser host materials with sub-μJ pump pulses. *Appl. Phys. B* **97,** 561 (2009).

221. Calendron, A.-L., Cankaya, H., Cirmi, G. & Kärtner, F. X. White-light generation with sub-ps pulses. *Opt. Express* **23,** 13866–13879 (2015).

222. Takara, H., Ohara, T., Yamamoto, T., Masuda, H., Abe, M., Takahashi, H. & Morioka, T. Field demonstration of over 1000-channel DWDM transmission with supercontinuum multi-carrier source. *Electron. Lett.* **41 (5),** 270–271 (2005).

223. Hartl, I., Li, X. D., Chudoba, C., Ghanta, R. K., Ko, T. H., Fujimoto, J. G., Ranka, J. K. & Windeler, R. S. Ultrahigh-resolution optical coherence tomography using continuum generation in an air–silica microstructure optical fiber. *Opt. Lett.* **26,** 608–610 (2001).

224. Jones, D. J., Diddams, S. A., Ranka, J. K., Stentz, A., Windeler, R. S., Hall, J. L. & Cundiff, S. T. Carrier-envelope Pphase control of femtosecond mode-locked lasers and direct optical frequency synthesis. *Science* **288,** 635–639 (2000).

225. Manzoni, C., Polli, D., Cirmi, G., Brida, D., Silvestri, S. D. & Cerullo, G. Tunable few-optical-cycle pulses with passive carrier-envelope phase stabilization from an optical parametric amplifier. *Appl. Phys. Lett.* **90,** 171111 (2007).

226. Negres, R. A., Hales, J. M., Kobyakov, A., Hagan, D. J. & Stryland, E. W. V. Two-photon spectroscopy and analysis with a white-light continuum probe. *Opt. Lett.* **27,** 270–272 (2002).

227. L'Huillier, A. & Balcou, P. High-order harmonic generation in rare gases with a 1-ps 1053-nm laser. *Phys. Rev. Lett.* **70 (6),** 774–777 (1993).

228. Farkas, G., Tóth, C., Moustaizis, S. D., Papadogiannis, N. A. & Fotakis, C. Observation of multiple-harmonic radiation induced from a gold surface by picosecond neodymium-doped yttrium aluminum garnet laser pulses. *Phys. Rev. A* **46 (7),** R3605–R3608 (1992).

229. Vampa, G., McDonald, C., Fraser, A. & Brabec, T. High-harmonic generation in solids: bridging the gap between attosecond science and condensed matter physics. *IEEE J. Sel. Top. Quantum Electron.* **21 (5),** 8700110 (2015).

230. Gaumnitz, T., Jain, A., Pertot, Y., Huppert, M., Jordan, I., Ardana-Lamas, F. & Wörner, H. J. Streaking of 43-attosecond soft-Xray pulses generated by a passively CEP-stable mid-infrared driver. *Opt. Express* **25 (22),** 27506 (2017).

231. Ghimire, S. & Reis, D. High-harmonic generation from solids. *Nature Phys.* **15,** 10–16 (2019).

232. Li, J., Lu, J., Chew, A., Seunghwoi, H., Jialin, L., Yi, W., He, W., Ghimire, S. & Chang, Z. Attosecond science based on high harmonic generation from gases and solids. *Nat. Commun.* **11,** 2748 (2020).

233. Yin, Z., Luu, T. T. & Wörner, H. J. Few-cycle high-harmonic generation in liquids: in-operando thickness measurement of flat microjets. *J. Phys. Photonics* **2,** 044007 (2020).

234. Durfee, C. G., Rundquist, A., Backus, S., Chang, Z., Herne, C., Kapteyn, H. C. & Murnane, M. M. Guided-wave phase-matching of ultrashort-pulse light. *J. Nonlinear Opt. Phys. Mater.* **8 (2),** 211–234 (1999).

235. Cohen, O., Lytle, A. L., Zhang, X., Murnane, M. M. & Kapteyn, H. C. Optimizing quasi-phase matching of high harmonic generation using counterpropagating pulse trains. *Opt. Lett.* **32,** 2975–2977 (2007).

236. Voronov, S. L., n I. Kohl, Madsen, J. B., Simmons, J., Terry, N., Titensor, J., Wang, Q. & Peatross, J. Control of laser high-harmonic generation with counterpropagating light. *Phys. Rev. Lett.* **87 (13),** 133902 (2001).

237. Silfvast, W. T. *Laser fundamentals* (Cambridge University Press, UK, 2004).

238. Tobey, R. I., Siemens, M. E., Cohen, O., Murnane, M. M., Kapteyn, H. C. & Nelson, K. A. Ultrafast extreme ultraviolet holography: dynamic monitoring of surface deformation. *Opt. Lett.* **32,** 286–288 (2007).

239. Sandberg, R. L., Song, C., Wachulak, P. W, Raymondson, D. A., Paul, A., Amirbekian, B., Lee, E., Sakdinawat, A. E., La-O-Vorakiat, C., Marconi, M. C., Menoni, C. S., Murnane, M. M., Rocca, J. J., Kapteyn, H. C. & Miao, J. High numerical aperture tabletop soft X-ray diffraction microscopy with 70-nm resolution. *Proc. Natl. Acad. Sci. USA* **105 (1),** 24–27 (2008).

240. Kim, Y. & Lee, J. Time-resolved photoemission of infinitely periodic atomic arrangements: correlation-dressed excited states of solids. *npj Comput. Mater.* **6,** 132 (2020).

241. Backus, S., Durfee, C. G., Murnane, M. M. & Kapteyn, H. C. High power ultrafast lasers. *Rev. Sci. Instrum.* **69,** 1207 (1998).

242. Bellini, M., Lynga, C., Tozzi, A., Gaarde, M. B., Hänsch, T. W., L'Huillier, A. & Wahlström, C.-G. Temporal coherence of ultrashort high-order harmonic pulses. *Phys. Rev. Lett.* **81 (2),** 297–300 (1998).

243. Ghimire, S., DiChiara, A. D., Sistrunk, E., Agostini, P., DiMauro, L. F. & Reis, D. A. Observation of high-order harmonic generation in a bulk crystal. *Nature Phys.* **7,** 138–141 (2011).

244. DiChiara, A. D., Sistrunk, E., Miller, T. A., Agostini, P. & DiMauro, L. F. An investigation of harmonic generation in liquid media with a mid-infrared laser. *Opt. Express* **17,** 20959–20965 (2009).

245. Luu, T. T., Yin, Z., Jain, A., Gaumnitz, T., Pertot, Y., Ma, J. & Wörner, H. J. Extreme– ultraviolet high–harmonic generation in liquids. *Nat. Commun.* **9,** 3723–8874 (2018).

246. Banerjee, S., Valenzuela, A. R., Shah, R. C., Maksimchuk, A. & Umstadter, D. High harmonic generation in relativistic laser–plasma interaction. *Phys. Plasmas* **9,** 2393 (2002).

247. Gu, P., Liu, S.-B. & Song, H.-Y. High harmonic generation in helium-filled slab waveguide. *Appl. Phys. B* **122 (1),** 1–6 (2016).

248. Boltaev, G. S., Ganeev, R. A., Kim, V. V., Abbasi, N. A., Iqbal, M. & Alnaser, A. S. High-order harmonics generation in the plasmas produced on different rotating targets during ablation using 1 kHz and 100 kHz lasers. *Opt. Express* **28 (13),** 18859–18875 (2020).

249. Harth, A., Guo, C., Cheng, Y.-C., Losquin, A., Miranda, M., Mikaelsson, S., Heyl, C. M., Prochnow, O., Ahrens, J., Morgner, U., L'Huillier, A. & Arnold, C. L. Compact 200 kHz HHG source driven by a fewcycle OPCPA. *J. Opt.* **20,** 014007 (2018).

250. Pupeikis, J., Chevreuil, P.-A., Bigler, N., Gallmann, L., Phillips, C. R. & Keller, U. Water window soft X-ray source enabled by 25 W few-cycle 2.2 m OPCPA at 100 kHz. *Optica* **7 (2),** 168–171 (2020).

251. Kulander, K. C., Schafer, K. J. & Krause, J. L. *Dynamics of short-pulse excitation, ionization and harmonic conversion. In: Piraux B., L'Huillier A., Rzazewski K. (eds) Super-Intense Laser-Atom Physics* (ATO ASI Series (Series B: Physics), vol 316. Springer, Boston, MA, 1993).

252. Protopapas, M., Lappas, D. G., Keitel, C. H. & Knight, P. The recollision picture in high harmonic generation. *1996 European Quantum Electronic Conference,* 224–224 (1996).

253. Lewenstein, M., Balcou, P., Ivanov, M. Y., L'Huillier, A. & Corkum, P. B. Theory of high-harmonic generation by low-frequency laser fields. *Phys. Rev. A* **49,** 2117 (1994).

254. Antoine, P., Carre, B., L'Huillier, A. & Lewenstein, M. Polarization of high-order harmonics. *Phys. Rev. A* **56 (6),** 4960 (1997).

255. Popruzhenko, S. V. Keldysh theory of strong field ionization: history, applications, difficulties and perspectives. *J. Phys. B* **47 (20),** 204001 (2014).

256. Keldysh, L. V. Ionization in the Field of a Strong Electromagnetic Wave. *Soviet Physics JETP* **20,** 1307 (1965).

257. Ammosov, M. V., Delone, N. B. & Krainov, V. P. Tunnel ionization of complex atoms and of atomic ions in an alternating electromagnetic field. *Sov. Phys. JETP* **64 (6),** 1191 (1986).

258. Kramida, A., Ralchenko, Y., Reader, J. & Team, N. A. *NIST Atomic Spectra Database* (National Institute of Standards and Technology, Gaithersburg, 2020).

259. Strauch, D. *Classical Mechanics: An Introduction* (Springer, 2009).

260. Zaïr, A., Guandalinic, M. H. A., Schapper, F., Biegert, J., Gallmann, L., S., U. K. A., Wyatt, Monmayrant, A., Walmsley, I. A., Cormier, E., Auguste, T., Caumes, J. P. & Salières, P. Quantum Path Interferences in High-Order Harmonic Generation. *Phys. Rev. Lett.* **100 (14),** 143902 (2008).

261. Rothhardt, J., Krebs, M., Hädrich, S., Demmler, S., Limpert, J. & Tünnermann, A. Absorption-limited and phase-matched high harmonic generation in the tight focusing regime. *New J. Phys.* **16,** 033022 (2014).

262. Coccia, E. How electronic dephasing affects the high-harmonic generation in atoms. *Mol. Phys.* **118 (23)** (2002).

263. Lai, C.-J. & Kärtner, F. X. The influence of plasma defocusing in high harmonic generation. *Opt. Express* **19,** 22377–22387 (2011).

264. Averchi, A., Faccio, D., Berlasso, R., Kolesik, M., Moloney, J. V., Couairon, A. & Trapani, P. D. Phase matching with pulsed bessel beams for high-order harmonic generation. *Phys. Rev. A* **77 (2),** 021802 (2008).

265. Kazamias, S., Douillet, D., Weihe, F., Valentin, C., Rousse, A., Sebban, S., Grillon, G., Auge, F., Hulin, D. & Balcou, P. Global optimization of high harmonic generation. *Phys. Rev. Lett.* **90 (19),** 193901 (2003).

266. Gaarde, M. B., Tate, J. L. & Schafer, K. J. Macroscopic aspects of attosecond pulse generation. *J. Phys. B: At. Mol. Opt. Phys.* **41 (13),** 132001 (2008).

267. Gouy, L. G. Sur une propriete nouvelle des ondes lumineuses. *C. R. Acad. Sci. Paris* **110,** 1251 (1890).

268. Salires, P., LHuillier, A. & Lewenstein, M. Coherence control of high-order harmonics. *Phys. Rev. Lett.* **74,** 3776 (1995).

269. Hofmann, C., Landsman, A. S. & Keller, U. Disentangling long trajectory contributions in two-colour high harmonic generation. *Appl. Sci.* **8,** 341 (2018).

270. Brugnera, L., Hoffmann, D. J., Siegel, T., Frank, F., Zaïr, A., Tisch, J. W. G. & Marangos, J. P. Trajectory selection in high harmonic generation by controlling the phase between orthogonal two-color fields. *Phys. Rev. Lett.* **107,** 153902 (2011).

271. Heyl, C. M., Güdde, J., L'Huillier, A. & Höfer, U. High-order harmonic generation with μJ laser pulses at high repetition rates. *J. Phys. B: At. Mol. Opt. Phys.* **45,** 074020 (2012).

272. Heyl, C. M., Arnold, C. L., Couairon, A. & L'Huillier, A. Introduction to macroscopic power scaling principles for high-order harmonic generation. *J. Phys. B: At. Mol. Opt. Phys.* **50,** 013001 (2017).

273. Auguste, T., Carre, B. & Salieres, P. Quasi-phase-matching of high-order harmonics using a modulated atomic density. *Phys.Rev. A* **76 (1),** 011802 (2007).

274. Peatross, J., Fedorov, M. V. & Kulander, K. C. Intensity-dependent phasematching effects in harmonic generation. *J. Opt. Soc. Am. B* **12,** 863 (1995).

275. Leonard, P. Refractive indices, verdet constants, and polarizabilities of the inert gases. *Atomic Data and Nuclear Data Tables* **14,** 21–37 (1987).

276. Tempea, G., Geissler, M., Schnurer, M. & Brabec, T. Self-phase-matched high harmonic generation. *Phys. Rev. Lett.* **84 (19),** 4329 (2000).

277. Der Linde, D. V., Engers, T., Jenke, G., Agostini, P., Grillon, G., Nibbering, E., Mysyrowicz, A. & Antonetti, A. Generation of high-order harmonics from solid surfaces by intense femtosecond laser pulses. *Phys. Rev. A* **52 (1),** R25 (1995).

278. Constant, E., Garzella, D., Breger, P., Mevel, E., Dorrer, C., Blanc, C. L., Salin, F. & Agostini, P. Optimizing high harmonic generation in absorbing gases: model and experiment. *Phys. Rev. Lett.* **82 (8),** 1668–1671 (1999).

279. Watts, J. F. *An introduction to surface analysis by electron spectroscopy* (Oxford University Press, 1990).

280. Becquerel, E. Mémoire sur les effets électriques produits sous l'influence des rayons solaires. *Comptes Rendus.* **9,** 561–567 (1839).

281. Smith, W. Effect of light on selenium during the passage of an electric current. *Nature* **7,** 303 (1873).

282. Hertz, H. Ueber einen Einfluss des ultravioletten Lichtes auf die electrische Entladung. *Annalen der Physik.* **267 (8),** 983–1000 (1887).

283. Stoletow, M. On a kind of electric current produced by ultra-violet rays. *Philosophical Magazine. Series 5* **26 (160),** 317–319 (1888).

284. Planck, M. On the law of distribution of energy in the normal spectrum. *Annalen der Physik.* **4 (3),** 553 (1901).

285. Siegbahn, K. & Edvarson, K. β-Ray spectroscopy in the precision range of 1:10^5. *Nuclear Physics* **1(8),** 137–159 (1956).

286. Siegbahn, K. Electron spectroscopy for atoms, molecules and condensed matter. *Nobel Lecture* (1981).

287. Turner, D. W. & Jobory, M. I. A. Determination of ionization potentials by photoelectron energy measurement. *J. Chem. Phys.* **37,** 3007 (1962).

288. Hüfner, S. *Photoelectron spectroscopy: principles and applications* (Springer, 3rd Edition, Berlin, Heidelberg, 2003).

289. Glasser, O. W. C. Roentgen and the discovery of the Roentgen rays. *AJR* **165,** 1033–1040 (1995).

290. Oguri, K., Kato, K., Nishikawa, T., Gotoh, H., Tateno, K., Sogawa, T. & Nakano, H. Time-Resolved Surface Photoelectron Spectroscopy of Photoexcited Electron and Hole Dynamics on GaAs Using 92 eV Laser Harmonic Source. *Jpn. J. Appl. Phys.* **51,** 072401 (2012).

291. Melzer, A., Kampa, D., Wang, J. & Fauster, T. Time-resolved photoemission at the Si(100)-Ga surface using a femtosecond higher-harmonic laser source. *Phys. Rev. B* **80,** 205424 (2009).

292. Gierz, I., Calegari, F., Aeschlimann, S., Cervantes, M. C., Cacho, C., Chapman, R., Springate, E., Link, S., Starke, U., Ast, C. R. & Cavalleri, A. Tracking Primary Thermalization Events in Graphene with Photoemission at Extreme Time Scales. *Phys. Rev. Lett.* **115,** 086803 (2015).

293. Bertoni, R., Nicholson, C. W., Waldecker, L., Hubener, H., Monney, C., Giovannini, U. D., Puppin, M., Hoesch, M., Springate, E., Chapman, R. T., Cacho, C., Wolf, M., Rubio, A. & Ernstorfer, R. Generation and Evolution of Spin-, Valley-, and Layer-Polarized Excited Carriers in Inversion-Symmetric WSe_2. *Phys. Rev. Lett.* **117,** 277201 (2016).

294. Locher, R., Castiglioni, L., Lucchini, M., Greif, M., Gallmann, L., Osterwalder, J., Hengsberger, M. & Keller, U. Energy-dependent photoemission delays from noble metal surfaces by attosecond interferometry. *Optica* **2,** 405–410 (2015).

295. Christensen, B., Raarup, M. & Balling, P. Photoemission with high-order harmonics: a tool for time-resolved core-level spectroscopy. *Nucl. Instrum. Methods Phys. Res. A* **615,** 114—126 (2010).

296. Tao, Z., Chen, C., Szilvasi, T., Keller, M., Mavrikakis, M., Kapteyn, H. & Murnane, M. Direct time-domain observation of attosecond final-state lifetimes in photoemission from solids. *Science* **353,** 62—67 (2016).

297. Plotzing, M., Adam, R., Weier, C., Plucinski, L., Eich, S., Emmerich, S., Rollinger, M., Aeschlimann, M., Mathias, S. & Schneider, C. M. Spin-resolved photoelectron spectroscopy using femtosecond extreme ultraviolet light pulses from high-order harmonic generation. *Rev. Sci. Instrum.* **87,** 043903 (2016).

298. Frietsch, B., Bowlan, J., Carley, R., Teichmann, M., Wienholdt, S., Hinzke, D., Nowak, U., Carva, K., Oppeneer, P. M. & Weinelt, M. Disparate ultrafast dynamics of itinerant and localized magnetic moments in gadolinium metal. *Nat. Commun.* **6,** 8262 (2015).

299. Suzuki, T., Shin, S. & Okazaki, K. HHG-laser-based time- and angle-resolved photoemission spectroscopy of quantum materials. *J. Electron Spectrosc. Relat. Phenom.* **251,** 147105 (2021).

300. Dakovski, G. L., Durakiewicz, T., Zhu, J. X., Riseborough, P. S., Gu, G., Gilbertson, S. M., Taylor, A. & Rodriguez, G. Quasiparticle dynamics across the full Brillouin zone of $Bi_2Sr_2Ca Cu_2O_8{+}\delta$ traced with ultrafast time and angle-resolved photoemission spectroscopy. *Struct. Dyn.* **2 (5),** 054501 (2015).

301. Einstein, A. Über einen die erzeugung und verwandlung des lichtes betreffenden heuristischen gesichtspunkt. *Annalen der Physik* **14,** 164–181 (1905).

302. Cahen, D. & Kahn, A. Electron energetics at surfaces and interfaces: Concepts and experiments. *Adv. Mater.* **15,** 271–277 (2003).

303. Broughton, J. Q. & Perry, D. L. Electron Binding Energies in The Study of Adsorption by Photoelectron Spectroscopy: The Reference Level Problem. *Surf. Sci.* **74 (1),** 307–317 (1978).

304. Helander, M., Greiner, M., Wang, Z. & Lu, Z. Pitfalls in measuring work function using photoelectron spectroscopy. *Appl. Surf. Sci.* **256 (8),** 2602–2605 (2010).

305. Egelhoff, W. F. Core-level binding-energy shifts at surfaces and in solids. *Surf. Sci. Rep.* **6 (6-8),** 253–415 (1987).

306. Klyushnikov, O. I. Method to determine the work function using X-ray photoelectron spectroscopy. *J. Struct. Chem.* **39 (6),** 944–947 (1998).

307. Schattke, W. & Hove, M. A. V. *Solid-state photoemission and related methods: theory and experiment* (Wiley & Co., 2003).

308. Macsić, Z. B. *Theoretical models of chemical bonding. Part 3: Molecular spectroscopy, electronic structure and intramolecular interactions* (Springer, Berlin, Heidelberg, 1991).

309. Berglund, C. N. & Spicer, W. E. Photoemission studies of copper and silver: theory. *Phys. Rev.* **136,** A1030 (1964).

310. Pendry, J. Theory of photoemission. *Surf. Sci.* **57,** 679–705 (1976).

311. Spicer, W. E. Photoemissive, photoconductive, and optical absorption studies of alkali- antimony compounds. *Phys. Rev.* **112,** 114 (1958).

312. Fermi, E. *Nuclear physics* (University of Chicago Press, 1950).

313. Dresselhaus, M. S., Dresselhaus, G. & Jorio, A. *Group theory: application to the physics of condensed matter* (Springer, 2007).

314. Jablonski, A. & Powell, C. J. Electron effective attenuation lengths in electron spectroscopies. *J. Alloys Compd.* **362,** 26—32 (2004).

315. Seah, M. P. & Dench, W. A. Quantitative electron spectroscopy of surfaces: A standard data base for electron inelastic mean free paths in solids. *Surf. Interface Anal.* **1,** 2—11 (1979).

316. Tanuma, S., Powell, C. J. & Penn, D. R. Calculations of electron inelastic mean free paths. V. Data for 14 organic compounds over the 50–2000 eV range. *Surf. Interface Anal.* **21(3),** 165—176 (1994).

317. Tanuma, S., Powell, C. J. & Penn, D. R. Calculations of electron inelastic mean free paths. IX. Data for 41 elemental solids over the 50 eV to 30 keV range. *Surf. Interface Anal.* **43(3),** 689—713 (2011).

318. Damascelli, A. Probing the electronic structure of complex systems by ARPES. *Phys. Scr.* **T109,** 61–74 (2004).

319. Sekreta, E. & Reilly, J. P. Direct observation of intersystem crossing in benzene by laser photoelectron spectroscopy. *Chem. Phys. Lett.* **149,** 482–486 (1988).

320. Syage, J. A. Ultrafast Measurements of Chemistry in Clusters: Excited-State Proton Transfer. *J. Phys. Chem.* **99 (16),** 5772—5786 (1995).

321. Suzuki, T. Time-resolved photoelectron spectroscopy of non-adiabatic electronic dynamics in gas and liquid phases. *Intl. Rev. Phys. Chem.* **31,** 265 (2012).

322. Neumark, D. M. Time-resolved photoelectron spectroscopy of molecules and clusters. *Annu. Rev. Phys. Chem.* **52,** 255—277 (2001).

323. Harris, C. B., Ge, N.-H., Lingle, R. L., McNeill, J. J. D. & Wong, C. M. Femtosecond dynamics of electrons on surfaces and at interfaces. *Annu. Rev. Phys. Chem.* **48,** 711–744 (1997).

324. Petek, H. & Ogawa, S. Femtosecond time-resolved two-photon photoemission studies of electron dynamics in metals. *Prog. Surf. Sci.* **56(4),** 239 (1997).

325. Sie, E. J., Rohwer, T., Lee, C. & Gedik, N. Time-resolved XUV ARPES with tunable 24–33 eV laser pulses at 30 meV resolution. *Nat. Commun.* **10,** 3535 (2019).

326. Stadtmüller, B., Emmerich, S., Jungkenn, D., Haag, N., Rollinger, M., Eich, S., Maniraj, M., Aeschlimann, M., Cinchetti, M. & Mathias, S. Strong modification of the transport level alignment in organic materials after optical excitation. *Nat. Commun.* **10,** 1470 (2019).

327. Zhu, X.-Y. Electronic structure and electron dynamics at molecule–metal interfaces: implications for molecule-based electronics. *Surf. Sci. Rep.* **56,** 1–83 (2004).

328. Gahl, C., Bovensiepen, U., Frischkorn, C. & Wolf, M. Electronic structure and electron dynamics at molecule–metal interfaces: implications for molecule-based electronics. *Phys. Rev. Lett.* **89,** 107402 (2002).

329. Johnson, A. S., Wood, D., Austin, D. R., Brahms, C., Gregory, A., Holzner, K. B., Jarosch, S., Larsen, E. W., Parker, S., Struber, C., Ye, P., Tisch, J. W. G. & Marangos, J. P. Apparatus for soft x-ray table-top high harmonic generation. *Rev. Sci. Instrum.* **89,** 083110 (2018).

330. Kapteyn, H. C. Practical tabletop "X-ray lasers" implemented using high harmonic generation. *Optical Society of America,* ET5A.1 (2016).

331. Fan, C. & Zhao, Z. *Synchrotron radiation in materials science: light sources, techniques, and applications* (Wiley, 2018).

332. Boutet, S. & Yabashi, M. *X-ray free electron lasers and their applications* (Springer, Cham, 2018).

333. Zhou, X., Wannberg, B., Yanga, W., Brouet, V., Sun, Z., Douglas, J., Dessau, D., Hussain, Z. & Shen, Z.-X. Space charge effect and mirror charge effect in photoemission spectroscopy. *J. Electron. Spectrosc.* **142 (1),** 27–38 (2005).

334. Frietsch, B., Carley, R., Döbrich, K., Gahl, C., Teichmann, M., Schwarzkopf, O., Wernet, P. & Weinelt, M. A high-order harmonic generation apparatus for time- and angle-resolved photoelectron spectroscopy. *Rev. Sci. Instrum.* **84 (7),** 075106 (2013).

335. Faure, J., Mauchain, J., Papalazarou, E., Yan, W., Pinon, J., Marsi, M. & Perfetti, L. Full characterization and optimization of a femtosecond ultraviolet laser source for time and angle-resolved photoemission on solid surfaces. *Rev. Sci. Instrum.* **83 (4),** 043109 (2012).

336. Passlack, S., Mathias, S., Andreyev, O., Mittnacht, D., Aeschlimann, M. & Bauer, M. Space charge effects in photoemission with a low repetition, high intensity femtosecond laser source. *J. Appl. Phys* **100 (2),** 024912 (2006).

337. Pietzsch, A., Föhlisch, A., Beye, M., Deppe, M., Hennies, F., Nagasono, M., Suljoti, E., Wurth, W., Gahl, C., Döbrich, K. & Melnikov, A. Towards time resolved core level photoelectron spectroscopy with femtosecond x-ray free-electron lasers. *New J. Phys.* **10 (3),** 033004 (2008).

338. Kutnyakhov, D. *et al.* Time- and momentum-resolved photoemission studies using time-of-flight momentum microscopy at a free-electron laser. *Rev. Sci. Instrum.* **91,** 013109 (2020).

339. Oloff, L.-P., Hanff, K., Stange, A., Rohde, G., Diekmann, F., Bauer, M. & Rossnagel, K. Pump laser-induced space-charge effects in HHG-driven time- and angle-resolved photoelectron spectroscopy. *J. Appl. Phys.* **119,** 225106 (2016).

340. Al-Obaidi, R., Wilke, M., Borgwardt, M., Metje, J., Moguilevski, A., Engel, N., Tolksdorf, D., Raheem, A., Kampen, T., Mähl, S., Kiyan, I. Y. & Aziz, E. F. Ultrafast photoelectron spectroscopy of solutions: space-charge effect. *New J. Phys.* **17,** 093016 (2015).

341. Leuenberger, D., Yanagisawa, H., Roth, S., Osterwalder, J. & Hengsberger, M. Disentanglement of electron dynamics and space-charge effects in time-resolved photoemission from *h*-BN/Ni(111). *Phys. Rev. B* **84 (12),** 125107 (2011).

342. Ulstrup, S. *et al.* Ramifications of optical pumping on the interpretation of time-resolved photoemission experiments on graphene. *J. Electron Spectrosc. Relat. Phenom.* **200,** 340–346 (2015).

343. Corder, C., Zhao, P., Bakalis, J., Li, X., Kershis, M. D., Muraca, A. R., White, M. G. & Allison, T. K. Ultrafast extreme ultraviolet photoemission without space charge. *Struct Dyn.* **5 (5),** 054301 (2018).

344. Hellmann, S., Rossnagel, K., Marczynski-Bühlow, M. & Kipp, L. Vacuum space-charge effects in solid-state photoemission. *Phys. Rev. B* **79,** 035402 (2009).

345. Graf, J., Hellmann, S., C. Jozwiak, C. L. S., Hussain, Z., Kaindl, R. A., Kipp, L., Rossnagel, K. & Lanzara, A. Vacuum space charge effect in laser-based solid-state photoemission spectroscopy. *J. Appl. Phys.* **107,** 014912 (2010).

346. Long, J. P., Itchkawitz, B. S. & Kabler, M. N. Photoelectron spectroscopy of laser-excited surfaces by synchrotron radiation. *J. Opt. Soc. Am. B* **13 (1),** 201–208 (1996).

347. Banfi, F., Giannetti, C., Ferrini, G., Galimberti, G., Pagliara, S., Fausti, D. & Parmigiani, F. Experimental evidence of above-threshold photoemission in solids. *Phys. Rev. Lett.* **94 (3),** 037601 (2005).

348. Megerle, U., Pugliesi, I., Schriever, C., Sailer, C. F. & Riedle, E. Sub-50 fs broadband absorption spectroscopy with tunable excitation: putting the analysis of ultrafast molecular dynamics on solid ground. *Appl. Phys. B* **96,** 215–231 (2009).

349. Zigmantas, D., Ma, Y., Read, E. & Fleming, G. *Nonlinear Femtosecond Optical Spectroscopy Techniques in Photosynthesis. Advances in photosynthesis and respiration, vol. 26* (Springer, Dordrecht, 2008).

350. Schomburg, H., Staerk, H. & Weller, A. Radical ion and triplet formation in electron transfer fluorescence quenching studied by nanosecond laser spectroscopy. *Chem. Phys. Lett.* **21 (3),** 433–436 (1973).

351. Ujj, L., Devanathan, S., Meyer, T. E., Cusanovich, M. A., Tollin, G. & Atkinson, G. H. New photocycle intermediates in the photoactive yellow protein from ectothiorhodospira halophila: picosecond transient absorption spectroscopy. *Biophys. J.* **75 (1),** 406–412 (1998).

352. Adeniyi, A. A., von Stein, P.-F. X., Bosman, G. W., Steenkamp, C. M., Chiweshe, T., von Eschwege, K. G. & Conradie, J. Probing ultrafast reaction mechanisms of photo-excited dithizone through transient absorption spectroscopy and computational CASSCF studies. *J. Opt. Soc. Am. B* **37,** A356–A366 (2020).

353. McCusker, J. K. Femtosecond absorption spectroscopy of transition metal charge-transfer complexes. *Acc. Chem. Res.* **36 (12),** 876–887 (2003).

354. Prendergast, F. G. Time-resolved fluorescence techniques: methods and applications in biology. *Curr. Opin. Struct. Biol.* **1 (6),** 1054–1059 (1991).

355. Roduner, E., Forbes, P., Krüger, T. & Kress, K. C. *Optical spectroscopy: fundamentals and advanced applications* (World Scientific, 2019).

356. Honda, S., Yokoya, S., Ohkita, H., Benten, H. & Ito, S. Light-harvesting mechanism in polymer/fullerene/dye ternary blends studied by transient absorption spectroscopy. *Phys. Chem. C* **115 (22),** 11306–11317 (2011).

357. Ombinda-Lemboumba, S., Plessis, A. D., Sparrow, R. W., Molukanele, P., Botha, L. R., Rohwer, E. G., Steenkamp, C. M. & Rensburg, L. V. Femtosecond pump probe spectroscopy for the study of energy transfer of light-harvesting complexes from extractions of spinach leaves. *S. Afr. J. Sci.* **105 (9-10),** 376–386 (2009).

358. Ohkita, H., Tamai, Y., Benten, H. & Ito, S. Transient absorption spectroscopy for polymer solar cells. *IEEE J. Sel. Top. Quantum Electron.* **22 (1),** 100–111 (2016).

359. Chang, Y., Carron, R., Ochoa, M., Bozal-Ginesta, C., Tiwari, A. N., Durrant, J. R. & Steier, L. Insights from transient absorption spectroscopy into electron dynamics along the Ga-Gradient in Cu(In,Ga)Se_2 Solar Cells. *Adv. Energy Mater.* **11 (8),** 2003446 (2021).

360. Miao, T. J. & Tang, J. Characterization of charge carrier behavior in photocatalysis using transient absorption spectroscopy. *J. Chem. Phys.* **152,** 194201 (2020).

361. Zhao, Q., Hazarika, A., Chen, X., Harvey, S. P., Larson, B. W., Teeter, G. R., Liu, J., Song, T., Xiao, C., Shaw, L., Zhang, M., Li, G., Beard, M. C. & Luther, J. M. High efficiency perovskite quantum dot solar cells with charge separating heterostructure. *Nat. Commun.* **10 (1),** 1–8 (2019).

362. Gesuele, F. Ultrafast hyperspectral transient absorption spectroscopy: application to single layer graphene. *Photonics* **6 (3),** 95 (2019).

363. Clark, B., Frost, T. & Russell, M. *UV spectroscopy: techniques, instrumentation and data handling* (Chapman and Hall, 1993).

364. Van Stokkum, I. H. M., Larsen, D. S. & van Grondelle, R. Global and target analysis of time-resolved spectra. *Biochim. Biophys. Acta, Bioenerg.* **1657,** 82—104 (2004).

365. Kanal, F., Keiber, S., Eck, R. & Brixner, T. 100-kHz shot-to-shot broadband data acquisition for high-repetition-rate pump–probe spectroscopy. *Opt. Express* **22,** 16965–16975 (2014).

366. Holzwarth, A. R. *Data Analysis of Time-Resolved Measurements* (Dordrecht, Springer, 1996).

367. Volpato, A., Bolzonello, L., Meneghin, E. & Collini, E. Global analysis of coherence and population dynamics in 2d electronic spectroscopy. *Opt. Express* **24 (21),** 24773—24785 (2016).

368. Lofroth, J.-E. Time-resolved emission spectra, decayassociated spectra, and species-associated spectra. *J. Phys. Chem.* **90,** 1160—1168 (1986).

369. Herman, P. & Lee, J. C. *The Advantage of Global Fitting of Data Involving Complex Linked Reactions* (Springer, New York, 2012).

370. Fita, P., Luzina, E., Dziembowska, T., Radzewicz, C. & Grabowska, A. Chemistry, photophysics, and ultrafast kinetics of two structurally related Schiff bases containing the naphthalene or quinoline ring. *J. Chem. Phys.* **125 (18),** 184508 (2006).

371. Kovalenko, S. A., Dobryakov, A. L., Ruthmann, J. & Ernsting, N. P. Femtosecond spectroscopy of condensed phases with chirped supercontinuum probing. *Phys. Rev. A* **59,** 2369 (1999).

372. Rudawski, P., Heyl, C. M., Brizuela, F., Schwenke, J., Persson, A., Mansten, E., Rakowski, R., Rading, L., Campi, F., Kim, B., Johnsson, P. & L'Huillier, A. A high-flux high-order harmonic source. *Rev. Sci. Instrum.* **80,** 073103 (2013).

373. Steingrube, D. S., Vockerodt, T., Schulz, E., Morgner, U. & Kovačev, M. Phase matching of high-order harmonics in a semi-infinite gas cell. *Phys. Rev. A* **80,** 043819 (2009).

374. Hafner, A., Anklamm, L., Firsov, A., Firsov, A., Lochel, H., Sokolov, A., Gubzhokov, R. & Erko, A. Reflection zone plate wavelength-dispersive spectrometer for ultra-light elements measurements. *Opt. Express* **23,** 29476–29483 (2015).

375. J.Metje, Borgwardt, M., Moguilevski, A., Kothe, A., Engel, N., Wilke, M., Al-Obaidi, R., Tolksdorf, D., Firsov, A., Brzhezinskaya, M., Erko, A., Kiyan, I. Y. & Aziz, E. F. Monochromatization of femtosecond XUV light pulses with the use of reflection zone plates. *Opt. Express* **22,** 10747–10760 (2014).

376. Myers, O. E. Studies of transmission zone plates. *Am. J. Phys* **19,** 359–365 (1951).

377. Brzhezinskaya, M., Firsov, A., Holldack, K., Kachel, T., Mitzner, R., Pontius, N., Schmidt, J.-S., Sperling, M., Stamm, C., Fohlisch, A. & Erko, A. A novel monochromator for experiments with ultrashort X-ray pulses. *J. Synchrotron Rad* **20,** 5227–530 (2013).

378. Schäfers, F. *The BESSY Raytrace Program RAY. In: A. Erko, M. Idir, T. Krist, A. G. Michette (eds) Modern Developments in X-Ray and Neutron Optics* (Springer, Berlin, Heidelberg, 2008).

379. Kan, C., Capjack, C. E., Rankin, R. & Burnett, N. H. Spectral and temporal structure in high harmonic emission from ionizing atomic gases. *Phys. Rev. A* **52 (6),** R4336–R4339 (1995).

380. Shin, H. J., Lee, D. G., Cha, Y. H., Hong, K. H. & Nam, C. H. Generation of Nonadiabatic Blueshift of High Harmonics in an Intense Femtosecond Laser Field. *Phys. Rev. Lett.* **83 (13),** 2544–2547 (1999).

381. Brunetti, E., Issac, R. & Jaroszynski, D. A. Quantum path contribution to high-order harmonic spectra. *Phys. Rev. A* **77 (2),** 023422 (2008).

382. Papadogiannis, N., Kalpouzos, C., Goulielmakis, E., Nersisyan, G., Charalambidis, D., Auge, F., Weihe, F. & Balcou, P. Kilohertz extreme ultraviolet light source based on femtosecond high-order harmonic generation from noble gases. *Appl. Phys. B* **73,** 687–692 (2001).

383. Altucci, C., Bruzzese, R., de Lisio, C., Nisoli, M., Stagira, S., Silvestri, S. D., Svelto, O., Boscolo, A., Ceccherini, P., Poletto, L., Tondello, G. & Villoresi, P. Tunable soft-x-ray radiation by high-order harmonic generation. *Phys. Rev. A* **61 (2),** 021801 (1999).

384. Wang, Y., Liu, Y., Yang, X. & Xu, Z. Spectral splitting in high-order harmonic generation. *Phys. Rev. A* **62,** 063806 (2000).

385. Fangchuan, Z., Zhong, L., Zhinan, Z., Zhengquan, Z., Ruxin, L. & Zhizhan, X. Spectral splitting of high-order harmonic emissions from ionizing gases. *Phys. Rev. A* **65,** 033808 (2002).

386. Zhong, F., Deng, J., Hu, X., Li, Z., Zhang, Z. & Xu, Z. The effect of ionization of gases on the high harmonic splitting. *Phys. Lett. A* **278,** 35–43 (2000).

387. Cucini, R. *et al.* Coherent narrowband light source for ultrafast photoelectron spectroscopy in the 17–31 eV photon energy range. *Struct. Dyn.* **7,** 014303 (2020).

388. Popmintchev, T., Chen, M.-C., Bahabad, A., Gerrity, M., Sidorenko, P., Cohen, O., Christov, I. P., Murnane, M. M. & Kapteyn, H. C. Phase matching of high harmonic generation in the soft and hard X-ray regions of the spectrum. *PNAS* **106 (26),** 10516–10521 (2009).

389. Falcao-Filho, E. L., Gkortsas, V. M., Gordon, A. & Kärtner, F. X. Analytic scaling analysis of high harmonic generation conversion efficiency. *Opt. Express* **17,** 11217–11229 (2009).

390. Velchev, I., Hogervorst, W. & Ubachs, W. Precision VUV spectroscopy of Ar I at 105 nm. *J. Phys. B: At. Mol. Opt. Phys* **32,** L511–L516 (1999).

391. Weingartshofer, A., Holmes, J., Caudle, G., Clarke, E. & KKrüger, H. Direct observation of multiphoton processes in laser-induced free-free transitions. *Phys. Rev. Lett.* **39 (5),** 269–270 (1977).

392. Glover, T. E., Schoenlein, R. W., Chin, A. H. & Shank, C. V. Observation of laser assisted photoelectric effect and femtosecond high order harmonic radiation. *Phys. Rev. Lett.* **76 (14),** 2468–2471 (1996).

393. Miaja-Avila, L., Lei, C., Aeschlimann, M., Gland, J. L., Murnane, M. M., Kapteyn, H. C. & Saathoff, G. Laser-assisted photoelectric effect from surfaces. *Phys. Rev. Lett.* **97 (11),** 113604 (2006).

394. Saathoff, G., Miaja-Avila, L., Aeschlimann, M., Murnane, M. M. & Kapteyn, H. C. Laser-assisted photoemission from surfaces. *Phys. Rev. A* **77 (2),** 022903 (2008).

395. Arrell, C. A., Ojeda, J., Mewes, L., Grilj, J., Frassetto, F., Poletto, L., van Mourik, F. & Chergui, M. Laser-assisted photoelectric effect from liquids. *Phys. Rev. Lett.* **117 (14),** 143001 (2016).

396. Chung, Y.-W. *Practical guide to surface science and spectroscopy* (Academic press, 2001).

397. Freda, M., Piluso, A., Santucci, A. & Sassi, P. Transmittance Fourier transform infrared spectra of liquid water in the whole mid-infrared region: temperature dependence and structural analysis. *Appl. Spectrosc.* **59 (9),** 1155–1159 (2005).

398. Petit, T. *et al.* Unusual Water Hydrogen Bond Network around Hydrogenated Nanodiamonds. *J. Phys. Chem. C* **121 (9),** 5185—5194 (2017).

399. Taylor, A. W., Lovelock, K. R. J., Deyko, A., Licence, P. & Jones, R. G. High vacuum distillation of ionic liquids and separation of ionic liquid mixtures. *Phys. Chem. Chem. Phys.* **12,** 1772—1783 (2010).

400. Li, P., Paul, D. R. & Chung, T.-S. High performance membranes based on ionic liquid polymers for CO_2 separation from the flue gas. *Green Chem.* **14,** 1052—1063 (2012).

401. Zhang, Z., Feng, J., Jiang, Y. & Feng, J. High-pressure salt templating strategy toward intact isochoric hierarchically porous carbon monoliths from ionic liquids. *RSC Adv.* **7,** 51096–51103 (2017).

402. Raheem, A. A. Investigations of Photoinduced Ultrafast Dynamics in Metal Coordination Complexes Using Time-Resolved Photoemission and Absorption Spectroscopy. *PhD thesis, Fachbereich Physik, Freie Universität Berlin* (2019).

403. Borgwardt, M., Wilke, M., Kiyan, I. Y. & Aziz, E. F. Ultrafast excited states dynamics of $[Ru(bpy)_3]^{2+}$ dissolved in ionic liquids. *Phys. Chem. Chem. Phys.* **18,** 28893–28900 (2016).

404. LeBlanc, D. C. *Statistics: Concepts and Applications for Science* (US, Jones and Bartlett, 2004).

405. Iikura, H., Tsuneda, T., Yanai, T. & Hirao, K. A Long-Range Correction Scheme for Generalized-Gradient-Approximation Exchange Functionals. *J. Chem. Phys* **115,** 3540–3544 (2001).

406. Balabanov, N. B. & Peterson, K. A. Systematically Convergent Basis Sets for Transition Metals. I. All-Electron Correlation Consistent Basis Sets for the 3d Elements Sc–Zn. *J. Chem. Phys.* **123,** 064107 (2005).

407. Kendall, R. A., Dunning, T. H. & Harrison, R. J. Electron Affinities of the First-row Atoms Revisited. Systematic Basis Sets and Wave Functions. *J. Chem. Phys* **96,** 6796–6806 (1992).

408. Bokarev, S. I., Bokareva, O. S. & Kühn, O. A Theoretical Perspective on Charge Transfer in Photocatalysis. The Example of Ir-Based Systems. *Coord. Chem. Rev.* **304-305,** 133–145 (2015).

409. Bokareva, O. S., Grell, G., Bokarev, S. I. & Kühn, O. Tuning Range-Separated Density Functional Theory for Photocatalytic Water Splitting Systems. *J. Chem. Theor. Comput.* **11,** 1700–1709 (2015).

410. Marenich, A. V., Cramer, C. J. & Truhlar, D. G. Universal Solvation Model Based on Solute Electron Density and on a Continuum Model of the Solvent Defined by the Bulk Dielectric Constant and Atomic Surface Tensions. *J. Phys. Chem. B* **113,** 6378–6396 (2009).

411. Hunger, J., Stoppa, A., Schrödle, S., Hefter, G. & Buchner, R. Temperature Dependence of the Dielectric Properties and Dynamics of Ionic Liquids. *Chem. Phys. Chem.* **10,** 723–733 (2009).

412. Hu, X., Zhang, S., Qu, C., Zhang, Q., Lu, L., Ma, X., Zhang, X. & Deng, Y. Ionic Liquid Based Variable Focus Lenses. *Soft Matter* **7,** 5941 (2011).

413. Bernales, V. S., Marenich, A. V., Contreras, R., Cramer, C. J. & Truhlar, D. G. Quantum Mechanical Continuum Solvation Models for Ionic Liquids. *J. Phys. Chem. B* **116,** 9122–9129 (2012).

414. Frisch, M. J., Trucks, G. W., Schlegel, H. B., Scuseria, G. E., Robb, M. A., Cheeseman, J. R., Scalmani, G., Barone, V., Petersson, G. A. & Nakatsuji, H. Gaussian 16 Revision C.01. 00003 (2016).

415. Huang, K. & Rhys, A. Theory of light absorption and non-radiative transitions in F-centres. *Proc. R. Soc. Lond. A* **204,** 406–423 (1950).

416. Kurahashi, N., Karashima, S., Tang, Y., Horio, T., Abulimiti, B., Suzuki, Y.-I., Ogi, Y., Oura, M. & Suzuki, T. Photoelectron spectroscopy of aqueous solutions: Streaming potentials of NaX (X = Cl, Br, and I) solutions and electron binding energies of liquid water and X. *J. Chem. Phys.* **140,** 174506 (2014).

417. Roos, A. & Ribbing, C. G. Interpretation of integrating sphere signal output for non-Lambertian samples. *Appl. Opt.* **27,** 3833–3837 (1988).

418. Jorge, A. B., Martin, D. J., Dhanoa, M. T. S., Rahman, A. S., Makwana, N., Tang, J., Sella, A., Cora, F., Darr, J. A. & McMilan, P. F. H_2 and O_2 evolution from water half-splitting reactions by graphitic carbon nitride materials. *J. Phys. Chem. C* **117,** 7178–7185 (2013).

419. Merschjann, C., Tschierlei, S., Tyborski, T., Kailasam, K., Orthmann, S., Hollmann, D., Schedel-Niedrig, T., Thomas, A. & Lochbrunner, S. Complementing graphenes: 1D interplanar charge transport in polymeric graphitic carbon nitrides. *Adv. Mater.* **27(48),** 7993—7999 (2015).

420. Zhang, H., Chen, Y., Lu, R., Li, R. & Yu, A. Charge carrier kinetics of carbon nitride colloid: a femtosecond transient absorption spectroscopy study. *Phys. Chem. Chem. Phys.* **18,** 14904–14910 (2016).

421. Godin, R., Wang, Y., Zwijnenburg, M. A., Tang, J. & Durrant, J. R. Time-Resolved Spectroscopic Investigation of Charge Trapping in Carbon Nitrides Photocatalysts for Hydrogen Generation. *J. Am. Chem. Soc.* **139 (14),** 5216—5224 (2017).

422. Alivisatos, A. P. Semiconductor Clusters, Nanocrystals, and Quantum Dots. *Science* **271 (5251),** 933–937 (1996).

423. Hollmann, D., Karnahl, M., Tschierlei, S., Kailasam, K., Schneider, M., Radnik, J., Grabow, K., Bentrup, U., Junge, H., Beller, M., Lochbrunner, S., Thomas, A. & Brückner, A. Structure–Activity Relationships in Bulk Polymeric and Sol–Gel-Derived Carbon Nitrides during Photocatalytic Hydrogen Production. *Chem. Mater.* **26,** 1727–1733 (2014).

424. Deifallah, M. & McMilan, P. F. Electronic and structural properties of two-dimentional carbon nitride graphenes. *J. Phys. Chem. C* **112,** 5447 (2008).

425. Ehrmaier, J., Rabe, E. J., Pristash, S. R., Corp, K. L., Schlenker, C. W., Sobolewski, A. L. & Domcke, W. Singlet-Triplet Inversion in Heptazine and in Polymeric Carbon Nitrides. *J. Phys. Chem. A* **123,** 8099–8108 (2019).

426. Vargas, W. E. & Niklasson, G. A. Applicability conditions of the Kubelka–Munk theory. *Appl. Opt.* **36,** 5580 (1997).

427. Tauc, J., Grigorovici, R. & Vancu, A. Optical properties and electronic structure of amorphous germanium. *Phys. Status Solidi* **15,** 627–637 (1966).

428. Davis, E. A. & Mott, N. F. Conduction in non-crystalline systems V. Conductivity, optical absorption and photoconductivity in amorphous semiconductors. *Philos. Mag.* **22,** 903–922 (1970).

429. Winter, B. Liquid microjet for photoelectron spectroscopy. *Nucl. Instrum. Methods Phys. Res. A: Accel. Spectrom. Detect. Assoc. Equip.* **601 (1),** 139–150 (2009).

430. Inoki, H., Seo, G. & Kanai, K. Synthesis of Graphitic Carbon Nitride under Low Ammonia Partial Pressure. *Appl. Surf. Sci.* **534,** 147569 (2020).

431. Hammer, P., Victoria, N. M. & Alvarez, F. Effects of increasing nitrogen concentration on the structure of carbon nitride films deposited by ion beam assisted deposition. *J. Vac. Sci. Technol. A* **18,** 2277–2287 (2000).

432. Souto, S., Pickholz, M., dos Santos, M. C. & Alvarez, F. Electronic structure of nitrogen-carbon alloys (aCNx) determined by photoelectron spectroscopy. *Phys. Rev. B* **57 (4),** 2536—2540 (1998).

433. Thürmer, S., Malerz, S., Trinter, F., Hergenhahn, U., Lee, C., Neumark, D. M., Meijer, G., Winter, B. & Wilkinson, I. Accurate vertical ionization energy and work function determinations of liquid water and aqueous solutions. *Chem. Sci.* **12,** 10558–10582 (2021).

434. Nishizawa, K., Kurahashi, N., Sekiguchi, K., Mizuno, T., Ogi, Y., Horio, T. & Suzuki, T. High-resolution soft X-ray photoelectron spectroscopy of liquid water. *Phys. Chem. Chem. Phys.* **13 (2),** 413—417 (2011).

435. Credidio, B., Pugini, M., Malerz, S., Trinter, F., Hergenhahn, U., Wilkinson, I., Thürmer, S. & Winter, B. Quantitative electronic structure and work-function changes of liquid water induced by solute. *Phys. Chem. Chem. Phys.* **24,** 1310—1325 (2022).

436. Manke, A.-M., Geisel, K., Fetzer, A. & Kurz, P. A water-soluble tin(iv) porphyrin as a bioinspired photosensitiser for light-driven proton-reduction. *Phys. Chem. Chem. Phys.* **16 (24),** 12029—12042 (2014).

437. Pellegrin, Y. & Odobel, F. Sacrificial electron donor reagents for solar fuel production. *C. R. Chim.* **20 (3),** 283—295 (2017).

438. Mazzanti, S., Kurpil, B., Pieber, B., Antonietti, M. & Savateev, A. Dichloromethylation of enones by carbon nitride photocatalysis. *Nat. Commun.* **11,** 1387 (2020).

439. Corp, K. L. & Schlenker, C. W. Ultrafast spectroscopy reveals electron-transfer cascade that involves hydrogen evolution with carbon nitride photocatalysts. *J. Am. Chem. Soc.* **139,** 7904–7912 (2017).

440. Grancini, G., Maiuri, M., Fazzi, D., Petrozza, A., Egelhaaf, H. J., Brida, D., Cerullo, G. & Lanzani, G. Hot exciton dissociation in polymer solar cells. *Nat Mater.* **12 (1),** 29–33 (2013).

441. Vazquez, H. & Troisi, A. Calculation of rates of exciton dissociation into hot charge-transfer states in model organic photovoltaic interfaces. *Phys. Rev. B* **88,** 205304 (2013).

442. Hertel, T., Fasel, R. & Moos, G. Charge-carrier dynamics in single-wall carbon nanotube bundles: a time-domain study. *Appl. Phys. A* **75,** 449—465 (2002).

443. Scheblykin, I. G., Yartsev, A., Pullerits, T., Gulbinas, V. & Sundström, V. Excited State and Charge Photogeneration Dynamics in Conjugated Polymers. *J. Phys. Chem. B* **111 (23),** 6303—6321 (2007).

444. Wang, H., Jiang, S., Chen, S., Zhang, X., Shao, W., Sun, X., Zhao, Z., Zhang, Q., Luo, Y. & Xie, Y. Insights into the excitonic processes in polymeric photocatalysts. *Chem. Sci.* **8,** 4087–4092 (2017).

445. Jing, L., Zhu, R., Phillips, D. L. & Yu, J. C. Photocatalysis: effective prevention of charge trapping in graphitic carbon nitride with nanosized red phosphorus modification for superior photo(electro)catalysis. *Adv. Funct. Mater.* **27,** 1703484 (2017).

446. Merschjann, C., Tyborski, T., Orthmann, S., Yang, F., Schwarzburg, K., Lublow, M., Lux-Steiner, M.-C. & Schedel-Niedrig, T. Photophysics of polymeric carbon nitride: An optical quasimonomer. *Phys. Rev. B* **87,** 205204 (2017).

447. Cowan, A. J., Tang, J., Leng, W., Durrant, J. R. & Klug, D. R. Water Splitting by Nanocrystalline TiO_2 in a Complete Photoelectrochemical Cell Exhibits Efficiencies Limited by Charge Recombination. *J. Phys. Chem. C* **114,** 4208–4214 (2010).

448. Ohkita, H. & Ito, S. Transient absorption spectroscopy of polymer-based thin-film solar cells. *Polymer* **52 (20),** 4397–4417 (2011).

449. Franchini, C., Reticcioli, M., Setvin, M. & Diebold, U. Polarons in materials. *Nat Rev Mater* **6,** 560–586 (2021).

450. Fridh, C., Åsbrink, L., Jonsson, B. & Lindholm, E. XIV. Photoelectron, uv, mass and electron impact spectra of s-triazine. *Int J Mass Spectrom Ion Phys* **8,** 85–99 (1972).

451. Holland, D., Shaw, D., Stener, M., Decleva, P. & Coriani, S. A study of the valence shell electronic states of s-triazine by photoabsorption spectroscopy and ab initio calculations. *Chem Phys* **477,** 96–104 (2016).

452. Ehrmaier, J., Janicki, M. J., Sobolewski, A. L. & Domcke, W. Mechanism of photocatalytic water splitting with triazine-based carbon nitrides: insights from iab initio/i calculations for the triazine–water complex. *Phys Chem Chem Phys* **20,** 14420–14430 (2018).

453. Ehrmaier, J., Karsili, T. N. V., Sobolewski, A. L. & Domcke, W. Mechanism of Photocatalytic Water Splitting with Graphitic Carbon Nitride: Photochemistry of the Heptazine–Water Complex. *J Phys Chem A* **121,** 4754–4764 (2017).

454. Ehrmaier, J., Rabe, E. J., Pristash, S. R., Corp, K. L., Schlenker, C. W., Sobolewski, A. L. & Domcke, W. Singlet-Triplet Inversion in Heptazine and in Polymeric Carbon Nitrides. *J Phys Chem A* **123,** 8099–8108. ISSN: 1089-5639, 1520-5215. `https://pubs.acs.org/doi/10.1021/acs.jpca.9b06215` (2019) (2019).

455. Koopmans, T. Ordering of Wave Functions and Eigenenergies to the Individual Electrons of an Atom. *Physica* **1,** 104–113 (1933).

456. Helgaker, T., Jorgensen, P. & Olsen, J. *Molecular Electronic-Structure Theory* (John Wiley and Sons, 2013).

457. Kasha, M. Characterization of electronic transitions in complex molecules. *Discuss. Faraday Soc.* **9,** 14–19 (1950).

458. Cristina, G. I. & Marazzi, M. *Theoretical and Computational Photochemistry* (Elsevier, 2023).

Publications

1. N. Kuzkova, I. Yu. Kiyan, I. Wilkinson and C. Merschjann
   Ultrafast dynamics in polymeric carbon nitride thin films probed by time-resolved EUV photoemission and UV-Vis transient absorption spectroscopy
   Phys. Chem. Chem. Phys. 25, 27094-27113 (2023).

2. N. Kuzkova, A. A. Raheem, S. I. Bokarev, I. Wilkinson and I. Yu. Kiyan
   Relaxation dynamics of electronically photoexcited $[Fe(CN)_6]^{3-}$ in water and an ionic liquid environment probed by femtosecond time-resolved EUV photoemission spectroscopy
   (in preparation)

3. I. Yu. Kiyan, N. Kuzkova, S. Ahsan, A. Firsov and I. Wilkinson
   Monochromatization of ultrashort light pulses from high harmonic generation in the 10 - 100 eV photon energy range with the use of reflective zone plates
   (in preparation)

Acknowledgements

Since childhood, I have had a passion for nature and science, and I have always been curious about how the world works and why there are different things around us. I dreamed of becoming a scientist who could contribute to society by exploring new horizons in the natural sciences. My research pathway included circumstances that many times pulled me in different directions, but I keep my dreams alive. At this stage of my scientific career, I feel grateful for all of the challenges that I have faced. Nonetheless, these challenges would not have been overcome without the presence of a number of dear colleagues, mentors and family members. Therefore, I would like to take this opportunity to thank the following people who have given their invaluable support and encouragement on the path to my doctoral degree.

I would first like to express my utmost gratitude to my primary supervisor *Dr. Iain Wilkinson* at Helmholtz-Zentrum Berlin, for his marvelous supervision, inspiration, unconditional guidance and kind support during my PhD. He made a great contribution to my scientific work and helped me develop as a researcher and as a person, always believing in me at every stage of my studies. Without his immense knowledge and dedication, this dissertation would not have materialised. I am incredibly proud and happy to have worked with him. He taught me about the beauty of scientific pursuit.

I would also like to thank *Prof. Martin Weinelt* at Freie Universität Berlin for his willingness to evaluate this thesis and for his insightful comments and suggestions.

I would like to say a special thank you to my co-supervisor *Dr. Igor Kiyan* at Helmholtz-Zentrum Berlin, for giving me the opportunity to conduct this PhD project in the ULLAS group, sharing his plentiful experience and assistance during the experiments. He has boosted my confidence in working with laser systems and TRPES as well as HHG setups autonomously, which made me grow as an independent researcher. I am very grateful for his senior guidance, tutelage, and patience during my doctorate studies.

From the bottom of my heart I would like to say big thank you for all the ULLAS and LIDUX group members, and generally, PS-ALTS team at Helmholtz-Zentrum Berlin, for their constant support and assistance throughout my project, which helped me to overcome many challenges at everyday work. I am greatly indebted to *Dr. Martin Wilke*, who was the first person to guide me through the practical lab work at the beginning of my PhD. I would also like to express my sincere gratitude to *Dr. Christoph Merschjann*, for his energy and enthusiasm invested in the TAS experiments. His practical guidance and precious advise on the data interpretation and analysis had a considerable impact on the formation of this dissertation. I am deeply grateful to *Dr. Ljiljana Puskar*, for her kind encouragement and assistance in performing FTIR experiments. I would like to extend my thanks to *Florian Gores* for all his help in developing and optimising the setups, his ingenious ideas and cordiality.

I would especially like to thank a few group members who have never hesitated to support me. Many thanks to *Dr. Karen Mudryk* for her outright friendship, for having my back at life's difficult moments and for celebrating with me when it was good. I also had great pleasure of working with *Md Sabbir Ahsan*, with whom I spent a lot of time together in the lab, optimising experiments and setups, and sharing experiences. Thank you for always allowing me to express my happiness and frustration and for reassuring me that all would be fine. I am very grateful to *Dr. Daniel Walke* for his fellowship, for giving insightful suggestions and for inspiring me to always take the extra step. I really enjoyed all the conversations and coffees with him, not only at work but also outside of it. I also wish to thank *Dr. Siqi Cheng* for providing a cooperative atmosphere at work and the many kindnesses he has shown to me.

I would like to express special gratitude to my former supervisors and institutions, without which my research path would not have been possible to begin with. I am greatly indebted and thankful to *Assoc. Prof. Andriy Yakunov* at Taras Shevchenko National University of Kyiv, who supervised me throughout the graduate studies. He has invested a lot of knowledge and energy in me, which I engrave in my personal and professional life everyday. It is difficult to find words to describe how much he inspired me and what impact he had on my future decision to pursue my studies abroad.

I am also deeply grateful to *Prof. Tullio Scopigno* at Sapienza University of Rome, for giving me the opportunity to carry out my master's research project as a visiting scholar in his group. He introduced me to ultrafast spectroscopy and shared his vast knowledge and extensive expertise. Grazie infinite, è stata un'esperienza fruttuosa e indimenticabile per me.

I would also like to specially thank *Dr. Noëmie Bastidon*, who was my former colleague and good friend at DESY, for her constant support and kind heart. My time in Hamburg would not have been so enjoyable without her presence. Merci du fond du coeur!

I wish to acknowledge Helmholtz-Zentrum Berlin for funding my doctorate studies and giving me the opportunity to be part of one of the world's leading international scientific communities.

Last but not least, I am grateful to my dear family, father *Volodymyr*, mother *Tetiana*, and brother *Serge*, who showed me the value of education at an early age and raised me as a comprehensively developed personality. This dissertation stands as a testament to all your unconditional love and faith. Dad, you have always been an example for me to follow as a scientist who is passionate about his work. I spent my childhood among astronomical telescopes and optical elements. I believe that at that moment in my life I fell in love with optics. Thank you for these unforgettable memories. My dearest mom, I owe you everything I have achieved. Your abilities of a wonderful physics teacher and a talented artist were given to me as a gift. It has helped me many times in my professional and personal life. I am very grateful for your constant love, moral support and daily blessings. Brother, you have always been my rear guard, but first of all, a friend who taught me very different things, from football to music. As the Oasis song says, 'Maybe you're the same as me. We see things they'll never see. You and I are gonna live forever'.

Найбільше я вдячна моїй дорогій родині, батькові Володимиру, матері Тетяні та брату Сержу, які змалку показали мені цінність освіти і виховали як всебічно розвинену особистість. Ця дисертація є свідченням усієї вашої безумовної любові та віри. Тату, ти завжди був для мене прикладом для наслідування як вченого, який захоплюється своєю роботою. Моє дитинство пройшло серед астрономічних телескопів і оптичних елементів. Я думаю, що саме в той момент свого життя я полюбила оптику. Дякую тобі за ці незабутні спогади. Моя найдорожча мамо, я зобов'язана тобі всім, чого досягла. Твої здібності чудового вчителя фізики і талановитого художника були дані мені як подарунок. Це багато разів допомагало мені в моєму професійному та особистому житті. Я дуже вдячна за твою постійну любов, моральну підтримку та щоденні благословення. Брате, ти завжди був моїм тилом, але перш за все другом, який навчив мене дуже різним речам, починаючи від футболу і закінчуючи музикою. Як говориться в пісні Oasis: «Може бути, ти такий же, як я. Ми бачимо те, чого вони ніколи не побачать. Ми з тобою будемо жити вічно».

Declaration of Authorship

Last name: Kuzkova
First name: Nataliia

I declare to the Freie Universität Berlin that I have completed the submitted dissertation independently and without the use of sources and aids other than those indicated. The present thesis is free of plagiarism. I have marked as such all statements that are taken literally or in content from other writings. This dissertation has not been submitted in the same or similar form in any previous doctoral procedure.

I agree to have my thesis examined by a plagiarism examination software.

Nataliia Kuzkova
13.01.2023